UNIVERSITÀ
DEGLI STUDI
FIRENZE

DIPARTIMENTO DI FISICA E ASTRONOMIA

CORSO DI DOTTORATO IN FISICA E ASTRONOMIA
CICLO XXXVII

A panchromatic journey in the quasar environment: wandering through the same place at different times

Un viaggio pancromatico nell'ambiente dei quasar: vagando per lo stesso posto in tempi diversi

Candidate
Bartolomeo Trefoloni (ID number DT31251)

Thesis Advisors
Prof.ssa Lusso Elisabeta
Prof. Risaliti Guido

Academic Year 2023/2024

Contents

Outline

Active Galactic Nuclei are the most luminous persistent sources in the Universe. The mechanism powering their emission is the accretion of matter onto a supermassive black hole (SMBH) at the center of a galaxy. Because of their prevalence and exceptional luminosities, ranging between $\sim 10^{40} - 10^{48}\,\mathrm{erg\,s^{-1}}$ they can be observed on cosmological distances. These characteristics make AGN a class of astrophysical sources of particular relevance for several reasons. The huge energy output of the SMBH has been shown capable of deeply influencing the galaxy harbouring the AGN. In light of this, AGN are deemed to be one of the key ingredients in the assembly history of the Universe. The traces of the symbiosis between the SMBH and the host galaxy are generally epitomised in a series of correlations between the mass of the SMBH and many of the host galaxy's characteristic parameters. At the same time, it has recently been shown that, employing the relation between their X-ray and UV luminosity, and thanks to an accurate selection, AGN can be turned into a new class of "standardised candles". Yet, both the comprehension of the importance of the AGN in shaping the host galaxy, as well as the cosmological implementation of AGN, subsume a profound understanding of the functioning of their innermost engine. The nuclear region is indeed a complicated environment, where multiple interacting components contribute to the spectral appearance of the AGN. Understanding the interplay between these different regions, as well as tracing their possible evolution over cosmic time is an essential step towards unveiling their relevance in the process of galaxy evolution and to unlock their full potential as standard candles.

In this thesis I investigated, adopting a multi-wavelength approach, from the X-rays, through the UV and optical up to the infrared, the properties of the different regions building the nuclear structure, tracing their evolution up to remote cosmic times.

In Chapter 1 I introduce the main AGN properties and the "Unified Model" of AGN. There I also briefly delve into their impact on their host galaxies and the challenges posed by the presence of SMBH at primordial times. Furthermore, I also introduce the current cosmological framework and its fundamental parameters. This cosmological framework is challenged by use of quasars as standard candles, recently made possible via a novel technique taking advantage of the relation between the X-ray and the UV luminosity in quasars, also presented in this Chapter.

The second Chapter (2) is devoted to explaining how my work was relevant for dispelling possible observational biases which could hinder the reliability of this new class of standard candles. In particular there I also focus on the remarkable regularity in the UV and optical properties of typical blue quasars, across a wide parameter space.

In Chapter 3 I analyse the optical and spectral properties of a unique sample. The sources described therein offer the unique possibility to study both the most luminous quasars at $z \sim 3$ for their cosmological application, as well as to shed light on the phenomenon of *X-ray weakness*.

Chapter 4 is dedicated to the evolution of the properties of the dusty torus in a large sample of blue quasars. In particular, there I test how the near-infrared spectral properties of this sample change as a function of the main disc continuum and redshift.

In the fifth Chapter (5) I shift the analysis of the spectral properties of AGN to remote cosmic times, investigating the characteristics of the broad line region in high-redshift ($z \gtrsim$6.5) probed by the optical Fe II in a sample of AGN observed by *JWST*.

Finally, the Chapter 6 is dedicated to summarise the results of this work and outline possible future developments.

Chapter 1

Introduction

Active Galactic Nuclei (AGN) are incredibly bright and powerful objects. Because of their luminosity and prevalence, I observe them across all cosmic times, and their effects on their host galaxies make them essential ingredients in the process of galactic evolution. In my research, I focused on the study of AGN both to demonstrate that they can be turned into powerful cosmological tools, but also because they are fascinating objects *per se.* AGN offer indeed the unique possibility to shed light on the mechanism of accretion onto super-massive black holes (SMBH) on a wide range of accretion parameters and trace its evolution throughout different cosmic epochs. In this Chapter I will introduce this class of astrophysical sources, focusing on their observational properties, the effect on their host galaxies and how they can be turned into a new class of *standardised candles.*

1.1 Active Galactic Nuclei

Approximately 1-10% of galaxies host a central region that exhibits emissions with intensities, spectral characteristics, and timing behaviors that cannot be explained by typical galactic components like stars, gas, or dust. These sources are called "Active galactic nuclei" (AGN). Within the AGN category, objects whose emission outshines the host galaxy are known as "Quasars" (Quasi-Stellar Objects, or QSOs). Quasars are the brightest persistent sources in the Universe, observable up to a redshift of about z~7, dating back to when the Universe was less than 1 billion years old.

AGN share several key characteristics:

- Extremely high luminosities, ranging from 10^{11} to a few 10^{14} solar luminosities ($L_\odot$), coming from regions smaller than one parsec.

- Their spectral energy distribution (SED) spans the whole electromagnetic spectrum, from gamma rays (in the case of jetted AGN) to radio, mainly due to synchrotron emission. The shape and the energies characterising the SED cannot be explained in terms of the combination of stellar spectra.

- Roughly 10% of AGN have relativistic jets which both models and observations find to be mostly aligned with the axis of the galaxy and extending up to the

Megaparsec scale. Such sources are prominent radio emitters with their radio luminosity (L_R) reaching as high as $L_R \sim 10^8 - 10^{10}\,L_\odot$.

- The presence of both emission lines with full width at half maximum (FWHM) both larger and smaller than 1,000 $\mathrm{km\,s^{-1}}$. As I will explain shortly, narrow lines (FWHM $\lesssim 1,000\mathrm{km\,s^{-1}}$) and broad lines (FWHM $\gtrsim 1,000\,\mathrm{km\,s^{-1}}$) are thought to be produced in two physically different regions.
- Variability both in the line and continuum emission with timescales spanning from hours to tens of years, depending on the waveband.

This ensemble of features cannot be explained by stellar emission alone. If the luminosity observed in AGN were due to stars, a stellar mass of $\sim 10^{10}\,M_\odot$ would have to be contained within a region less than 1 pc, which is an unfeasible scenario, since such a system would collapse into a black hole (BH). The only known physical process capable of producing such powerful emissions is the accretion of matter onto a BH. The extreme gravitational potential enables a highly efficient conversion of mass into energy, with efficiencies reaching up to 28% of the rest energy (mc^2), far exceeding the $\sim 0.7\%$ efficiency of nuclear fusion processes. The widely accepted explanation for the primary AGN emission is an accretion disc around a SMBH, with mass in the range $10^6 - 10^9\,M_\odot$. The radiation coming from the accretion disc is then reprocessed by other regions within the nuclear environment and re-emitted in other wavebands, thus giving rise to a complicated SED.

1.1.1 The unified model of AGN

From an historical perspective, AGN are classified on the basis of their observational properties in different bands. Here I briefly highlight the main taxonomic categories.

- **Luminosity**: low-luminosity AGN are generally referred to as Seyfert galaxies, after Carl Seyfert who first classified them as AGN in 1943. These sources have a bolometric luminosity (L_{bol}) in the range $L_{bol} \sim 10^{41} - 10^{44}\,\mathrm{erg\,s^{-1}}$. Because of the relatively low luminosity, it is possible to discern their host galaxy, generally a spiral. The high-luminosity tail of the AGN population is occupied by quasars, which exhibit luminosities between $L_{bol} \sim 10^{44} - 10^{48}\,\mathrm{erg\,s^{-1}}$.
- **Width of emission lines**: objects presenting both broad and narrow emission lines are called Type 1 AGN, while objects only displaying narrow emission lines are referred to as Type 2 AGN.
- **Radio emission**: AGN can be defined as radio-loud or Radio-quiet on the basis of the presence or absence of substantial radio emission. The radioloundess parameter is generally defined as $R = L_\nu(5\,\mathrm{GHz})/L_\nu(4400\,\mathrm{Å})$, where L_ν denotes the monochromatic luminosity at a given frequency. Objects above $R = 10$ are categorised as radio-loud.
- **Radio morphology**: in the case of the presence of a radio-emitting jet, sources with a brighter jet towards their central galaxy and fainter toward the outer extremities of the lobes (also called edge-darkened) are called Fanaroff-Riley 1. Objects whose jets are edge-brightened and more luminous than their

counterparts are named Fanaroff-Riley 2. In the case of a line of sight co-axial with the jet, the object is called a Blazar.

The increasing number of observations of AGN presenting new features, following the discovery of initial Seyfert's galaxies, led to an expansive taxonomy. Yet, since the "80s the idea of a Unified Model of AGN began to gain success. This model proposed that the innermost nuclear region was fairly similar in all AGN, while the observed diversity was mainly due to different sightlines to the central engine. A breakthrough discovery to confirm this theory was the finding of broad lines in the polarised optical spectra of NGC 1068 (Antonucci and Miller 1985). The presence of broad lines also in an archetypal Type 2 Seyfert galaxy, meant that the innermost region of Type 1 and Type 2 AGN were chiefly the same, with the observational differences being produced by some obscuring medium. Prompted by the observational evidence, the Unified Model of AGN was proposed in 1995 (Urry and Padovani 1995). This model encapsulated all the observational differences within a simple picture as sketched in Fig. 1.1.

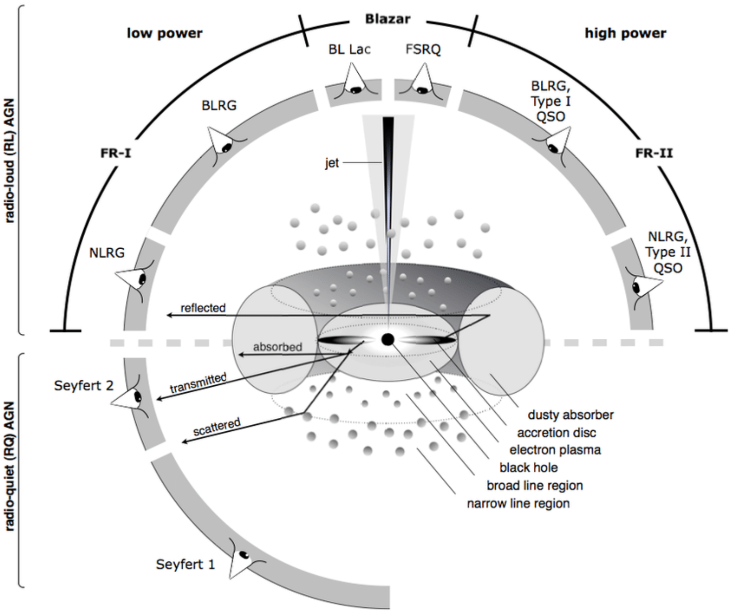

Figure 1.1. A sketch of the Unified Model of AGN (Beckmann and Shrader 2012). The different classes of AGN and the physical regions characterising the nuclear environment are labelled accordingly.

According to this picture, the engine of an AGN consists in an accretion disc around a SMBH which produces the main UV and optical continuum (see Fig.1.2). The main continuum from the accretion disc is then reprocessed by physically distinct regions. In the high-energy tail of the AGN SED, the UV photons are boosted via inverse Compton scattering at X-ray energies by a hot plasma called "corona", producing a comptonisation spectrum. If a jet is present, subatomic particles can be accelerated at relativistic speeds by shocks and Compton scattering, producing Gamma-rays. The synchrotron emission arising from the jet also characterises the radio spectrum of radio-loud AGN. Clouds of gas both close to the nuclear region and on galactic scales are responsible for the line emission. As already mentioned, narrow and broad lines are routinely observed in the optical and UV spectra of AGN. These two classes of lines display significantly different line widths, with the former having FWHM $\lesssim 1,000\,\mathrm{km\,s^{-1}}$ and the latter FWHM $\gtrsim 1,000\,\mathrm{km\,s^{-1}}$. This bi-modality hints at the fact that line emission is produced in -at least- two physically different regions. Broad permitted lines are produced in the innermost, dense ($n_e > 10^6\,\mathrm{cm^{-3}}$) region (BLR), likely below the parsec scale. Here dust-free clouds are thought to have somewhat virialised motions with velocities of the order of some thousand $\mathrm{km\,s^{-1}}$. On the other hand, narrow lines, which are both permitted and forbidden[1], exhibit smaller FWHM and are therefore thought to be far from the direct influence of the BH, on galactic scales in the narrow line region (NLR). In particular, the presence of forbidden lines points in the direction of a low-density environment for these lines to be produced ($n_e < 10^6\,\mathrm{cm^{-3}}$).

Another crucial element within the Unified Model is the dusty torus. This structure encircles the accretion disc on the parsec scale, being itself the likely reservoir of gas and dust ultimately feeding the accretion process. The torus is composed of molecular gas and dust at temperatures of the order of $T \sim 10^2 - 10^3\,\mathrm{K}$, outside the sublimation radius. Its emission, which is basically a re-processing of the disc continuum, dominates the IR SED of AGN. The torus is believed to be the most important structure within the AGN to deliver the obscuration responsible for the division in Type 1 and Type 2 AGN. Lowly inclined line of sights with respect to the disc (and torus) axis allow the observed to detect the presence of broad lines within the innermost funnel of the torus. However, highly inclined line of sights towards the central engine are obstructed by this structure, thus resulting in a Type 2 AGN. Notably, the torus might also be responsible for a reflection component in the X-rays.

It is important to stress that the several components constituting the AGN are tightly interconnected. The result of the interplay between the physical regions of the AGN is a series of well-know relations between different features of the AGN SED. For instance, the coupling between the X-ray corona and the UV disc is captured by the so-called $L_X - L_{UV}$ relation (which is discussed in depth in Sec.1.3). Here, an increase of one order of magnitude in the UV luminosity is followed by a concomitant increase of roughly 0.6 orders of magnitudes in the X-rays. Similarly, a non-linear relation (in logarithm) relates the optical emission coming from the disc and the near-infrared from the dusty torus. Although this relation is more thoroughly described in Chapter 4, it is possible to anticipate that this behaviour can is explained within the so-called "receeding torus", whereby the solid angle covered by the dusty torus tends to decrease for increasing disc luminosity. There are also other well-known correlations between the continuum luminosity and the

---

[1] The terms “permitted” and “forbidden” lines denote emission lines related to electronic transitions either allowed or disallowed by the electric dipole rule, respectively. Transitions from states with short lifetimes result in permitted lines, while metastable states with longer lifetimes produce forbidden transitions, which means that they are produced at a much reduced rate. Forbidden transitions are not usually observed in high-density environments where collisional de-excitation is more likely to occur than radiative de-excitation. A “critical density” can typically be defined, above which forbidden lines are not observed.

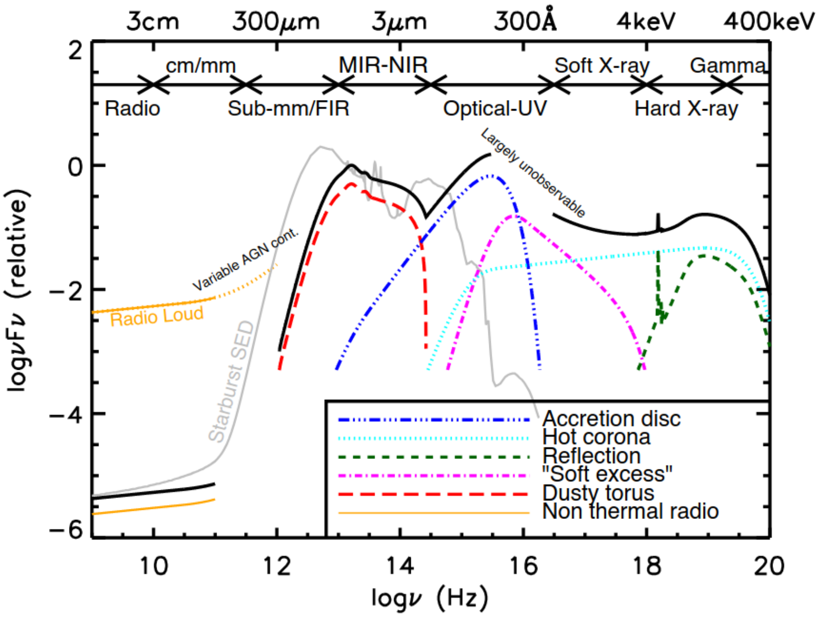

Figure 1.2. A sketch of the average SED of a Type 1 AGN (Harrison 2014). The physical regions responsible for the emission in each wave-band are labelled accordingly.

emission lines. As an example the equivalent width of high ionisation broad lines (e.g. C IV) tends to decrease for increasing continuum luminosity, a relation known as the Baldwin effect (Baldwin 1977). Many other correlations between the spectral features of AGN are known, such as those falling under the name of Eigenvector 1, discussed in 5.

A key question concerning the evolution of the physical mechanisms underlying the AGN phenomenon, which I will try in part to address in this thesis, is whether these correlations evolve with cosmic time. The question might be even more profound: does the SED of AGN even evolve with cosmic time? Any dependence of these relations with the redshift would imply that also the physical regions building the nucleus, or the way they interact, are actually evolving following the passing of time.

1.1.2 AGN in the context of galaxy evolution

The vast amounts of energy produced by the accretion process does not only affect the central regions but also the evolution of the entire host galaxy. There is indeed abundant observational evidence for a tight connection between properties of the AGN and those of the host galaxy, which is epitomised in several correlations between, for instance, the black hole mass and the velocity dispersion of the bulge stars (Ferrarese and Merritt, 2000, $\mathrm{M_{BH}} - \sigma$ relation), the black hole mass and the bulge luminosity (Gebhardt et al., 2000, $\mathrm{M_{BH}} - \mathrm{L_B}$), or the black hole mass and the stellar mass of the galaxy (Marconi and Hunt, 2003, $\mathrm{M_{BH}} - \mathrm{M_B}$). The several possible ways by which an AGN interacts with the surrounding gas, and ultimately influences the evolution of the galaxy harbouring it, fall under the concept of "AGN feedback". Feedback can be divided into two main modes, either radiative or kinetic. The radiative (or "quasar") mode is linked to high-luminosity AGN, where most energy is released via radiation or winds from the accretion disc, sometimes accompanied by radio jets. This mode drives gas outflows that expel material from the galaxy. This process can, therefore, ultimately halt star formation within the galaxy, by effectively starving it of the necessary materials for further growth. The kinetic (or "jet") mode is more frequently associated with low-power AGN, where the jets can create bubbles and cavities in the surrounding gas. The net effect of the jet is to heat the gas within the halo and prevent it from cooling and condensing to form stars. Kinetic feedback is especially significant in cluster environments, where it prevents the "cooling flow" of gas, thus inhibiting star formation across entire galaxy clusters. While the distinction between these two modes is clear in extreme cases (e.g., high-luminosity AGN and cool-core clusters), in more typical AGN, the separation can be less obvious.

Although it is still a matter of debate, AGN feedback has often been invoked as a likely responsible for the transition from star-forming to quenched galaxies for decades (e.g. Silk and Rees 1998). There is growing observational evidence for AGN outflows to deplete cold molecular gas, which is crucial for star formation (e.g. Cicone et al. 2014; Harrison et al. 2018). These outflows often reach velocities of hundreds to thousands of km s^{-1} (depending on the probed gas phase), expelling gas from galactic discs and bulges and even managing to shut down star formation entirely (e.g. Feruglio et al. 2010; Sturm et al. 2011). Yet, the reality behind the interplay between AGN outflows and star formation is perhaps more intricate. As a matter of fact, there are also pieces of evidence for AGN potentially triggering star formation under certain circumstances. Outflows or jets might compress gas in specific regions, leading to promote localised peaks of star formation (e.g. Zinn et al. 2013). The ambivalent role of the AGN within its own galactic environment as both a quenching and a potentially triggering agent of star formation suggests a complex interplay that depends on factors such as AGN luminosity, the phase of galactic evolution, as well as on the surrounding environment.

Another clue about the role of AGN in shaping their host galaxies comes from the evolution of the star formation rate density (SFRD) with redshift (Fig.1.3). Noticeably, The SFRD shows a dramatic evolution with the redshift, peaking at $z \sim 2-3$ (the so-called "cosmic noon") and declining towards the present time (Madau and Dickinson 2014). Interestingly also the AGN activity shows a peak coinciding with that of the SFRD (Shankar et al. 2008), thus suggesting that AGN could have been relevant in quenching star formation at these redshifts. At closer cosmic times, the AGN feedback likely depleted (or heated up) most of the gas reservoir necessary to fuel star formation, ultimately leading to the downturn in star formation.

Within this picture, massive galaxies merge to generate a massive black hole surrounded by dense gas feeding both star formation and an active nucleus. The power of the nucleus then blows the gas away, leaving a red, dead elliptical galaxy (e.g. Springel et al. 2005). The same mechanism is also called for explaining the cosmic downsizing of AGN (e.g. Scannapieco et al. 2005): the most luminous and massive AGN were more numerous at $z \sim 2-2.5$ (the "quasar epoch"), while became increasingly rarer at lower redshifts, with the least luminous AGN having been observed to peak around $z \sim 1$. This behaviour is antithetical to the expectations of a hierarchical cold dark matter Universe, where the most massive objects aggregate

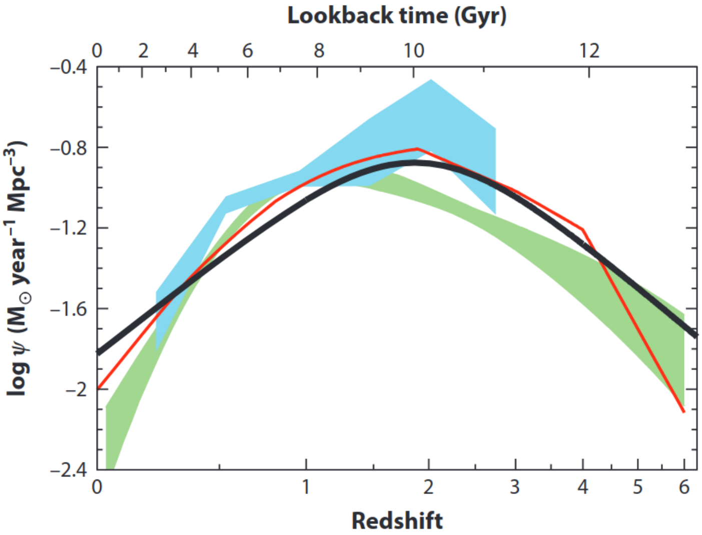

Figure 1.3. Comparison between the star formation and the black hole accretion history from Madau and Dickinson (2014). The thick solid curve is the best fit for the star formation density while the red curve and shaded areas represent the black hole accretion history from X-ray (green and red, respectively Shankar et al. 2008 and Aird et al. 2010) and infrared (azure, Delvecchio et al. 2014). The radiative efficiency here is set to $\epsilon = 0.1$. The comoving black hole accretion rates are scaled to match the star formation history.

last. The conclusion is that something is quenching quasar behavior, and the most widely accepted solution is AGN feedback.

Also from a theoretical perspective, AGN feedback is a key ingredient in the process of galaxy evolution. Cosmological simulations (e.g. Illustris, EAGLE, TNG) incorporated AGN feedback as an essential component in order to reproduce realistically galaxy populations and distributions. Here, the feedback provided by AGN has been shown to be a fundamental agent in preventing the formation of too many stars in massive galaxies. A key result obtained by the implementation of AGN feedback in simulations it the successful reproduction of the observed star formation quenching (e.g. Vogelsberger et al. 2014; Schaye et al. 2015). Also, the average star formation rates and the cold gas fraction observed at low redshift would not be reproduced without the addition of AGN feedback in the simulation framework.

Whilst the direct connection between the black hole activity and its possible effects on galactic scales remains enigmatic, the symbiosis between the SMBH and the host galaxy is apparent. Understanding how this interplay evolves at different cosmic times, yields the potential to unveil the physical mechanism at the basis of this fundamental connection.

1.1.3 Tracing the accretion history of the Universe

A growing number of high redshift ($z > 4$) quasars has been discovered in the last decades. Although very rare, with number densities around $\sim 1\,\mathrm{Gpc}^{-3}$, the discovery of SMBH, up to primordial times, severely challenges our understanding of both the accretion mechanism and black holes formation. For instance, assuming a constant accretion at the Eddington limit and a radiative efficiency of ϵ=0.1, quasars powered by SMBH with $\mathrm{M_{BH}} \sim 10^9 - 10^{10}\,\mathrm{M_\odot}$ at z> 6, would require initial black hole "seeds" with $\mathrm{M_{BH}} \sim 10^3\,\mathrm{M_\odot}$ at z ~20 (e.g. Zappacosta et al. 2023). Although these objects are not likely representative of the whole AGN population at these redshifts, which is mostly made of fainter undetected sources, the prediction of at least as many of these sources as observed represents a test for any plausible cosmological model.

Several mechanisms have been proposed to grow such massive BH at these remote cosmic epochs. They could either form from heavy seeds ($10^4 - 10^6\,\mathrm{M_\odot}$) accreting close to the Eddington limit (e.g. Volonteri 2010; Valiante et al. 2016), or from lighter seeds ($\sim 100\,\mathrm{M_\odot}$) undergoing burst of super-Eddington accretion (e.g. Volonteri et al. 2015; Pezzulli et al. 2016). Another viable possibility is represented by the growth through coalescence with other BH during galaxy mergers in the framework of the hierarchical structure formation (e.g. Volonteri et al. 2003; Tanaka and Haiman 2009). Yet, the fairly large merger time-scales (up to tens of Gyr at these redshift), appear to lean against this scenario.

Leaving aside more exotic explanations (e.g. "dark stars" or primordial BH), the first generation of stars, known as Pop III stars, are the most likely candidates for producing seed BH. They are expected to be massive ($10 - 1,000\,\mathrm{M_\odot}$), due to the inefficient cooling of primordial metal-poor gas, and hence short lived (e.g. Heger et al. 2003; Hirano et al. 2015). Yet, despite a supposedly "top-heavy" initial mass-function, which is still poorly constrained, the initial seed masses from these remnants would be quite small. A constant Eddington accretion for ~0.8 Gyr would be needed to barely reach $10^9\,\mathrm{M_\odot}$.

Regardless of their origin, quasars trace the most advanced stage of the cosmic assembly and chemical enrichment at all times. Indeed quasars are both expected (e.g. Costa et al. 2014) and observed (e.g. Cantalupo et al. 2014; Mignoli et al. 2020; Overzier 2022) to reside in overdense regions of the cosmic web, and therefore likely highlight the spots where the largest gas resevoirs flow into. Both the star formation (and the consequent chemical enrichment) as well as the accretion process are therefore promoted by the availability of fuel to convert into stars and to accrete onto the BH. The prevalence of luminous quasars in overdense and metal rich regions has often been epitomised in the so-called luminosity-metallicity relation ($\mathrm{L - Z}$ relation; Hamann and Ferland 1993, 1999; Dietrich et al. 2003b). In these cosmic knots, the first generation stars might have been able to promptly produce heavy elements even at $z \gtrsim 6$, and rapidly enriching the environment of α-elements owing to type II supernovae.

A likely consequence of this early enrichment is the fact that the rest-frame UV/optical spectral properties of quasars do not seem to evolve from these remote cosmic epochs to low redshift, as I will discuss more thoroughly in Chapter 2. Albeit some known trends with the luminosity (e.g. the Baldwin effect (Baldwin 1977) high-redshift quasars have generally been observed to match the spectral properties of typical sources at $z \lesssim 1$ (e.g. Kuhn et al. 2001; Mortlock et al. 2011; Hao et al. 2013b; Banados et al. 2018; Fan et al. 2023). Similar considerations apply to the strength of broad emission lines, which several works argued not to evolve with cosmic time Croom et al. 2002; Stepney et al. 2023).

To conclude, our comprehension of SMBH formation and growth is still far form complete. The luminosity of quasars allows us to detect them up to primordial times, helping us to trace the assembly history of the Universe. Larger samples of these high-redshift sources are obviously desirable with the aim of testing the seeming similarity between low- and high-redshift objects. At the same time, as I will discuss in Chapter 5, new deep observations carried out by the James Webb Space Telescope (*JWST*) started raising the veil on the population of faint AGN at high redshift, previously undetected. Such population of low-mass AGN ($\mathrm{M_{BH}} \sim 6-8\,\mathrm{M_{\odot}}$) showed remarkably different features with respect to local AGN, leading to the urgent questions: why are these sources so different from the local one? Are these the progenitors of low-z AGN? If so, how does the transition occur? These are unavoidable questions if I aim to obtain a more comprehensive understanding of AGN and their role in galaxy evolution.

1.2 The cosmological context

Here I briefly introduce the cosmological framework to set the stage for the discussion about the relevance of AGN as standard candles.

1.2.1 The ΛCDM model

The flat Lambda Cold Dark Matter (ΛCDM) cosmological model is the prevailing model in cosmology, describing the evolution and the structure of the Universe from the Big Bang to the present. The foundation of the ΛCDM model rests on three main constituents: first, the Universe is spatially flat (the "flat" part), the second keystone is the presence of the "so-called" Cosmological Constant Λ, associated with dark energy, and the third being the cold dark matter (CDM). The fact that the geometry of the Universe is Euclidean, means that its expansion is not affected by curvature, and therefore locally correct Newtonian calculations can be extended to cosmological scales. The Cosmological Constant is a term initially introduced by Einstein to allow for a static Universe. In our current knowledge the Cosmological Constant adopted a different meaning, and now represents the energy (called dark energy, DE) driving the accelerated expansion of the Universe. Observations from Type Ia supernovae and the cosmic microwave background (CMB) confirm that this acceleration has been ongoing since about five billion years after the Big Bang. DE constitutes approximately 68% of the Universe's total energy density. The "CDM" portion of the model stands for Cold Dark Matter, a hypothetical form of matter that interacts gravitationally but does not emit, absorb, or reflect light, making it invisible to current detection methods. The adjective "cold" characterise the flavour of dark matter currently favoured by observational and theoretical constraints. Unlike hot dark matter, which moves relativistically (near the speed of light), cold dark matter consists of slower-moving particles. This property allows CDM to clump together, forming the gravitational wells that lead to the formation of galaxies and other large-scale cosmic structures. This component is estimated to account for 27% of the total mass-energy content in the Universe.

The physical backbone of ΛCDM is General Relativity, and this framework gained consensus thanks to observational data from the CMB, galaxy surveys, and supernovae. The CMB, a relic radiation from the early Universe, provides a "snapshot" of the Universe when it was only 380,000 years old. Its uniformity and small fluctuations offer insights into the density, composition, and geometry of the Universe. In particular, the CMB anisotropies, mapped by space missions like COBE, WMAP, and Planck, align remarkably well with the predictions of the ΛCDM model. Furthermore, the large-scale structure of the Universe exhibits a web-like pattern of voids, filaments, and clusters, consistent with the gravitational influence of cold dark matter in the model. Furthermore, in the "90s observations of Supernovae Ia unveiled the accelerated cosmic expansion, which ultimately led to the re-introduction of Λ with the role of driving the expansion. Lastly, the abundance of light elements traced by observations finely matches that predicted for the primordial nucleosynthesis following the Big Bang, within the ΛCDM framework. All these pieces of evidence (together with other) collectively corroborate the ΛCDM as the "standard model" for cosmology.

1.2.2 Distance Measurements

Distances on cosmological scales ultimately depend on the parameters of the assumed cosmological model. One of the key problems in cosmology is to work out the inverse problem, that is to use the known distance or physical size of an astrophysical source, to constrain the cosmological parameters. In this effort, it is important to distinguish between different distances, with slightly different meanings in cosmology. The "comoving distance" is defined as the distance between two points in the coordinates frame following the expansion of the Universe. The comoving distance remains constant in time if the points are only moving due to the Hubble flow. In particular, the comoving distance between the observer and a distant object at redshift z can be expressed as

$$D_c = \frac{c}{H_0} \int_0^z \frac{dz''}{E(z'')} \tag{1.1}$$

where H_0 is the Hubble constant and the term $E(z) = H(z)/H(0)$ (first Friedmann equation) encapsulates the effect of the cosmological model and its defining parameters. In order to inspect the several contributions coming into play to define the comoving distance, it is possible to expand the first Friedmann equation as

$$E(z) = \frac{1}{\sqrt{\Omega_{m,0}\,(1+z)^3 + \Omega_{r,0}\,(1+z)^4 + \Omega_{k,0}\,(1+z)^2 + \Omega_{\Lambda,0}}} \tag{1.2}$$

with $\Omega_{i,0}$ being the density parameters respectively for matter ($\Omega_{m,0}$), radiation ($\Omega_{r,0}$) and spatial curvature ($\Omega_{m,0}$). Within the flat ΛCDM framework, the Universe is assumed to be flat (a feature confirmed so-far by observations), therefore $\Omega_{k,0} = 0$.

The "proper distance" (D_p) between two points at a given cosmic time t is instead the distance measured along the geodesic connecting them in the three-dimensional spatial slice of the Universe at that time. This is conceptually equivalent to ideally stop the expansion of the Universe at the time t and directly measure the spatial distance. The scale factor $a(t)$ is defined so that the two distances agree at current time t_0 with $a(t_0) = 1$ and $D_p(t) = a(t)\, D_c$.

Other cosmological distances can be defined. The "transverse comoving distance" (D_M) describes the comoving distance between two events at the same redshift (A and B) or distance, separated on the sky by an angle $\delta\theta$, which is $D_{AB} = D_M\,\delta\theta$. Depending on the curvature of the Universe the transverse comoving distance has a different expression:

$$\mathrm{D_M} = \begin{cases} \mathrm{D_H}\,\frac{1}{\sqrt{\Omega_k}}\sinh(\sqrt{\Omega_k}\frac{\mathrm{D_C}}{\mathrm{D_H}}) & \text{if } \Omega_k > 0 \\ \mathrm{D_C} & \text{if } \Omega_k > 0 \\ \mathrm{D_H}\,\frac{1}{\sqrt{\Omega_k}}\sin(\sqrt{\Omega_k}\frac{\mathrm{D_C}}{\mathrm{D_H}}) & \text{if } \Omega_k > 0 \end{cases} \quad . \tag{1.3}$$

The aforementioned distances only depend on the cosmological parameters and the redshift of the point in the space. Assuming a cosmological model it is possible to derive the distance to the source. Yet, as already mentioned, in cosmology the inverse problem is often more interesting, that is inferring the cosmological parameters, given the redshift and some known distance or physical size. Unfortunately, this is not a straightforward task, since it first requires to find some "standard rulers" or "standard candles", that are objects whose size or luminosity are known. With this information, it is possible to compute the "angular diameter distance" or the "luminosity distance" which directly depend on the cosmological parameters. In particular the "angular diameter distance" is defined as the ratio of the physical transverse size of an astronomical source (d) to its angular size ($\Delta\theta$) in radians $\mathrm{D_A} = \mathrm{d}/\Delta\theta$. It is related to the transverse comoving distance as

$$\mathrm{D_A} = \frac{\mathrm{D_M}}{1+\mathrm{z}} \tag{1.4}$$

If the actual size of an astrophysical source is known, by measuring its apparent size and its redshift it is possible to test the $\mathrm{D_M} - \mathrm{z}$ relation within a cosmological model. In an expanding but Euclidean flat Universe, the observed flux is lower than in a static Universe because the observed rate at which photons cross the $t = t_0$ surface centered on the source and containing the observer. In particular the flux is lower by a factor (1 + z) than the rate at which they were emitted and redshifted to the observed wavelength $\lambda_e = \lambda_e \times (1+z)$.

$$\mathrm{F} = \left(\frac{\mathrm{L}}{4\pi \mathrm{D_C^2}}\right)\left(\frac{1}{1+\mathrm{z}}\right)^2 \tag{1.5}$$

It is possible to define the "luminosity distance" so that the flux-luminosity relation resembles the classical inverse-square law, by assigning $\mathrm{D_L} = (1+\mathrm{z})\,\mathrm{D_C}$. This relation allows to use sources whose luminosities are known to act as "standard candles". Since their luminosity is known *a priori* and their flux can be reliably measured, it is possible to estimate their distance without assuming any cosmological model. Instead of the luminosity distance, for historical reasons the Hubble–Lemaître diagram, that is the relation between the redshift and the distance of a source, employs the "distance modulus" (DM), defined as

$$\mathrm{DM} = 5\log\left(\frac{\mathrm{D_L}}{10\mathrm{pc}}\right) \tag{1.6}$$

Typical examples of standard candles are the Cepheid stars, measured up to ~20 Mpc and supernovae Ia (SNeIa) observed up to z ~2. In order to introduce the discussion on how to select a standard candle, a topic also relevant for the implementation of AGN in cosmology, I will now briefly introduce how supernovae have been implemented as standard candles.

1.2.3 Supernovae as standard candles

A white dwarf star in a binary system can accrete mass from its companion star. The maximum mass for the white dwarf is the "Chandrasekhar mass" ($\simeq 1.44\,\mathrm{M}_\odot$), that is the mass above which the electron degeneracy pressure cannot prevent the collapse, in case of low rotational velocity. Above this threshold, the core of the star is thought to reach the carbon fusion, thus igniting a runaway process. A substantial fraction of the carbon and oxygen in the white dwarf is converted into heavier elements. Within a short amount of time, the energy released in this process exceeds the binding energy of the star, thus resulting in a supernova explosion whose luminosity is comparable with that of the host galaxy. The luminosity reaches a peak of $M_B \sim -19.5$ and declines within some tens of days.

Although the physics behind the SNeIa explosions is the same, their peak luminosity exhibits a spread of about half a magnitude. In order to turn supernovae into real standard candles the "Phillips relation" (Hamuy et al. 1996) is generally employed. This relation links the peak luminosity with the decline rate of the light curve in supernovae. Using this relation it is possible to take advantage of SNeIa as an accurate distance indicator by calibrating their maximum luminosity. Still, supernovae must be calibrated to obtain absolute distances: for this purpose, Cepheid stars in the common redshift range can be used building a further step on the so-called "cosmological distances ladder", where every new distance indicator is calibrated on the previous (and closer) ones in a range where they are both available.

Once the redshift and the distance of a source are known it is possible to build the so-called "Hubble–Lemaître" diagram, that is the relation between the distance modulus and the redshift. The shape of this diagram crucially depends on the cosmological parameters and can be therefore used to constrain them. For instance, in the 1990s the implementation of the SNeIa as standard candles led to the discovery of the accelerated expansion of the Universe, paving the way for the re-introduction of the cosmological constant Λ. In the next Section, I will show how luminosity distances can be estimated using the relation between the X-ray and UV luminosities in quasars, i.e. the $\mathrm{L_X - L_{UV}}$ relation. The use of this well known feature in quasar SEDs has recently driven new interest on this class of astrophysical objects for their possible implementation as cosmological tools.

1.3 The $\mathrm{L_X - L_{UV}}$ relation

1.3.1 The physical context

The non-linear relation between the X-ray and UV luminosity in quasars has been known since the "70s, following the first X-ray surveys (Tananbaum et al. 1979; Zamorani et al. 1981; Avni and Tananbaum 1982. This relation has been observed to hold on several thousand quasars, spanning from the local Universe up to quasars at the epoch of reionisation. This relation, often referred to as the $\mathrm{L_X - L_{UV}}$ relation (or

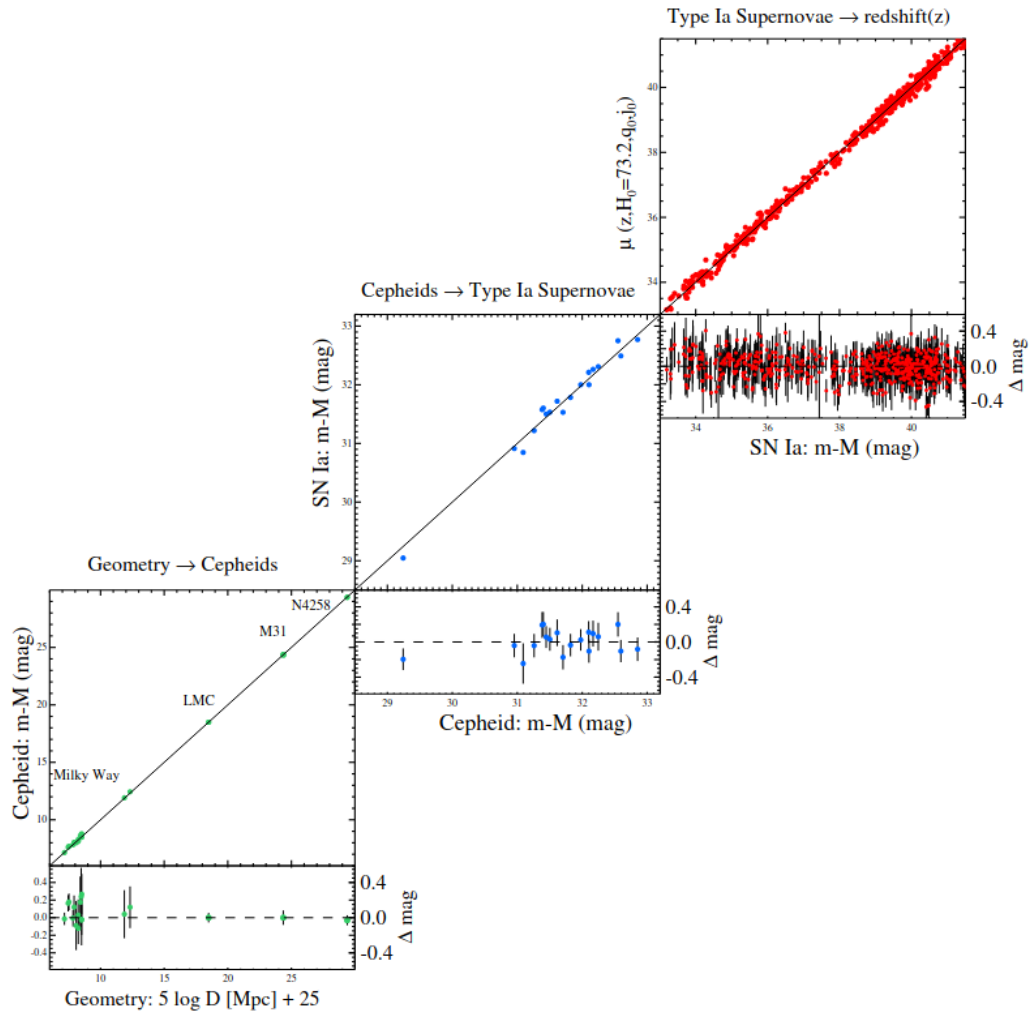

Figure 1.4. An example of the "cosmological distances ladder" from Riess et al. (2016). From the bottom left to the top right, pairs of geometric and Cepheid-based distances are shown, then Cepheid and SN Ia-based distances and lastly, SN and redshift-based distances provide the measurement of the Hubble constant. At each step, geometric or calibrated distances on the horizontal axis are used to calibrate a relative distance indicator on the vertical axis via the determination of the distance modulus or H_0.

its by-product, the $L_{2,500\,\text{Å}} - \alpha_{\text{ox}}$[2] relation) likely reflects the interplay between two physically distinct regions of the AGN. The UV emission is produced in the accretion disc powering the AGN, where the gravitational energy of the infalling material is partially transformed into radiation. The X-ray emission originates in a plasma of hot relativistic electrons (the already mentioned "corona") whose properties are still obscure, but which is thought to boost the seed UV photons via inverse Compton scattering processes. The $L_X - L_{UV}$ relation is generally parametrised as

$$\log(L_X) = \alpha\ \log(L_{UV}) + \beta \tag{1.7}$$

---

[2] The index $\alpha_{ox} = 0.384 \log(F_X/F_{UV})$ describes the slope of the power-law joining 2,500 Å with 2 keV.

where $\mathrm{L_X}$ and $\mathrm{L_{UV}}$ are the monochromatic luminosities respectively at 2 keV and 2,500 Å. Although these energies are mainly employed for historical reasons, it has been recently shown that they are good proxies for the respective band emissions, and suitable to reduce the observed dispersion (Signorini et al. 2023b). The exact nature of the physical process underlying the relation is still not clear, yet recent studies have confirmed that most of the observed dispersion reported in early literature samples (δ=0.35-0.40), was mostly due to observational effects (Lusso et al. 2015). Indeed for the samples with the highest-quality observations, the intrinsic dispersion (i.e. the amount of dispersion not ascribable to measurement uncertainties) can be as low as 0.09 dex[3] (Sacchi et al. 2022). The tightness of the relation, coupled with its ubiquity has two noticeable consequences. First, the mechanism coupling the accretion disc and corona must be strongly regular and, as I will show shortly, it does not show any appreciable evolution through cosmic time. Secondly, the non-linearity of the relation allows to use the observed X-ray and UV fluxes to infer the luminosity distance as

$$\log(\mathrm{D_L}) = \frac{1}{2-2\alpha}\left[\log(\mathrm{f_X}) - \alpha\,\log(\mathrm{f_{uv}})\right] + \beta'' \tag{1.8}$$

with $\beta'' = \beta + (\alpha - 1)\log(4\pi)$. Clearly, $\alpha \neq 1$ is a key requirement in order to determine $\mathrm{D_L}$, and this is verified for the latest quasar compilations which give $\alpha \simeq 0.6$. This holds regardless of the cosmological model, thus enabling us to turn quasars into a new class of *standardised candles*. In this case the adjective "standardised" refers to the process needed to select a clean sample of blue unobscured quasars (described in Sec. 1.3.2) which allows to minimise the observed dispersion.

1.3.2 Turning quasars into *standardised candles*

In order to define a class of standard candles several requirements should be met. The luminosity of the class of objects should either be standard or standard-isable and it should be observed on a wide range of redshifts. Although the luminosity in quasars is not standard by any means, being these sources highly variable and spanning several orders of magnitudes in luminosity, even weak correlations between spectral features and luminosity can, in principle be employed for cosmological measurements. The large dispersions and the observational biases can be mitigated by increasing the sample size and by a careful set of selection criteria. Another crucial requirement is that the relation employed to derive the luminosity distance is not evolving with time. Here I describe how, in a series of work, it has been demonstrated that the $\mathrm{L_X} - \mathrm{L_{UV}}$ relation does not show any evolution with redshift, and that the selection of blue unobscured quasars with reliable X-ray measurements drastically reduces the observed dispersion.

Selection criteria

The first studies on the $\mathrm{L_X} - \mathrm{L_{UV}}$ relation (or its alternative version the $\alpha_{ox} - L_{UV}$ relation) reported a significant scatter around the best-fit relation ($\delta = 0.3 - 0.4$).

---

[3] The term "dex" (decimal exponent) is used here to refer to any number or ratio"s order of magnitude, which is its base-10 logarithm.

Yet, in a series of recent works (Lusso et al. 2015; Lusso and Risaliti 2016; Risaliti and Lusso 2019; Lusso et al. 2020) it has been demonstrated that this can be majorly reduced (down to $\delta \simeq 0.20$) only by adopting quality cuts on the parent sample. Although, I will come back on this point in the dedicated chapter (2), I briefly anticipate how the parent sample for the latest compilation of quasars employed for cosmological purposes (Lusso et al. 2020) was assembled. Basically, it was obtained by cross-matching the UV data coming from the Sloan Digital Sky Survey Data Release 14 (SDSS-DR14) and those in the X-rays from the *XMM-Newton* and the *Chandra* source catalogues. Additional sparse samples with dedicated observations were also added chiefly to sample the very low and the very high redshift ranges. Here I explain how the subsequent filtering is carried out.

Broad Absorption Line and Radio-Loud quasars. Quasars displaying broad (FWHM$\gtrsim$1,000 km s^{-1}) absorption lines (BALs) are removed from the sample as they generally exhibit absorption features in the X-ray band (e.g. Gallagher et al. 2002; Vignali et al. 2003), leading to unreliable X-ray fluxes. These objects are identified in the catalogue through the "BALnicity index" measured close to the C IV emission line. Additionally, also radio-loud quasars ($R = L_{\nu,6\mathrm{cm}}/L_{\nu,2,500\text{Å}}$) are discarded from the parent sample. This is mainly due to the fact that radio-loud quasars show larger X-ray luminosities with respect to radio-quiet sources (e.g. Worrall et al. 1987; Fossati et al. 1998), likely due to a jet polluting the purely coronal emission.

Host galaxy contamination and reddening. In the optical and UV two main effects can concur to hamper a proper determination of the quasar continuum at 2,500 Å, namely the host galaxy contamination and dust reddening. The first effect mostly affects low-luminosity AGN where the nuclear emission does not clearly outshine the host galaxy. As a result the measured luminosity does not correspond to the intrinsic one due to the additional (non-negligible) host contribution. Dust reddening is instead responsible for the extinction of UV emission, thus reducing the actual observed luminosity. The extinction caused by dust is differential, being more pronounced towards shorter wavelengths, and therefore produces a redder-than-intrinsic UV spectrum. With the aim of mitigating both these effects, a colour cut is applied to the parent sample. Basically, only sources with UV and optical colours *close* to that of a blue unobscured quasar are retained. In practice, the UV and optical SED is defined as the combination of a power-law in the range 3,000 Å–1 μm with slope Γ_1 and a one in the range 1,450–3,000 Å with slope Γ_2. Typical unobscured quasars cluster around $(\Gamma_1, \Gamma_2) = (0.82, 0.40)$ (Richards et al. 2006). In the final sample, only objects consistent with a low degree of reddening given the typical colours are retained. This is estimated by reddening the average quasar SED assuming a Small Magellanic Cloud extinction curve in steps of increasing extinction E(B-V) and retaining only the sources with E(B-V)$\leq$0.1. This translates into selecting all the sources within the region $\sqrt{(\Gamma_1 - 0.82)^2 + (\Gamma_2 - 0.40)^2} \leq 1.1$ in the $\Gamma_1 - \Gamma_2$ plane. This selection has also the effect of discarding sources with unusual SEDs or flawed photometry.

X-ray absorption. The X-ray coronal emission in quasars can be absorbed due to gas and dust along the line of sight. This can occur mostly because of dust-free gas within the BLR and because of gas and dust in the obscuring torus. This effect obviously reduces the X-ray emission, as the measured luminosity is lower than the intrinsic. Sources affected by this observational effect must therefore be excluded by the sample. Conversely to what happens in the optical/UV, gas absorption is more efficient at lower energies, therefore affecting more effectively the soft-X ($E \lesssim 0.5$ keV) band than the hard-X ($E \gtrsim 0.5$ keV) band. The net effect of absorption in the X-rays can be seen as a decrease of the photon index Γ_X. When this theoretical prediction is coupled with the observational evidence of the non-evolution with z of the X-ray spectra of quasars (e.g. Nanni et al. 2017, but see also Zappacosta et al. 2023 for hint of evolution at $z \sim 6.5$), unobscured quasars in the X-rays can be selected via a cut in the photon index. The typical photon index for blue unobscured quasars is $\Gamma_X = 1.9 - 2.0$ (e.g. Bianchi et al. 2009; Young et al. 2009). Therefore the selection of X-ray unabsorbed sources is performed by allowing only quasars with $1.7 < \Gamma_X < 3.0$ in the sample, where Γ_X in this case is estimated using X-ray photometry. Sources with Γ_X lower than the threshold value are likely to be absorbed, while those with $\Gamma_X > 3.0$ are probably experiencing some "exotic" coronal state.

Eddington (Malmquist) bias. The Eddington (or Malmquist) bias consists in the observational effect whereby a variable source is detected in a flux-limited survey only in case of a positive fluctuation of its flux. This, in turn, translates into an overestimate of the typical X-ray flux for that source, which is measured in a high state. When this effect affects a significant number of sources in the sample, the result is a flattening of the $\mathrm{L_X} - \mathrm{L_{UV}}$ relation. In order to avoid this effect, a filter on X-ray fluxes is applied, and all the objects falling below a threshold, dependent on the intrinsic dispersion of the $\mathrm{L_X} - \mathrm{L_{UV}}$ relation as well as on the flux limit of each observation, are removed. In particular, for each quasar the criterion for acceptance is:

$$\log(\mathrm{f_{2keV,exp}}) - \log(\mathrm{f_{min}}) < \mathrm{k}\delta \tag{1.9}$$

where $\log(\mathrm{f_{2keV,exp}})$ is the expected 2 keV flux given the 2,500 Å flux, δ is the dispersion of the $\mathrm{L_X} - \mathrm{L_{UV}}$, while k is the parameter determining the strength of the applied filter. Assuming $\alpha = 0.60$ and a standard flat ΛCDM cosmology, $\log(\mathrm{f_{2keV,exp}})$ can be expressed as:

$$\log(\mathrm{f_{2keV,exp}}) = (\alpha - 1)\log(4\pi) + (2\alpha - 2)\log(\mathrm{D_L}) + \alpha\log(\mathrm{f_{UV}}) + \beta \tag{1.10}$$

The minimum detectable flux is determined for each X-ray observation by considering the length of the observation and the position of the source in the detector. It is not trivial to derive a credible value for k. In Risaliti and Lusso (2019), adopting a set of simulations, it was found that k=2 gives the best trade-off between obtaining solid estimates of the inferred cosmological parameters and not obliterating the sample size. To determine the optimal value of k, in particular, a mock sample of X-ray and UV fluxes was generated assuming the $\mathrm{f_X} - \mathrm{f_{UV}}$ relation and an intrinsic dispersion of δ=0.15. Different values of $\mathrm{L_X}$ and $\mathrm{L_{UV}}$ were derived adopting different values of the comological parameters $\boldsymbol{\Omega}_i$. For each simulated dataset, the filter for the Eddington bias was applied for different values of k. The final k was chosen so as to match the $\boldsymbol{\Omega}_i$ values assumed after fitting the mock data in search for the best fitting cosmological parameters. Although slightly circular (assuming a $L_X - L_{UV}$ relation and the slope, in order to derive the expected fluxes) this method proved consistent with many different sets of comsological parameters. Therefore, the choice of k is not expected to influence the predicting power of quasars for determining the cosmological parameters.

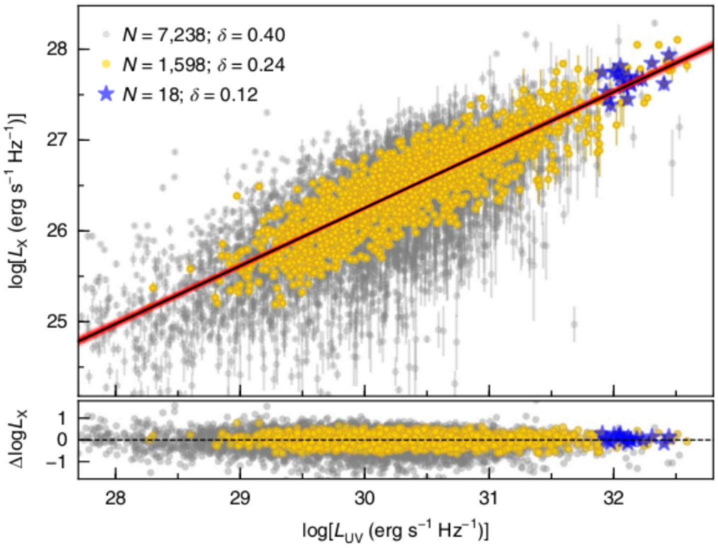

Figure 1.5. The effect of the selection criteria on the $L_X - L_{UV}$ relation as shown in Risaliti and Lusso (2019). Starting from an initial sample of ~7,300 quasars with an intrinsic dispersion of $\delta = 0.40$, the quality cuts filter out a high-quality sample with a much lower dispersion $\delta = 0.24$. In case of pointed observations on luminous quasars, the dispersion can be as low as $\delta = 0.12$ (blue stars).

Applying all the aforementioned selection criteria, the observed dispersion in the $L_X - L_{UV}$ relation can be significantly reduced from $\delta \simeq 0.40$ (grey dots) to $\delta \simeq 0.22 - 0.25$ (yellow dots) as shown in Fig. 1.5. It is also interesting to note that the dispersion can be even lower in the case of pointed observations ($\delta = 0.12$, Sacchi et al. 2022), as opposed to archival data, as indicated by the blue stars again in Fig. 1.5. This sample is made of some of the most luminous blue quasars at $z = 3.0 - 3.3$ described in Nardini et al. (2019b). Although I will come back on this sample in Chapter 3, here I point out that these objects were targeted by *XMM-Newton* during dedicated observations. The quality of X-ray observations is therefore notably better than the average of the sample where the sources are serendipitously observed.

The non-evolution with redshift

Another key requirement for the elegibility of a class of sources as a standard candle is the non-evolution (or a physically well described evolution) with redshift of the underlying physical mechanism. The physics subsumed by the supernovae explosions is not expected to change from the local Universe up to the farthest observed supernovae. A similar requirement must be fulfilled also by the $L_X - L_{UV}$ relation, in order to employ it for cosmological applications. Throughout the series of works dedicated to the implementation of quasars as standard candles, the evolution with redshift of the relation has been consistently ruled out in increasingly larger samples. This was done by basically analysing the $f_X - f_{UV}$ flux relation (instead of the $L_X - L_{UV}$) in small *enough* redshift bins, so that the fluxes can be used as proxies for the luminosities. The size of the redshift bin is chosen so that the dispersion introduced by the variation in D_L is negligible with respect to the observed dispersion in the sample. In particular, considering for instance $\delta = 0.3$ (which is a very conservative estimate with respect to the current value) an interval $\Delta \log(D_L) < 0.15$ is required, thus leading to $\Delta \log(z) < 0.1$. If this binning leaves enough sources in each redshift bin for a statistically meaningful analysis, the $f_X - f_{UV}$ relation can be fit therefore assessing whether the slope of the relation exhibits any evolution with z.

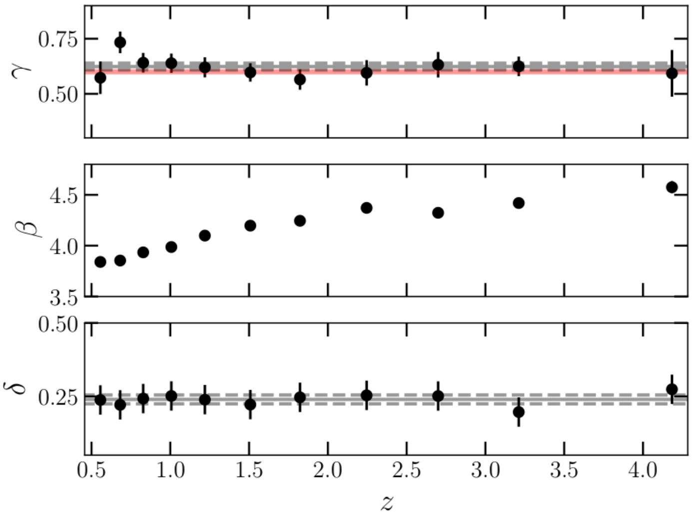

Figure 1.6. The non-evolution with z of the slope of the $f_X - f_{UV}$ relation γ, as shown in Risaliti and Lusso (2019). The red line marks the average value $\gamma = 0.6$. As the parameter β is directly proportional to the distance modulus, the trend of β with z simply reflects the quasar Hubble–Lemaître diagram. The dispersion of the best fit relation also does not evolve with the redshift being $\delta = 0.24 \pm 0.05$

Fig. 1.6 shows the non-evolution of the slope of the $f_X - f_{UV}$ relation up to $z \sim 4$ from Risaliti and Lusso (2019). This test demonstrates that the mechanism linking the UV and X-ray emission does not show any clear evolution from the local Universe up to remote cosmic epochs. Since β'' is a normalisation in Eq. 1.8, without a theoretical model describing the $L_X - L_{UV}$ relation it is not possible to give an estimate for it. The evolution of β'' with z can be assessed by comparing the quasar Hubble–Lemaître diagram with the supernovae one in the common redshift range. Indeed, the “zero-point” of the $DM - z$ relation can be measured for SNe, but is unknown for quasars. Consequently, β'' is one of the parameters left free to vary in the joint fit of the $DM - z$ relation for SNe and quasars, with the purpose of cross-calibrating the DM of the two groups of sources. This procedure is analogue to the calibration process of the steps in the "distance ladder" shown in Fig. 1.4. As it is clear from Fig. 2.17, the match in the common redshift range is excellent, thus meaning that the possibility of a redshift evolution of this parameter is unlikely. Alternatively, i) there can be some kind of redshift evolution -yet unknown- affecting the SNe in the same way; ii) the evolution of the normalisation parameter starts exactly at $z > 1.4$ where it is not possible to compare the two classes of sources anymore. However, both these possibilities seem very unlikely, therefore the use of the $L_X - L_{UV}$ for cosmological applications can be regarded as safe.

1.3.3 Results of the cosmological application

The selection of a clear sample of blue unobscured quasars is ultimately aimed to build a supernovae+quasar Hubble–Lemaître diagram, which is the relation between the distance modulus and the redshift. Since, as shown in Sec. 1.2.2 the luminosity distance, and therefore the distance modulus, depends on the cosmological parameters, therefore the best fit of this relation can constrain the parameters characterising a given cosmological model. In Fig. 1.7 I show the Hubble–Lemaître diagram for the latest compilation of quasars (Lusso et al. 2020). There are several features here to be noted. Firstly, as already mentioned in the previous section, the shape of the quasar Hubble–Lemaître diagram matches that of the SNe remarkably well in the common redshift range. Although the much larger scatter of the quasar distance moduli, the average values at different redshifts (used for visualisation purposes only) closely resemble those of the supernovae. Moreover, the average values at $z \gtrsim 2$ lie systematically below the expectations from the ΛCDM model (black dashed line), thus pointing to some possible inconsistency of the data with the high-redshift extrapolation of the standard model whose parameters are inferred using the SNe up to $z \sim 1.4$.

A possible way to quantify this deviation from the flat ΛCDM model is the use of a cosmographic approach (e.g. Risaliti and Lusso 2019; Bargiacchi et al. 2021). This fitting technique basically relies on the use of the functional form $\mathrm{D_L} = \mathrm{k} \sum_\mathrm{i} \mathrm{a_i} [\log(1+\mathrm{z})^\mathrm{i}]$ whose coefficients can be *a posteriori* related to the cosmological parameters of a given model. In particular, $k = \ln(10)\, c/H_0$ and $a_1 = 1$ in order to reproduce the Hubble diagram at low redshift. The fit excellently reproduces the data just using an expansion up to the third order. Within the ΛCDM model, it is possible to derive the expected coefficients $a_2(\Omega_m)$ and $a_3(\Omega_m)$ and compare them with the best fit ones. Fig. 1.8 highlights the 4σ discrepancy between the a_2 and a_3 parameters inferred from the fit and those derived from the ΛCDM model. Interestingly, the discrepancy arises when adding the high redshift data, in the range where only quasars are available. Yet, the remarkable match between the quasars and supernovae in the common redshift range (up to $z \sim 1.4$), coupled with the non-evolution with z of the $L_X - L_{UV}$ relation, corroborates the reliability of this finding.

The high redshift discrepancy with the flat ΛCDM model leaves room for testing alternative cosmological models. It is possible to modify the dark energy equation of state, and allow its density to vary with redshift (the wCDM model). In this framework, which is just an example among the many possible alternative cosmological models, the best fit is obtained with a high matter density ($\Omega_M > 0.4$) and a free dark energy density parameter of $w <$ -1, which means, a dark energy density increasing with time.

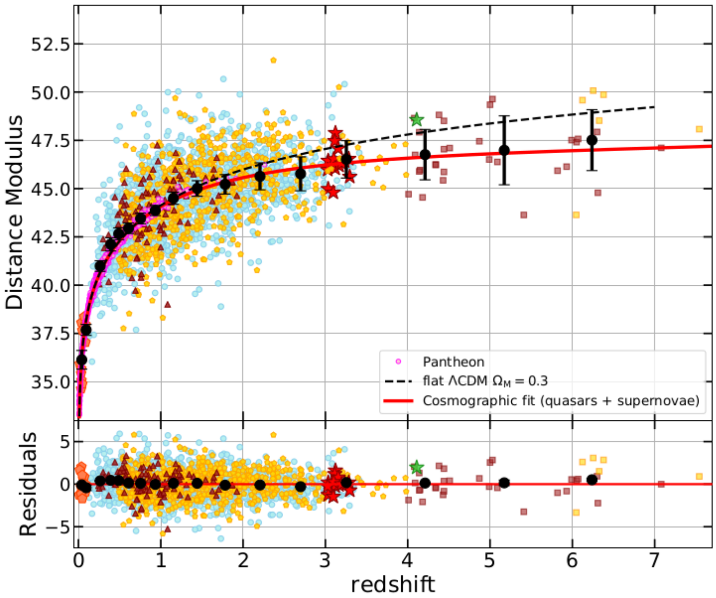

Figure 1.7. Joint supernovae+quasar Hubble–Lemaître diagram for the cleaned sample described in Lusso et al. (2020). Supernovae from the *Pantheon* sample (Scolnic et al. 2018) are shown in magenta, while all the other symbols and colours represent different subsets of the quasar sample. The red line represents a fifth order cosmographic fit of the data (see text), while the black points are averages (along with their uncertainties) of the distance moduli in narrow (logarithmic) redshift intervals. The dashed black line shows a flat ΛCDM model fit with $\Omega_M = 0.3$. It is clear that above $z \sim 2$ observations start to detach significantly from the flat ΛCDM model. The bottom panel shows the residuals with respect to the cosmographic fit and the black points are the averages of the residuals over the same redshift intervals.

1.3.4 Summary and open issues

The implementation of quasars as standard candles led to outstanding results. Their luminosity and prevalence makes them a suitable tool to bridge between the classical low-redshift standard candles and the early Universe probes (e.g. the CMB, the baryonic acoustic oscillations, BAO). If more sources were added to the cosmological sample the tension with the current standard cosmological model could become irreconcilable. In this case, already at this stage the data show a mild preference for the so-called "interacting dark sectors" models, where dark matter and dark energy interact with each other or with other fields, rather than evolving independently. The consequences for this finding, which critically relies on the use of high-redshift standard candles would be dramatic.

However, in order for these results to acquire robustness a more thorough understanding of $L_X - L_{UV}$ relation as well as of the properties of the AGN building the sample will be key.

From a theoretical standpoint, a fully consistent modellisation of the disc-corona interplay has not been reached yet, despite several attempts (e.g. Lusso and Risaliti 2017; Arcodia et al. 2019). For instance, the shape, the position and the thermodynamical properties of the corona are still obscure. Evidence is growing,

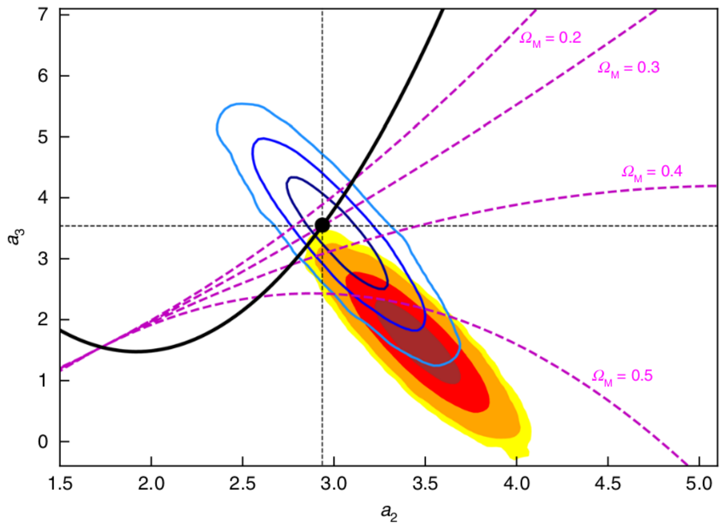

Figure 1.8. The $a_2 - a_3$ plane derived by fitting the quasar+supernovae joint Hubble–Lemaître diagram. The black line shows the a_2 and a_3 values derived from the flat ΛCDM model, with the dot marking the values corresponding to $\mathbf{\Omega}_\lambda = 0.3$. The intensity of the colour from red to yellow marks 1σ, 2σ, 3σ and 4σ confidence levels. The blue contours have the same meaning but were computed employing only the data below $z = 1.4$. The difference between the blue and the red contours shows how the high redshift data, where only quasars are available, are key to drive the tension with the flat ΛCDM model. The dashed magenta lines represent the cosmographic expansions of alternative cosmological models. In particular, a wCDM model (see text) is assumed and different values of a_2 and a_3 with different values of $\mathbf{\Omega}_m$ shown in the labels.

mostly thanks to X-ray polarimetry, for a more *slab*-like or *wedge* corona (e.g. Gianolli et al. 2023), suggesting to abandon the oversimplified *lamp-post* corona. It is not clear, however, given the low statistics and the requirements for X-ray polarimetry to be performed, how typical the results obtained so far might be. Additionally, the physics behind magnetic loops invoked to allow the energy transfer between disc and corona, is still oject of debate.

From an observational perspective, subtle biases could hide in the cleaned parent sample in the form of residual host galaxy contamination and reddening which have not been filtered out by the photometric selection criteria. For instance, the DM values presented in the Hubble–Lemaître diagram in Fig.1.7 is proportional to L_{UV}. An increasing amount of reddening could, in theory, be responsible for the observed tension with the flat ΛCDM model. Another main concern regards how typical the sources in the filtered sample are. Are the remaining objects typical? Do their spectral properties show any evolution, on average, with the redshift? These are questions which are, at least in part, addressed in Chapter 2, where I show the results of the analysis on the average UV and optical spectral properties of the cosmological sample.

As discussed so far, the relation between the UV and X-ray emission, has been shown to be remarkably tight once cleaned from observational issues. For a typical quasar the UV and the X-ray emission are well coupled together, meaning that the radiation coming from the accretion disc is efficiently reprocessed and boosted in the X-rays in the corona. In some cases the X-ray emission can be obscured due to some intervening gas (and dust) along the line of sight. In these cases the source appears to be X-ray obscured, and drops below the $L_X - L_{UV}$ relation. At the same time, there are also objects whose X-ray emission is weak even without displaying the signs of X-ray absorption, which are called *X-ray weak* quasars. This class of sources, whose incidence in literature appears to vary with the Eddington ratio, represents a subset of the main quasar population whose X-ray properties are particularly enigmatic. It is not clear what mechanism can halt, or at least alter, the coronal reprocessing albeit a typical blue optical continuum. Speculatively, some kind of outflow, perhaps promoted at higher accretion rates, could be capable of reducing the coronal emission by starving it of its seed UV photons. Although the broad-band UV/optical SED would be barely affected by such mechanism, the broad emission lines could bear the traces of this non-standard accretion state. I explored this possibility on a unique sample of quasars at z ~3 with dedicated X-ray and rest-frame UV/optical observations in Chapter 3.

Chapter 2

Quasars as standard candles: spectroscopic validation of the cosmological sample

2.1 Outline

In this part of my thesis, I analysed the sample of quasars described in the previous Chapter, recently assembled to investigate the non-linear relation between their monochromatic luminosities at 2500 Å and 2 keV and to exploit quasars as a new class of "standardized candles". The use of this technique for cosmological purposes relies on the non-evolution with redshift of the UV-optical spectral properties of quasars, as well as on the absence of possible contaminants such as dust extinction and host galaxy contribution. I addressed these possible issues by analysing the spectral properties of the cosmological quasar sample. I produced composite spectra in different bins of redshift and accretion parameters (M_{BH}, L_{bol}), to investigate any possible evolution of the spectral properties of the continuum of the composites with these parameters. I found a remarkable similarity amongst the various stacked spectra. Apart from the well known evolution of the emission lines with luminosity (i.e. the Baldwin effect) and black hole mass (i.e. the virial relation), the overall shape of the continuum, produced by the accretion disc, does not show any statistically significant trend with black-hole mass, bolometric luminosity, or redshift (z). The composite spectrum of this quasar sample is consistent with negligible levels of both intrinsic reddening (with a colour excess E(B-V)$\lesssim$ 0.01) and host galaxy emission (less than 10%) in the optical. I also tested whether unaccounted dust extinction could explain the discrepancy between the cosmographic fit of the Hubble–Lemaître diagram and the concordance ΛCDM model. The average colour excess required to solve the tension should increase with redshift up to unphysically high values (E(B-V)$\simeq$ 0.1 at $z > 3$) that would imply that the intrinsic emission of quasars is much bluer and more luminous than ever reported in observed spectra. The similarity of quasar spectra across the parameter space excludes a significant evolution of the average continuum properties with any of the explored parameters, confirming the reliability of the sample for cosmological applications. Lastly, dust reddening cannot account for the observed tension between the Hubble–Lemaître diagram of quasars and the ΛCDM model. The results described in this Chapter were compiled in Trefoloni et al. (2024c).

2.2 Context and aims of the work

As already mentioned, quasars are the most luminous persistent sources in the Universe and, as such, they enable its investigation up to redshifts of $z > 6$ (e.g. Mortlock et al. 2011; Banados et al. 2018; Yang et al. 2020; Wang et al. 2021; Zappacosta et al. 2023). Thanks to their ubiquity and high luminosity, these sources were quickly recognised as powerful cosmological probes. Since the 1970s, correlations between quasars' observables have been employed to determine their distances. The discovery of the Baldwin effect (i.e. the emission-line equivalent widths anti-correlate with the quasar luminosity; Baldwin 1977) envisaged that quasars could be utilised as cosmological probes. Techniques involving similar relations have been subsequently developed (see Section 6 in Czerny et al., 2018 for a detailed review). Yet the large dispersion as well as the scarcity of suitable sources, have in most cases limited their applicability for measuring the expansion parameters (e.g. H_0). Other attempts to extract cosmological information from quasars are based on the broad line region (BLR; Elvis and Karovska 2002) or dust (Yoshii et al., 2014) reverberation mapping in combination with spectro-astrometric measurements (SARM; Wang et al. 2020), the Eigenvector 1 main sequence (Marziani and Sulentic 2014), or the X-ray excess variance (La Franca et al. 2014).

In the last decade, the efforts of my group have been mostly devoted to developing and refining the implementation of quasars as "standardised candles" via the $L_X - L_{UV}$ relation as thoroughly discussed in 1.3. Although a comprehensive description of the physical mechanism underlying the $L_X - L_{UV}$ relation is still missing (e.g. Nicastro 2000; Merloni 2003; Lusso and Risaliti 2017; Arcodia et al. 2019), its observational evidence is extremely solid. The intrinsic dispersion of the relation can indeed be as low as 0.09 dex in case of samples with high quality data (Sacchi et al. 2022).

In addition to important implications for accretion physics, the non-linearity of the $L_X - L_{UV}$ relation, combined with the non-evolution with redshift of its parameters (e.g. Risaliti and Lusso, 2019), makes it a useful tool to determine the luminosity distance of quasars and thus transforms them into a new class of "standardisable candles". This new category of standard candles becomes particularly convenient when it comes to populating the intermediate redshifts between the farthest supernovae at $z \sim 2$ (Scolnic et al., 2018) and the CMB. Despite a good agreement with the ΛCDM model in the low-redshift regime of the Hubble–Lemaître diagram, a 3-4σ tension with the model, driven by the quasar data at earlier cosmic epochs ($z > 1.5$), has been reported (Risaliti and Lusso 2019; Bargiacchi et al. 2021; Sacchi et al. 2022; Bargiacchi et al. 2022; Lenart et al. 2023).

In Lusso et al. (2020), henceforth L20, it is discussed how the latest compilation of 2,421 quasars for cosmological purposes was produced, describing how the measurements of X-ray and UV luminosities were performed. However, in order to validate the selection criteria adopted to build the sample, ther are still possible issues that could be present to some extent: i) an evolution with redshift of the slope of the optical and UV continuum and ii) the contamination of host galaxy in the optical and flux attenuation due to dust and gas. In this part of my theis I mainly focus on a spectral confirmation of the robustness of the selection criteria. In particular, I aim at demonstrating, by means of composite spectra, that the continuum of the sample (in which the UV proxy $L_{2500\,\text{Å}}$ is evaluated) does not show any appreciable evolution with redshift. At the same time, the spectral composites are a useful tool to reveal the presence of residual (i.e., still present despite the selection cuts) dust extinction and/or host galaxy contribution. To the end of investigating any possible spectral diversity among the objects constituting the cosmological sample, I employed stacked templates. The lack of a significant evolution of the continuum among the stacked spectra, representative of different regions of the parameter space, ensures the universality of the accretion mechanism powering the optical–UV emission.

Specifically, these are the main points addressed in this Chapter. i) directly verifying how close the average spectral properties of the cosmological sample are to those of typical blue quasars, by means of composite spectra in different regions of the $\mathrm{M_{BH}} - \mathrm{L_{bol}} - \mathrm{z}$ parameter space; ii) estimating the degree of host galaxy contamination; iii) quantifying the effect of intrinsic dust absorption in the sample of quasars. The last two effects would influence the estimates of $f_{2500\,\text{Å}}$ and therefore undermine the cosmological application of the $\mathrm{L_X} - \mathrm{L_{UV}}$ relation. Employing spectral data to understand – and if necessary, account for – such possible observational effects, that can alter both X-ray and UV measurements would definitely corroborate the evidence that the observed discrepancy with the concordance cosmological model is not due to observational issues.

2.3 The data set

The quasar sample analysed here was published by L20 and is made of 2,421 sources within the redshift range $0.13 < z < 5.42$. The data set was produced by merging seven different subsamples available from the literature.

The *Sloan Digital Sky Survey* data release 14 (SDSS-DR14, Pâris et al. 2018) was cross-matched with the *XMM-Newton* 4XMM-DR9 (Webb et al. 2020) catalogue of serendipitous sources, the second release of the *Chandra Source Catalogue* (CSC2.0, Evans et al. 2010) and the AGN sample described in Menzel et al. (2016), belonging to the *XMM–Newton* XXL survey (XMM–XXL, PI: Pierre), producing respectively the SDSS-4XMM, the SDSS-Chandra, and the SDSS-XXL samples.

Local quasars ($0.009 < z < 0.1$) with available UV data from the *International Ultraviolet Explorer* (IUE) in the Minkulski Archive for Space Telescopes (MAST) and X-ray data were included in the sample to anchor the normalisation of the quasar Hubble diagram with Type Ia supernovae.

To improve the coverage at high redshifts, three samples of quasars with pointed observations were added. I added the sample of 29 luminous quasars at redshift $3.0 < z < 3.3$ with dedicated *XMM-Newton* X-ray observations described in Nardini et al. (2019b) (which are also discussed in Chapter 3), the 53 high redshift ($z > 4.01$) quasars from Salvestrini et al. (2019), and the 25 quasars at $z > 6$ from Vito et al. (2019).

In order to produce such a compilation, several selection criteria were adopted, which are essentially those already described in 1.3. Therefore, I only briefly highlight the main filters adopted here. All the selected sources are radio quiet[1] and not flagged as broad absorption line (BAL) quasars according to the SDSS-DR14 quasar catalogue (Pâris et al. 2018), which was the latest release at the time of the L20 analysis. A broadband photometric spectral energy distribution (SED) was build for each source, and only quasars with UV-optical colours close to the ones of typical blue quasars (Richards et al. 2006) were retained. In addition, steep X-ray spectra ($1.7 < \Gamma < 2.8$) and deep enough X-ray observations (to avoid the Eddington bias), were required. Such properties make the L20 sample a truly unique sample of blue quasars, sharing a high degree of homogeneity in terms of broadband properties and observational data. The present work is focused on the spectral properties of the sources with available SDSS data, which constitute the bulk (~93%) of the sample.

2.4 Methods

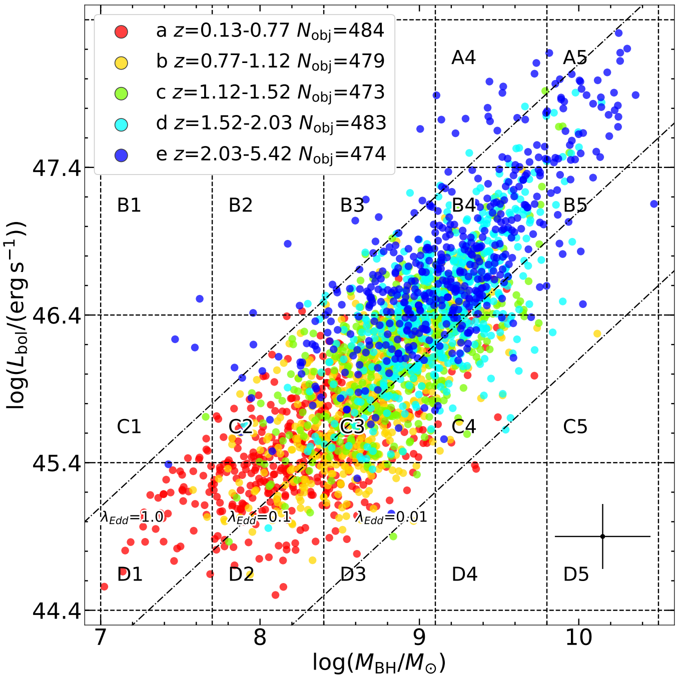

Figure 2.1. Parameter space of $\log \mathrm{M_{BH}} - \log \mathrm{L_{bol}}$ for the quasar sample published in L20 with colour-coded redshifts. Dot-dashed lines represent constant λ_{Edd} values. Typical uncertainties on $\log(\mathrm{M_{BH}})$ and $\log(\mathrm{L_{bol}})$ are represented in the bottom-right corner.

---

[1] I applied the usual criteria based on the ratio between the flux density at 6 cm and 2500 Å, i.e. AGN with $R = F(6\,\mathrm{cm})/F(2500\,\text{Å}) < 10$ are considered radio quiet (Kellermann et al., 1989).

2.4.1 The parameter space

My aim here is to study whether the continuum properties of the cosmological sample evolve with redshift or any of the governing parameters of the quasar spectrum, namely $\mathrm{L_{bol}}$, $\mathrm{M_{BH}}$ and λ_{Edd}, where L_{Edd} is the luminosity at the Eddington limit). To this end, I considered the latest quasar catalogue by Wu and Shen (2022, henceforth WS22), who compiled continuum and emission-line properties for 750,414 broad-line quasars from the SDSS DR16, including physical quantities such as single-epoch virial $\mathrm{M_{BH}}$, $\mathrm{L_{bol}}$, and λ_{Edd}. I also gathered the latest spectral data available for each source in the sample, hence the spectra of ~4% of the sources belong to the DR17 release, where calibration files have been updated (Abdurro'uf et al., 2022).

Fig. 2.1 presents the $\log \mathrm{L_{bol}} - \log \mathrm{M_{BH}}$ plane for the sample. The partition of the plane was defined by seeking the balance between a large number of bins to improve the sensitivity on the parameters ($\mathrm{L_{bol}}$, $\mathrm{M_{BH}}$) that control the average spectrum, and a statistically robust number of objects in each region. I further divided the sample into five redshift intervals, $z = [0.13, 0.77, 1.12, 1.52, 2.03, 5.42]$, each one containing a similar number of objects (roughly 480 objects per bin). The resulting grid is shown in Fig. 2.1. The width of the $\log \mathrm{M_{BH}}$ ($\log \mathrm{L_{bol}}$) bins is 0.7 dex (1 dex), large enough to encompass the large systematic uncertainties associated with the estimate of this quantity, typically 0.3 dex (but up to 0.4 dex in case of C IV-based $\mathrm{M_{BH}}$, e.g. Shen et al. 2011; Kratzer and Richards 2015; Rakshit et al. 2020). The points of the grid are $\log \mathrm{M_{BH}} = [7.0, 7.7, 8.4, 9.1, 9.8, 10.5]$ and $\log \mathrm{L_{bol}} = [44.4, 45.4, 46.4, 47.4, 48.4]$. This procedure defines a 3D grid made of $5 \times 5 \times 4 = 100$ bins. The individual cells are labelled using the following nomenclature: increasing capital letters (A, B, C, D) denote decreasing bolometric luminosity across the bins, while increasing numbers (1, 2, 3, 4, 5) mark increasing average black hole masses, and increasing lower-case letters (a, b, c, d, e) represent increasing redshift intervals, which are also colour-coded according to the values in the legend.

Clearly, not all the bins are densely, nor uniformly populated. Lower redshift quasars preferentially occupy the lower luminosity and black hole mass region, whereas higher redshift sources are observed at higher values of both $\mathrm{L_{bol}}$ and $\mathrm{M_{BH}}$. Moreover, there are cells in the $\mathrm{L_{bol}} - \mathrm{M_{BH}}$ plane where the barycentre of the sources is close to the edge of a given interval (e.g. B2, B5, C1). In these cases, low sample statistics would produce not only low signal-to-noise (SNR) composite spectra, but also a stack not fully representative of its nominal locus in the parameter space.

To select the regions in the $\log \mathrm{M_{BH}} - \log \mathrm{L_{bol}}$ plane populated enough to be included in the stacking analysis, I quantified the probability that a statistical fluctuation in terms of $\log \mathrm{M_{BH}}$ and $\log \mathrm{L_{bol}}$ of objects in adjacent bins pushed them into a given region. I simulated 1000 mock samples starting from the actual distribution of $\log \mathrm{M_{BH}}$ and $\log \mathrm{L_{bol}}$ in each bin within the grid. The values of $\log \mathrm{M_{BH}}$ and $\log \mathrm{L_{bol}}$ are then scattered by a value drawn from a Gaussian distribution whose amplitude was set by the total uncertainty on each given data point. In doing so, I conservatively assumed the largest possible systematic uncertainty on both parameters and summed it in quadrature to the statistical uncertainty reported in WS22. For the bolometric corrections, I assumed a systematic uncertainty of ~50% on $\log \mathrm{L_{bol}}$ for each data point in the plane, suitable in case the bolometric correction is performed on the rest-frame 1350 Å luminosity (see Shen et al. 2011), which translates into $\lesssim 0.22$ dex. The systematic uncertainty on $\log \mathrm{M_{BH}}$ was assumed to be 0.40 dex, a value based on the C IV calibration (i.e. the least reliable one). As a consequence of the random scatter, the points of the mock sample distribution could escape the bin where the original data were instead contained. I then computed the average $\log \mathrm{M_{BH}}$ and $\log \mathrm{L_{bol}}$ of the resulting scattered points and retained only the regions within the parameter space where in at least 90% of the mock samples the average $\log \mathrm{M_{BH}}$ and $\log \mathrm{L_{bol}}$ remained within the bin. I refer to bins retained by this procedure as bins meeting the "representativeness criterion". In general, 44 bins out of 100 in the parameter space do not contain any object, while 25 bins are excluded by the aforementioned criterion. The whole selection procedure ultimately excluded 69 scarcely populated bins (with less than nine objects), and it ensures that the composite spectrum is truly representative of its associated region in the parameter space. At the end of this procedure, 2,316 objects were retained in the parameter space.

2.4.2 Building the stacks

The spectra were collected according to their PLATE, MJD and FIBERID reported in WS22.[2] I produced the stacked spectra and adopted a bootstrap recipe for the evaluation of the uncertainty on the stacks (more quantitative assessments on how different stacking prescriptions affect the results are explored in the Supplementary Material section 2.8) in each of the selected regions following the steps described below.

Each spectrum was corrected for Galactic absorption assuming the value for the colour excess E(B-V) available in the WS22 catalogue (Schlafly and Finkbeiner 2011) and a Fitzpatrick (1999) extinction curve. Then, the de-reddened spectra were shifted to the rest frame.

All the spectra in the same redshift bin were resampled, by means of linear interpolation, onto a fixed wavelength grid. The grid was defined in the interval $\lambda_1 - \lambda_2$ with a fixed dispersion $\Delta\lambda$ so as to cover the shortest and the longest rest-frame wavelengths in each redshift interval. The values for $\lambda_1, \lambda_2, \Delta\lambda$ are listed in Table 2.1. The value for $\Delta\lambda$ was chosen in order to preserve the SDSS observed frame resolution also in the rest frame spectra, similarly to what described in Section 3.2 of Berk et al. (2001, VB01), assuming an observed frame spectral resolution of ~2000 at 6500 Å.

Also a few quality cuts were applied. Objects with more than 10% of the pixels flagged as bad (AND_MASK > 0) in their SDSS spectra were excluded. Also objects where the normalisation wavelength $\bar{\lambda}$ (the wavelength chosen to scale all the spectra in the cell) was not covered in the rest-frame spectrum were excluded.

The average flux in each spectral channel and the relative uncertainty were evaluated adopting a bootstrap technique. In brief, a number of spectra equal to the total number of objects in the bin is drawn, allowing for replacement. These spectra are normalised by their flux value at the reference wavelength $\bar{\lambda}$, and an average stack is produced. This procedure is repeated with new draws until the

---

[2] The spectrum of SDSS J124406.96+113524.2 could not be found. However, this quasar belongs to a region where there are ~60 objects, thus I expect that its inclusion would not play any significant difference in the resulting stack.

desired number of stacks is reached. Subsequently, in each spectral channel the distribution of the normalised fluxes is computed, a 3σ clipping is applied, and the median value (less affected by possible strong outliers) is chosen. The uncertainty on the median value was evaluated as the semi-inter-percentile range between 1st and 99th percentile of the latter distribution.

The information about the relevant quantities adopted in each redshift interval is shown in Table 2.1. I explored different possible ways of combining the spectra, averaging the flux in each spectral channel and estimating the uncertainty. How these assumptions affect the resulting composites and the subsequent results, is presented in the Supplementary Material 2.8.1 and 2.8.1. All the composite spectra are presented in Supplementary Material 2.8.6.

Redshift interval (1)	$N_{\rm obj}$ (2)	λ_1 (3)	λ_2 (4)	$\Delta\lambda$ (5)	$\bar{\lambda}$ (6)
0.13–0.77	484	2062	9200	2.2	5100
0.77–1.12	479	1722	5876	1.7	4200
1.12–1.52	473	1448	4906	1.4	3100
1.52–2.03	483	1205	4127	1.2	2200
2.03–5.42	474	569	3432	0.7	1450

Table 2.1. Stacking parameters. Redshift interval (1), number of sources within the redshift interval (2), lower (3) and upper (4) wavelengths of the wavelength grid, fixed dispersion (5), and reference wavelength (6). All wavelengths are reported in units of Å.

2.4.3 Spectral fit of the composites

To estimate the characteristic spectral quantities of the continuum (chiefly the slope α_λ of the power law $f_\lambda \propto \lambda^{-\alpha_\lambda}$) and the emission lines, in particular the rest-frame equivalent width (EW), the full width at half-maximum (FWHM), and the peak offset velocity ($v_{\rm off}$), I performed the spectral fits of all of the composite spectra. To this end I adopted a custom-made code, based on the IDL MPFIT package (Markwardt, 2009), which takes advantage of the Levenberg-Marquardt technique (Moré, 1978) to solve the least-squares problem. The main goal here is a faithful reproduction of the continuum, in order to investigate whether the continuum slope and consequently the 2500 Å flux exhibit any significant evolution with the accretion parameters.

The baseline model is given by a continuum power law pivoting at different emission-free wavelengths depending on the redshift interval (3000 Å in the three bins at $z < 1.52$, 2200 Å in the two bins at $z \geq 1.52$), a set of emission lines, the Balmer continuum, and a set of iron templates convolved with a Gaussian line-of-sight velocity distribution whose weights are free parameters in the fit. Each line required a different decomposition: the C IV line was generally fitted with two Lorentzian profiles (one broad, one narrow). A single broad Lorentzian profile combined with the iron templates is able to adequately reproduce the Mg II profile. The Hβ was modelled by considering a core narrow Gaussian component whose FWHM could not exceed ~1000 km s^{-1} and a broad component whose analytical shape (Gaussian

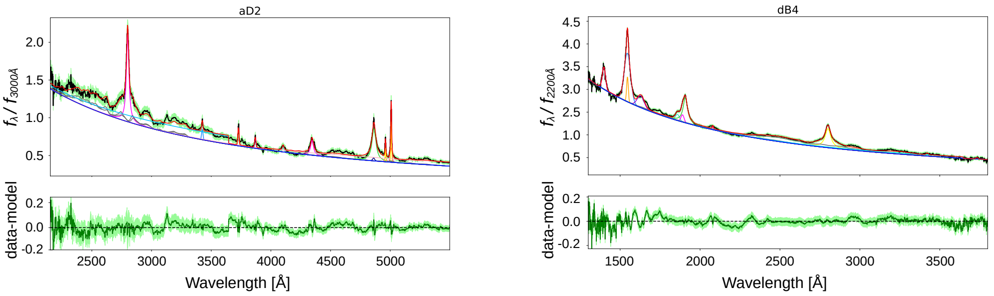

Figure 2.2. Examples of a low-redshift bin (left) and a high-redshift bin (right) fit. The continuum power law is marked in blue, Fe II templates in grey, emission lines in different colours (orange, purple, green, cyan). The total model is depicted in red.

or Lorentzian) was chosen each time to best reproduce the data. Here the choice of the emission line profile is merely empirical, and based on the best-fit residuals. It is possible that wider tails of the Lorentzian profile do a better job in reproducing a potential faint very broad outflow component. The [O III] doublet was modelled with Gaussian or Lorentzian profiles with a ratio of the [O III]λ4959Å to λ5007Å components fixed at one to three. In addition, other weaker forbidden ([Ne V] λ3426, [O II] λ3727, [Ne III λ3869]) and permitted (Hγ, Hδ) emission lines were included to improve the residuals. Above $\log(\mathrm{L_{bol}}/(\mathrm{erg\,s^{-1}})) \gtrsim 46$ the host galaxy contribution at optical wavelengths is expected to be negligible with respect to the quasar emission (Shen et al. 2011; Jalan et al. 2023). Therefore, I only added an elliptical galaxy template from Assef et al. (2010) to the model, to account for possible galactic emission, only in the two lowest redshift bins, where the bulk of the sample has $\mathrm{L_{bol}}$ close or below above value and the rest-frame wavelengths sampled in these redshift ranges could be imprinted by galactic emission. The fits were performed adopting the same wavelength interval within the same redshift bin to avoid mismatches between the adopted continuum windows. The fitting wavelengths are listed in Table 2.2 and examples of a low- and a high-redshift fits are shown in the left and right panels of Fig. 2.2, respectively.

Redshift interval (1)	λ_1 (2)	λ_2 (3)	$\bar{\lambda}$ (4)
0.13–0.77	2150	5500	3000
0.77–1.12	2150	5500	3000
1.12–1.52	1700	4500	3000
1.52–2.03	1300	3800	2200
2.03–5.42	1300	3200	2200

Table 2.2. Fit parameters. Redshift interval (1), lower (2) and upper (3) wavelengths, and normalisation wavelength (4) of the stacks. All wavelengths are reported in units of Å.

The uncertainties on the relevant parameters were estimated by means of mock samples. For each composite I produced 100 mock samples by adding a random value to the actual flux, extracted from a Gaussian distribution whose amplitude was set by the uncertainty value in that spectral channel. I then fitted the mock samples and evaluated the 3σ clipped distribution of the relevant parameters. The final uncertainty on the reported parameters was estimated as the standard deviation of such a distribution.

2.5 Results

2.5.1 The full sample and literature composite spectra

As a reference for the whole sample I produced a stacked spectrum collecting all the spectra of the L20 sample matching the quality criteria. The result is shown in Fig. 2.3. The procedure adopted to produce the template is the same as described in 2.4.2. The normalisation wavelength $\bar{\lambda}$ was set to 2200 Å, as this is the only relatively emission-line-free continuum window available for most of the objects in the sample.

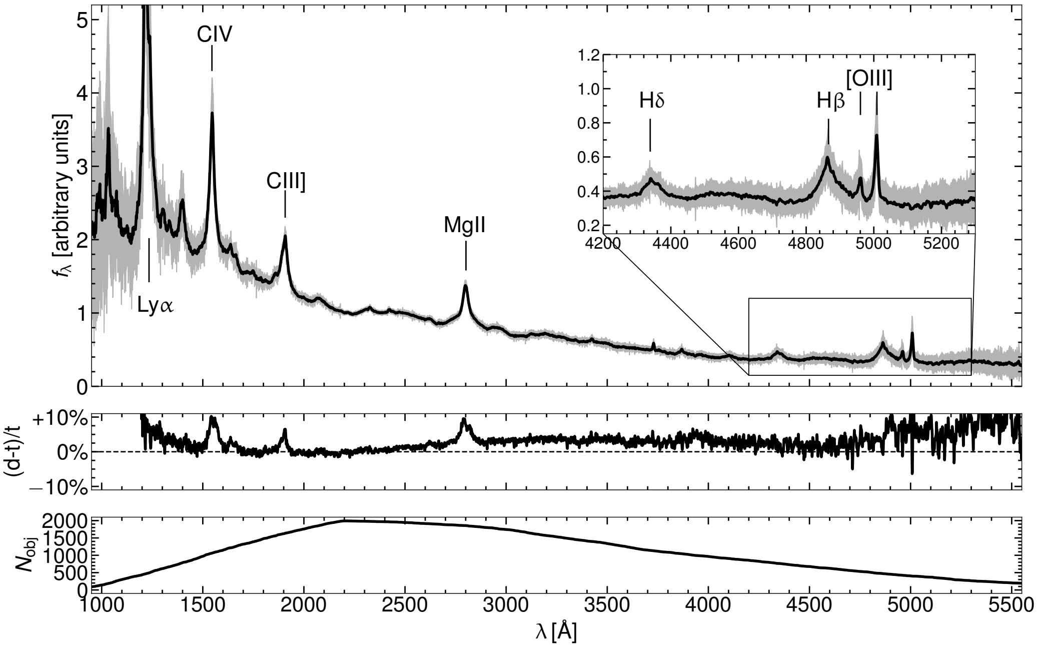

Figure 2.3. Spectral composite of the L20 sample. *Top panel:* Composite spectrum of the cosmological sample described in this Chapter. The Lyα emission line is cut for visualisation purposes. The inset zooms in on the Hβ–[O III] region. The main emission lines are labelled accordingly. *Middle panel:* relative residuals with respect to the VB01 template. *Bottom panel:* number of objects contributing to each spectral channel.

To place the sample in a broader context, I compared the new template with other literature average spectra, namely Francis et al. (1991), Brotherton et al. (2001), VB01, Selsing et al. (2016), and Harris et al. (2016).

The composite spectrum by Francis et al. (1991) was produced using 718 objects from the Large Bright Quasar Survey (LBQS) with absolute magnitude in the B-band $M_B \leq -20.5$ and redshifts in the range $0.05 < z < 3.36$; this sample is strongly biased towards luminous objects at high redshift. The FIRST Bright Quasar Survey (FBQS, Brotherton et al., 2001) took advantage of FIRST radio observations of known point-like sources with colour indices[3] $O - E < 2.0$ and $E < 17.8$ from the Palomar Observatory Sky Survey I (POSS-I). This match yielded 636 sources, here I show only the composite spectrum made of the radio-quiet sources as a comparison.

The first SDSS quasar template was produced by VB01, who selected 2204 sources between $0.004 \leq z \leq 4.789$ based on the SDSS colour difference (Richards et al., 2001), a non-stellar continuum, and at least one broad (FWHM > 500 km s^{-1}) permitted emission line. The sample adopted by Harris et al. (2016) was instead based on the Baryon Oscillation Spectroscopic Survey (BOSS; Dawson et al. 2012), as part of SDSS-III (Eisenstein et al. 2011), aimed at characterizing the effects of the baryon acoustic oscillations (BAO) on the distribution of luminous red galaxies and studying the Lyα forest in high-redshift quasars. These purposes resulted in a sample of 102,150 objects between $2.1 \leq z \leq 3.5$ (see Harris et al. 2016 for more details about the sample selection). Given the redshift range covered by such sources, the comparison with this composite spectrum was possible only in the UV up to ~3000 Å. Lastly, Selsing et al. (2016) observed with XSHOOTER/ *VLT* a sample of seven bright ($r \lesssim 17$) quasars between $1.0 < z < 2.1$, for which galactic contribution should be regarded as negligible.

The comparison between the template produced here and the literature ones is shown in Fig. 2.4. Note that, the y-axis represents λf_λ, rather than the usual flux density. The agreement is generally good, especially in the region between 1100-4000 Å. At shorter wavelengths, the intergalactic medium (IGM) can affect the composites differently, according to the distribution in redshift of the individual spectra upon which the stacks are based (e.g. Madau 1995; Faucher-Giguere et al. 2008; Prochaska et al. 2009). On the red side, instead, some intrinsic differences start to become visible. This composite is almost indistinguishable from the VB01 composite, but these two seem flatter than the others. There are several explanations for this slight difference in the long-wavelength end of the composites. First, the colour selections performed to select the quasar candidates is not homogeneous among the different samples, thus the SDSS objects that constitute the VB01 sample as well as ours could present slightly redder indices in the optical range below $z = 0.8$. Secondly, it is possible that the host galaxy, whose contribution is negligible in the UV (see Sec. 2.5.5) plays a minor role in flattening the optical side of the spectra. VB01 estimated the galaxy contribution to be roughly 7-15% at the Ca II λ3934 wavelengths, and a similar fraction can be estimated in this global composite. On the other hand, the other surveys and the Selsing et al. (2016) sample are made, on average, of more luminous objects for the same redshift (see inset in Fig. 2.4). It is therefore likely that the galactic contribution in those templates is even lower than in ours.

Throughout this Chapter, I will refer to the full sample template as a reference to compare to the composite spectra of the individual bins in the $\mathrm{M_{BH}} - \mathrm{L_{bol}} - z$ space, unless differently stated.

---

[3] More details about the POSS-I photometric system can be found in Evans (1989).

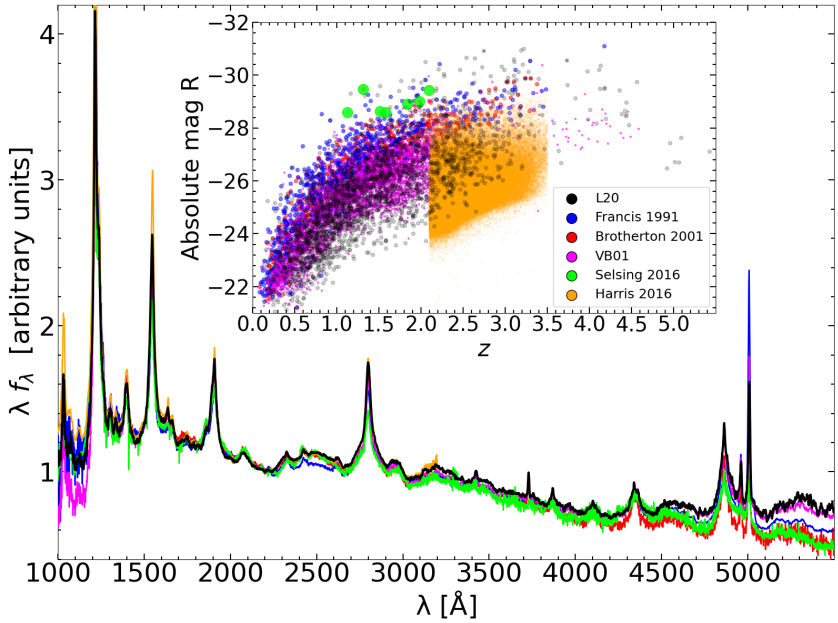

Figure 2.4. Comparison between the quasar template produced here and others from the literature. All the templates are scaled by their emission at 2200 Å. The agreement on the UV side, apart from minor differences in the Fe II pseudo-continuum, specifically the 2250-2650 Å and the 3090-3400 Å bumps, is apparent. The Lyα emission line is cut for visualisation purposes. The inset shows the distribution of the absolute R magnitude against the redshift for the different samples reported.

2.5.2 Non-evolution with redshift

A key observational feature bridging local and high-redshift quasars is the apparent similarity of their optical–UV continuum up to primordial times (e.g. Banados et al. 2018; Yang et al. 2020; Wang et al. 2021). However, if the quasar spectra showed even a subtle evolution with redshift, the accretion physics underlying the X-ray to UV relation could also be evolving, making quasars unsuitable candidates as standard candles. Given the wide range in terms of redshift covered by the sample, it is natural to expect to be capable of detecting any such possible effect. This would appear as a systematic difference in the slope of the continuum produced by the accretion process at different cosmic times.

As a very basic step to check for any evolution with redshift of the spectral properties within the sample, in Fig. 2.5 I compare the average spectra in the redshift bins with the global composite (described in Sec. 2.5.1), obtained by stacking the spectra of all the sources in the sample. I find a very good agreement with the global composite at all redshifts, without any clear evidence of evolution, apart from the known trends of the emission lines, whose FWHM varies with M_{BH} (i.e. the virial relation; e.g. Peterson et al. 2004) and whose EW anti-correlates with L_{bol} (i.e. the Baldwin effect; Baldwin 1977).

The visual agreement is confirmed by a more quantitative assessment presented in the bottom-right panel in Fig. 2.5. There I show the slope of the continuum evaluated in continuum intervals sampled at different redshifts by the spectral composites. The slopes are generally consistent within 1σ, and no systematic trends are observed. The optimal agreement between the composite spectrum in every redshift bin and the global composite, as well as among the different redshift composites, demonstrates the non-evolution of the average continuum properties of the sample across cosmic time.

In addition, as discussed in Section 2.5.1, the global sample composite exhibits a remarkable agreement with the average SDSS spectrum described in VB01, meaning that the stacks in the different redshift bins are also similar to the spectrum of a typical blue quasar. Since even this direct comparison reveals that the average continuum properties of the sample do not suggest any redshift evolution, I now investigate and characterise in more detail how the sample behaves across the $\log \mathrm{M_{BH}} - \log \mathrm{L_{bol}}$ parameter space.

2.5.3 Analysis of the evolution of the continuum slope of the stacks

The fits of the stacked spectra returned the slope of the continuum in each bin of the parameter space. I thus explored whether any possible evolution of the continuum slope exists throughout the sample. With the term slope (α_λ), I denote the slope of the continuum power law underlying the emission lines roughly between 1300 and 5500 Å. This wavelength range is sampled differently in the different redshift bins: for instance in the lowest redshift bin only the interval 2200-5500 Å is available, while in the highest redshift bin the composite spectra were fitted over the interval 1300-3200 Å. I also underline that, here I never assign a physical meaning to the slope of the continuum, adopting it exclusively as a comparative parameter. The physical meaning of such a parameter would require the assumption of a physical continuum model, generally an accretion disc, but see also e.g. Antonucci et al. (1989) for some limitations, whose implications go beyond the scope of this thesis.

In Fig. 2.6, I show the values of the slope in the redshift bins as a function of $\log \mathrm{M_{BH}}$, $\log \mathrm{L_{bol}}$, and $\log \lambda_{\mathrm{Edd}}$. To avoid dust reddening or galaxy contamination, a broad selection in terms of photometric colours has been performed when constructing the cosmological sample (see Section 1.3). I briefly repeat here the process: for each object, the slope of the power law in the $\log \nu - \log(\nu f_\nu)$ space was computed in the rest-frame ranges 3000-10000 Å (Γ_1) and 1450-3000 Å (Γ_2). Objects whose photometric colours were compatible with those of typical blue quasars, $\Gamma_1 = 0.82$ and $\Gamma_2 = 0.40$ (Richards et al., 2006), only tolerating mild reddening, i.e. E(B-V) < 0.1, were selected. Converting the photometric indices Γ in terms of spectral slopes as $\alpha_\lambda = -\Gamma - 1$, the expected slopes in the 3000-10000 Å and the 1450-3000 Å ranges, respectively covered by the low and high redshift bins, are $\alpha_{\lambda,1} = -1.82$ and $\alpha_{\lambda,2} = -1.40$. Although this process operates a sort of pre-selection on the possible continuum slopes, I note that only roughly 20% of the starting sample is excluded according to this colour selection.

In Fig. 2.6 I show the slopes of the continuum evaluated in the bins of the parameter space. I mark with a hollow circle the values of the bins with a low N_{obj} which would be excluded as a result of the representativeness criterion described in Sec. 2.4.1. The values cluster around $\alpha_\lambda = -1.50$ with a standard deviation of $\sigma_\alpha = 0.14$, showing little or no evolution from low to high redshift. Considering also the excluded bins, the results are not significantly altered as the mean value

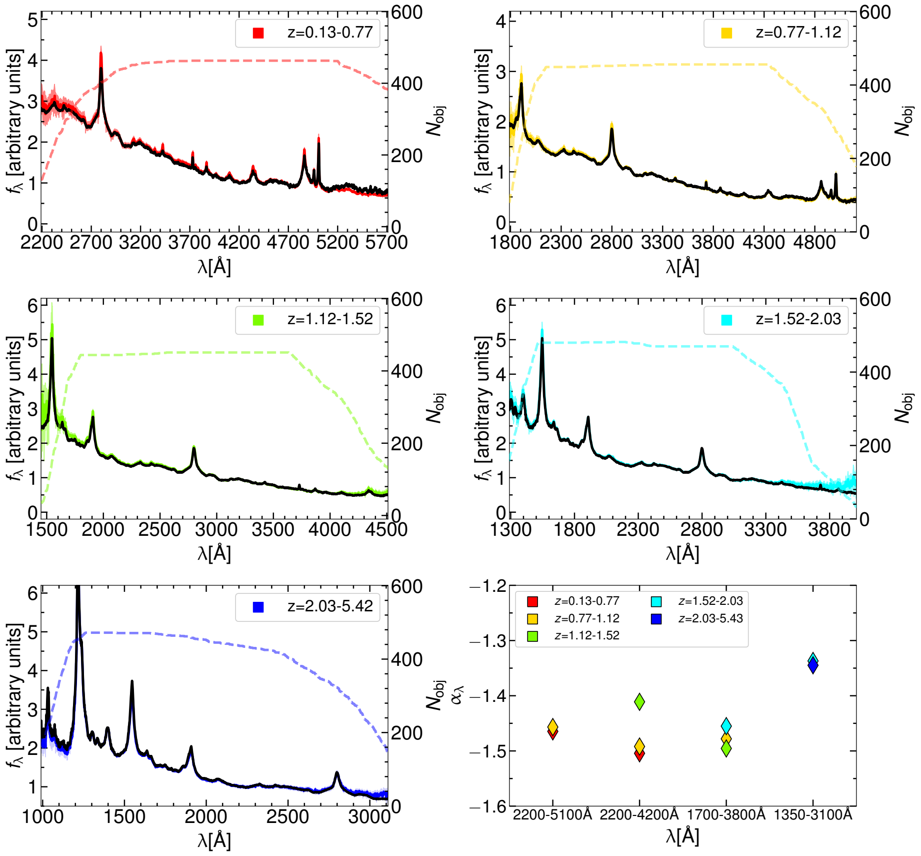

Figure 2.5. Composite spectra divided in redshift bins superimposed to the full sample composite. The dashed line denotes the number of objects contributing to the stack in each spectral channel. The composite spectra in each bin are scaled to match the template respectively at 4200 Å for the low redshift bin, 3000 Å for the $z = [0.77 - 1.12)$, $z = [1.12 - 1.52)$, $z = [1.52 - 2.03)$ bins, and 2200 Å for the highest redshift bin. In the bottom-right panel I show the slopes of the continuum evaluated in different pairs of continuum windows, which are generally consistent.

negligibly shifts to $\alpha_\lambda = -1.51$ and the standard deviation to $\sigma_\alpha = 0.17$. The slope average value is close to those expected from the Richards et al. (2006) typical photometric index and from the templates of blue quasars described in Sec. 2.5.1, whose continuum slopes, evaluated using the fitting routine employed here, are reported in the inset panel of Fig. 2.13. It useful to recall that the slopes are evaluated using different continuum windows at different redshifts. For a fixed value of M_{BH} (or equivalently L_{bol}), the distribution in the observed slopes is therefore partly due to the spread along the other axis of the parameter space, which is anyway modest, and partly driven by the different continuum windows.

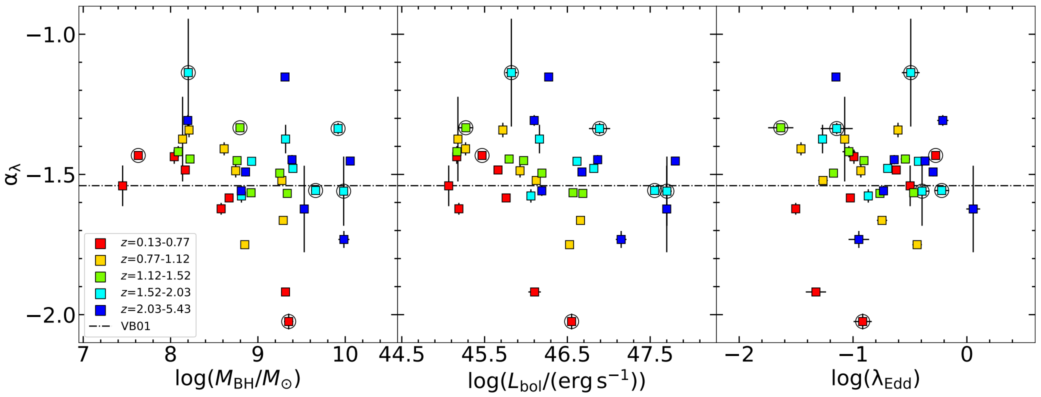

Figure 2.6. Values of the slope of the continuum produced by the spectral fits. Bins not meeting the representativeness criterion are marked with a circle. The slope of the VB01 template (dot-dashed line) is shown as an external reference. Different pairs of line-free windows were adopted to define the continuum in each bin.

I assessed the degree of correlation between the slope and the axes of the parameter space by means of the Spearman rank correlation index S (correlation increases in modulus from 0 to 1). I do not find any significant trend with any of the accretion parameters, (i.e. $|S| \leq 0.3$ and associated $p-$values > 0.05). The inclusion of the bins excluded as a result of the representativeness criterion, does not change significantly the correlation index, as I show in Supplementary Material 2.8.4.

In addition to exploring the evolution of the continuum within the parameter space, I also explored how the number of sources in each bin affects the continuum properties with respect to the global template. In particular, in Fig. 2.7 I present the relative difference between the continuum slope of the continuum for each bin ($\alpha_{\rm bin}$) and the full sample composite ($\alpha_{\rm FS}$) evaluated in the same wavelength range $\Delta\alpha = 1 - \alpha_{\rm bin}/\alpha_{FS}$ against the number of objects in the bin. Regardless of the redshift, the difference decreases in modulus for increasingly populated bins, as if the samples were drawn from a single population. In this picture, the spread in the observed slopes results from sample variance, rather than from an actual evolution with the accretion parameters explored.

2.5.4 Comparison of the 2500 Å monochromatic fluxes

I produced the normalised monochromatic 2500 Å fluxes ($f_{2500\,\text{Å}}$) by interpolating the continuum resulting from the best fit slope and assuming a unitary monochromatic flux at 3000 Å. In Fig. 2.8 I present $f_{2500\,\text{Å}}$ against $\log \rm M_{BH}$, $\log \rm L_{bol}$, and $\log \lambda_{\rm Edd}$ in order to study any possible evolution. In principle, a systematic change of the $f_{2500\,\text{Å}}$ with the accretion parameters would require a correction to "standardise" the UV proxy. However, there is evidence against this possibility.

In Signorini et al. (2023b) it is shown that the monochromatic 2500 Å flux is a good UV proxy for the $\rm L_X - L_{UV}$ relation, although other wavelengths in the range 1350-5100 Å can perform equally well (see also Jin et al. 2024). Therefore, even assuming different slopes, the UV term of the $\rm L_X - L_{UV}$ relation would hardly be affected.

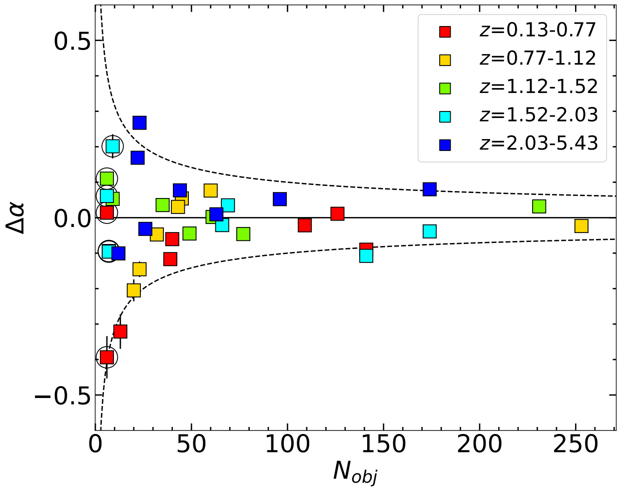

Figure 2.7. Values of $\Delta\alpha$ ($\Delta\alpha = 1 - \alpha_{\mathrm{bin}}/\alpha_{FS}$) in the bins of this parameter space as a function of the objects in each bin. Bins not meeting the representativeness criterion are marked with a circle. The dashed lines define the $\sim 1/\sqrt{N_{\mathrm{obj}}}$ envelope characterising the standard error on the average slope assuming a standard deviation $\sigma_\alpha = 1$.

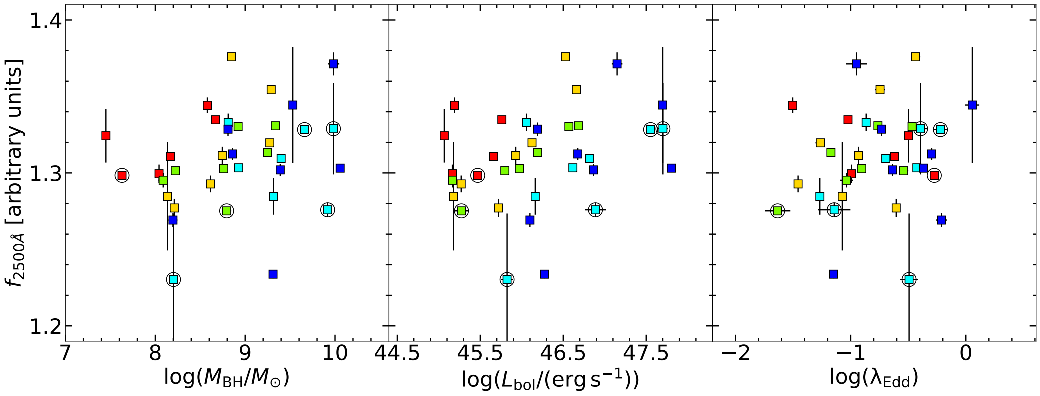

Figure 2.8. Values of the normalised 2500 Å fluxes along the axes of the parameter space, assuming a common normalisation of the continuum at 3000 Å in all the bins. Bins not meeting the representativeness criterion are marked with a circle.

Here I aimed at quantifying the effect on the monochromatic 2500 Å fluxes of the differences in the spectroscopic slopes within the sample. The slopes are comprised between roughly [−2.0, −1.1], with the extremal values found in scarcely populated bins (respectively 9 and 6 objects), which would be excluded as a result of the procedure described in Sec. 2.4.1. Since the goal here is to corroborate the sample for its cosmological application, it is possible to estimate how much the spread in the observed slopes affects, for instance, the distance modulus (DM) estimates. Here I show that, even assuming a systematic evolution in the continuum slope with one of the explored parameters (an occurrence which is not supported by this analysis), the variation induced in the $f_{2500\AA}$ would propagate into a negligible difference in the DM for the cosmological application. It can be easily checked that, expressing

DM in terms of $f_{2500\text{Å}}$, and adopting the expression (see Risaliti and Lusso 2015, 2019; Lusso et al. 2020)

$$\mathrm{DM} = 5\left[\frac{\log f_{\mathrm{X}} - \beta - \gamma\,(\log f_{2500\,\text{Å}} + 27.5)}{2(\gamma-1)} - \frac{1}{2}\log(4\pi) + 28.5\right] \\ - 5\,\log(10\,\mathrm{pc}), \tag{2.1}$$

where f_{X} and $f_{2500\,\text{Å}}$ are, respectively, the X-ray and UV flux densities in units of erg s^{-1} cm^{-2} Hz^{-1}. The parameter $\log f_{2500\,\text{Å}}$ is normalised to the value of 27.5, whereas the logarithm of the luminosity distance is normalised to 28.5. The $\gamma = 0.600 \pm 0.015$ term is the slope of the $\mathrm{L_X} - \mathrm{L_{UV}}$ relation reported in L20, and β is the intercept. Here it is possible to express the 2500 Å monochromatic flux in a power-law form pivoting at 5100 Å (i.e. the farthest among the explored characteristic wavelengths). By differentiating Eq. 2.1 with respect to the slope of the continuum α_λ

$$\Delta DM = \left|-\frac{5\gamma}{2(\gamma-1)}\log\left(\frac{2500}{5100}\right)\right|\Delta\alpha_\lambda. \tag{2.2}$$

The standard deviation of the observed slopes (σ_α=0.17) can be substituted as a measure of the spread of the $\Delta\alpha_\lambda$ term. The DM variation, ΔDM~0.2 in modulus, is not sufficient to explain the differences observed with the ΛCDM at high redshifts (see 2.12). If, as it is safe to believe, 2500 Å is a better approximation to the UV pivot point than 5100 Å , the average Δ DM is expected to be even smaller.

2.5.5 Host galaxy contamination

Although the broadband properties of the objects included in the sample are designed to minimise the additional contribution of the host galaxy in the quasar spectrum, here I perform an a posteriori test based on the spectral data to estimate the average degree of host galaxy emission in the sample. In Rakshit et al. (2020) a host galaxy–quasar decomposition was performed using a principal component analysis (PCA, Yip et al. 2004) in two windows close to 4200 Å and 5100 Å, obtaining reliable results for ~12,700 objects below redshift $z \leq 0.8$. I employed these measurements to assess the level of residual (i.e. not filtered out by the cosmological sample selection criteria) host galaxy contamination within the quasars of the sample. With this aim, I built a purposefully designed sample of sources below z = 0.8 to ensure the coverage of both the host fraction indices, from the latest WS22 catalogue by adopting the following criteria.

I considered only the objects for which the host galaxy fraction indices at 4200 Å (HOST_FR_4200) and 5100 Å (HOST_FR_5100) were both evaluated, with values ranging continuously from 0 (quasar-dominated emission) to 1 (galaxy-dominated emission). If any of the two indices was flagged as not measured (i.e. = −999), the object was discarded.

I defined the host galaxy fraction index (HGF) and created 10 bins of width ΔHGF = 0.1. A source was given a HGF index when both the 4200 Å and the 5100 Å fractions fell within the same HGF bin in order to define an unambiguous index. The sample so constructed had 5748 objects.

I then stacked the spectra of the objects in each bin according to the same procedure described in Sec. 2.4.2. In Fig. 2.9 I show the stacked spectra as a function of their HGF index. To perform a fair comparison, I also produced a stack of all the 529 sources with SDSS spectra in the cosmological sample with $z \leq 0.8$ (shown in black). On average, the quasars in the low redshift tail of the sample retain minimal levels ($\lesssim 10\%$) of host galaxy contamination below 5400 Å, in good agreement with VB01 who report a galaxy flux fraction between 7% and 15% on the basis of the Ca II λ3934 absorption feature. At redder wavelengths, the host contribution is expected to become increasingly important. In addition, it is worth noting that the difference is terms of continuum slope and line strength is more evident in the UV region of the spectra, where the template exhibits the best match with the other samples of blue quasars. This test confirms that the UV proxy adopted for the $L_X - L_{UV}$ relation is not systematically affected by host galaxy contamination.

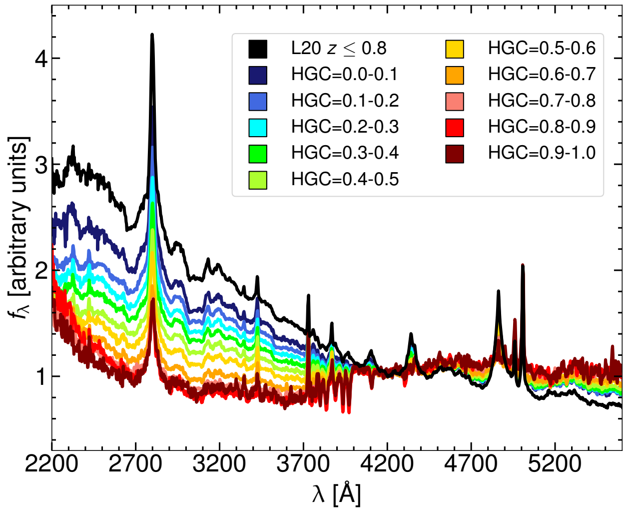

Figure 2.9. Comparison between the stacks in bins of HGF and the reference spectrum (black) for the $z \leq 0.8$ interval, as colour-coded in the legend. All the spectra are scaled to their 4200 Å flux. Increasingly host-dominated composites exhibit flatter UV continua.

2.5.6 Intrinsic extinction

The aforementioned photometric selection is designed to exclude dust reddened quasars, by retaining only sources near the locus in the Γ_1 - Γ_2 plane where blue unobscured quasars are expected to reside (Richards et al. 2006). I again checked, a posteriori, that the spectra composing the sample only accept minimal levels of extinction, and three arguments in favour of this hypothesis can be brought.

First, as a general consideration, I find a very good agreement between the stacks and the VB01 SDSS template, which is made of sources whose colour-selection had been designed to select blue quasars (Richards et al., 2001). The agreement is excellent – especially on the bluer UV side, the extinction is higher for most of the extinction curves – also with the other average spectra shown in Sec. 2.5.1. This implies that, if the quasars used to build such templates are not redder than the average, the same should hold for this sample. I also recall that, by selection, the VB01 template was built using objects with at least one broad emission line, thus the presence of Type 2 obscured objects should be negligible.

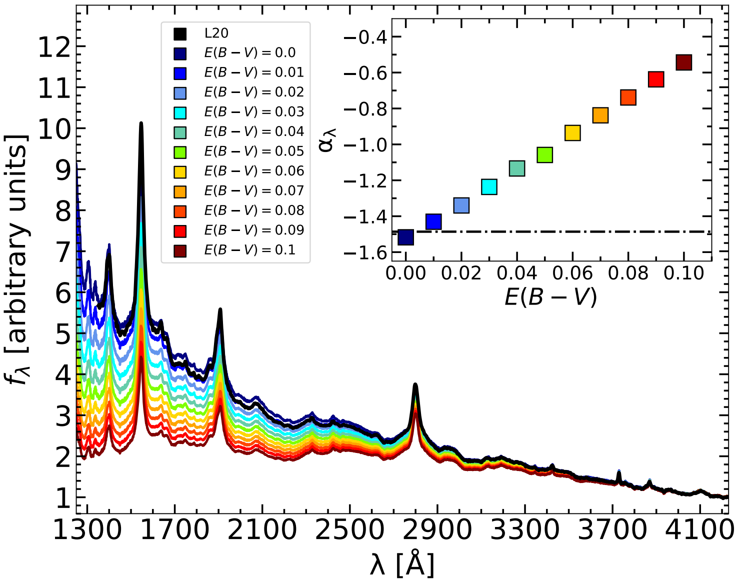

Figure 2.10. Extinction of the VB01 template according to the colour-coded values. All the spectra are scaled by their 4200-Å flux, where extinction becomes less relevant. The black spectrum is the full sample stack and is in very good agreement with a low degree of extinction. The inset shows the best-fit slope in the range 1300-4100 Å of the VB01 template reddened as a function of the E(B-V) value. The black dot-dashed line represents the slope of the continuum fitted to this sample stack. Minimal levels of extinction are allowed to match the reddened template with the composite. I note that the visual match between the L20 and the VB01 reddened template depends slightly on the scaling wavelength, while the slope derived from the fits does not.

As a second test, to get a more quantitative assessment of the effect on the spectral slope of increasing reddening, I reddened the VB01 template under the reasonable hypothesis that this is representative of the intrinsic spectrum of a typical blue quasar. I reddened the template with increasing E(B-V) from 0 to 0.1 with steps of 0.01, using the extinction curve described in Gordon et al. (2016) for an average Small Magellanic Cloud (SMC) extinction curve, which according to several authors is a good approximation of the AGN extinction curve (see e.g. Brotherton et al. 2001; Hopkins et al. 2004), and then checked the agreement with the full sample stack. A more detailed discussion on how a different extinction curve can affect this procedure is presented in Supplementary Material 2.8.2, where other prescriptions are explored. In brief, I found that the variation of the continuum slope for a given colour excess derived adopting the Gordon et al. (2016), used to account for intrinsic reddening throughout this work, is the closest to the average (see Fig. 2.17). The result of the reddening procedure is shown in Fig. 2.10. The best match is obtained for minimal levels of intrinsic reddening, i.e. E(B-V)$\lesssim 0.01$, an estimate similar to that provided by Reichard et al. (2003) on the basis of spectral data from the SDSS early data release. To quantify this effect, I performed a spectral fit of the reddened templates in the region between 2200 and 3400 Å, and compared the slope of the continuum with that obtained by the fit of the stack in the same region. This test confirmed the finding emerging from a crude comparison of the overall spectral shape, that is a continuum slope consistent with a low degree of intrinsic extinction. The slopes resulting from the spectral fit of the reddened templates are shown in the inset of Fig. 2.10. I note that, choosing a different template than VB01 would produce analogous results, given the similarity of all the explored templates in the near UV.

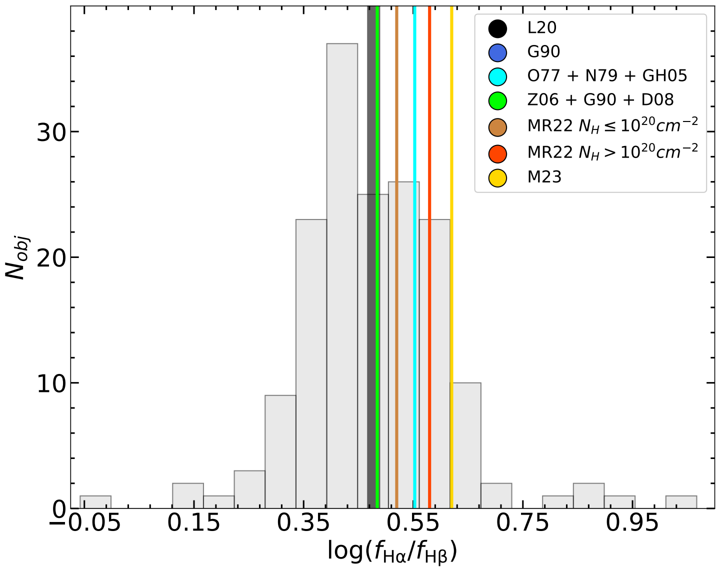

Figure 2.11. Distribution of $\log(\mathrm{H}\alpha_{\rm br}/\mathrm{H}\beta_{\rm br})$ for the sources in the sample with available data. The mean values from other literature samples (Osterbrock, 1977, O77, Neugebauer et al., 1979, N79, Goodrich, 1990, G90, Greene and Ho, 2005, GH05, Zhou et al., 2006, Z06, Dong et al., 2007, D07, Mejía-Restrepo et al., 2022, MR22, Ma et al., 2023, M23) are also shown for reference according to the colour code. The mean of these values is shown in black. The BASS sample described in Mejía-Restrepo et al. (2022) has been split according to the column density $N_{\rm H}$ inferred from the X-ray analysis.

Finally, I estimated the Balmer decrement of the low-redshift sources with available broad Hα and Hβ emission lines to assess possible levels of intrinsic extinction of the BLR. Dong et al. (2007) computed the distribution of the broad-line Balmer decrement $\mathrm{H}\alpha_{\rm br}/\mathrm{H}\beta_{\rm br} \equiv f(\mathrm{H}\alpha_{\rm br})/f(\mathrm{H}\beta_{\rm br})$ for a sample of 446 low-redshift ($z \lesssim 0.35$) blue AGN, finding that the distribution can be well approximated by a log-normal, with a mean value of $\langle \log(\mathrm{H}\alpha_{\rm br}/\mathrm{H}\beta_{\rm br}) \rangle = 0.486$ and a standard deviation of 0.03. A value of log(3.1)=0.49 is generally adopted for the Balmer decrement in the narrow line region in AGN (Halpern and Steiner, 1983; Gaskell and Ferland, 1984), while it is found to vary widely according to different BLR conditions (e.g. Dong et al., 2007 and references therein).

In this context, large Balmer decrements are interpreted as due to local reddening, as also suggested by large ratios between infrared emission and broad lines (Dong et al., 2005) and significant X-ray absorption (Wang et al., 2009). In Fig. 2.11, I show the distribution of $\log(\mathrm{H}\alpha_{\mathrm{br}}/\mathrm{H}\beta_{\mathrm{br}})$ ratios assuming the values reported in the WS22 catalogue for the 167 objects in the sample with reliable Hα and Hβ measurements (see Sec. 4 of WS22 for the detailed criteria). The mean value of the distribution is $\langle\log(\mathrm{H}\alpha_{\mathrm{br}}/\mathrm{H}\beta_{\mathrm{br}})\rangle = 0.48$, and the standard deviation is 0.14. Under the assumption that the sample of blue quasars described in Dong et al. (2007) retains, on average, minimal levels of BLR extinction (see their Sec. 4.1), I find that the intrinsic extinction is negligible, at least for the low redshift sample.

Finally, the combination of the three tests proposed here strongly suggests that intrinsic reddening should be minimal accross the entire redshift range covered by the sample.

2.5.7 Is the ΛCDM tension driven by reddening?

One of the main consequences of reddening would be the underestimate of the 2500 Å monochromatic fluxes. A relatively small amount of extinction, such as E(B-V) $\simeq 0.1$, would diminish the 5100-Å flux by ~25%, but the extincted radiation would be roughly double (depending on the assumed extinction curve) at 2500 Å, as a result of the differential cross section of dust. The net effect of extinction is thus the underestimation of the DM, enhancing the tension between the cosmographic best-fit model and the high-redshift ($z \gtrsim 2$-3) extrapolation of the ΛCDM model (Risaliti and Lusso, 2019; Bargiacchi et al., 2023). Here I focus on the possibility that the observed tension with the ΛCDM model is caused by local dust extinction affecting the UV measurements. To this end, I performed the following exercise, neglecting any possible effects on the X-ray fluxes. I assumed that the difference between the DM predicted by ΛCDM and that based on the $\mathrm{L_X} - \mathrm{L_{UV}}$ relation is entirely driven by local (i.e. at the source redshift) extinction on $f_{2500\,\text{Å}}$. Therefore, assuming a standard extinction curve, it is possible to evaluate the average E(B-V) by which $f_{2500\,\text{Å}}$ should be de-extincted in order to match the predicted DM. With this quantity in hand, the UV spectra can be consequently de-reddened to check how much their intrinsic shapes would differ from those observed. In the following, the term "de-reddened" will be used to indicate the extinction-corrected spectral fluxes that produce a DM complying with the ΛCDM model.

Fig. 2.12 shows the samples used for this purpose. I gathered spectral data of objects at $z \geq 1$, and divided them into 8 logarithmically equi-spaced redshift bins. For each of them, I evaluated the average redshift and $\mathrm{DM_{obs}}$ values. The DM can be written in terms of $f_{2500\,\text{Å}}$ by using Eq. 2.1 as:

$$\mathrm{DM} = -\frac{5}{2}\,\frac{\gamma}{\gamma-1}\log f_{2500\,\text{Å}} + C, \tag{2.3}$$

where C includes the X-ray flux contribution, the normalisation β, and the other constants. Assuming that the measured DM values are affected by reddening, it is possible to evaluate the amount of extinction needed to place the intrinsic DM exactly onto the ΛCDM expectations and de-redden $f_{2500\,\text{Å}}$ accordingly. Such a

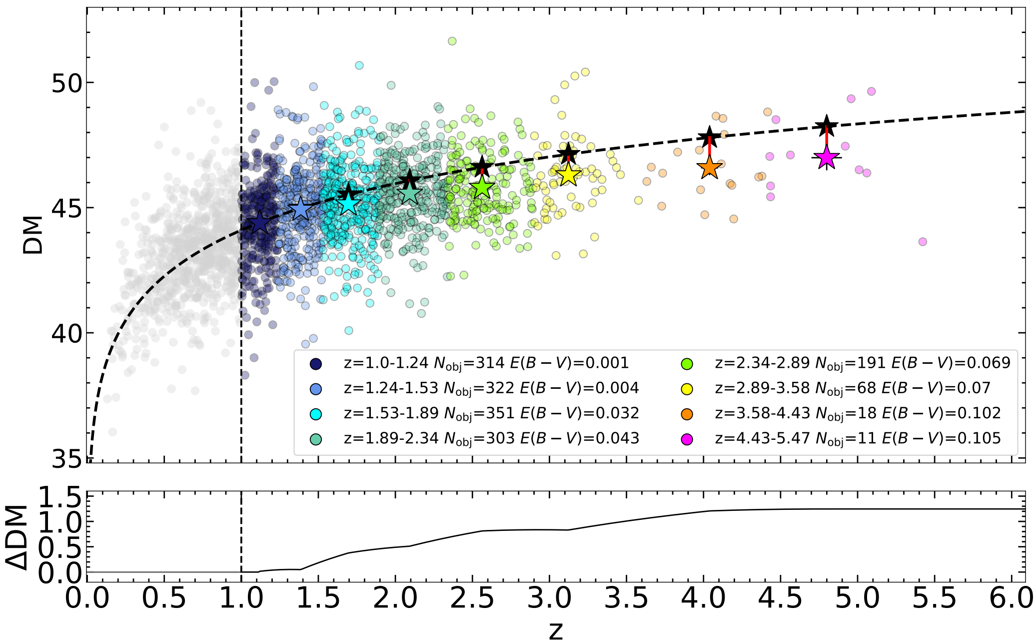

Figure 2.12. Effect of the intrinsic extinction on the Hubble–Lemaître diagram. *Top panel:* Hubble–Lemaître diagram of the sources used to investigate the possible effects of local reddening. The redshift bins used for this purpose are colour-coded in the legend together with the number of objects per bin and the corresponding E(B-V). Coloured stars represent the average values in each redshift bin, while black stars mark the ΛCDM model expectations, with red segments joining these two values. Increasingly high values of E(B-V) are needed in order to produce the observed tension with the concordance cosmological model. *Bottom panel*: Difference between the predicted and observed distance modulus (ΔDM). Values are not extrapolated below $z = 1.0$ and above $z = 4.8$.

correction can be expressed as (see Supplementary Material 2.8.5 for the explicit derivation):

$$E(B-V) = \Delta\mathrm{DM}\,\frac{1}{R_V}\,\frac{A_V}{A_{2500\,\text{Å}}}\,\frac{1-\gamma}{\gamma}, \tag{2.4}$$

where ΔDM is the difference between the average distance modulus in a given redshift bin according to the ΛCDM model and that observed based on the $\mathrm{L_X} - \mathrm{L_{UV}}$ relation. Assuming a selective to total extinction ratio $R_V = 3.1$ and the SMC extinction curve from Gordon et al. (2016) used above, the values listed in the legend of Fig. 2.12 can be retrieved.

Next, I produced the composite spectrum in each bin, de-reddened it by applying the E(B-V) values found in the previous step, and performed the spectral fits to each of them to evaluate the slope of the continuum. I show the so-derived spectra and the slopes of the continuum obtained by means of spectral fits in Fig. 2.13. The slopes characterising the continua of the de-reddened spectra are not compatible with the expectations based on literature samples, as shown in the inset of Fig. 2.13. Indeed, moving towards higher redshift, under the hypothesis of local reddening, the selection would be biased towards intrinsically bluer objects with increasing amounts of extinction, whose UV slopes are anomalously steeper with respect to those typically found in blue quasars, while still delivering similar spectral shapes at all redshifts.

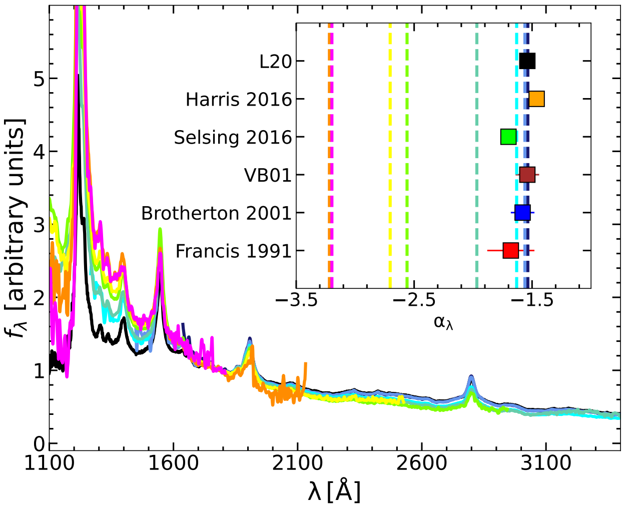

Figure 2.13. De-reddened stacks, according to the same colour code as in Fig. 2.12, scaled by their mean emission between 1770 Å and 1810 Å. For comparison, the VB01 template is also shown in black as an external reference, rather than the usual L20 template. The rising continuum slopes with increasing redshift (and extinction) are clearly observed. Inset: UV continuum slopes of the literature samples described in Section 2.5.1 and plotted in Fig. 2.4 (squares), against the slopes of the de-reddened spectra (dashed lines).

With the aim to explore the consequences of de-reddening the spectra by such amounts in terms of quasar physics, I built the semi-analytic (i.e. using the bin-averaged data and adopting analytic approximations from the literature in the other bands) intrinsic quasar SED in each redshift bin and computed the hard X-ray (2-10 keV) to bolometric corrections ($k_{\mathrm{bol,X}}$) to be compared with other literature samples. Anomalously high $k_{\mathrm{bol,X}}$ would further testify the selection of a very peculiar class of objects at high redshift, seemingly at odds with the typical spectral properties upon which the sample is built, verified so far.

In order to produce the average SEDs I built a semi-analytical parametrisation, similar to that discussed in Marconi et al. 2004 (M04). For wavelengths $\lambda > 1\ \mu$m I adopted a power-law spectrum $L_\nu \propto \nu^{\alpha_\nu}$, with slope $\alpha_{\nu,\mathrm{IR}} = 2$ as in the Rayleigh-Jeans tail of the disc. Between $1\ \mu\mathrm{m} > \lambda > 1200$ Å I adopted the spectral index $\alpha_{\nu,\mathrm{UV}}$ found in the fits of the de-reddened spectra, under the assumption that at high redshift and high luminosity the continuum can be approximated as a single power law. In the range $1200\ \text{Å} > \lambda > 600$ Å I chose the average far UV spectral slope $\alpha_{\nu,\mathrm{FUV}} = -1.70$ described in Lusso et al. (2015), who took into account a statistical correction on the neutral hydrogen column density of the inter-galactic medium. On the X-ray side, I used the *pexrav* model (Magdziarz and Zdziarski 1995) in the XSPEC software (Arnaud 1996) to simulate a power-law spectrum with a photon index Γ equal to the average photometric photon index derived from *XMM-Newton* photometry (see Sec. 2.5.8) with cutoff at 500 keV, and a reflection component with solid angle of 2π, inclination angle of $\cos i = 0.5$, and solar metal abundances.[4] Each X-ray spectrum was then scaled to the average 2 keV luminosity in each bin.

Lastly, I connected the 600 Å and the 0.5 keV luminosities with a power law. I defined 8 template SEDs according to the 8 values of $L_{2500\,\text{Å},\text{int}}$ and $\alpha_{\nu,\text{UV}}$, and used them to compute the hard X-ray (2-10 keV) bolometric corrections $k_{\text{bol,X}}$. I estimated the uncertainty on $k_{\text{bol,X}}$ by building 100 mock SEDs in each bin assuming Gaussian distributions for the adopted parameters with standard deviations $\sigma(\alpha_{\nu,\text{IR}}) = 0.1$, $\sigma(\alpha_{\nu,\text{UV}})$ equal to the uncertainty on the continuum slope evaluated from the fit of each de-reddened spectrum, $\sigma(L_{2500\,\text{Å},\text{int}})$ equal to the standard deviation on the mean of the $L_{2500\,\text{Å},\text{int}}$ values in each redshift bin, $\sigma(\alpha_{\nu,\text{FUV}}) = 0.6$, $\sigma(L_{2\,\text{keV}})$ and $\sigma(\Gamma)$ equal to the standard deviation on the mean of the $L_{2\,\text{keV}}$ and Γ distributions in each redshift bin.

The average SEDs resulting from this procedure are shown in Fig. 2.14, together with other literature samples as considered in Duras et al. 2020 (D20). The $k_{\text{bol,X}}$ values from the de-reddened SEDs clearly detach from the high-luminosity extrapolation of the M04 best-fit relation. At the same time, they are all located on the upper envelope of the D20 best fit for luminous Type 1 sources. This implies that, if such sources existed, the cosmological sample would be made of an exotic population made of the most luminous, yet dust-extincted quasars. These sources would exhibit the highest known bolometric conversion factors, while still showing the UV-optical colours and spectral properties of typical blue quasars. Moreover, if these SED templates are consistent by construction with M04, which then represents a proper comparison, the same does not hold for the empirical SEDs in D20. Indeed, I did not include any physically motivated emission in the spectral region between the far UV and the soft X-rays, as I only linked the $L_{600\,\text{Å}}$ and $L_{0.5\,\text{keV}}$ with a straight power law, while in the latter work the authors could also rely on far-UV photometry from GALEX. In order to quantify the possible inconsistency of the average estimates with those from the other literature samples, I performed a basic fit of the $k_{\text{bol,X}} - \text{L}_{\text{bol}}$ relation in the de-reddened sources. I adopted a simple power-law functional form, which is a good approximation for the high luminosity ($\text{L}_{\text{bol}} \geq 10^{46}$ erg s^{-1}) end of the D20 distribution:

$$\log(k_{\text{bol,X}}) = a + b \left[\log \left(\frac{\text{L}_{\text{bol}}}{10^{47.5}\,\text{erg}\,\text{s}^{-1}} \right) \right]. \tag{2.5}$$

The best fit parameters and their respective uncertainties are listed in Table 2.3. In Fig. 2.14 I show the $k_{\text{bol,X}} - \text{L}_{\text{bol}}$ relation for the sample and the D20 compilation of type-1 objects. The bolometric corrections of the higher redshift bins are located outside the 95% confidence interval for the best fit of the high-luminosity tail of the D20 distribution (red pentagons). The offset a of the best fit relation for these sources is significantly higher (3.7σ) than for those from D20. I checked that this result is not biased by the choice of the luminosity threshold for the objects included in the fit, by performing again the fit increasing the threshold by steps of $\Delta \log(\text{L}_{\text{bol}}/\text{erg}\,\text{s}^{-1}) = 0.5$

---

[4] This is a simplistic description of the X-ray spectrum, as I do not take into account the so-called "soft excess" component, nor any additional spectral complexity. However, for the sake of simplicity and consistence with M04 I adhere to this description.

from 45.5 to 47. In each case, the high-redshift ($z \gtrsim 2.5$) bolometric correction factors remain located above the 95% confidence interval. In conclusion, the bolometric correction estimates derived from the average de-reddened SEDs are significantly offset with respect to the expectations for high-luminosity Type 1 quasars, hinting at a seemingly exotic – and yet unknown – population.

	a	b
This work	2.402±0.042	0.484±0.050
D20	2.184±0.041	0.455±0.040

Table 2.3. Results of the fit of the $k_{\mathrm{bol,X}} - \mathrm{L_{bol}}$ relation for this sample and the template SEDs of the most luminous sources in D20.

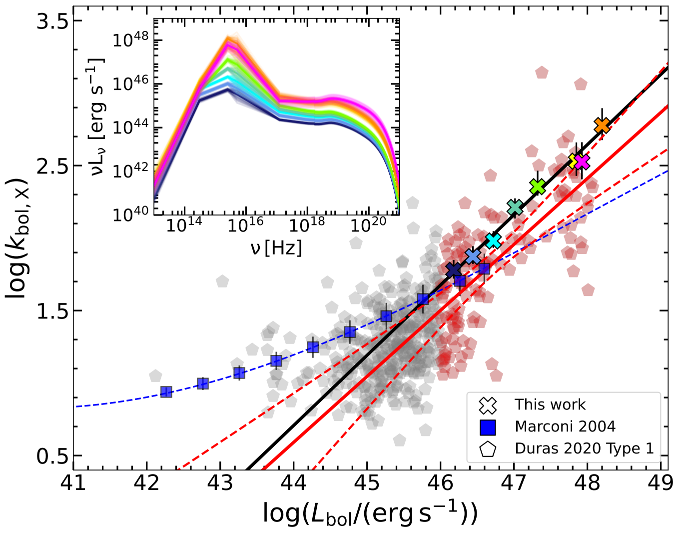

Figure 2.14. Average hard X-ray bolometric corrections in each redshift bin. As a term of comparison, I report the $k_{\mathrm{bol,X}}$ for the semi-analytical SED templates from M04 (blue squares) and the empirical ones from D20 (pentagons). The blue dashed line represents the best-fit reported in M04. Black and red continuous lines show, respectively, the best fit of the sample and the D20 objects in the high $\mathrm{L_{bol}}$ ($\geq 10^{46}$ erg s^{-1}) regime. The red dashed lines represent the 95% confidence interval of the best-fit regression line for the selected high-luminosity objects from D20 (red pentagons). The values of $k_{\mathrm{bol,X}}$ from the high-redshift, de-reddened SEDs are inconsistent with the extrapolation of the lower luminosity trend from M04, and steadily offset with respect to the best fit of the D20 high-luminosity type-1 quasars. Inset: average SEDs in each redshift bin, according to the same colour code as in Fig. 2.12. The shaded area is given by the individual mock SEDs in each bin.

As a result of all the tests performed in this Section, I conclude that a dust extinction scenario as an explanation for the tension with the ΛCDM model emerging in the quasar Hubble–Lemaître diagram seems disfavoured for several reasons. Firstly, significant amounts of extinction at high redshift, in combination with steeper than the average UV spectra, are required in order to reconcile the tension with the ΛCDM model, unless a cosmological evolution drives from high-redshift extremely blue sources to low-redshift typical quasars. Secondly, the reddening should increase with redshift, in opposition to the current paradigm of increasing dust with time (see, e.g. Aoyama et al., 2018, and references therein). In addition, the dust content in the high-redshift quasars should increase by the exact amount needed to compensate for the steepening of the intrinsic spectrum, thus producing the typical spectrum of blue quasars at all redshifts. Lastly, the hard X-ray bolometric correction factors derived from the average de-reddened SEDs are in tension with the high luminosity extrapolation from known sources.

All the above considerations would imply the selection of exotic objects at high redshift whose emission properties are intrinsically different from those at lower redshift and luminosity, while their apparent broadband properties are consistent with those of typical blue quasars.

2.5.8 The X-ray stacks

The availability of X-ray data, which underlies the creation of the L20 sample, allowed to address the question on the evolution of the shape of X-ray emission with respect to the accretion parameters and redshift. However, at this stage, a full stacking of the X-ray spectra, taking into account the largely different redshift intervals sampled, as well as the different response functions is still unfeasible. For this reason, I adopted a slightly different approach and built "photometric X-ray stacks". The intrinsic X-ray spectrum of an unobscured quasar above 0.2 keV can be roughly described as a power law with spectral index $\alpha = 1 - \Gamma$, where Γ is the photon index. For the sample, the best estimate for the Γ parameter is the photometric photon index ($\Gamma_{\rm ph}$) derived following the procedure described in Section 4 of L20 (where also a more detailed description of photometric spectral indices and of their limitations can be found). Although the photometric Γ values are somewhat less reliable than those spectroscopically derived ($\Gamma_{\rm sp}$), the lack of a systematic offset in the $\Delta\Gamma$ distribution (defined as $\Delta\Gamma = \Gamma_{\rm sp} - \Gamma_{\rm ph}$) and its non-evolution with redshift mean that it is safe to use these estimates in a statistical sense. For each source I built a synthetic spectrum between 0.2 and 10 keV using $\Gamma_{\rm ph}$ and the 2 keV flux reported in L20. Then, the procedure to build the X-ray stacks is analogous to that explained in Sec. 2.4.2.

It is to be noted, however, that the X-ray stacks are less informative than those produced in the UV-optical for at least two reasons: 1) they are not computed using the actual X-ray spectra, but rather photometric proxies, which are not sensitive to the peculiar features of each spectrum other than the steepness of the spectrum itself; 2) the quality cuts performed in the X-ray selection (especially that concerning the lower limit on the photon index, i.e. $\Gamma_{\rm ph} - \delta\Gamma_{\rm ph} > 1.7$, with $\delta\Gamma_{\rm ph}$ being the uncertainty) are more conservative, given the generally lower quality of the X-ray data, and thus have a much greater impact on obliterating the spectral diversity than the optical cuts. Nonetheless, the analysis of the slope of the stacked X-ray spectra provides valuable information about the goodness of the selection as well as the possible evolution of the X-ray properties within this parameter space. In Fig. 2.15 I recover the well-known correlation between $\Gamma - \log\lambda_{\rm Edd}$ (Shemmer et al.,

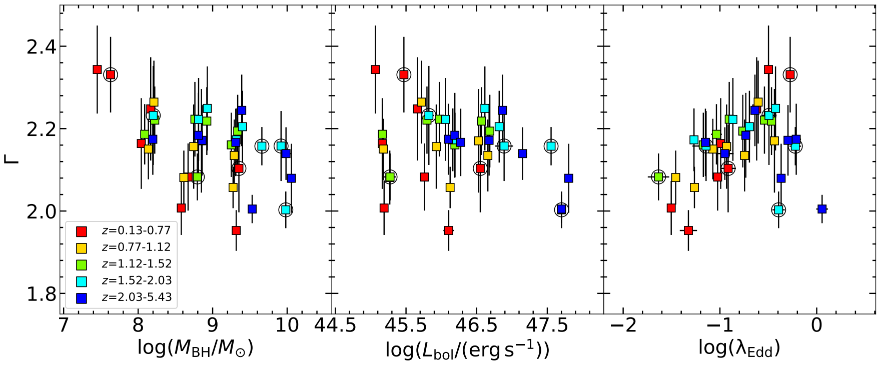

Figure 2.15. Values of Γ for X-ray stacks across the parameter space. Bins not meeting the representativeness criterion are marked with a circle.

2008; Risaliti et al., 2009; Jin et al., 2012; Brightman et al., 2013; Trakhtenbrot et al., 2017), with a correlation index $S = 0.38$. Interestingly, the correlation index is marginally larger for the $\Gamma - \log \mathrm{M_{BH}}$ ($S = -0.41$), but this could be due to the way the photometric data were grouped to produce the stacks, rather than to an intrinsically tighter correlation.

In theory, the dependence of the 2 keV fluxes on $\mathrm{M_{BH}}$ or λ_{Edd} implies that adding one of these parameters, or both, to the $\mathrm{L_X} - \mathrm{L_{UV}}$ space, the dispersion could be further narrowed down. For instance, the dependence on $\mathrm{M_{BH}}$, proportional to the Mg II FWHM, has been explored in Signorini et al. (2023b), where it has been shown that the inclusion of this parameter has a negligible effect in improving the intrinsic dispersion of the relation. At the same time, the zero-covariance between the X-ray flux estimated at the pivot point (i.e., the effective-area-weighted average energy of any given band of interest) and Γ (see Section 4 in L20) assures that even a systematic steepening of the photon index would not affect the estimates of the X-ray luminosity.

2.6 Discussion of the results

The suitability of quasars as "standardized candles" relies upon the consistency of the method (i.e. the absence of selection/analysis biases, or correction thereof) and the intrinsic non-evolution of quasar spectra with redshift. Although increasingly larger samples are desirable, my group has been lately devoting a substantial effort to investigate any possible issues affecting the L20 sample with SDSS spectral coverage. In this context, this section of work has been chiefly focused on the analysis of the average spectral properties of 2,316 of the sources described in L20. The main results obtained through the various analyses performed in the previous sections are the following: 1) The overall shape of the composite spectra (apart from emission-line properties) does not show any clear evolution across the explored parameter space. 2) Host galaxy contamination is not a major issue in sources below $z \leq 0.8$, and it is therefore expected to be completely negligible for the bulk of the sample, at higher redshfit and luminosity. 3) The cosmological sample is compatible, on average, with a low degree of intrinsic extinction, E(B-V) $\lesssim 0.01$. 4) The deviation of the cosmographic best fit of the quasar–SN Ia Hubble–Lemaître diagram from the ΛCDM model reported by my group is unlikely to be caused by dust reddening, based on the spectral properties of the sample. These findings have far-reaching consequences on the physical properties of the sources described here, as well as on the solidity of the criteria adopted to select the cosmological sample.

The similarity of quasar spectra has led through the years to the production of several composite spectra (e.g. Francis et al. 1991, VB01, Zheng et al. 1997a; Brotherton et al. 2001; Harris et al. 2016), which have found large employment as templates for the typical quasar emission, in terms of line and continuum properties. In this case, building high signal-to-noise composite spectra allowed to explore the spectral diversity within the parameter space underlying SMBH accretion. There is no clear evidence for a redshift-dependent evolution of the average continua in the sample, as the agreement with either the global L20 or the independent VB01 composite spectra does not deteriorate with redshift. This appears to hold up to very high redshift, where luminous quasars have been observed to show spectral properties very akin to those seen at lower redshift (e.g. Fig. 1 in Mortlock et al. 2011). Under the paradigm that such emission is driven by SMBH accretion, these results would imply that the emission mechanism underlying the observed spectra does not vary significantly in the blue quasars spanning the last 12 Gyr. Although the expected correlations between line equivalent width and continuum luminosity (i.e. the Baldwin effect, Baldwin 1977) and between line width and BH mass (virial relations; e.g. Peterson et al. 2004) are observed within the saple, the non-evolution of the continuum shape of the composite spectra with any of the quantities in the parameter space is remarkable (see Fig. 2.18 in Supplementary Material 2.8.6).

Contamination from the host galaxy light is a known issue when trying to isolate the AGN component (e.g. Baldwin et al. 1981; Kauffmann et al. 2003). This effect is capable, in principle, of inducing the overestimate of the actual 2500-Å fluxes, by introducing a spurious UV contribution and eventually biasing the estimate of the cosmological parameters based on the quasar $L_X - L_{UV}$ relation. For this reason, the sample selection criteria require steep photometric continua to single out sources where the contribution from the galactic stellar component is negligible with respect to the AGN emission (Elvis et al. 1994; Richards et al. 2006; Elvis et al. 2012; Krawczyk et al. 2013; Hao et al. 2013a). As shown in Section 2.5.5, host galaxy contamination does not play a major role in the sample, as I generally observe steep continua, coupled with the lack of strong stellar absorption features and weak narrow emission lines from stellar photoionisation. These findings are particularly evident on the UV side of the spectrum, where the composites are dominated by higher redshift, luminous objects, in which the host contribution is expected to be negligible above $L_{bol} \sim 10^{46}$ erg s^{-1} (Shen et al. 2011). A detailed disentanglement of the host galaxy and quasar emission by means, for instance, of a principal component analysis (e.g. Yip et al. 2004) is beyond the scope of this work. Nonetheless, it is possible to roughly estimate the average incidence of host galaxy light by comparing the absorption features between the full sample composite and VB01. The EW of the Ca II λ3934 absorption in the full sample composite (0.7 ± 0.4 Å) is similar to that observed in the VB01 template (0.9 ± 0.1 Å), yet a fair comparison is hampered by the differences in the resolution and the signal to noise between the two templates. This goes in the direction of the sample having an average host contribution comparable to that of VB01, deemed 7%-15% at such wavelengths, with an incidence decreasing bluewards.

Recently, Zajaček et al. (2023) have investigated the possibility that luminosity distance measurements based on the $\mathrm{L_X - L_{UV}}$ relation are biased by extinction on a sample of 58 quasars at $z \lesssim 1.7$ with available reverberation mapping data (Khadka et al. 2023). In the latter work, the authors used Mg II time-delays to infer distances by means of the radius–luminosity relation (Mg II R-L relation, with intrinsic dispersion $\sigma \sim 0.3$ dex; Khadka et al., 2022). Assuming that the difference between the distances based on the Mg II R–L and $\mathrm{L_X - L_{UV}}$ relations were attributable to local reddening, and adopting different cosmological models, they derive an intrinsic colour excess E(B-V) $\simeq$ 0.002-0.003, an amount of extinction that would be intrinsic to all Type 1 quasars. However, such an effect, even if present, would still not be enough to explain the reported high-redshift tension with the current cosmological model.

In this framework, the shape of the quasar continuum can be interpreted as ultimately resulting by the combination of two main parameters: the intrinsic spectral slope of the UV spectrum and the column density of gas and dust causing the extinction. The degeneracy between these two parameters could be capable, in principle, of producing similar spectra by combining increasingly larger amounts of dust in high redshift, luminous sources with intrinsically steeper spectra (e.g. Xie et al. 2015). There are several reasons to believe instead that dust extinction, even if present in small amounts in the sample, is not systematically biasing my results. First, the photometric selection, besides excluding sources where the host galaxy significantly reddens the UV-optical SED, also singles out objects where the amount of dust extinction is expected to be negligible. Indeed, assuming that the photometric slopes of the average quasar SED described in Richards et al. (2006) are truly representative of blue quasars, by selection, the colour excess of the sources described here should not exceed E(B-V) $\simeq$ 0.1. I also note that the incidence of significantly reddened objects with E(B-V) $>$ 0.1, at least in early SDSS data (whose average properties are encapsulated in the VB01 template) was estimated to be modest, below $<2\%$ according to Hopkins et al. (2004). In this work, I took a step further, searching a posteriori for spectral signatures of dust reddening, but I found none. Moreover, the distribution of the broad-line Balmer decrements from the Hα and Hβ reported in the WS22 catalogue for the low-redshift tail ($z < 0.57$) of the sample is in excellent agreement with other samples made of allegedly unobscured sources (e.g. Zhou et al. 2006; Dong et al. 2007). In Section 2.5.6 I showed that the spectral shape of the global template built here is consistent with the VB01 template reddened by minimal levels of local extinction, i.e. E(B-V) $\lesssim$ 0.01. Similar conclusions are also drawn in Reichard et al. (2003) who estimated the intrinsic reddening in non-BAL AGN from the early SDSS release to be E(B-V)$\sim$ 0.004. This implies, under the assumption that the VB01 template is made of mostly blue unobscured quasars, a low incidence of reddening (dust/gas extinction) and galactic contamination. Finally, the similarity of the spectral shape between the sample and other quasar composite spectra from several surveys designed to select luminous blue quasars (Francis et al. 1991; Brotherton et al. 2001; VB01; Selsing et al. 2016; Harris et al. 2016) can be interpreted as a proof of the lack of significant reddening, and a clue of the non-evolution through cosmic time of the intrinsic emission properties of quasars. The other possible explanations to interpret the overall agreement among composite spectra from different samples involve a certain degree of fine-tuning. Several samples of quasars on different scales of luminosity and redshift should have intrinsically steep spectral shapes and significant amounts of dust, but still producing similar spectral shapes. As a corollary to this consideration, one should also conclude that all the quasars used to build the average SEDs available in the literature (Richards et al. 2006; Krawczyk et al. 2013; Gu 2013), whose colours have been adopted to select the sample, are also affected by the same issue.

If the tension with the ΛCDM in the Hubble–Lemaître diagram were to be attributed to dust reddening, a constant extinction with redshift would not be enough. This would require a differential extinction (increasing with redshift) combined with increasingly steeper intrinsic spectra, resulting in observed spectral shapes virtually independent of redshift.

Yet, this introduces additional questions, as larger intrinsic luminosities would also imply larger SMBH masses, enlarging the discrepancy between the largest possible SMBH masses in the Eddington-limited regime and those observed, unless the accretion efficiency varies systematically at high redshift (see, for example, Inayoshi et al. 2020 and Lusso et al. 2022 for recent reviews on this topic). In addition, significant local extinction E(B-V)$\sim$ 0.1 would imply an intrinsic UV flux larger by a factor whose exact value depends on extinction curve, but on average between 3 and 4 times at 1450 Å. In turn, assuming as a rough approximation a first order constant bolometric correction, the intrinsic bolometric luminosity should be accordingly larger than the observed one. Therefore, the total mass in black holes in the Universe as evaluated by Sołtan (1982), would need a significant increase with increasing redshift, unless the M_{BH} values are already underestimated by similar amounts. The same argument applies when considering greybody-like extinction curves (e.g. Gaskell et al. 2004), which do not modify the continuum slope, but underestimate the bolometric luminosities.

The discrepancy between the observed DM and those derived in the ΛCDM framework cannot even be solved invoking for cosmic opacity on the 2500 Å photons which would cause the observed DM to diminish. In addition, an opposite effect on DM would arise when considering cosmic opacity acting on X-ray photons. It is possible to thus consider the decrease in the DM caused by the dimming of the UV emission as an upper limit to the detachment from the ΛCDM model caused by free electrons extinction along the line of sight. In quantitative terms, the extrapolation of the cosmic dimming values derived for SNe Ia in B band in Zhang 2008; Hu et al. 2017 lie below 0.02 at $z < 3$, while the Hubble–Lemaître diagram (Fig.2.12) shows much larger values, as ΔDM approaches 1 at $z = 3$. Alternatively, some ubiquitous – yet unknown – material in the IGM should be responsible for a grey-body like absorption, though this option seems unlikely.

On the X-ray side, gas absorption plays an opposite role with respect to the UV counterpart, as the correction for absorption would increase the departure from the ΛCDM model. Generally speaking, the incidence of gas absorption among these sources is minimised by the $\Gamma_{\rm ph} > 1.7$ criterion. In addition, this effect is further mitigated at high redshift by the shift within the observed 0.5-2 keV band of much higher rest-frame energies, for which the effect of gas absorption becomes increasingly weaker. Indeed, in all the high-redshift objects for which a dedicated X-ray spectral analysis was performed (Vito et al. 2019; Nardini et al. 2019b; Salvestrini et al. 2019; Sacchi et al. 2022), column densities in excess of 10^{23} cm^{-2} would be required to modify the spectral slope and thus affect the extrapolated rest-frame 2 keV flux, but such values were generally excluded.

As a final consideration, the results of the spectroscopic analysis described in this work ultimately prove the reliability of the photometric selection criteria adopted in the series of works dedicated to using quasars as standard candles. Using the photometric cuts, rather than the more time-consuming spectroscopic analysis, will allow us to considerably enlarge the cosmological sample with the forthcoming surveys (e.g. LSST, DESI), while retaining a high degree of consistency with the spectroscopic properties.

2.7 Summary and conclusions

In this parth of my thesis, I presented a thorough analysis of the average spectral properties of 2,316 sources with available SDSS data from the sample described in Lusso et al. (2020). Here my main aims were to investigate the possible evolution of the UV-optical properties with redshift, and to study the possible systematic effects (e.g. host galaxy contamination, dust extinction) that could undermine the validity of quasars as standard candles. To this end, I built spectral composites in the parameter space defined by $\mathrm{M_{BH}}$, $\mathrm{L_{bol}}$, and redshift to investigate how the spectral properties of the cosmological sample vary as a function of the key accretion parameters and cosmic time. I also carried out specific tests to determine the presence of residual galactic contamination and dust reddening based on their spectral signatures.

The main findings for this part of my work are listed below:

- Apart from the line emission, which varies according to well-known relations with $\mathrm{L_{bol}}$ and $\mathrm{M_{BH}}$, I report a strong similarity in terms of continuum shapes among the composite spectra across the explored parameter space. The slopes of the continuum of the composite spectra cluster around $\langle\alpha_\lambda\rangle = -1.50 \pm 0.14$ without any statistically significant correlations (i.e. $|S| \leq 0.3$) with the explored parameters ($\mathrm{M_{BH}}$, $\mathrm{L_{bol}}$, z). This points to a non-evolution of the broadband continuum emission within the sample with respect to the considered parameters.

- The global composite spectrum shows a good agreement with other templates of typical blue quasars as well as with the individual composite spectra in the various regions of the parameter space. This confirms that the L20 catalogue is, on average, made of typical objects.

- By comparing the composite spectrum of the low-redshift ($z \leq 0.8$) sources with SDSS objects affected by heavy host galaxy contamination, I were able to verify that host galaxy emission is negligible in the sample. I estimate the host galaxy fraction at optical wavelengths to be $\lesssim$10%, and likely even lower at UV wavelengths.

- After performing several tests, as listed in Section 2.5.6, I demonstrated that the objects constituting the L20 sample are consistent with a low degree of intrinsic extinction, with an average colour excess value E(B-V)$\lesssim$ 0.01.
- I showed that the tension between the cosmographic best fit of the joint quasar-SN Ia Hubble–Lemaître diagram, and the ΛCDM model cannot be simply accounted for by allowing for cosmic opacity or differential dust extinction. Otherwise, a colour excess E(B-V)$\gtrsim$ 0.1 increasing with z, accompanied by anomalously steep UV spectra, should ubiquitously affect high-z sources while delivering similar spectral shapes at all redshifts.
- The spectroscopic analysis carried out in this work corroborates the photometric selection criteria adopted to define a sample of quasars with typical properties. This in turn allows for the continued use of the more efficient photometric cuts rather than a more time-consuming individual spectroscopic analysis.

The search for possible systematics performed in this work has broad implications for the cosmological applications of quasars. First, the spectral confirmation that dust or galaxy contamination do not significantly affect, without invoking peculiar or anomalous explanations, the cosmological sample further corroborates the reliability of the methods and results employed by my group. In this context, quasars emerge as consistent standardisable candles, and the high-redshift deviation from the current cosmological model remains outstanding. Secondly, as the method has proven fruitful in producing large samples of homogeneous sources, it is possible to extend and refine its application to the forthcoming data from new facilities. As a matter of fact, the extended ROentgen Survey with an Imaging Telescope Array (eROSITA, Merloni et al., 2012) began populating the pivotal $z \sim 1$ region in the X-ray domain, allowing for a more robust cross-calibration between quasars and SNe Ia and a more precise determination of Ω_Λ (Lusso, 2020). In the mid- to long-term future, the cross-match between *Euclid* (Laureijs et al. 2011) and LSST (Ivezić et al. 2019) observations in the optical–UV and *Athena* (and/or other proposed facilities) in the X-rays will significantly enlarge the sample, helping to fill up the region at intermediate to high redshift. New large and reliable samples will be key to testing the cosmological models in synergy with other well-established probes with the intent to precisely constrain the cosmological parameters.

2.8 Supplementary Material

2.8.1 Stacking methods

To build the stacks, I considered different techniques to resample the flux values, average them, and estimate the uncertainty in each spectral channel. The abbreviations in italics are used to denote these options in Table B.1.

Stacking algorithm

Here I list the stacking algorithms adopted to combine the single spectra into the composites.

Direct stacking (*avg*): each spectrum was rebinned on a fixed wavelength grid designed to contain all the possible wavelengths in the same redshift bin. Then, each spectrum was normalised (see below). In each spectral channel the final flux was computed as the mean, median, or geometric mean of the normalised non-zero fluxes. The uncertainty on the flux on a spectral channel was computed as the standard deviation or the inter-percentile deviation divided by the number of objects contributing to the spectral channel.

MC resampling (*mc*): a target number was decided before the stacking (generally $N_{\rm target} = 10{,}000$). Then, I randomly extracted $N_{\rm target}$ spectra allowing for replacement and created a mock spectrum by randomizing the flux according to the uncertainty vector, in the same way as described in Section 2.4.3 to generate the mock spectra. The mock spectra are subject to the same procedure as in the case of direct stacking.

Bootstrap resampling (*bs*): a target number was decided before the stacking (generally $N_{\rm target} = 200$). Then I randomly extracted $N_{\rm draw}$ spectra allowing for replacement and stacked them together to create the i-th composite spectrum. $N_{\rm draw}$ was chosen to be equal to the total number of good spectra in the bin, according to the quality criteria defined in Sec. 2.4.2. This procedure was performed $N_{\rm target}$ times, building the distribution of the mean fluxes in each spectral channel. The final spectrum in each spectral channel was obtained as the mean of the mean fluxes and the uncertainty as the standard deviation.

Normalisation

Here I list the normalisation options adopted to scale the single spectra during the combination process.

Monochromatic (*mcr*): the spectrum is normalised by its value at a certain wavelength $\bar{\lambda}$, generally chosen in a relatively emission-free region. Actually, the normalisation is not performed using the exact monochromatic interpolated flux, but rather the mean flux values in a wavelength range (10-100 Å) around $\bar{\lambda}$, in order to avoid anomalously high or low fluxes due to bad pixels.

Integral (*itg*): the spectrum is normalised by its integral over the whole wavelength range.

Average estimator

Here I list the several estimators adopted to get the average value in each spectral channel when building the spectral composites.

Mean: the direct mean is the most straightforward way to average the flux in each spectral channel. However, especially close to the wings of the spectra where the SNR lowers, composites are more prone to anomalously high fluxes, likely due to bad pixels.

Median: using the median value in each spectral channel is safer when there are strong outliers, such as bad pixels, which can significantly alter the average flux. Moreover, the median spectrum preserves the relative fluxes of the emission features (see Sec. 3 in VB01).

Geometric mean (*gmean*): the geometric mean spectrum preserves instead the global continuum shape. Indeed, it can be shown (Sec. 3 in VB01) that the geometric mean of a distribution of spectra describable as power laws is equivalent to a power law with a spectral index given by the arithmetic mean of the spectral indices $\langle f_\lambda \rangle_{gmean} \propto \lambda^{-\langle \alpha_\lambda \rangle}$.

Uncertainty estimator

Here I list the estimators adopted to evaluate the uncertainty on the average flux in each spectral channel.

Standard deviation (*std*): the uncertainty is estimated as the standard deviation of the non-zero normalised fluxes divided by the square root of the objects contributing to a spectral channel.

Semi-interpercentile range (*pct*): the uncertainty is estimated as half the difference between the 99^{th} and 1^{st} percentile values divided by the square root of the objects contributing to a spectral channel.

The test bin

To test how the different stacking options could affect the final result I performed all the 36 possible combinations of the stacking options using the averagely populated ($N_{\mathrm{obj}} = 77$) bin "cB4". For the MC (bootstrap) stacks 10,000 (200) re-samples were performed.

I performed the spectral fits of all the test-bin stacks, in order to assess whether the slope of the continuum and the monochromatic fluxes were affected by the choices adopted for building the stack. In Fig. 2.16 I show that α_λ, f_λ, and Γ are barely sensitive to the different stacking assumptions, as their relative variations are of the order of 2%.

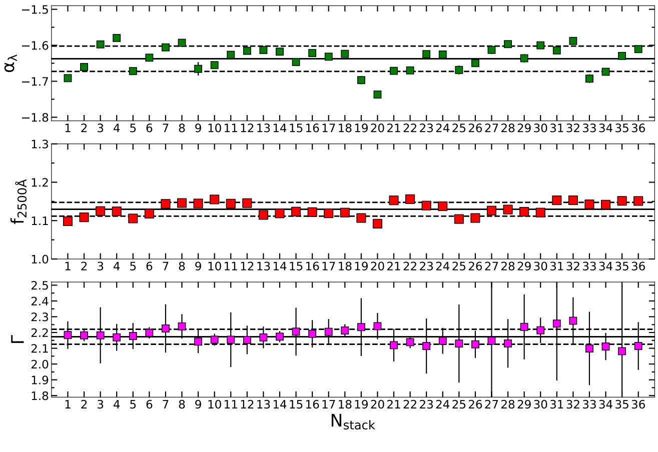

Figure 2.16. Stack-to-stack variations of α_λ (green), 2500-Å monochromatic flux (red), and X-ray Γ (violet). The solid black line represents the mean value, and dashed lines enclose values within a standard deviation. Stacks are numbered according to Table B.1.

$N_{\rm stack}$	stack features	$N_{\rm stack}$	stack features	$N_{\rm stack}$	stack features
1	avg gmean int pct	13	bs gmean int pct	25	mc gmean int pct
2	avg gmean int std	14	bs gmean int std	26	mc gmean int std
3	avg gmean mcr pct	15	bs mean itg std	27	mc gmean mcr pct
4	avg gmean mcr std	16	bs gmean mcr std	28	mc gmean mcr std
5	avg mean int pct	17	bs mean int pct	29	mc mean int pct
6	avg mean int std	18	bs mean int std	30	mc mean int std
7	avg mean mcr pct	19	bs mean mcr pct	31	mc mean mcr pct
8	avg mean mcr std	20	bs mean mcr std	32	mc mean mcr std
9	avg median int pct	21	bs median int pct	33	mc median int pct
10	avg median int std	22	bs median int std	34	mc median int std
11	avg median mcr pct	23	bs median mcr pct	35	mc median mcr pct
12	avg median mcr std	24	bs median mcr std	36	mc median mcr std

Table 2.4. Labelling of the test-bin stacks. Abbreviations correspond to those defined in the list of stacking options in Section 2.8.1.

2.8.2 Impact of the extinction curve

With the end to explore the effect of the choice of the extinction curve adopted to redden or de-redden the composites throughout this work, I tested different extinction curves on the composite spectrum in the "cB4" bin. I included SMC-like curves (Prevot et al. 1984; Gordon et al. 2016), as well as AGN-derived extinction curves (Gaskell et al. 2004; Gallerani et al. 2010, excluding BALs; Wild et al. 2011; Zafar et al. 2015). After de-reddening the composite I performed the spectral fit to infer the slope of the continuum α_λ and compare it to that of the actual composite. I show the results of this procedure in Fig.2.17. The slope of the de-reddened spectrum assuming the Gordon et al. (2016) SMC-like curve (adopted in this work) is close to the average of the distribution. The strongest outlier in the extinction distribution is the Gaskell et al. (2004) extinction curve, which is akin to a grey-body for wavelengths below $\lesssim 3300$ Å, and therefore does not alter the spectral shape at short wavelengths. However, their sample is based on 72 radio-selected quasars with the addition of mostly radio-quiet objects from the LBQS survey, and it is possible, as already suggested by Hopkins et al. (2004), that the flattening of their extinction curve is driven by the spectral properties of the radio-loud quasars in their sample. The choice of a SMC-like curve as representative of the intrinsic quasar extinction curve seems also justified by the findings of the latter work. There, the authors found a red tail in the distribution of SDSS photometric colours according to different redshifts. This trend proved to be consistent with SMC-like reddening, but not with Large Magellanic Cloud- or Milky Way-like.

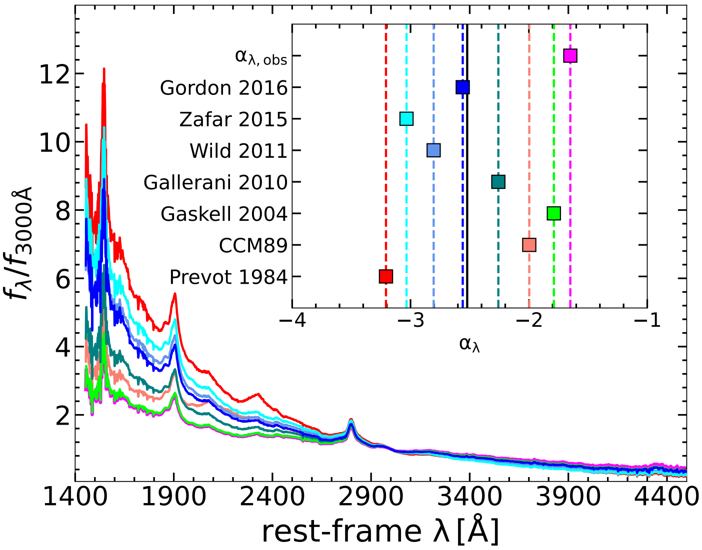

Figure 2.17. Test-bin composite spectrum de-reddened according to different extinction curves reported in the inset and assuming E(B-V)=0.1 and R_V = 3.1. The slopes produced from the spectral fits according to the different extinction curves are represented in the inset. The spectrum and the slope of the continuum before the de-reddening ($\alpha_{\lambda,\ obs}$) are reported in magenta as references. The slope derived assuming the extinction curve from Gordon et al. (2016) is the closest to the average (black line).

2.8.3 Table of results

In Table 2.5 I report all the average accretion parameters of the bins in which the parameter space is divided, as well as the spectral properties of the composites.

bin	$N_{\rm obj}$	$\log(\rm M_{BH}/M_\odot)$	$\log(\rm L_{bol}/erg\,s^{-1})$	$\log(\lambda_{\rm Edd})$	α_λ	$f_{2500\,\text{Å}}$	Γ	$\Delta\alpha$
aC1	6	7.63 ± 0.02	45.47 ± 0.02	−0.27 ± 0.02	−1.432 ± 0.005	1.298 ± 0.001	2.33 ± 0.09	0.014± 0.002
aD1	40	7.45 ± 0.03	45.07 ± 0.03	−0.50 ± 0.03	−1.541 ± 0.073	1.324 ± 0.018	2.34 ± 0.11	−0.060± 0.010
aC2	109	8.17 ± 0.02	45.66 ± 0.02	−0.62 ± 0.02	−1.484 ± 0.007	1.311 ± 0.002	2.25 ± 0.13	−0.022± 0.003
aD2	126	8.04 ± 0.02	45.16 ± 0.02	−0.99 ± 0.02	−1.437 ± 0.025	1.299 ± 0.006	2.16 ± 0.11	0.011± 0.002
aC3	141	8.67 ± 0.01	45.76 ± 0.02	−1.02 ± 0.02	−1.584 ± 0.007	1.335 ± 0.002	2.08 ± 0.08	−0.090± 0.014
aD3	39	8.58 ± 0.02	45.19 ± 0.02	−1.50 ± 0.03	−1.623 ± 0.021	1.344 ± 0.005	2.01 ± 0.07	−0.117± 0.018
aB4	6	9.35 ± 0.05	46.55 ± 0.05	−0.92 ± 0.08	−2.025 ± 0.028	1.446 ± 0.007	2.10 ± 0.11	−0.394± 0.060
aC4	13	9.32 ± 0.05	46.10 ± 0.08	−1.33 ± 0.09	−1.919 ± 0.013	1.419 ± 0.003	1.95 ± 0.05	−0.321± 0.049
bC2	60	8.21 ± 0.02	45.72 ± 0.03	−0.61 ± 0.03	−1.342 ± 0.026	1.277 ± 0.006	2.26 ± 0.10	0.077± 0.012
bD2	45	8.14 ± 0.03	45.18 ± 0.02	−1.07 ± 0.04	−1.374 ± 0.151	1.285 ± 0.035	2.15 ± 0.07	0.054± 0.010
bB3	20	8.85 ± 0.04	46.53 ± 0.03	−0.44 ± 0.04	−1.751 ± 0.003	1.376 ± 0.001	2.17 ± 0.13	−0.205± 0.031
bC3	253	8.75 ± 0.01	45.93 ± 0.02	−0.93 ± 0.02	−1.487 ± 0.024	1.311 ± 0.006	2.16 ± 0.10	−0.023± 0.004
bD3	43	8.61 ± 0.02	45.27 ± 0.02	−1.46 ± 0.03	−1.409 ± 0.023	1.293 ± 0.005	2.08 ± 0.07	0.030± 0.005
bB4	23	9.29 ± 0.03	46.66 ± 0.05	−0.75 ± 0.04	−1.664 ± 0.004	1.354 ± 0.001	2.13 ± 0.09	−0.145± 0.022
bC4	32	9.27 ± 0.03	46.12 ± 0.04	−1.26 ± 0.04	−1.521 ± 0.007	1.320 ± 0.002	2.06 ± 0.05	−0.047± 0.007
cC2	35	8.22 ± 0.02	45.80 ± 0.04	−0.54 ± 0.04	−1.445 ± 0.011	1.301 ± 0.003	2.22 ± 0.08	0.036± 0.000
cD2	9	8.09 ± 0.05	45.17 ± 0.05	−1.04 ± 0.06	−1.419 ± 0.020	1.295 ± 0.005	2.19 ± 0.07	0.053± 0.001
cB3	49	8.92 ± 0.02	46.57 ± 0.02	−0.47 ± 0.03	−1.565 ± 0.003	1.330 ± 0.001	2.22 ± 0.08	−0.045± 0.000
cC3	231	8.76 ± 0.01	45.97 ± 0.02	−0.90 ± 0.11	−1.451 ± 0.008	1.303 ± 0.002	2.22 ± 0.09	0.032± 0.000
cD3	6	8.79 ± 0.05	45.27 ± 0.08	−1.63 ± 0.02	−1.333 ± 0.011	1.275 ± 0.003	2.08 ± 0.06	0.110± 0.001
cB4	77	9.34 ± 0.02	46.69 ± 0.02	−0.76 ± 0.02	−1.568 ± 0.004	1.331 ± 0.001	2.19 ± 0.09	−0.046± 0.000
cC4	61	9.25 ± 0.01	46.19 ± 0.02	−1.17 ± 0.02	−1.495 ± 0.006	1.313 ± 0.002	2.16 ± 0.08	0.002± 0.000
dC2	9	8.20 ± 0.05	45.82 ± 0.07	−0.49 ± 0.08	−1.137 ± 0.192	1.230 ± 0.043	2.23 ± 0.12	0.201± 0.034
dB3	66	8.93 ± 0.02	46.62 ± 0.02	−0.43 ± 0.02	−1.453 ± 0.005	1.303 ± 0.001	2.25 ± 0.10	−0.021± 0.000
dC3	141	8.81 ± 0.02	46.06 ± 0.02	−0.87 ± 0.02	−1.577 ± 0.024	1.333 ± 0.006	2.22 ± 0.10	−0.108± 0.002
dA4	7	9.66 ± 0.05	47.55 ± 0.04	−0.22 ± 0.06	−1.557 ± 0.004	1.328 ± 0.001	2.16 ± 0.05	−0.094± 0.001
dB4	173	9.40 ± 0.01	46.82 ± 0.02	−0.70 ± 0.02	−1.479 ± 0.011	1.309 ± 0.003	2.20 ± 0.09	−0.039± 0.000
dC4	69	9.32 ± 0.02	46.16 ± 0.03	−1.27 ± 0.03	−1.374 ± 0.051	1.285 ± 0.012	2.17 ± 0.08	0.035± 0.001
dA5	7	9.98 ± 0.03	47.70 ± 0.06	−0.39 ± 0.06	−1.560 ± 0.123	1.329 ± 0.030	2.00 ± 0.04	−0.096± 0.008
dB5	6	9.92 ± 0.02	46.89 ± 0.13	−1.14 ± 0.14	−1.336 ± 0.020	1.276 ± 0.005	2.16 ± 0.08	0.061± 0.001
eC2	22	8.20 ± 0.05	46.10 ± 0.04	−0.21 ± 0.05	−1.308 ± 0.019	1.269 ± 0.004	2.17 ± 0.09	0.169± 0.004
eB3	96	8.86 ± 0.02	46.68 ± 0.02	−0.30 ± 0.03	−1.491 ± 0.016	1.312 ± 0.004	2.17 ± 0.09	0.052± 0.001
eC3	63	8.81 ± 0.03	46.19 ± 0.02	−0.73 ± 0.03	−1.558 ± 0.018	1.329 ± 0.004	2.18 ± 0.10	0.010± 0.000
eA4	26	9.53 ± 0.04	47.70 ± 0.04	−0.06 ± 0.06	−1.623 ± 0.154	1.344 ± 0.038	2.00 ± 0.03	−0.032± 0.003
eB4	174	9.39 ± 0.02	46.87 ± 0.02	−0.64 ± 0.02	−1.447 ± 0.017	1.302 ± 0.004	2.24 ± 0.09	0.080± 0.002
eC4	23	9.31 ± 0.04	46.27 ± 0.02	−1.15 ± 0.03	−1.152 ± 0.012	1.234 ± 0.003	2.17 ± 0.08	0.268± 0.006
eA5	44	10.06 ± 0.03	47.80 ± 0.04	−0.37 ± 0.04	−1.452 ± 0.004	1.303 ± 0.001	2.08 ± 0.08	0.077± 0.002
eB5	12	9.98 ± 0.06	47.15 ± 0.06	−0.95 ± 0.09	−1.732 ± 0.030	1.371 ± 0.008	2.14 ± 0.06	−0.101± 0.003

Table 2.5. Relevant quantities for each bin of the parameter space.

2.8.4 Correlation index tables

In Table 2.6 I report the correlation index S between the slope α_λ and the accretion parameters, including/excluding the bins ruled out by the representativeness criterion.

subsample	$\alpha_\lambda - \log \mathrm{M_{BH}}$	$\alpha_\lambda - \log \mathrm{L_{bol}}$	$\alpha_\lambda - \log \lambda_{\mathrm{Edd}}$
all	$(-0.300, 0.067)$	$(-0.263, 0.110)$	$(-0.006, 0.972)$
selected	$(-0.281, 0.125)$	$(-0.229, 0.214)$	$(-0.017, 0.928)$

Table 2.6. Correlation index and associated $P - value$ (S, P) pairs for the UV and optical slopes against the accretion parameters. In the top row all the bins are included in the computation, in the bottom only those meeting the representativeness criterion.

2.8.5 Reddening expression

In this section, I explicitly derive Eq. 2.1. I begin from Eq. 7 in L20 in order to express the distance modulus DM starting from the luminosity distance d_L computed from the $\mathrm{L_X} - \mathrm{L_{UV}}$ relation:

$$\mathrm{DM} = 5\left[\frac{\log f_{\mathrm{X}} - \beta - \gamma\,(\log f_{2500\,\text{Å}} + 27.5)}{2\gamma - 1} - \frac{1}{2}\log(4\pi) + 28.5\right] - 5\,\log(10\,\mathrm{pc}).$$

Keeping only the dependence on $f_{2500\text{Å}}$, DM can be written as

$$\mathrm{DM} = 5\,\frac{\gamma}{2(\gamma - 1)}\log f_{2500\,\text{Å}} + \theta,$$

where θ encapsulates all the terms where $f_{2500\,\text{Å}}$ does not appear. Next, I assume, by hypothesis, that the observed UV fluxes are significantly extincted to the point that the discrepancy from the ΛCDM model that I report is driven by such extinction. it is possible to then denote the observed DM as

$$\mathrm{DM_{ext}} = -5\,\frac{\gamma}{2(\gamma - 1)}\log f_{2500\,\text{Å},\mathrm{ext}} + \theta,$$

and the intrinsic (unextincted) DM as

$$\mathrm{DM_{int}} = -5\,\frac{\gamma}{2(\gamma - 1)}\log f_{2500\,\text{Å},\mathrm{int}} + \theta.$$

The intrinsic UV flux is related to the extincted one by

$$f_{2500\,\text{Å},\mathrm{int}} = f_{2500\,\text{Å},\mathrm{ext}}\,10^{0.4\,e_\lambda\,R_V\,E(B-V)}$$

where e_λ is the assumed extinction curve, R_V is the total to selective extinction ratio, and E(B-V) is the colour excess. it is possible to then write $\mathrm{DM_{int}}$ in terms of the extincted UV flux:

$$\mathrm{DM_{int}} = -5\,\frac{\gamma}{2(\gamma - 1)}\left[\log f_{2500\,\text{Å},\mathrm{ext}} + 0.4 e_\lambda\,R_V\,E(B - V)\right] + \theta.$$

The difference between the intrinsic and the observed distance moduli (ΔDM) thus becomes

$$\Delta\mathrm{DM} = \mathrm{DM}_{\mathrm{int}} - \mathrm{DM}_{\mathrm{ext}} = -5\,\frac{\gamma}{2(\gamma-1)}\,0.4 e_{\lambda}\,R_V\,E(B-V).$$

Supposing that the $\mathrm{DM}_{\mathrm{int}}$ is the DM corresponding to the ΛCDM model, ΔDM can be evaluated by imposing $\mathrm{DM}_{\mathrm{int}} = \mathrm{DM}_{\Lambda\mathrm{CDM}}$. By isolating the E(B-V) term, Eq. 2.1 is found:

$$E(B-V) = \frac{\Delta\mathrm{DM}}{-\frac{5}{2}\frac{\gamma}{\gamma-1}\,0.4\,R_V\,\frac{A_{2500\,\text{Å}}}{A_V}}.$$

2.8.6 Synopsis of the UV stacks

In Fig. 2.18, I show all the UV spectral stacks across the parameter space in different colours according to their redshift bin, along with the average spectrum of the whole sample in black as a reference. Regions without any spectrum are those discarded in Sec. 2.4.1. Only the UV side for the spectra is shown, as the optical one is only available in the lower redshift bins.

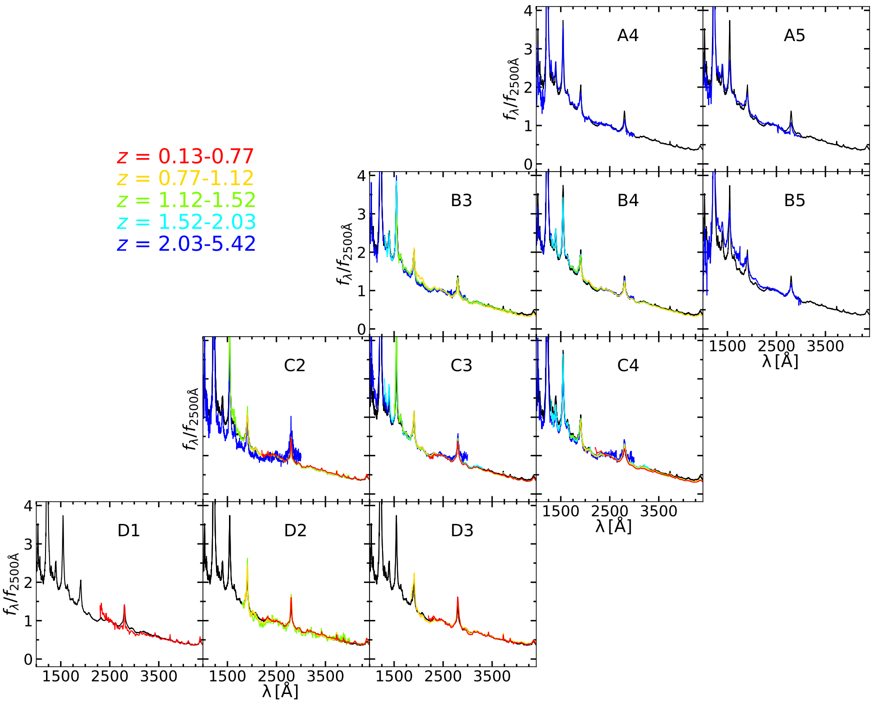

Figure 2.18. Similarity of the stacked spectra across the parameter space. All the spectra are normalised by their average emission between 2490–2510 Å. The black spectrum represents the average spectrum of the full sample. Only spectra of the bins meeting the representativeness criterion are included in the plot.

Chapter 3

The most luminous quasars at z=3.0-3.3

3.1 Outline

In this part of my thesis, I present the analysis of the rest frame ultraviolet and optical spectra of 30 bright blue quasars at $z \sim 3$, originally selected to expand the cosmological sample at high redshift with high quality X-ray observations. Previous works, based on pointed *XMM-Newton* observations, found an unexpectedly high fraction ($\approx 25\%$) of X-ray weak quasars in this sample. The latter sources also display a flatter UV continuum and a broader and fainter C IV profile in the archival UV data with respect to their X-ray normal counterparts. Here I present new observations with the Large Binocular Telescope in both the zJ (covering the rest frame ≃2300–3100 Å) and the K_S (≃4750–5350 Å) bands. I estimated the black hole masses and Eddington ratios from the available rest frame optical and UV emission lines (Hβ, Mg II), to update the previous C IV-based estimates. This allowed to find that these $z \sim 3$ quasars are on average highly accreting ($\langle \lambda_{\rm Edd} \rangle \simeq 1.2$ and $\langle {\rm M_{BH}} \rangle \simeq 10^{9.7} {\rm M_{\odot}}$), but without any significant difference in $\lambda_{\rm Edd}$ or $\rm M_{BH}$ between X-ray weak and X-ray normal quasars. From the zJ spectra, I derived the properties (e.g. flux, equivalent width) of the main emission lines (Mg II, Fe II), finding that X-ray weak quasars display higher Fe II/Mg II ratios with respect to typical quasars. Fe II/Mg II ratios of X-ray normal quasars are instead consistent with other estimates up to $z \simeq 6.5$, corroborating the idea of already chemically mature broad line regions at early cosmic time. The K_S spectra reveal that all the X-ray weak quasars present generally weaker [O III] emission (EW<10 Å) than the normal ones. The sample as a whole, however, abides by the known X-ray-[O III] luminosity correlation, hence the different [O III] properties are likely due to an intrinsically weaker [O III] emission in X-ray weak objects, associated to the shape of the spectral energy distribution. These results can be interpreted in the framework of accretion-disc winds. The results of this part of my thesis have been published in Trefoloni et al. (2023).

3.2 Context and aims of the work

The tight interplay between the corona and the accretion disc could in principle vary with the bolometric luminosity and/or the Eddington ratio. At high $\lambda_{\rm Edd}$, for instance, the framework of a geometrically thin and optically thick disc (Shakura and Sunyaev, 1973) could break down, as the disc is expected to thicken (Abramowicz et al. 1988; Chen and Wang 2004; Wang et al. 2014), a behaviour also shown by simulations (Ohsuga and Mineshige 2011; Jiang et al. 2014, 2016, 2019; Sądowski et al. 2014). Moreover, perturbations to the standard accretion process could be associated with the presence of powerful accretion-disc winds, directly driven by the nuclear activity (e.g. Proga 2005). Highly efficient accretion is an ideal condition for the launch of such outflows (Zubovas and King 2013; Nardini et al. 2015; King and Pounds 2015; Nardini et al. 2019a), which could justify the observed relations between the SMBH mass and the galaxy properties (e.g. the $\rm M_{BH}-\sigma$ relation; Ferrarese and Merritt 2000; Gebhardt et al. 2000; Marconi and Hunt 2003; King 2005), although it is not yet clear whether and how AGN-driven outflows can affect their host galaxies.

Remarkably, at high $\lambda_{\rm Edd}$ several quasar samples sharing similar UV properties have recently shown an enhanced fraction of objects ($\approx 25\%$) whose X-ray spectra are relatively flat ($\langle\Gamma \simeq 1.6\rangle$) and underluminous (by factors of $> 3-10$) with respect to what is expected according to the $L_{\rm X}-L_{\rm UV}$ relation (e.g. Luo et al. 2015; Nardini et al. 2019b; Zappacosta et al. 2020; Laurenti et al. 2022), in many cases without any clear evidence for absorption as revealed by the spectral analysis.

A high $\lambda_{\rm Edd}$ is also conducive to a higher prominence of the Fe II emission line complex (e.g. Boroson and Green 1992a; Marziani et al. 2001; Zamfir et al. 2010; Shen and Ho 2014). This feature, in turn, can be employed to investigate the chemical enrichment of the broad-line region of quasars through the Fe II/Mg II ratio up to very high redshift ($z \lesssim 7$). The Fe II/Mg II ratio seems to correlate with $\lambda_{\rm Edd}$ and $\rm M_{BH}$, but does not show any clear trend with the AGN luminosity (e.g. Dong et al. 2011; Shin et al. 2019, 2021). Despite numerous studies (e.g. Kawara et al. 1996; Thompson et al. 1999; Iwamuro et al. 2002, 2004; Dietrich et al. 2003a; Barth et al. 2003; Freudling et al. 2003; Maiolino et al. 2003; Tsuzuki et al. 2006; Jiang et al. 2007; Kurk et al. 2007; Sameshima et al. 2009, 2020; De Rosa et al. 2011, 2014; Mazzucchelli et al. 2017; Shin et al. 2019), it is still unclear whether any evolutionary trend of this ratio exists, also because of the large uncertainties on the measurements of this quantity.

In particular, this section of my thesis is dedicated to the analysis of the spectral properties of 30 luminous quasars ($\rm L_{bol} > 8 \times 10^{46}$ erg s^{-1}) at redshift $z = 3.0-3.3$ whose X-ray and UV properties had previously been investigated respectively in Nardini et al., 2019b, N19 and Lusso et al., 2021, L21. Here, I focus on the Mg II λ2798 emission line probed by dedicated observations at the Large Binocular Telescope (LBT) in the zJ band, and on the Hβ–[O III] complex for a subsample observed in the $K_{\rm S}$ band. Here, my main aim is to investigate whether any evidence of a difference in the optical-UV properties (e.g. emission line strengths, continuum) exists, echoing the difference between the X-ray properties of the two subsamples.

Throughout this Chapter, I will refer to X-ray normal quasars as the N group, and to X-ray weak quasars and weak candidates as the W+w group (i.e. no distinctioni is made between X-ray weak, W, and weak candidates, w). There are several possible definitions for the X-ray weakness based, for instance on the X-ray bolometric correction or on the $\mathrm{L_X - L_{UV}}$ relation itself. Here I adhere to the one based on the optical to X-ray index α_{OX}, defined as $\alpha_{OX} = 0.384 \log(F_X/F_{UV})$. Basically, I computed the distribution of the differences between the observed and predicted values for α_{OX}, where the predicted values were computed assuming as a reference the $F_X - F_{UV}$ relation determined from the 30 objects in the sample of blue quasars described in Risaliti and Lusso (2019) in the same redshift range as the $z \sim 3$ sample. X-ray weak quasars are defined as those that fall at more (negative values) than 3 σ from the peak of the $\Delta_{\alpha_{OX}}$ distribution, while X-ray weak candidates those falling at 2 σ.

3.2.1 The data set

The quasar sample analysed here consists of 30 luminous quasars ($\mathrm{L_{bol}} > 10^{46.9}$ erg $\mathrm{s^{-1}}$) at $z \sim 3$, for which X-ray observations were obtained through an extensive campaign performed with *XMM-Newton*. This sample, selected in the optical from the Sloan Digital Sky Survey (SDSS) Data Release 7 (Abazajian et al., 2009) as representative of the most luminous, intrinsically blue radio-quiet quasars, boasts by construction a remarkable degree of homogeneity in terms of optical-UV properties. The selection of this sample adhered to the already mentioned prescriptions adopted to select blue quasars suitable for the cosmological implementation, in this case focusing on the most luminous sources at $z = 3.0 - 3.3$. While the reader interested in the previous analyses should refer to N19 and L21, I briefly summarise the main results below.

About two-thirds of the sample show X-ray luminosities in agreement with the values expected from the $L_{\mathrm{X}} - L_{\mathrm{UV}}$ relation, and an average continuum photon index of $\Gamma_{\mathrm{X}} \sim 1.85$, fully consistent with AGN at lower redshift, luminosity, and $\mathrm{M_{BH}}$ (e.g. Just et al. 2007; Piconcelli et al. 2005; Bianchi et al. 2009). Their 2–10 keV band luminosities are in the range $4.5 \times 10^{44} \leq L_{2-10\,\mathrm{keV}} \leq 7.2 \times 10^{45}$ erg $\mathrm{s^{-1}}$, representing one of the most X-ray luminous samples of radio-quiet quasars ever observed. Conversely, one-third of the sources are found to be underluminous by factors of $\gtrsim 3$–10. X-ray absorption at the source redshift is not statistically required in general by the fits of the X-ray spectra and, despite the poor quality of the data in a handful of cases that does not allow us to definitely exclude some absorption, column densities $N_{\mathrm{H}}(z) > 3 \times 10^{22}$ $\mathrm{cm^{-2}}$ can be confidently ruled out.

In L21 the C IV λ1549 emission line properties (e.g. EW; line peak velocity, v_p) and UV continuum slope were investigated as a function of the X-ray photon index and 2–10 keV flux. In summary, it was found that the composite spectrum of X-ray weak quasars is flatter ($\alpha_\lambda \sim -0.6$) than that of X-ray normal quasars ($\alpha_\lambda \sim -1.5$). The C IV emission line is on average fainter in the X-ray weak sample, but only a modest blueshift (600–800 km $\mathrm{s^{-1}}$) is reported for the C IV lines of both stacks. This emission feature is found to be broader in the *W+w* stacked spectrum where it exhibits a higher FWHM ($\simeq$ 10,000 km $\mathrm{s^{-1}}$) than in the N spectrum ($\simeq$ 7,000 km $\mathrm{s^{-1}}$), but still in agreement with previous results on the topic at similar redshifts (e.g. Shen et al., 2011; Richards et al., 2002a) and luminosities (e.g. Vietri et al., 2018). Successively, a comparison sample from Timlin III et al. 2020, filtered out according to the standard selection criteria, was added in order to expand the dynamical range of the parameters of interest. This matched sample revealed statistically significant trends of C IV ν_p and EW with UV luminosity at 2500 Å for both X-ray weak and X-ray normal quasars, as well as the correlation between X-ray weakness and the EW of C IV. Additionally, a statistically significant correlation between the hard X-ray flux and the integrated C IV flux for X-ray normal quasars, extending across more than three (two) decades in C IV (X-ray) luminosity, was found. Notably, X-ray weak quasars deviate from the main trend by more than 0.5 dex.

To interpret these results, a possibility is that X-ray weakness might arise in a starved X-ray corona picture, possibly associated with an ongoing disc-wind phase. If the wind is ejected in the vicinity of the black hole, the accretion rate across the final gravitational radii will diminish, so depriving a compact, centrally confined corona of seed UV photons and resulting in an X-ray weak quasar. However, at the largest UV luminosities ($> 10^{47}$ erg s^{-1}), there will still be sufficient ionising photons that can explain the "excess" C IV emission observed in the X-ray weak quasars with respect to normal sources of similar X-ray luminosities (see Fig. 14 in L21).

3.2.2 LUCI/LBT observations

In addition to the effects on the C IV emission line, the main interest in this study is assessing whether the dearth of X-ray photons could affect other emission lines, such as the [O III] $\lambda\lambda 4959, 5007$Å doublet, whose production needs at least $\simeq$ 35 eV ($\simeq$ 354 Å) photons, and the Hβ line. Moreover, wavelengths longer than 2200 Å, not covered by the SDSS spectra in this redshift interval, are key to determining the continuum fluxes at rest frame 2500 Å and to inspecting the UV Fe II and Fe III emission often included among the characteristic parameters of X-ray weak quasars (e.g. Leighly et al. 2007a; Marziani and Sulentic 2014; Luo et al. 2015). Therefore, observations of this spectral interval are important for several reasons. For instance, the analysis of the Mg II emission line provides generally more reliable estimates of BH masses than the C IV-based estimates. These revised M_{BH} allow, in turn, to test more reliably whether any systematic difference between the BH masses and Eddington ratios of the X-ray weak and normal quasars is present. Additionally, it is possible to estimate the Fe II/Mg II ratio in the sample, which has been, in several works investigated as a proxy of the BLR gas metallicity at high redshift (e.g. Shin et al. 2019; Wang et al. 2022b; Jiang et al. 2024).

To investigate these issues, my group was awarded observing time with the two LBT Utility Cameras in the Infrared (LUCI1 and LUCI2, Ageorges et al., 2010) at the 8.4 m Large Binocular Telescope (LBT) located on Mount Graham (Arizona), to carry out near-infrared spectroscopy of the $z \sim 3$ quasars in the zJ and K_S bands. LUCI observations were performed between November 2018 and April 2021 with the zJ filter coupled with grism G200 and the K_S filter coupled with grism G150, covering an observed range of 0.9–1.2 μm and 1.95–2.40 μm, respectively. A slit width of $1''$ was employed, providing a spectral resolution $R = 1050$–1200 in zJ and 2075 in K_S. The journal of the observations is shown in Tables 3.1 and 3.3, where the seeing measured during the observations and the average signal-to-noise ratio (S/N) in the observed wavelength ranges 1.05–1.10 μm and 2.04–2.20 μm of the final flux-calibrated spectra are listed.

Observations in the zJ band were performed for all the quasars but one (J1507+2419), which was too faint to be observed with an exposure time comparable with the rest of the sample. Regarding the K_S observations, a further constraint on the redshift ($z = 3.19 - 3.29$) within the sample was dictated by the requirement that the [O III] emission line falls in a wavelength range ($2.10 - 2.15$ μm) with good atmospheric transmission. This condition allowed us to observe only nine targets, for which the K_S spectroscopic data[1] were acquired from November 2018 to April 2019 with seeing of around $0.7'' - 1.0''$.

The 2D raw spectra were reduced by the LBT Spectroscopic Reduction Center at INAF – IASF Milano, with a reduction pipeline optimised for LBT data (Scodeggio et al., 2005; Gargiulo et al., 2022) performing the following steps. For each source, calibration frames are created for both LUCI1 and LUCI2. Imaging flats and darks are used to create a bad pixel map, applied to every single observed frame, along with a correction for cosmic rays. Dark and flat-field corrections are applied independently to each observed frame through a master dark and a master flat, obtained from a set of darks and spectroscopic flats. A master lamp describes the inverse solution of the dispersion to be applied to individual frames to calibrate in wavelength and remove any curvature due to optical distortions. The mean accuracy achieved for the wavelength calibration is 0.26 Å in the K_S band and 0.22 Å (0.25 Å) for LUCI1 (LUCI2) in the zJ band. The 2D wavelength-calibrated spectra are then sky-subtracted following the method described in Davies (2007). The flux calibration is then applied to the 2D spectra through the sensitivity function, obtained from the spectrum of a star observed close in time and air-mass to the scientific target. Finally, wavelength- and flux-calibrated, sky-subtracted spectra are stacked together, and the 1D spectrum of the source is extracted. The zJ (K_S) flux calibration was checked by convolving each spectrum with the 2MASS J (K_S) filter to compute its J- (K_S-) band Vega magnitude, and then corrected to match to the observed value reported by SDSS DR16v4 (Ahumada et al., 2020). The uncertainty on the flux-calibrated spectrum was estimated as the squared sum of a statistic term given by the mean rms of left and right telescopes and a calibration factor $\Delta m/m = (m_{\rm LBT} - m_{\rm 2MASS})/m_{\rm 2MASS}$.

There is no overlapping region between the LBT zJ and the SDSS spectra, which leaves a small gap between them. Since the two segments of each spectrum were not collected simultaneously, part of the observed flux gap can be due to some intrinsic variation of the emission, but it is reasonable to expect this contribution to be rather small since more luminous quasars tend to be less variable in time (e.g. Uomoto et al., 1976; Cristiani et al., 1995; Wilhite et al., 2008). Systematics in the flux calibration could also be involved, but in principle their contribution should be small since SDSS spectrophotometric calibration is accurate to 4% rms for point sources (Adelman-McCarthy, 2008). LBT flux re-calibration factors with respect to the 2MASS J (K_S) filter are in the range $0.6 - 1.9$ ($0.4 - 1.7$) with a mean value of 1.02 (0.93).

---

[1] K_S observations were performed with LUCI1 only.

Table 3.1. Log of the LUCI/LBT zJ observations.

Name	(a) Obs. Date	(b) t_{exp}	(c) S/N	(d) Seeing	(e) Instr.
J0301−0035	2019 Sep 28	1320	49	1.0	LUCI1
J0304−0008	2019 Sep 28	1680	43	1.0	LUCI1
J0826+3148	2019 Oct 17	1920	28	1.0	LUCI1
J0835+2122	2019 Oct 17	1680	35	1.1	LUCI1
J0900+4215	2020 Feb 02	480	22	1.2	LUCI2
J0901+3549	2020 Feb 02	1200	24	0.8	LUCI2
J0905+3057	2020 Feb 03	1680	27	1.1	LUCI2
J0942+0422	2020 Nov 12	960	24	1.2	LUCI1+LUCI2
J0945+2305	2020 Dec 26	6000	37	1.0	LUCI1+LUCI2
J0947+1421	2020 Dec 26	840	33	0.9	LUCI1+LUCI2
J1014+4300	2020 Dec 26	720	46	0.8	LUCI1+LUCI2
J1027+3543	2020 Dec 26	840	17	0.8	LUCI1+LUCI2
J1111−1505	2021 Apr 02	2700	26	0.9	LUCI1+LUCI2
J1111+2437	2021 Jan 09	3360	33	1.4	LUCI1+LUCI2
J1143+3452	2021 Jan 12	2160	33	1.0	LUCI1+LUCI2
J1148+2313	2021 Jan 17	1440	23	0.8	LUCI1+LUCI2
J1159+3134	2021 Jan 17	1800	18	0.9	LUCI1+LUCI2
J1201+0116	2021 Apr 02	960	35	0.9	LUCI1+LUCI2
J1220+4549	2021 Jan 31	1500	35	0.8	LUCI1+LUCI2
J1225+4831	2021 Feb 01	1920	18	0.7	LUCI1+LUCI2
J1246+2625	2020 Jun 23	1200	25	0.7	LUCI2
J1246+1113	2020 Jun 23	2400	15	0.8	LUCI2
J1407+6454	2020 Jun 23	1080	30	0.8	LUCI2
J1425+5406	2020 Jun 26	1050	29	0.9	LUCI2
J1426+6025	2020 Jun 27	300	15	0.8	LUCI2
J1459+0024	2020 Jun 27	1650	12	0.9	LUCI2
J1532+3700	2020 Jun 26	900	21	0.9	LUCI2
J1712+5755	2019 Oct 19	960	12	1.1	LUCI1
J2234+0000	2019 Sep 28	1350	16	0.9	LUCI1+LUCI2

Table 3.2. (a) Observation Date; (b) Total exposure; (c) Signal-to-noise ratio in the observed wavelength range 1.05–1.10 μm; (d) Average seeing of the observation in arcseconds; (e) LUCI camera used for the observation.

Table 3.3. Log of the LUCI1/LBT K_S observations.

Name	(a) Obs. Date	(b) t_{exp}	(c) S/N	(d) Seeing
J0303−0023	2018 Nov 06	2400	25	0.9
J0304−0008	2018 Nov 07	2420	15	1.0
J0945+2305	2018 Nov 08–09	4960	18	0.7
J0942+0422	2018 Nov 11	1650	38	1.0
J1220+4549	2019 Jan 26	2875	10	1.0
J1111+2437	2019 Jan 26	2645	21	1.0
J1201+0116	2019 Jan 28	800	29	1.7
J1425+5406	2019 Feb 28	2415	42	0.8
J1426+6025	2019 Apr 27	600	51	1.0

Table 3.4. (a) Observation Date; (b) Total exposure; (c) Signal-to-noise ratio in the observed wavelength range 2.04–2.20 μm; (d) Average seeing of the observation in arcseconds.

3.3 Analysis

3.3.1 Fitting procedure

The spectral fits of the zJ and K_S data were both performed through a custom-made code, based on the IDL MPFIT package (Markwardt, 2009), which takes advantage of the Levenberg–Marquardt technique (Moré, 1978) to solve the least-squares problem.

The region roughly between 2400 Å and 3200 Å corresponding to the rest frame of the zJ spectra is mainly characterised by Fe II and Fe III emission lines (which blend in a pseudo-continuum), the Balmer continuum, and the Mg II 2798 Å emission line. In this region there are only two small continuum windows between 2650–2670 Å and 3030–3070 Å (Mejía-Restrepo et al., 2016), but the former was often included in the atmospheric absorption band that affects the range ∼1.11–1.16 μm in the observed frame. This, together with the lack of other bright emission lines and/or other continuum windows, led to the problem of having only one narrow interval to anchor the power-law continuum, thus leading to a degeneracy between the slope of the power law and the strength of iron emission.

In order to break this degeneracy, I followed a similar approach to that described in Vietri et al. (2018). I adopted the same value of the continuum power-law slope as derived from the SDSS spectra in L21 for each source. In the six cases where multiple SDSS observations were available (J0303–0023, J0303–0008, J111–1505, J1159+3134, J1407+6454, J1459+0024), I assumed the average of the individual best-fit spectral indices. I then accounted for the remaining emission with the required number of Fe II templates, as produced by different synthetic photoionisation models through the CLOUDY simulation code (Ferland et al., 2013), and convolved with different Gaussian profiles with a velocity dispersion of up to 7,000 km s^{-1}. Broad Gaussian components (FWHM > 1,000 km s^{-1}) were added in some cases, to provide a more faithful description of the iron profile. This procedure gave satisfactory results for most of the spectra. Furthermore, in the Supplementary Material (3.7.1) I report on checking the reliability of fixing the power-law slope in order to match that of the continuum underlying the C IV line and the continuum windows at bluer wavelengths, and I compared how I estimated the strength of Fe II with that in the archival data.

The model adopted to fit the K_S spectra included a multi-Gaussian (one broad, one or two narrow) deconvolution for the emission lines (i.e. Hβ λ4861 and [O III] $\lambda\lambda$4959, 5007), and Fe II templates to account for the optical iron emission. The ratio of the core [O III] λ4959 to λ5007 components was fixed at one to three, and a blue component for both [O III] lines was also included to account for possible outflows from the NLR. Examples of the fits performed on typical LBT zJ- and K_S-band spectra are shown, respectively, in Fig. 3.1 and Fig. 3.2.

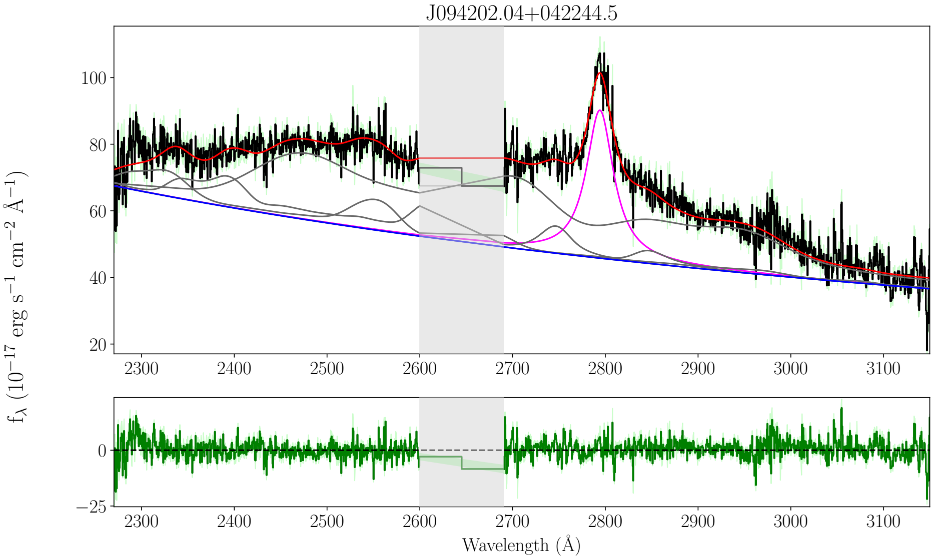

Figure 3.1. Example of LBT zJ spectral fit. *Top panel*: Spectrum (black), global model (red), and model components of a typical LBT zJ fit (J0942+0422). The continuum power law is shown in blue, the Mg II line in magenta, the iron pseudo-continuum in dark grey. The shaded light grey band corresponds to the observed-frame atmospheric absorption window at 1.11–1.16 μm and is not included in the fit. *Bottom panel*: Global model residuals (green).

3.3.2 Composite spectra

To build the composite LBT spectra for the X-ray weak and X-ray normal quasars, I followed a similar procedure to the one described in 2.4.2. For the sake of consistency with the assumptions made in L21 where the stacks of the C IV region had been performed, I excluded from the stack the radio-bright (J0900+4215), the two broad absorption line quasars (J0945+2305, J1148+2313), and the reddest (J1459+0024) quasar. As the last three are X-ray weak, the purpose of this exclusion was to avoid an enhanced flatness of the resulting composite spectrum as a result of their BAL–red nature. This further selection brought the X-ray weak group of LBT zJ (K_S) spectra down to seven (four) objects. Here I briefly mention the procedure adopted:

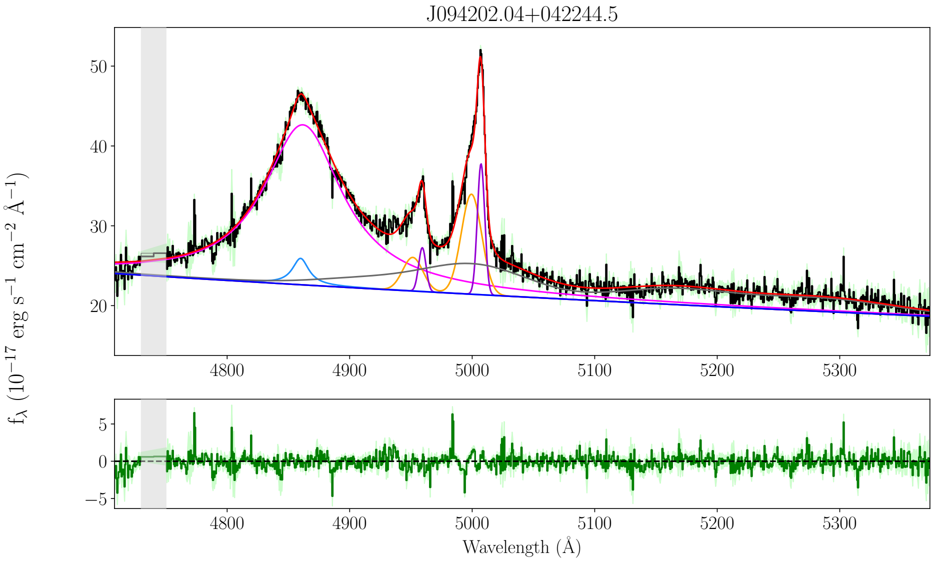

Figure 3.2. Example of LBT K_S spectral fit. *Top panel*: Spectrum (black), global model (red), and model components of a typical LBT K_S fit (J0942+0422). The continuum power law is shown in blue, the broad and narrow Hβ in magenta and turquoise, the [O III] doublet in orange and violet, and the iron pseudo-continuum in dark grey. The shaded light grey band is affected by poor atmospheric transmission and is not included in the fit. *Bottom panel*: Global model residuals (green).

1. I corrected the quasar flux density[2] f_λ for Galactic reddening by adopting the E(B-V) estimates from Schlegel et al. (1998) and the Galactic extinction curve from Fitzpatrick (1999) with $R_V = 3.1$.

2. I generated a rest frame wavelength array with fixed dispersion for the zJ (K_S) spectra with $\Delta\lambda$ equal to 2.25 Å (2.39 Å), roughly corresponding to the resolution at the central wavelength of the observed spectra (R=1125 at 1.05 μm and R=2075 at 2.105 μm, respectively, for zJ and K_S), shifted to the rest frame according to the mean quasar redshift.

3. I shifted each quasar spectrum to the rest frame and linearly interpolated over the rest frame wavelength array with fixed dispersion $\Delta\lambda$, while conserving its flux.

4. I normalised every spectrum by their integrated flux over the wavelength ranges 2400–3100 Å (zJ) and 4800–5300 Å (K_S), which are covered by all the spectra.

5. I extracted the median value of the normalised fluxes in each spectral channel. The uncertainty on the median flux in a spectral channel was estimated as the 95% semi-interquartile range of the fluxes divided by the square root of the number of spectra in that channel.

---

[2] In the following, I use the word "flux" to mean the flux density (i.e. flux per unit wavelength) unless specified otherwise.

The spectral stacks obtained with the procedure described above are shown in Figures 3.3 and 3.4 for the zJ and the K_S data, respectively. As a reference, I also overplot the average quasar spectrum from VB01 already introduced in 2.4.2. Extrapolating the slope of the continuum found in L21 to the wavelengths covered by the LBT spectra, the flatter continuum in the X-ray weak composite hints at a larger EW of Fe II compounds, as also suggested by the analysis of the individual sources. I discuss this point further in Section 2.5. Despite the emission line differences, the two composites are in broad agreement with the reference spectrum, thus implying no strong evolution of the general spectral properties of the $z \sim 3$ sample with respect to AGN at other redshifts.

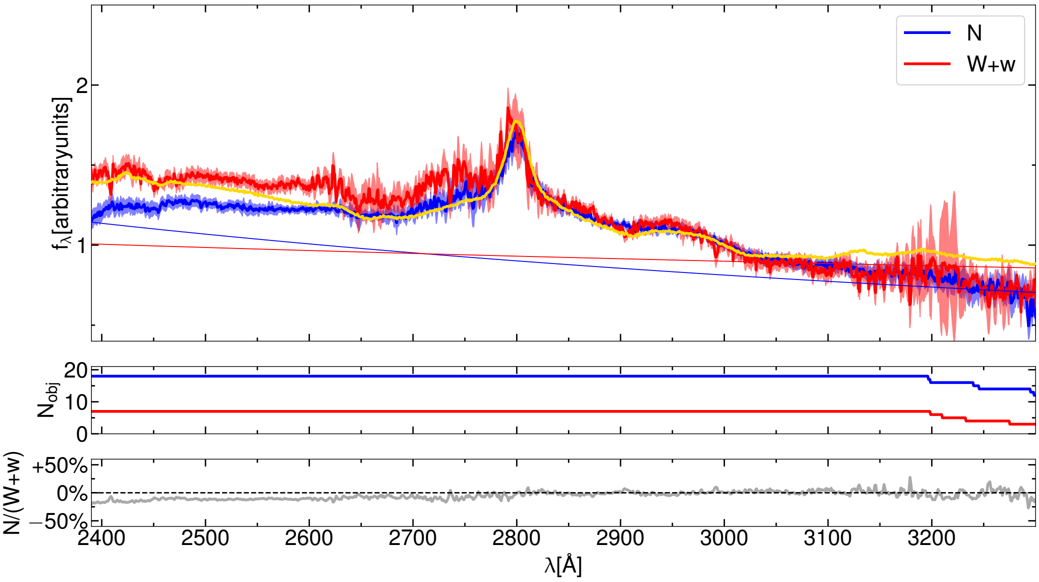

Figure 3.3. Composite LBT zJ spectra for N and W+w quasars. *Top panel*: Median LBT zJ spectra for the X-ray normal (N, in blue) and the X-ray weak (W+w, in red) subsamples. The gold spectrum is the average quasar spectrum from VB01. Fluxes are normalised by their value at 3000 Å. The continuum power laws are the extrapolation of those found at UV wavelengths (i.e. SDSS). *Middle panel*: Number of spectra contributing to each spectral channel, following to the same colour-coding. *Bottom panel*: Ratio of the N spectrum to the W+w spectrum.

3.3.3 Black hole masses and Eddington ratios

I computed single-epoch M_{BH} from the available emission lines with known reliable virial relations for each object. In the SDSS spectra, the C IV λ1549 line is available for the whole sample, whereas the Mg II λ2798 line, present in all the LBT zJ spectra, in 18/29 cases is fully or marginally hidden by atmospheric absorption, hindering a reliable determination of its FWHM. Hβ was used for the nine objects in the LBT K_S subsample. It is well known that BH masses from different lines have a different reliability: Hβ-based masses are generally regarded as the benchmark (see e.g. Denney, 2012; Shen, 2013; Dalla Bontà et al., 2020a), but in this case they are only available for a minority of sources. Mg II-based masses are consistent,

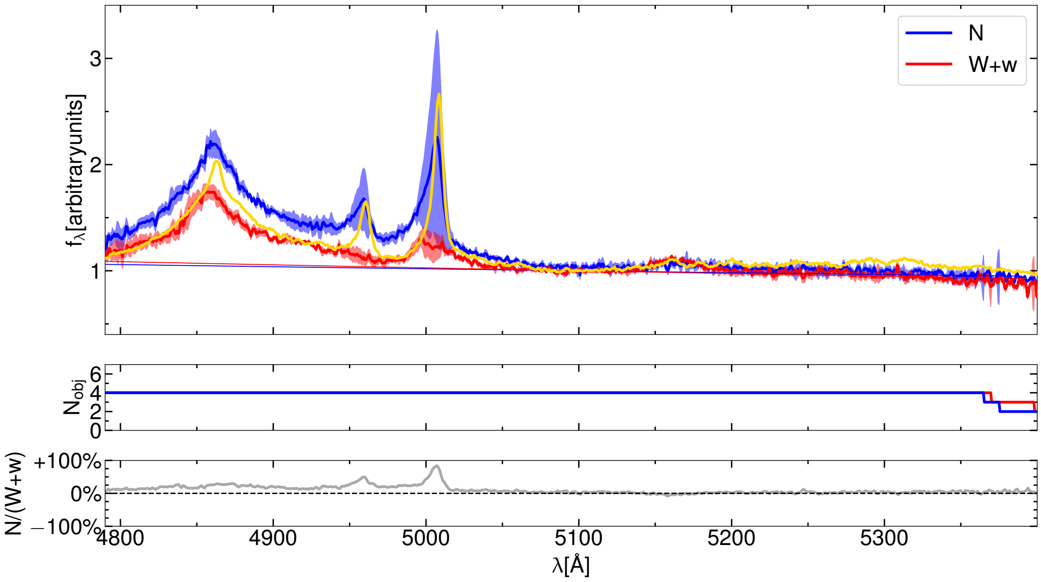

Figure 3.4. Composite LBT K_S spectra for N and $W+w$ quasars. *Top panel*: Median LBT K_S spectra for the X-ray normal and the X-ray weak subsamples. The colour-coding is the same as in Figure 3.3. Fluxes are normalised by their value at 5100 Å. *Middle panel*: Number of spectra contributing to each spectral channel, following the same colour-coding. *Bottom panel*: Ratio of the N spectrum to the W+w spectrum.

within their non-negligible systematic uncertainty (~0.3-0.4 dex; Shen et al. 2011), with the Hβ values. On the other hand, while C IV-based masses only provide a very rough estimate of the mass of the black hole powering the AGN, this emission feature is present for every object in the sample, and in 18/29 objects this is the only available tool to estimate the BH mass. The inclusion of C IV-based BH masses comes with two caveats. First, the C IV emission line centroid can show blueshifts up to about 10,000 km s^{-1} with respect to the systemic redshift, suggesting the presence of an outflowing phase (Baskin and Laor, 2005a; Richards et al., 2006), not compatible with the virial assumption under which BH masses are estimated. This can cause an overestimate of the BH mass by up to an order of magnitude (e.g. Kratzer and Richards, 2015). Second, C IV calibrations should be considered with caution since they are affected by significant scatter due to different systematics, eventually allowing us to derive BH masses only at the price of large uncertainties, $\gtrsim$ 0.4 dex (Shen et al., 2011; Shen and Liu, 2012; Rakshit et al., 2020; Wu and Shen, 2022). To mitigate these issues, BH masses based on the C IV FWHM were estimated by adopting the corrections described in Coatman et al. (2017), suitable for objects with a blueshifted C IV emission. I employed the offset velocities reported in L21 to perform the correction of the FWHM and subsequently of M_{BH} for objects whose blueshifts are positive, whereas the correction factors were set to unity otherwise (3/29 objects) since the authors themselves cautioned against using their correction in case of negative blueshift (i.e. redshift) of the C IV line centroid.

I estimated single-epoch masses based on the continuum luminosity (λL_λ) evaluated close to the considered emission line and its FWHM through the expression

$$\log\left(\frac{\mathrm{M_{BH}}}{M_\odot}\right) = A + B\,\log\left(\frac{\lambda L_\lambda}{10^{44}\mathrm{erg\,s^{-1}}}\right) + 2\,\log\left(\frac{\mathrm{FWHM}}{\mathrm{km\,s^{-1}}}\right), \tag{3.1}$$

where the A and B coefficients were calibrated by different authors for each line as

$$(A, B) = \begin{cases} (0.71, 0.53) & \text{C IV 1549 Å} \quad \text{Coatman et al. (2017)} \\ (0.74, 0.62) & \text{Mg II 2798 Å} \quad \text{Shen et al. (2011)} \\ (0.70, 0.50) & \mathrm{H}\beta \quad \text{Bongiorno et al. (2014)}. \end{cases} \tag{3.2}$$

The wavelengths 1350 Å, 3000 Å, and 5100 Å were adopted to estimate the continuum luminosity for the C IV, Mg II, and Hβ emission lines, respectively. The data availability from the UV to the visible for nine objects allowed us to verify the reliability of the calibrations by comparing pairs of BH mass estimates. SMBH masses from the C IV line were compared to those already estimated in Wu and Shen (2022). To this end, I computed the distribution of the differences $\Delta\log(\mathrm{M_{BH}}) = \log(\mathrm{M_{BH,CIV}}) - \log(\mathrm{M_{BH,SDSS}})$. The mean value and the standard deviation of this distribution are $\langle\Delta\log(\mathrm{M_{BH}})\rangle = -0.05$ and $\sigma_{\Delta\log(\mathrm{M_{BH}})} = 0.3$. The minor offset of the distribution could be due to the prescription for the evaluation of the BH mass (in Wu and Shen 2022 the authors adopted the calibration from Vestergaard and Peterson 2006) and/or to the fitting procedure, but in general no strong outliers are found.

For all the objects whose spectra included the Hβ emission line, the Mg II λ2798 line and the 3000 Å luminosity were also available; therefore it was possible to provide an additional estimate of the BH masses and compare them with the Hβ-based values. C IV- and Mg II-based BH masses against Hβ-based masses are shown in Figure 3.5. The uncertainty is dominated by the systematic term (0.4 dex for C IV and 0.3 dex for Mg II and Hβ-based masses), being the statistical uncertainty on the BH masses on average 17% for the C IV, 5% for the Hβ, and 2% for the Mg II estimates. The fiducial mass for each object was derived as a weighted mean, using as weight the total uncertainty on each mass estimate, given by the square root of the squared sum of the systematic term and the statistical term. BH masses are listed in Table A1 together with the best-fit line and continuum parameters.

Eddington ratios were calculated by assuming the standard definition of $L_{\mathrm{Edd}} = 1.26\times10^{38}\,(\mathrm{M_{BH}/M_\odot})$ erg s^{-1}. The $\mathrm{L_{bol}}$ value was computed for each object as stated in N19, by employing the 1350 Å monochromatic luminosity available from SDSS photometry and the bolometric correction of Richards et al. (2006). Considering the uncertainties on the BH masses, and the uncertainties on the bolometric conversion factors, which in the case of the 1350 Å luminosity can be up to 50% (Richards et al., 2006), it is possible to only give crude estimates of the Eddington ratios. I found that, on average, these sources are close to the Eddington limit, with a median λ_{Edd} of 0.9, which is expected given the very high luminosities observed in the $z \sim 3$ sample.

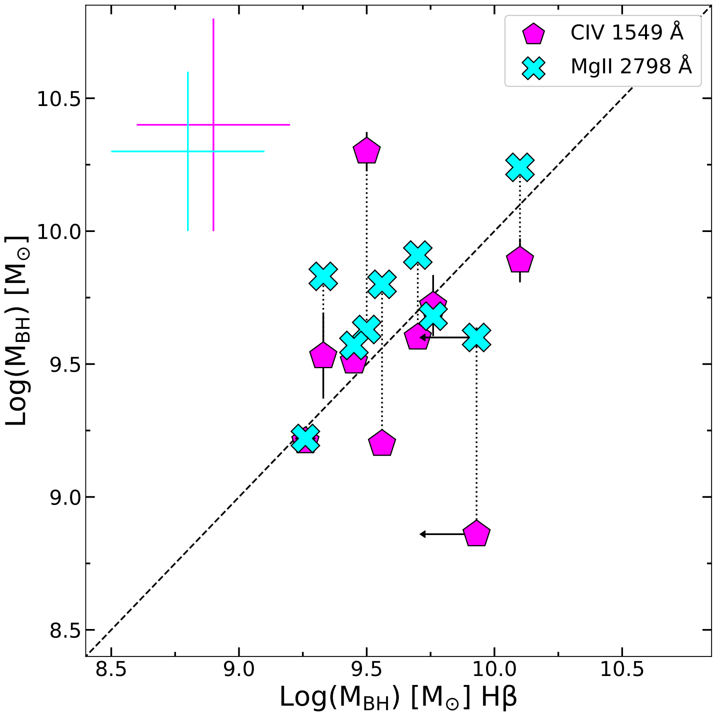

Figure 3.5. Single-epoch M_{BH} comparison. The estimates based on C IV λ1549 (magenta pentagons) and Mg II λ2798 (cyan crosses) are shown against the broad Hβ values. The typical systematic uncertainty of the calibrations is shown in the top left corner with the same colour-coding, while the dashed black line represents the 1:1 relation. The dotted lines join BH mass estimates for the same object according to different emission lines. The Hβ BH mass for J1111+2437 is denoted as an upper limit since the line profile is not well defined.

3.4 Results

3.4.1 Mg II and Fe II emission

Intense Fe II emission and high Fe II/Mg II ratios are typically observed for X-ray weak sources (e.g. PHL 1811; Leighly et al. 2007a). I thus estimated the rest frame equivalent width for both the Mg II line and the Fe II emission complex to assess whether possible differences arise between the X-ray weak and X-ray normal quasars in the sample. However, the significance[3] of any difference between the two samples is limited by the small statistics (18 N vs 10 W+w objects, excluding the radio bright J0900+4215 in the LBT zJ, and 4 N vs 5 W+w objects in the LBT K_S spectral samples).

I found that the mean value of EW Mg II with the standard error of the mean for the N group is $\langle$EW Mg II$\rangle_N$=59±9 Å, while $\langle$EW Mg II$\rangle_{W+w}$=66±13 Å for the W+w group, without any statistically significant difference between the two samples.

---

[3] Throughout this work, the significance is reported as $m\sigma$ with $m = |<x_N> - <x_{W+w}>|/\sqrt{\sigma^2_{x_N}/n_N + \sigma^2_{x_{W+w}}/n_{W+w}}$, where $<x_i>$ is the mean value, σ_i the standard deviation, and n_i the size of the *i-th* sample.

However, potential differences could be diluted by the blend of Mg II with the Fe emission. In this analysis, I considered all the Mg II lines for which the full profile was available, including BAL quasar J0945+2305 (the other BAL and the reddest object did not show an analysable Mg II profile). However, the results do not change excluding the latter source.

The mean EW Fe II of the N sample is $\langle$EW Fe II $\rangle_N$=292±40 Å, which is somewhat smaller than the value obtained for the W+w sample, $\langle$EW Fe II$\rangle_{W+w}$=469±70 Å. The difference is statistically significant at the 2.2σ level, and a Kolmogorov–Smirnov (KS) test provides a p-value=0.017, implying that the two distributions are indeed different at the 98.3% level. In the estimate of Fe II mean values I neglected the source J1225+4831, whose power-law continuum as extrapolated from the SDSS spectrum is significantly steeper than that required to adequately fit the Mg II emission line. Even attempting a free-slope fit, there is a very faint Fe II contribution.

Both EW Fe II and EW Mg II were estimated by normalising the integrated flux of the line by the continuum flux at 3000 Å, as generally done for such ratios (e.g. Sameshima et al., 2020). The ratio of the equivalent widths of Fe II to Mg II shows, on average, a higher value for the W+w sample, $\langle$Fe II/Mg II$\rangle_{W+w}$=8.4±1.4, than for the N sample, $\langle$Fe II/Mg II$\rangle_N$=4.4±0.5.

Figure 3.6 shows the $\Delta\alpha_{\rm OX}$ (the difference between the observed $\alpha_{\rm OX}$ and that predicted from the $\alpha_{\rm OX} - L_{\rm UV}$ relation for objects within the same redshift interval of the sample),[4] an index of X-ray weakness, as a function of the Fe II/Mg II ratio. On average, the Fe II/Mg II ratio is higher in X-ray weak quasars with respect to X-ray normal ones. I also colour-coded EW C IV to compare this trend with the modest decrease in C IV with increasing X-ray weakness observed in L21. I assessed this trend by means of a Spearman's rank test, which yielded a correlation index of $r_S = -0.6$ with p-value 0.04. A possible origin for this trend is discussed in Sect. 3.5, in terms of increased Fe II$_{\rm UV}$ emission in X-ray weak quasars associated with outflow-induced shocks and turbulence. The statistical uncertainty on the Fe II/Mg II ratio was estimated by fitting 100 mock spectra for each source: the flux in every spectral channel was created by adding a random value to the actual flux, extracted from a Gaussian distribution whose amplitude was set by the uncertainty value in that spectral channel. After fitting every mock sample, the distribution of the Fe II/Mg II values was computed, and the uncertainty was set as the standard deviation of the distribution, after applying a 3σ clipping.

In Figure 3.7 I show the estimates of Fe II/Mg II for the sample of ten quasars where the Mg II line was observed (excluding J0900+4215, which is flagged as radio bright), in comparison with other literature samples probing different redshift intervals (Dietrich et al., 2003a; Maiolino et al., 2003; De Rosa et al., 2011; Mazzucchelli et al., 2017; Shin et al., 2019; Sameshima et al., 2020). I found that, on average, there is no clear trend for an evolution in the Fe II/Mg II ratio across cosmic time, which implies already chemically enriched BLR regions at high redshift. To verify this trend quantitatively, I performed a Spearman's rank order probability test by using the X-ray normal quasars only together with the other samples, in order to avoid any possible bias introduced by the boosted Fe II/Mg II ratios of X-ray weak sources. I

---

[4] For a more detailed discussion about how the values of $\Delta\alpha_{\rm OX}$ are evaluated, I refer to Section 2.3 of L21, and references therein.

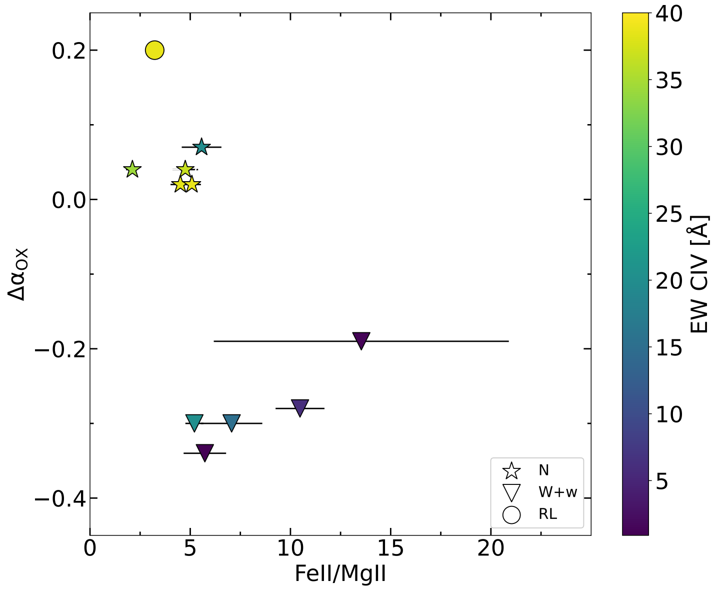

Figure 3.6. $\Delta\alpha_{OX}-$(Fe II/Mg II) plane for N (stars) and $W+w$ (triangles) sources. The radio-loud quasar J0900+4215 is shown as a circle. The $\Delta\alpha_{OX}$ value, as a proxy to X-ray weakness, is compared to the newly observed properties of the Mg II region and the relative intensity of the C IV emission (see colour bar at right). An increasing trend of the Fe II/Mg II ratio with increasing X-ray weakness can be seen.

then performed a linear fit of all the data sets together with EMCEE (Foreman-Mackey et al., 2013). The Spearman's test yielded a correlation coefficient of −0.26, revealing a mild trend of decreasing Fe II/Mg II ratio with redshift, marginally significant with a p-value 0.01. Yet this seeming decreasing trend is mostly driven by the upper limits and by the very high redshift points by Mazzucchelli et al. (2017) which are also the most uncertain. Indeed, The fit of the Fe II/Mg II$-z$ relation then provides evidence for a flat slope, confirming a non-significant evolution of this ratio across cosmic time. Although the highest redshift sample from Mazzucchelli et al. (2017) exhibits systematically lower values than those at lower redshift, the same authors note that the uncertainties are so large that the consistency with a non-evolving Fe II/Mg II ratio cannot be ruled out. Excluding this sample from the regression analysis, I find an even lower correlation coefficient (0.002, with p-value = 0.99), and again a slope virtually consistent with zero ($m = 0.01 \pm 0.01$). However, it is possible that, at very high redshift ($z \gtrsim 6$), a genuine depletion of iron, symptomatic of the presence of young stellar populations in the galaxies hosting these quasars, might be observed.

Our results further confirm the interpretation that samples at high redshifts, biased towards high luminosities (i.e. $L_{bol} > 10^{46}$ erg s^{-1}), presumably host SMBHs in already chemically mature galaxies (e.g. Kawakatu et al., 2003; Juarez et al., 2009). The values of their Fe II/Mg II ratios are consistent with those at lower redshifts. Possible systematic effects and a consistency check on the ability of the method employed here to reproduce the iron emission in these objects are discussed in Supplementary Material 3.7.1.

A strong correlation between the Fe II/Mg II ratio and the Eddington ratio has been observed, but not with the BH mass (Sameshima et al., 2017, see also Dong et al. 2011). Since the *N* and the *W+w* samples are fairly homogeneous in terms of BH masses and Eddington ratios (see Sect. 3.5), it is unlikely that one of these parameters is the fundamental driver of the observed difference. Theoretical works using CLOUDY simulations showed that several physical properties can impact the Fe II/Mg II ratio, such as gas density and microturbulence (Verner et al., 2003; Baldwin et al., 2004; Sameshima et al., 2017; Temple et al., 2020).

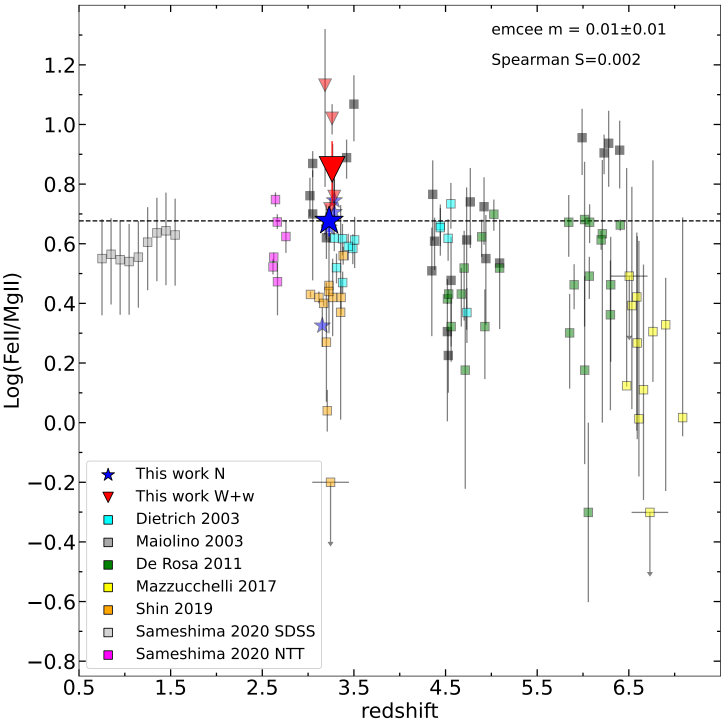

Figure 3.7. log(Fe II/Mg II) − z plane. *N* sources (blue stars) follow the expectations for objects at similar redshift, whereas *W+w* sources (red triangles) are located at the top of the distribution around $z \sim 3$. The black dashed line represents the mean F II/Mg II ratio of *N* quasars extrapolated over the entire redshift range.

3.4.2 Hβ properties

The nine rest frame optical spectra enabled us to investigate the properties of the Hβ–[O III] complex. On average, X-ray weak sources display a weaker Hβ emission than X-ray normal ones. The mean value of the EW for the *W+w* group is $\langle \mathrm{EW\,H}\beta\rangle_{W+w}$=73±8 Å , whereas it is $\langle \mathrm{EW\,H}\beta\rangle_{N}$=108±11 Å for the *W+w* sample, a difference that is statistically significant at the 2.6σ level.

In order to assess whether the Fe emission of X-ray weak sources is also enhanced in the optical band, I checked the Fe II/Hβ ratio, which is a standard optical indicator of the metallicity as discussed more thoroughly in 5.6.4, generally evaluated as the intensity ratio of the integrated flux of Fe II between 4434 Å and 4684 Å to that of Hβ (e.g. Boroson and Green, 1992a; Marziani and Sulentic, 2014). The relative intensities of the optical Fe emission are statistically consistent, as the average equivalent width of the optical Fe II of the N sample is $\langle$EW Fe II$_{\rm opt}\rangle_N$=16±6 Å, whereas the W+w sample yielded $\langle$EW Fe II$_{\rm opt}\rangle_{W+w}$=24±9 Å. The ratio is $\langle$Fe II$_{\rm opt}$/H$\beta\rangle_N$=0.14±0.06 for the N sources, and $\langle$Fe II$_{\rm opt}$/H$\beta\rangle_{W+w}$=0.36±0.13 for the W+w sources; therefore the mild difference between the Fe II/Hβ ratios is just mimicking the difference between the Hβ profiles of the two samples. Even so, I caution that the 4434–4684 Å interval over which the optical Fe II is generally sampled in the literature is not included in these spectra, and I thus had to rely on a full extrapolation for this estimator. For this reason, I also checked whether any difference could be found in the observed region using the equivalent width of the Fe II$_{\rm opt}$ emission between 4900 Å and 5300 Å, which is instead directly observed and included in the fits shown here. Also in this case, the difference remains marginal as the N and W+w groups respectively yield $\langle$Fe II$_{\rm opt}$/H$\beta\rangle_N$=0.31±0.07 and $\langle$Fe II$_{\rm opt}$/H$\beta\rangle_{W+w}$=0.72±0.32.

The ratio of UV to optical Fe II emission is higher for X-ray weak sources, being $\langle$Fe II$_{\rm UV}$/Fe II$_{\rm opt}\rangle_N$=13±4 and $\langle$Fe II$_{\rm UV}$/Fe II$_{\rm opt}\rangle_{W+w}$=26±9, in line with the expectations of higher ratios of UV to optical Fe II emission for increasingly weaker SEDs in the extreme UV (EUV), as shown in Leighly et al. (2007a). I note, however, that these results are not directly comparable with those in the third panel of Fig. 24 in Leighly et al. (2007a) since the Fe II emission here was evaluated on a much shorter interval (4900–5300 Å) than theirs (4000–6000 Å).

3.4.3 [O III] properties

In the context of the unified model, the [O III] is produced in the NLR, on galactic scales, and is believed to be an isotropic indicator of the AGN strength in both Type 1 and Type 2 AGN (e.g. Mulchaey et al. 1994; Bassani et al. 1999; Netzer 2009a, and references therein). The [O III] luminosity ($L_{\rm [O\,III]}$) is a secondary indicator of the nuclear luminosity, depending on the fraction of continuum radiation within the opening angle of the torus reaching the gas in the NLR, but is also influenced by local properties such as the NLR clumpiness, its covering factor, and the amount of dust extinction (e.g. Ueda et al., 2015).

The EW [O III] value can be considered as a proxy of the inclination of our line of sight to the AGN accretion disc (e.g. Risaliti et al. 2011; Shen and Ho 2014). Bisogni et al. (2017) investigated in detail the distribution of EW [O III] in the SDSS DR7, showing that EW [O III] $>$ 30 Å generally corresponds to high inclination angles, while lower values reflect the intrinsic EW [O III] distribution. Only one of these objects (J0303−0008) displays an EW [O III] in excess of 30 Å, thus possibly being observed at relatively high inclination (yet still likely within $\theta \lesssim 60°$, see Sect. 3.5). The mean (median) value of EW [O III] in the sample is 14.4±7.6 (3.7) Å, or 6.6±2.3 Å after excluding the strong [O III] emitter, consistent with the median value of the EW [O III] distribution from the current SDSS release (Wu and Shen, 2022), which is 14.1 Å, and well below the 30 Å threshold where inclination effects should become relevant.

With the aim of putting the sample into a broader context, I compared the results concerning the [O III] emission with other samples of luminous high-redshift quasars in the literature. The sample analysed in Vietri et al. (2018), part of the WISSH survey, exhibits extremely weak [O III] profiles, with a median value of 1.5 Å. The

19 AGN at $z \sim 2$ from the SUPER sample described in Kakkad et al. (2020) yield, instead, a median value of 14.2 Å, although these sources span a wide interval in terms of bolometric luminosity ($10^{45.4}$–$10^{47.9}$ erg s^{-1}). When matching the SUPER sample in luminosity with the quasars analysed here (i.e. considering only the objects with L_{bol} exceeding $10^{46.9}$ erg s^{-1}), the median value of EW [O III] decreases slightly to 11.6 Å.[5] Lastly, the median EW [O III] for the GNIRS–DQS quasars (Matthews et al., 2023) equals 12.7 Å; I note that for this sample ~ 15% of the sources have an unreliable EW measurements because of the weak [O III] profile. Although the cumulative EW [O III] distribution of these luminous high-redshift samples clusters around the same peak of the global SDSS quasar distribution (Wu and Shen, 2022), objects with high equivalent width become relatively rare, as shown in the right side panel in Fig. 3.8. For instance, the fraction of objects with EW [O III] > 50 Å in the SDSS catalogue is ~10%, while the joint incidence in all the mentioned high-redshift samples is about 2%, although some systematic effects could marginally modify this estimate given the non-uniform analysis of the different samples (e.g. continuum fitting windows, different Fe templates).

The weaker [O III] profiles in very luminous quasars with respect to the global SDSS population is likely related to the luminosity evolution of this parameter. It has been shown that the EW of the [O III] core component anti-correlates with $L_{5100\,\text{Å}}$, which can be regarded as a proxy of L_{bol} (Shen and Ho, 2014). Two effects might come into play. Assuming that the intrinsic $L_{[\text{O III}]}$ does not evolve significantly with L_{bol} (or z), the observed anti-correlation would be mainly driven by inclination, whereby high-L_{bol} high-z sources are preferentially observed with a face-on line of sight. Otherwise, if $L_{[\text{O III}]}$ is increasing more slowly than L_{bol} (e.g. Shen 2016), a trend of decreasing EW [O III] should be observed, as for the standard Baldwin effect (Baldwin 1977; see also Sect. 4.1 of Ueda et al. 2015 for other possible effects).

As observed for other emission lines (C IV, Hβ), generally less prominent line profiles are found in W+w objects also for the [O III] $\lambda\lambda$4959,5007 doublet (see also Green 1998). The mean values for the two subsamples are $\langle$EW [O III]$\rangle_N$=16.6±5.6 Å and $\langle$EW [O III]$\rangle_{W+w}$=4.5±1.5 Å, giving a ~2.1σ tension. In this computation I conservatively excluded from the N sample the only high-[O III] emitter, J0303−0008, whose nuclear and environmental properties have recently been investigated in Perna et al. (2023), for which inclination effects might be non negligible. The EW [O III] values of all the other sources suggest that these are likely seen at relatively low inclination instead, and hence the tentative difference between the strength of the [O III] emission in N and W+w quasars could be due to intrinsic effects. At this stage, it is therefore more informative to consider $L_{[\text{O III}]}$ rather than EW [O III]. As no systematic difference between the geometric properties (size, covering factor) or physical properties (metallicity, density) of the NLR in X-ray weak and X-ray normal quasars are expected, it can be argued that the main driver of $L_{[\text{O III}]}$ is the line emissivity (e.g. Baskin and Laor 2005b), which ultimately depends on the shape of the EUV–soft X-ray SED.

---

[5] For the SUPER sample, EW [O III] is not directly reported by the authors, so it was estimated here as $L_{[\text{O III}]}/L_{5100\,\text{Å}}$. This normalisation could produce a slightly overestimated EW [O III] in case of a steeply decreasing optical continuum. However, by assuming an average continuum slope $\alpha_\lambda = -0.42$ from VB01, normalising at 5100 Å rather than at 5007 Å has a negligible effect on EW [O III].

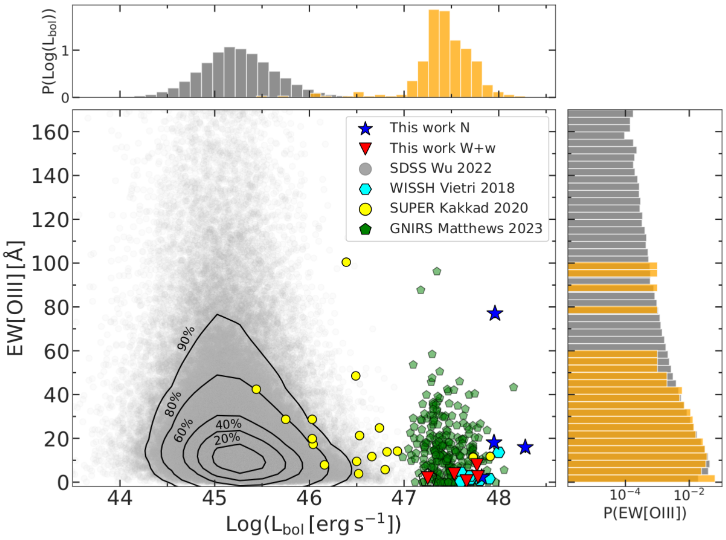

Figure 3.8. Distribution of EW [O III] of this and other literature samples, as a function of bolometric luminosity. Side panels show the probability density of the quantities represented in the plot. BAL J0945+2305 is shown as an open pentagon. All but one of these objects show low EW [O III] (<30 Å), suggesting a non-edge-on line of sight. Generally, luminous high-redshift quasars tend to cluster around low EW [O III] values.

If the range of [O III] intensities observed is caused by intrinsic differences in the unobservable portion of the SED, a correlation with the X-ray emission should be expected, as the level of the latter determines the SED steepness. Several studies have investigated the relation between [O III] and X-ray emission, finding a high degree of correlation (e.g. Mulchaey et al. 1994; Panessa et al. 2006; Meléndez et al. 2008; Ueda et al. 2015). Because they are both proxies of the intrinsic power of the central engine, L_X and $L_{[\text{O III}]}$ are naturally expected to correlate in the case of Type 1 objects, where the line of sight does not cross the dusty torus; the correlation holds also in Type 2 objects, when considering absorption–corrected L_X. In Figure 3.9 I show the relation between the hard (2–10 keV) X-ray and the [O III] luminosity of the quasars in this sample together with other reference samples (Panessa et al., 2006; Meléndez et al., 2008; Ueda et al., 2015). I also include the objects with currently available [O III] and X-ray data from Laurenti et al. (2022) and, in the high-luminosity tail, also those from the WISSH and SUPER samples. For the WISSH and the Laurenti et al. (2022) samples I also divided the sources into X-ray normal and X-ray weak according to their $\Delta\alpha_{OX}$ value, adopting a conservative threshold of $\Delta\alpha_{OX} \leq -0.3$ to define X-ray weakness. Objects whose [O III] emission is barely detectable are labelled as upper limits. This sample seems to follow the trend of less luminous objects, even though, J0303−0023, because of its very faint [O III], is slightly below the other N sources. The L_X values of J0945+2305 and J1425+5406 are labelled as upper limits, being marginally detected as stated in N19. Remarkably, despite their weak [O III] profiles, X-ray weak objects do not drop out from the main trend of the $L_{[\text{O III}]}-L_X$ relation.

I also tested, at least qualitatively, the possibility that the lower $L_{[\text{O III}]}$ in X-ray weak objects were due to dust extinction in the NLR. I did not have the possibility

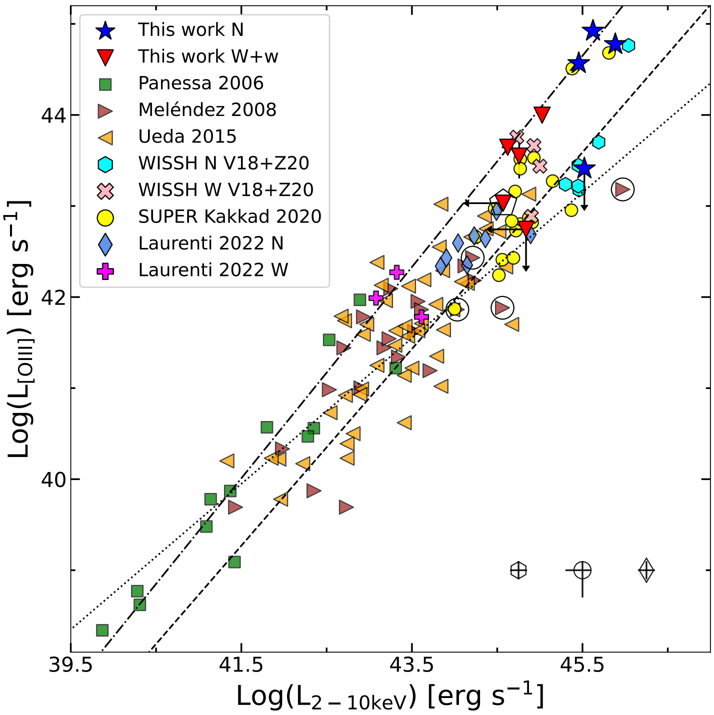

Figure 3.9. Log($L_{[\text{O III}]}$)–Log($L_{2\text{–}10\text{ keV}}$) plane. The dot-dashed, dotted, and dashed lines represent respectively the best fits for the Panessa et al. (2006), Meléndez et al. (2008), and Ueda et al. (2015) samples. Other luminous high-redshift samples with currently available [O III] and X-ray data from the WISSH (Vietri et al. 2018; Zappacosta et al. 2020) and SUPER (Kakkad et al., 2020) surveys, as well as the less luminous sample from Laurenti et al. (2022) including some X-ray weak objects, are also shown. Our objects where the [O III] is barely detectable (i.e. J0303−0023 and J1425+5406) are represented as upper limits. The circled data are defined as radio-loud by the authors. BAL J0945+2305 is shown as an open pentagon. The typical uncertainties for the WISSH, SUPER, and Laurenti et al. (2022) samples are shown at the bottom of the plot.

to use the Balmer decrement, the most straightforward way to assess local extinction, because the Hα line is not covered by the LBT spectra. I thus assumed that N and W+w quasars had intrinsically similar [O III] emission lines, but the latter subsample suffered from a greater dust extinction. Then, I considered N quasars with average [O III] emission (i.e. I excluded J0303−0023, whose emission is barely detectable, and J0304−0008, the brightest [O III] emitter) and allowed for increasing dust extinction. The detailed procedure is explained in Supplementary Material 3.7.2. Even in the case of significant reddening, E(B-V)=0.2, [O III] is still clearly detectable. A high degree of extinction is also disfavoured by the locus occupied in the $\Gamma_{1450-3000\,\text{Å}} - \Gamma_{0.3-1\,\mu\text{m}}$ plane (see Fig. 2 of L21) by the whole sample, which was selected in order to include blue unobscured quasars.

I finally note that the [O III] profile does not generally reveal signatures of strong outflows, with the only exception of J0942+0422, where a fairly broad (~1200 km s^{-1}) component is detected, blueshifted with respect to the core component by ~470 km s^{-1} (Fig. 3.2). It is possible, however, that in some cases, where the [O III] profile is weak and blended with Fe II$_{\rm opt}$, any blueshifted [O III] component resulted undetectable even if present.

3.4.4 Relation to accretion parameters

The quasars at high redshift constituting this sample were chosen so as to display a high degree of homogeneity in the UV, being very luminous with a blue spectrum, according to the cosmological sample selection criteria. It was then found that on the X-ray side the sources are far less homogeneous since the sample also includes a significant fraction of X-ray weak objects. The following analysis then focused on the spectroscopic optical-UV properties to find any evidence for differences accompanying the X-ray weakness in the *W+w* sample.

The newly estimated (and generally more reliable for 11/29 objects) BH masses, as well as the Eddington ratios, allowed us to investigate further what the key accretion parameters of the sample are, and to test the possibility that the observed differences between the two X-ray groups could be associated with their location in this parameter space. In Figure 3.10 I present the relation between the Eddington ratio and the X-ray photon index for the sample, together with other recent samples in the literature formed by both super- and sub-Eddington accretors. Although with a huge scatter, a steeper Γ is observed as $\lambda_{\rm Edd}$ increases. The Spearman's rank test for the $z \sim 3$ sample, together with other non-weak sources (shown in Fig. 3.10), produced a correlation index $r_S = 0.47$, lower than the values reported by Liu et al. (2021): $r_S = 0.72$ with a p-value= 1.27×10^{-8} for their full sample, and $r_S = 0.60$ with a p-value= 0.004 for the super-Eddington subsample, which represents the tightest correlation found so far for highly accreting sources.

I performed a linear regression using the module EMCEE allowing for intrinsic dispersion, removing known X-ray weak objects and sources whose Γ was fixed in the X-ray spectral analysis. The former were removed as their coronal emission is possibly experiencing a non-standard phase; the latter were removed because the poor quality of the data did not allow a simultaneous estimate of both Γ and $N_{\rm H}$. The resulting slope is $\beta = 0.16 \pm 0.03$, somewhat flatter than other previous findings ($\beta = 0.31 \pm 0.01$, Shemmer et al. 2008; $\beta = 0.31 \pm 0.06$, Risaliti et al. 2009; $\beta = 0.57 \pm 0.08$, Jin et al. 2012; $\beta = 0.32 \pm 0.05$, Brightman et al. 2013), but fully consistent with Trakhtenbrot et al. (2017), who report $\beta = 0.17 \pm 0.04$ for hard X-ray selected AGN in the *Swift*/BAT spectroscopic survey (BASS).

For 11/29 objects the UV–optical analysis yielded more robust estimates of the BH masses based on Hβ and/or Mg II. I did not find any statistically significant difference in the average M$_{\rm BH}$ between *N* and *W+w* sources: the mean BH mass for the *N* group is $\langle \log({\rm M_{BH}/M_\odot}) \rangle_{\rm N} = 9.7 \pm 0.1$, and $\langle \log({\rm M_{BH}/M_\odot}) \rangle_{\rm W+w} = 9.8 \pm 0.1$ for the *W+w* group. As this sample was selected to have high and uniform bolometric luminosity (with a standard deviation of ~0.1 dex), and because the BH masses are nearly identical, it is also natural to expect that the Eddington ratios should not differ significantly. The mean (median) values are $\langle \lambda_{\rm Edd} \rangle_N = 1.6 \pm 0.4$ (0.9) and $\langle \lambda_{\rm Edd} \rangle_{W+w} = 0.5 \pm 0.1$ (0.4). The slight difference between the mean (median) values is likely due to the marginally higher bolometric luminosity of the *N* sample, $\langle \log({\rm L_{bol}/erg\,s^{-1}} \rangle_{\rm N} = 47.84 \pm 0.04$, with respect to the *W+w* sample,

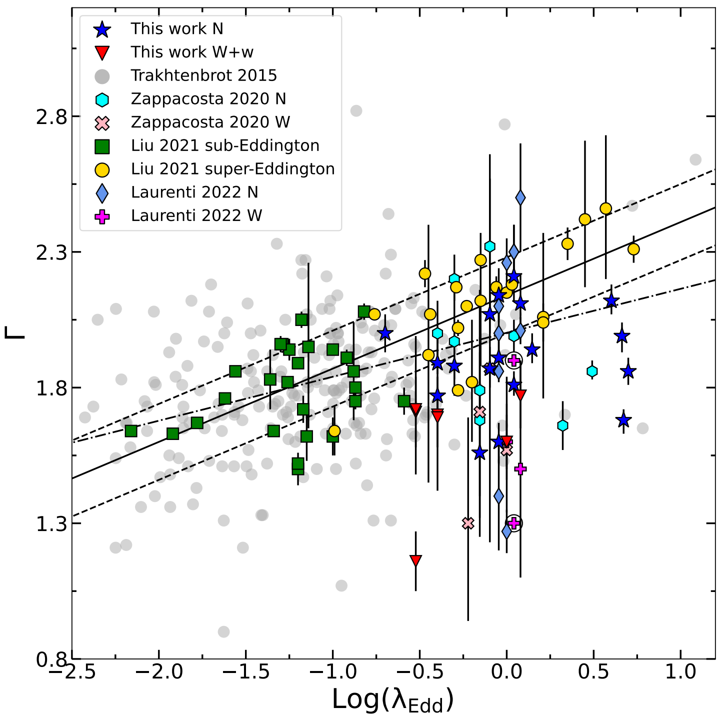

Figure 3.10. Γ–$\log(\lambda_{\rm Edd})$ plane. Highly accreting samples are labelled as indicated in the legend. Circled sources have a fixed Γ in their X-ray analysis. The black continuous line represents the best fit from Liu et al. (2021), which produced a slope $\beta = 0.27 \pm 0.04$, while the dashed line represents the 1σ dispersion. The dot-dashed line is the best fit including all the samples (except the sources from Trakhtenbrot et al. 2017, for which there was no information about possible X-ray weak sources), which results in a flatter slope $\beta = 0.16 \pm 0.03$.

$\langle\log(\mathrm{L_{bol}}/\mathrm{erg\,s^{-1}}\rangle_{\mathrm{W+w}} = 47.58 \pm 0.06$.

The higher fraction of X-ray weak objects reported in high-$\lambda_{\rm Edd}$ quasar samples (N19; Zappacosta et al. 2020; Laurenti et al. 2022) compared to the general AGN population (Pu et al., 2020) hints at some modification of the interplay between the corona and the disc emission in the high-accretion regime. The strength of the emission from the corona with respect to the disc can be roughly estimated through the indicator $\alpha_{\rm OX}$. In Figure 3.11 I show $\alpha_{\rm OX}$ as a function of the Eddington ratio for different AGN samples. The resulting anti-correlation (Lusso et al. 2010; but see also Section 4.2 in Liu et al. 2021, and references therein) displays a rather large spread since sources with similar $\lambda_{\rm Edd}$ can span several orders of magnitude in terms of bolometric luminosity (which ultimately governs the SED steepness).

Nonetheless, the relation should naturally tighten including the BH mass into the parameter space: for a given $\lambda_{\rm Edd}$, the higher the $\mathrm{M_{BH}}$, the higher the $\mathrm{L_{bol}}$. Liu et al. (2021) proposed that the scatter of the relation is due to a non-edge-on view on a more fundamental plane in the $\alpha_{\rm OX} - \lambda_{\rm Edd} - \mathrm{M_{BH}}$ space. In Figure 3.12, all the Type 1 AGN samples shown in Figure 3.11 are superimposed on the relation found by Liu et al. (2021), which include the extreme BH hole mass tail of the quasar population at high redshift. Remarkably, the *N* quasars sit nicely on the

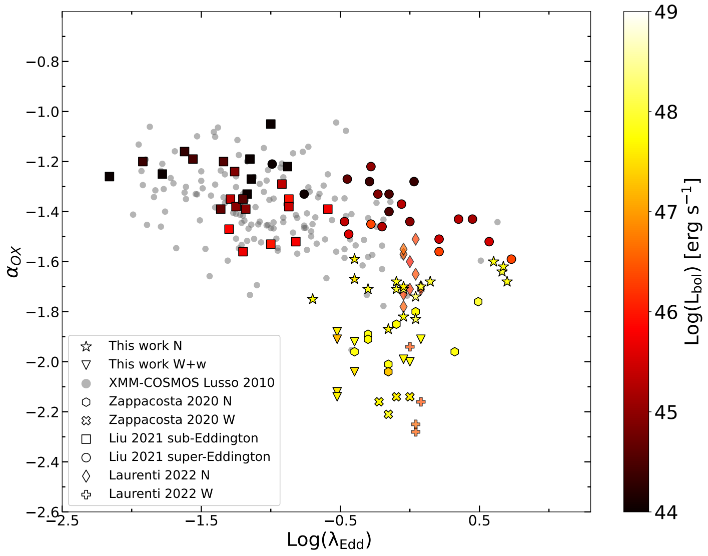

Figure 3.11. $\alpha_{\rm OX}$ against $\log(\lambda_{\rm Edd})$. The different symbols refer to the different samples (see legend). The bolometric luminosity is colour-coded and, for a fixed Eddington ratio value, spans 3–4 orders of magnitude.

extrapolation of the best-fit regression line, whereas the *W+w* group drops far below, exhibiting lower $\alpha_{\rm OX}$ than the other sources in the same $\lambda_{\rm Edd}$–$M_{\rm BH}$ domain. The $\alpha_{\rm OX}$ parameter is still very steep, also for other groups of very luminous quasars such as those from Zappacosta et al. (2020) and Laurenti et al. (2022), but also the bulk of X-ray normal sources of these samples is slightly below the prediction (by ~ -0.2). Very luminous sources could behave differently from the expectations, suggesting that, if a universal relation existed, it could be steeper, or that the high and low ends of the BH mass–Eddington ratio distribution cannot be jointly described by a linear relation with $\alpha_{\rm OX}$. The sources of Liu et al. (2021), whose fit I extrapolated, were selected with criteria similar to ours, being radio-quiet, non-BAL, and with good-quality X-ray data ($S/N > 6$). However, no criteria about their optical-UV emission (e.g. luminosity, photometric indices) were applied. Moreover, in 7/48 objects with multiple X-ray data available, the authors chose the high-flux objects, and this choice could, to some extent, affect the comparison. Furthermore, the sources analysed in Zappacosta et al. (2020) were chosen to study the impact of outflows driven by hyper-luminous quasars. It is thus possible that the mismatch between the selection criteria can also reduce the general agreement of the results. Overall, a better sampling of the very luminous, highly accreting side of the distribution will be key to assessing whether the accretion mechanism is the same on very different scales of its governing parameters.

3.5 Discussion of the results

As a general consideration, two different flavours of X-ray weakness exist, as it is possible to find both intrinsic and apparent X-ray weak sources. The former are likely associated with the physics of the corona, which is not efficiently producing

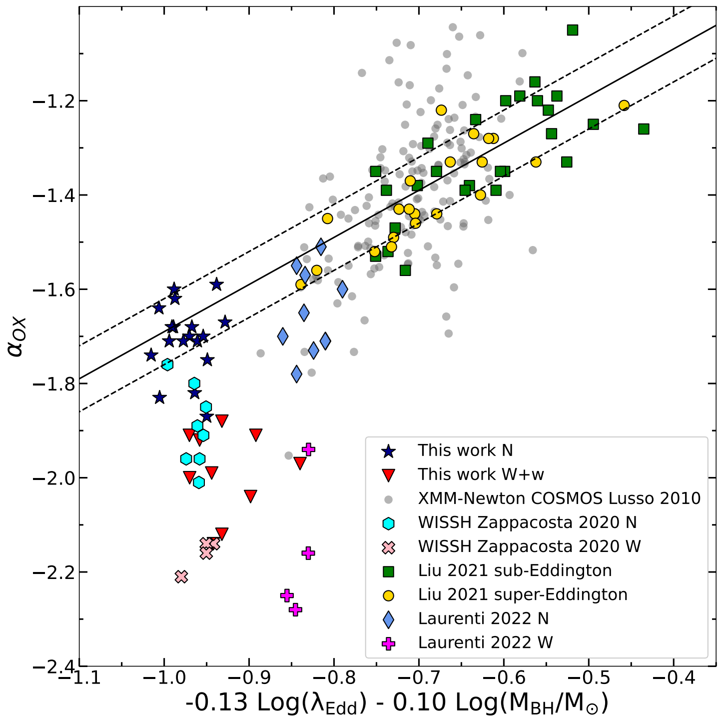

Figure 3.12. Edge-on view on the $\alpha_{\rm OX} - \lambda_{\rm Edd} - \rm M_{BH}$ space. The various samples are listed in the legend. The solid line is the best regression as found by Liu et al. (2021), while the dashed lines represent the 1σ dispersion. Quasars with high BH masses and high accretion rates extend the range of the relation. The bulk of X-ray normal sources follow the extrapolation of the relation calibrated on less luminous sources at lower redshifts.

the normal X-ray emission, and a wide range of weakness factors and photon indices are produced. PHL 1811 is the most extreme case of the first kind, given its very steep photon index $2.0 < \Gamma < 2.6$ (but see Wang et al. 2022a), the variability, and the ~2 orders of magnitude weakness. The latter sources are instead related to some kind of absorption (e.g. slim disc, failed and/or clumpy wind, warm absorber) along the line of sight. The objects described here do not clearly fit in either of these two classes, being in some way intermediate between them, showing flatter ($\Gamma \lesssim 1.7$) spectra in the absence of clear absorption and moderate weakness factors. This is why it is important to understand their prevalence among the AGN population and their underlying physics.

The analysis of the X-ray data in N19 revealed an anomalously high fraction (≈25%) of X-ray weak ($\gtrsim$ 3–10 times fainter than expected) objects. Although in some cases (the few marginal detections, plus J1201+01 and J1459+0024) the quality of the data is not good enough to completely rule out some level of absorption, in general, a column density exceeding $N_H(z) > 3 \times 10^{22}$ cm^{-2} can be ruled out. This is a consequence of the lack of any cutoff around 1 keV associated with X-ray absorption.

In L21, it is reported a correlation between X-ray and C IV luminosity, which holds for X-ray normal objects over the whole range probed by an extended control sample ($10^{43.5} - 10^{45.5}$ erg s^{-1} in $L_{2\,\rm keV}$ and $10^{43} - 10^{46}$ erg s^{-1} in $L_{\rm C\,IV}$), whereas

X-ray weak sources lie below that main sequence. In absolute terms, X-ray weak objects present more luminous C IV lines than expected for quasars with similar X-ray luminosity. Even so, X-ray weakness might lead to a less efficient population of the excited level (~8 eV above the ground state) that is collisionally excited because of the X-ray heating of the gas. Such a relation (holding for the N sources) is probably a by-product of the more general $\alpha_{\rm OX} - L_{\rm UV}$ relation.

With respect to N quasars, $W + w$ quasars do not show strikingly different blueshifts of the C IV line, but on average shallower (i.e. broader and less prominent) line profiles. This could be due to two reasons (at least): (i) fast, mostly equatorial outflows are present among X-ray weak quasars, but the low-inclined line of sight offsets their observational footprints, and (ii) the difference in C IV emission between N and W+w objects is caused by some mechanism affecting the region where the photons producing the C IV come from. By analysing ~190,000 spectra from the seventeenth SDSS data release, Temple et al. (2023) found that high ($\geq$ 1,000 km s^{-1}) median C IV blueshifts are observed only in quasars with high SMBH masses ($\rm M_{BH} \geq 10^9\, M_\odot$) and high Eddington ratios ($\lambda_{\rm Edd} \geq 0.2$). The $z \sim 3$ sample analysed here fulfils both requirements of high BH masses and high Eddington ratios, so all the sources could be, in principle, in the outflow phase. The fact that C IV blueshifts are observed around or slightly less than 1,000 km s^{-1}, on average, can be explained as a projection effect whereby mostly equatorial winds are observed under low inclination angles. In this framework the fraction of X-ray weak objects could be related to the wind duty cycle (e.g. Fiore et al. 2023), which is otherwise poorly known. it is possible to set a lower limit to the wind persistence based on the concomitant [O III] weakness. Assuming the relation for the single-zone [O III]-emitting region described in Baskin and Laor (2005b), which is $R_{\rm NLR} = 40\,(\lambda L_\lambda/10^{44})^{0.45}$ pc, where $\lambda L_\lambda \sim 10^{47}$ erg s^{-1} for these objects, the size of the NLR is ~1 kpc. Hence, it would take $t \sim R_{\rm NLR}/c$ ~3000 yr for the NLR to respond to changes in the nuclear activity. Considering that the longer light-travel time within the NLR would dilute any more rapid nuclear flickering, the wind lifetime should be at least $\approx 10^4$ yr.

In addition, at least qualitatively, the X-ray normal and weak UV stacks in the top panel of Fig. 7 in L21, are remarkably similar to the C IV core and wind-dominated stacks depicted in Fig. 5 of Temple et al. (2021). In particular, the N (W+w) stack is more similar to the C IV core-dominated (wind-dominated) one. The W+w and wind-dominated stacks share the broader and shallower line profile and the flatter continuum, although the latter spectrum exhibits more extreme properties in terms of lower line equivalent width and higher offset velocity than that described here.

In principle, the lack of seed photons causing the lower intensity of the C IV emission could be due to some kind of shielding triggered by the high-accretion regime: a puffed-up disc (e.g. Luo et al. 2015) could prevent ionising photons from reaching the BLR and intercept part of the X-ray emission, causing absorption along the line of sight. According to this model, the line of sight to these sources should cross the absorber, thus favouring a more *edge-on* geometry (still preserving the Type 1 nature of these AGN). Considering the thickness of the disc bulge and its density, it would be expected to detect absorption in the X-rays well in excess of $N_{\rm H} \gtrsim 10^{23}$ cm^{-2}, but the sample does not fulfill this condition. In the few cases where it is not possible to completely rule out absorption, due to the quality of the data, it is possible that complex absorption from the winds launched in these sources plays a role in producing X-ray weakness (e.g. Jin et al. 2023), thus linking X-ray and line weakness. Yet, distinguishing between these alternative scenarios is extremely difficult without high quality X-ray data and (nearly) simultaneous UV-optical observations.

In Section 3.4.2 I reported higher values of EW Hβ for the X-ray normal sources with respect to the weak ones. Interestingly, other samples containing X-ray weak sources with available optical data exhibit a similar behaviour. The average values for N and W objects in the WISSH sample described in Vietri et al. (2018) are $\langle$EW H$\beta\rangle_N$=62±7 Å and $\langle$EW H$\beta\rangle_W$=47±7 Å, different at the ~1.6σ level. A statistically more significant difference is found for the objects analysed in Laurenti et al. (2022), for which the SDSS data from the Wu and Shen (2022) catalogue yield the values $\langle$EW H$\beta\rangle_N$=51±6 Å and $\langle$EW H$\beta\rangle_W$=25±4 Å, giving a ~3.7σ tension.[6]

I thoroughly discussed the [O III] properties and the relation between the [O III] and X-ray emission in the sample in Section 3.4.3. The low (<30 Å) EW suggests that inclination does not play a major role in the findings discussed here, as it is generally regarded to be significant for EW [O III] > 30 Å. Highly inclined ($\theta > 60°$) lines of sight are also disfavoured by a luminosity argument. Assuming, for instance, a 75° inclination, which might still not intercept the dusty torus at these luminosities (e.g. Sazonov et al. 2015), the geometric correction $1/\cos\theta$ would yield a factor of $\simeq 4$, shifting the average $\log(\mathrm{L_{bol}/erg\,s^{-1}})$ of the $z \sim 3$ quasars upwards by 0.6 dex to ~48.4, when only one source in the entire Wu and Shen (2022) catalogue has a higher luminosity.

Weaker [O III] profiles, as discussed in Section 3.4.3, are generally found with increasing $\mathrm{L_{bol}}$, which is likely due to an intrinsic decrease in the $L_{[\mathrm{O\,III}]}$ with respect to the continuum and, to a lesser extent, to an inclination effect whereby more luminous object are preferentially observed at smaller polar angles. Finally, the possibility of a reduced [O III] emission because of extinction in the NLR of X-ray weak sources is disfavoured (see Supplementary Material 3.7.2), and would call for an unknown causal connection between very different scales (i.e. $\sim 10^{-3}$ and 10^{3} pc).

Another notable feature found in this analysis is the trend of higher EW Fe II$_{\mathrm{UV}}$ and Fe II/Mg II ratio for X-ray weak sources, in line with the expectations for prototypical X-ray weak quasars (see e.g. the analyses of PHL 1811 by Leighly et al. 2007a,b). These, and some other features characterizing X-ray weak objects, are consistent with the trends expected in the 4D Eigenvector 1 (4DE1; Sulentic et al. 2000b). The transition between the so-called populations B and A (mainly driven by accretion rate and orientation, see e.g. Shen and Ho 2014) happens with the increase of the optical Fe emission, the offset velocity of the C IV emission line, and a decrease of the equivalent of the width of EW C IV and EW [O III] emission lines (see respectively supplementary Figure E4 and Figure 1 in main text in Shen and Ho 2014). The exact position of these objects along the 4DE1 main sequence is unclear. In particular, it is not possible to evaluate the canonical estimator

---

[6] In both of these samples the average EW Hβ is smaller than for the sources described here, for which the line falls close to the edge of the K_{S} spectra and the absolute value of its equivalent width strongly depends on the exact placement of the continuum and on the adopted iron template. However, the relative difference between N and W+w objects goes in the same direction in all three samples.

R_{Fe} (R_{Fe}=EW Fe II$_{\mathrm{opt}}$/EW Hβ) as the 4434–4684 Å optical Fe complex falls just bluewards of the K_{S} spectra. Even assuming the 4900–5300 Å interval as a proxy of the canonical one, the two samples are not segregated in the FWHM Hβ–R_{Fe} plane. Considering their uncertain position along the R_{Fe} axis and the homogeneity of these sources in terms of accretion rate and orientation, which are believed to be the main drivers along the sequence, it is not straightforward to understand the differences between the N and W+w sources within the 4DE1 formalism.

This notwithstanding, it is necessary an attempt to piece together all the available observational evidence in order to find a mechanism capable of explaining the following results on the W+w sources: i) X-ray weakness in the absence of clear X-ray absorption (which still cannot be ruled out in some objects); ii) the generally weaker and shallower line profile of C IV (and optical lines such as Hβ and [O III]), although still more luminous than expected for normal quasars with similar X-ray luminosity; iii) the tentative trend of higher Fe II/Mg II.

The generally larger incidence of X-ray weak objects in highly accreting samples also deserves some further considerations. Several studies have recently pointed out that the fraction of X-ray weak quasars could be enhanced when the objects are accreting at near-Eddington rates. Zappacosta et al. (2020) found that about 40% of their sources (belonging to the WISSH sample) have $\Delta\alpha_{\mathrm{OX}} < -0.3$ and also display C IV shifts of over 5,000 km s^{-1}, but the column density of the absorber is generally (in three out of four objects) below 10^{23} cm^{-2}. The same trend at lower luminosity ($\mathrm{L_{bol}} = 10^{46.0} - 10^{46.6}$ erg s^{-1}) and redshift ($z \simeq$0.4–0.7) is observed in the sample analysed by Laurenti et al. (2022), where ~30% of their objects exhibit X-ray weakness without requiring absorption. Conversely, the high-λ_{Edd} sample of Liu et al. (2021) does not contain any X-ray weak object as the lowest value of $\Delta\alpha_{\mathrm{OX}}$ is −0.14. This sample is made of less luminous ($\mathrm{L_{bol}} < 10^{46.3}$ erg s^{-1}) low-redshift ($z \leq 0.25$) quasars. It is worth noting that there the authors selected the sample discarding, among the other criteria, X-ray and UV–optical absorbed sources, and choosing the X-ray high-flux state in case of multiple observations. The latter selection criterion could partially explain the lack of X-ray weak objects.

It is also possible that variability is enhanced in highly accreting objects (e.g. Ni et al. 2020), and some of the observed weakness could be due to negative fluctuations. However, all the objects with multiple observations (see Sect. 5.1 and Table 3 in N19) do not show transitions between the W and N states. Another example of a persistent X-ray weak condition is shown in Laurenti et al. (2022): J0300−08 was targeted in 2011 by the *Neil Gehrels Swift Observatory* (Gehrels et al., 2004), then observed by *XMM-Newton* in 2018 and again by *Swift* in 2021. All these observations (*Swift* only provided 3σ upper limits) reported an X-ray flux below the expectations. Generally speaking, it is possible that a high accretion rate can enhance the possibility of finding a quasar in an X-ray weak state, and can provide clues about the possible underlying mechanism (e.g. a shielding wind, a photon-trapping disc, a puffed-up slim disc).

Putting together all the pieces of information, the best phenomenological guess is represented by the sketch in Figure 3.13. Specifically, a powerful outflowing phase depletes the inner region of the accretion disc, causing a dearth of the seed UV radiation feeding the coronal X-ray emission, while part of the UV radiation is powering the wind. The change in the local accretion rate can have little impact on

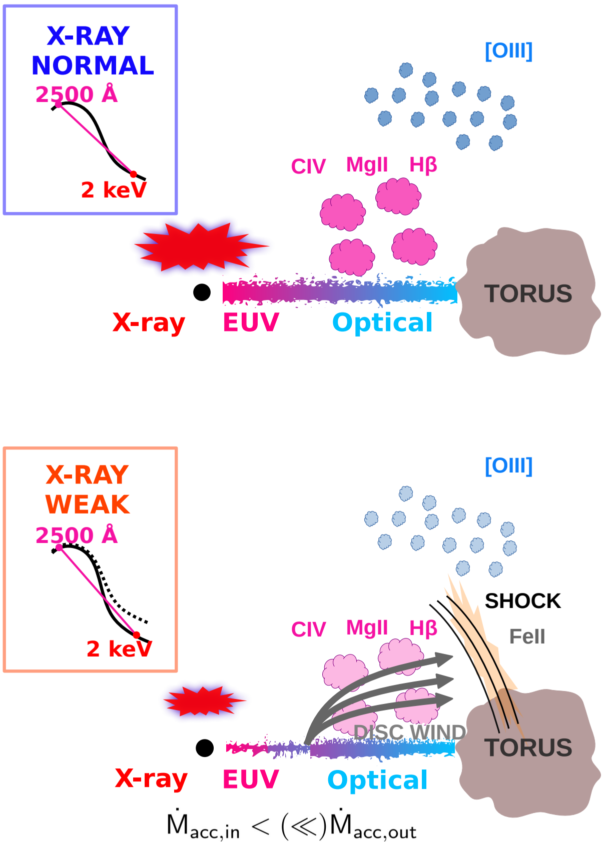

Figure 3.13. Sketch of the observational features of X-ray normal (top) and weak (bottom) quasars. In the weak case a powerful wind affects the X-ray coronal emission. The outflowing phase depletes the UV-radiating inner disc, and the Comptonisation process falls short of seed radiation. The resulting X-ray flux is thus reduced without the need for absorption. Shocks at the interface between the disc wind and the BLR gas can enhance the Fe II/Mg II ratio in X-ray weak sources. The observer is assumed to be on top, but a rather wide range of viewing angles remains compatible with the Type 1 nature of these sources. Since the line of sight is not expected to be significantly inclined with respect to the disc axis, as suggested by the very high bolometric luminosity of the sample and confirmed by the low EW [O III], outflow footprints like absorption dips or strong blue wings in C IV could be hidden. On larger scales, the [O III] luminosity mimics the X-ray behaviour, being lower in the X-ray weak sample, but fully consistent with the high-luminosity extrapolation of the $L_{[\mathrm{O\,III}]}$–L_{X} relation. The weaker line emission in X-ray weak sources, here depicted by more tenuous colours, is associated with the difference in the SED shape, as systematic differences between the BLR/NLR in X-ray weak and normal sources are not expected. This a mechanism is more likely to be found in highly accreting sources, where conditions are conducive to the launch of powerful winds, and hence the enhanced X-ray weak fraction in high λ_{Edd} objects.

the near- to far-UV SED, but a more dramatic effect on the extreme UV (inaccessible to observations) and X-ray emission. If the corona is starved and intrinsically weak, X-ray weakness can be explained without invoking any shielding, which, otherwise, would require moderate to high inclination. The *low-inclination* perspective is in line with the observed high luminosity, the mild blueshift of the C IV line (due to the mostly equatorial propagation of radiatively driven winds; e.g. Proga 2003), and the small values of EW [O III] (which, however, also depend on the SED shape).

Despite the reduced X-ray heating, the C IV emission is weaker but not suppressed since an ample reservoir of ionising photons is still present at high luminosities. Moreover, a crucial contribution to the strength of the C IV line also comes from the X-ray heating of the gas, which, by means of electron–ion collisions, populates the C IV excited state. Krolik and Kallman (1988) determined the energy of the continuum photons mainly contributing to the line emission for the most important emission lines, based on different continuum assumptions between ~0.01–2 keV. Both C IV and Hβ rely on the Lyman continuum photons between 13.6–24.5 eV, and also on the continuum intensity at 300–400 eV and 300–800 eV, respectively, which is likely suppressed in the SED of X-ray weak objects, producing the generally lower equivalent widths observed in such sources.

On the other hand, the higher incidence of Fe II/Mg II is rather puzzling. A high value of Fe II/Mg II ~ 15.5 (Leighly et al. 2007a,b) is observed in the prototypical intrinsically X-ray weak quasar PHL 1811, but in that case it is accompanied by a soft ($\Gamma = 2.3 \pm 0.1$) X-ray emission, which not reported here for the $W{+}w$ sources. Weakness in the sample is accompanied by flatter photon indices than the average $\Gamma = 1.9$ (Piconcelli et al., 2005; Bianchi et al., 2009) found in the unobscured quasar population. Following Leighly et al. (2007b, see their Figure 24 and the relative SED in Figure 11 in Casebeer et al. 2006), increasingly EUV-deficient SEDs would produce higher values of both Fe II/Mg II and Fe $\mathrm{II_{UV}}$/Fe $\mathrm{II_{opt}}$. In this sample, N objects display an average Fe II/Mg II value of 4.4 for N and 8.4 for $W{+}w$, which is consistent with a softer EUV SED for X-ray weak with respect to X-ray normal objects. In addition the average values for Fe $\mathrm{II_{UV}}$/Fe $\mathrm{II_{opt}}$ are qualitatively in line with the predictions in Leighly et al. (2007b), with 13 ± 4 for the N and 26 ± 9 for the $W{+}w$ subsample (see Sect. 3.4.2).

There have been claims (e.g. Sameshima et al. 2011, Temple et al. 2020) that the Fe II emission could be enhanced by the presence of shocks and microturbulence, as already noted in Baldwin et al. (2004), which, in this case, could be possibly linked to the outflowing phase. Shocks from the disc wind could thus facilitate the formation of the Fe II pseudo continuum in parallel to the main ionisation process due to the coronal emission. This could link, at least phenomenologically, the X-ray weakness to the higher Fe $\mathrm{II_{UV}}$/Mg II that observed. Further analyses are needed to thoroughly investigate this suggestion: collecting simultaneous and gapless spectra from the rest frame optical to the UV (a task currently possible for the $z \sim 3$ sample with a ground-based spectrograph such as VLT X-SHOOTER) would definitely improve the reliability of the analysis and our understanding of the impact on the line properties of the different regions of the SED in X-ray weak and normal objects.

3.6 Summary and conclusions

In this part of my thesis, I presented the optical and middle UV analysis of the $z \sim 3$ quasars whose X-ray and far-UV spectral properties were described, respectively, in Nardini et al. (2019b) and in Lusso et al. (2021). The main goal pursued in this work was to investigate additional spectral features that can distinguish X-ray weak (*W+w*) from X-ray normal (*N*) quasars. To this end, employed dedicated observations at the Large Binocular Telescope in both the rest frame UV and optical bands, respectively observed in the zJ and K_S bands between 2018 and 2021.

The main findings for this part of my thesis are listed below:

- I confirmed, by combining C IV, Mg II, and Hβ virial mass estimates, that the black holes hosted in these high-redshift quasars belong to the very high-mass tail of the BH mass distribution. Their masses had already grown up to $\sim 10^9 - 10^{10}\ M_\odot$ when the Universe was about 2 Gyr old. Given the bolometric luminosity estimated from the 1350 Å monochromatic flux, I derived the Eddington ratio for each object, confirming that the whole sample is made of highly accreting quasars ($\lambda_{\rm Edd} \sim 0.1$–5, with a median of 0.9).

- By fixing the slope of the continuum in order to match that of the SDSS counterpart, I found that *W+w* objects generally exhibit more prominent Fe II$_{\rm UV}$ emission and, in turn, higher Fe II/Mg II ratios with respect to *N* objects. Wind-related microturbulence and shocks in outflows could enhance the Fe II production in X-ray weak sources.

- Comparing the estimates of the Fe II/Mg II ratios of the *N* objects with other literature samples, I found that they are in line with the expectations for quasars at similar redshifts. I also confirmed that there is no evidence for an evolving ratio across cosmic time up to $z \sim 6.5$, pointing towards a prior chemical enrichment of the BLRs.

- The EW [O III] emission is generally low (< 20 Å) in all but one of these objects. This suggests that inclination effects do not play a major role, as sources observed under high viewing angles usually display EW [O III] $\gtrsim$ 30 Å. The lower EW of several emission lines (C IV, Hβ, [O III]) in X-ray weak quasars could be related to the decrease of EUV photons responsible for the line production. The $L_{\rm [O\,III]}$ of the X-ray weak and normal quasars are consistent with the high-luminosity extrapolation of the $L_{\rm [O\,III]}$–$L_{2-10\,\rm keV}$ relation from other samples in literature.

- The presence of a mostly equatorial disc wind could explain all the observational features reported so far on this sample. Part of the UV radiation would not be reprocessed in the X-ray corona causing intrinsic X-ray weakness (i.e. not due to absorption). A modest inclination of the line of sight to the disc is consistent with the EW [O III] values found and with the huge bolometric luminosities. In this case, the typical footprints of an outflow, such as a prominent blue wing or absorption dips in the C IV profile, might be missed. A higher Fe II$_{\rm UV}$ emission in X-ray weak quasars could be attributed to microturbulence and shocked regions at the interface between the outflow and the BLR medium.

This part of my work demonstrated that X-ray weak and X-ray normal quasars also show different trends in their emission-line properties. Nearly simultaneous observations at rest frame optical–UV wavelengths and in X-rays are key to constraining the broadband ionising continuum in both populations. In the future, the results of this kind of analysis need to be confirmed on statistically larger quasar samples, possibly extending at both lower and higher redshifts to better study the evolution of the X-ray weakness fraction and of the related emission-line properties.

3.7 Supplementary Material

3.7.1 Possible systematics on Fe II emission, and a consistency check

It is important to explore, at least qualitatively, the possible systematic differences on the estimate of the Fe II_{UV} emission with other samples in literature. A first issue to be taken into account is the fact that most results are obtained using an iron emission template (Vestergaard and Wilkes, 2001; Tsuzuki et al., 2006) or some modified version of it, whereas I modelled the Fe pseudo-continuum as the emission of several synthetic BLRs with different ionisation, metallicity and microturbulence parameters. Different fitting approaches may also affect the results. Fixing the spectral slope provides a decent baseline to the iron emission in the majority of the cases, but the modelling of the overall emission is not always optimal, and in one case (J1111+2437) the slope is likely too flat to adequately reproduce the data. A detailed study of how these systematics can affect the results can also be found in Section 5.3 of Shin et al. (2019).

Ideally, a larger spectral range to fit the continuum would be needed, pivoting on two (or more) continuum windows and covering the interval 2200–3090 Å, in order to have both a more robust determination of the continuum and a direct estimate of the whole Fe II_{ii} emission without relying on extrapolations at shorter wavelengths. Whilst the first of these two problems is present in the sample, the second should be a minor issue as the extrapolation on the blue side is generally limited to an interval ~100 Å wide, with the bulk of the iron emission covered by the observations. Although the issues mentioned above could affect a fair comparison with the other literature samples, the difference between the average values for the N and the W+w groups should not be influenced by these possible systematics, as both the N and the W+w average would eventually be affected in the same way.

I performed a consistency check of the capability of my fitting technique to reproduce the iron emission. I selected a sample of 100 quasars present in the SDSS DR17 catalogue whose spectra had already been analysed in Wu and Shen (2022), and I performed the fit again, focusing on a reliable reproduction of the iron pseudo-continuum. To this end, I applied some filters in order to build an ad hoc sample: since EW Fe II in the Wu and Shen (2022) catalogue is evaluated between 2250–2650 Å I required this wavelength interval to be fully present in all the spectra, together with the Mg II and the C IV emission lines and the nearby continuum windows for a robust estimate of the continuum. I also required that both the emission lines satisfied the quality cuts suggested by the authors (see their Table 2 and relative discussion in Section 4), namely $F_{\text{line}}/\sigma_{F_{\text{line}}} > 2$, $38 < \log{(L_{\text{line}}/\text{erg}\,\text{s}^{-1})} < 48$ and $N_{\text{pix,line}\,\text{complex}} > 0.5 \times N_{\text{pix,line}\,\text{complex}\,\text{max}}$, which sets the minimum fraction of available pixels for the fit. Moreover, I filtered out sources affected by BALs by imposing the BAL_PROB field equal to 0, since these features could hamper a proper determination of the continuum. Finally, I also required a detected iron emission by requiring FEII_UV_EW>0. I sorted out the sources according to their SNR_MEDIAN_ALL parameter, and selected 100 of the best-quality spectra, avoiding objects affected by bad pixels and spurious features. Successively, I performed a one-by-one analysis, fitting each of them, adopting the same double-Gaussian (1 broad, 1 narrow) deconvolution adopted in Wu and Shen (2022), but using two sets of the iron templates used here. After a careful visual inspection of the results, I estimated the EW Fe II for each object, and compared it against the catalogue values. The distribution of the relative differences between these estimates and the catalogue values $\Delta\mathrm{Fe\,II}=(\mathrm{EW\,Fe\,II_{ours}}-\mathrm{EW\,Fe\,II_{catalogue}})/\mathrm{EW\,Fe\,II_{catalogue}}$ is illustrated in Fig. 3.14. The offset of the distribution is minimal, $\langle\Delta(\mathrm{Fe\,II})\rangle=0.002$, and most of the sample (95%) is consistent within a factor of ~2 with the catalogue estimates. Even in the case of strong iron emission both the continuum and the Fe II profile are well reproduced. This check led to some considerations. First, despite some scatter, in general there is not a strong systematic offset between my estimates and the reference values This points to the fact that using the region including the C IV line and its neighbouring continuum windows to estimate the continuum power law produces reliable results also in the Mg II region. Second, it is possible to think of the dispersion of the residuals as a crude estimate of the uncertainty that one might get when comparing the Fe II/Mg II ratios estimated here against those evaluated adopting other templates. Third, the good reproduction of the iron emission, even in the case of high EW Fe II, confirms that the analysis described here is capable of accurately sampling even the high-equivalent width tail of the EW Fe II distribution.

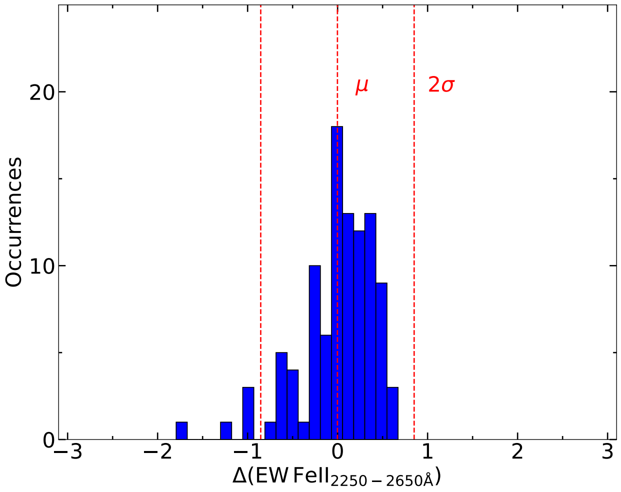

Figure 3.14. Distribution of residuals between the EW Fe II estimated according to the methods explained here and catalogue values for the SDSS control sample.

3.7.2 A check on [O III] extinction

I checked for the presence of dust extinction affecting the [O III] emission in X-ray weak quasars by applying increasing reddening to the [O III] emission of X-ray normal quasars. If the dearth of [O III] emission in *W+w* quasars were not intrinsic, but instead due to extinction, the average line profile of *N* quasars, once reddened, would be similar to the *W+w* profile. To rule out this possibility, I performed the following

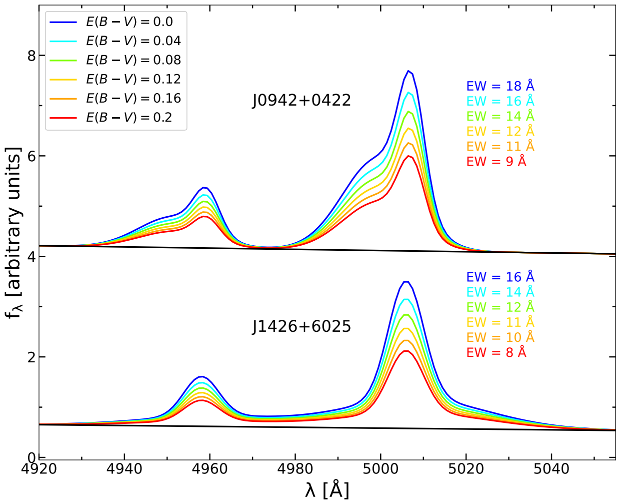

Figure 3.15. [O III] region of J0942+0422 and J1426+6025 reddened according to different E(B-V) values (see colour-coding in legend). All the spectra are normalised by the $f_{5100\text{Å}}$ of the continuum. The spectra of J0942+0422 were shifted for visualisation purposes.

exercise: adopting the best fit model for the [O III] emission, I reddened the line profile with increasing values of E(B-V) and evaluated at each step the EW of the line, checking whether this was compatible with the average EW [O III] for X-ray weak sources. To this end, I only considered the N quasars with average emission, excluding J0303−0023, whose [O III] is barely detectable, and J0304−0008 whose [O III] is the brightest. I assumed the extinction curve from Gordon et al. (2016) available in the *dust_extinction* package of the Astropy software (Robitaille et al. 2013), adopting an absolute to selective extinction ratio $R_V = A_V/E(B-V) = 3.1$ and choosing a SMC-like extinction curve. I then corrected the rest frame 4900–5200 Å emission for increasing values of extinction E(B-V) from 0 (unobscured) to 0.2 (reddened), which is twice the value adopted for the selection of blue continuum emission for a standard quasar SED (Richards et al., 2006), with steps of $\Delta E(B-V) = 0.02$. The results of this procedure are shown in Fig. 3.15. Even in the case of significant reddening the [O III] profile is not suppressed to the level observed in the *W+w* subsample, and the EW [O III] of the reddened spectra are still well above the median value for the X-ray weak sample (2.4 Å). It is thus credible that the [O III] emission of X-ray weak quasars is unlikely to be affected by extinction.

Chapter 4

The evolution of NIR properties in blue quasars

4.1 Outline

A fundamental ingredient in the Unified Model of AGN is the obscuring torus, whose innermost, hottest region dominates the near infrared (NIR) emission. Characterising the change in the torus properties and its interplay with the main AGN emission is key for our understanding of AGN physics, evolution and classification. Its covering factor (CF) is largely responsible for the classification of AGN on the basis of the detection of broad emission lines. It is still not clear whether the torus properties evolve over time and how they relate with the accretion parameters of the nucleus. In this part of my thesis, I aim at investigating the evolution of the NIR properties with the redshift and the bolometric luminosity of the AGN. To this end, I assembled a large dataset of ~36,000 Type 1 AGN between $0.5 < z < 2.9$ and $45.0 < \log(L_{\rm bol}/({\rm erg/s})) < 48.0$ with UV, optical and near-infrared photometry. I produced average spectral energy distributions in different bins of the $z - L_{\rm bol}$ parameter space to estimate how the NIR SED evolves according to these parameters. I found that the NIR luminosity decreases for increasing $L_{\rm bol}$ at any redshift. At the same time, the shape of the NIR SED in the sample is consistent with a non-evolution with z. As a consequence, all the explored proxies for the CF exhibit significant anti-correlations with $L_{\rm bol}$, but not with z. Additionally, the CF also shows a shallower anti-correlation with the Eddington ratio ($\lambda_{\rm Edd}$), yet current systematic uncertainties, as well as the limited dynamical range, do not allow us to precisely constrain the role of the Eddington ratio. Lastly, I derived the covering factor from the ratio between the NIR and optical luminosity and I employed it to set a lower limit for the X-ray obscuration at different redshifts. The results of the analysis presented here are contained in Trefoloni et al. (2024a).

4.2 Context and aims of the work

As already discussed, in the so-called Unified Model (Antonucci 1993; Urry and Padovani 1995), the observational diversity of AGN in terms of spectral properties is explained as the result of different lines of sight to the central engine. A key ingredient of the unified model is the obscuring torus, a dusty and gaseous structure on pc scales, surrounding the accretion disc. In this framework, an unobscured (Type 1) AGN is observed when the line of sight does not cross the obscuring material, while the inner engine is hidden by the toroidal obscurer in case of an obscured (Type 2) AGN. This observational classification can also be interpreted in terms of escape probability of the light through the spatial distribution of clumpy elements forming the torus, thus allowing for a less strict division between Type 1 and Type 2 AGN (see e.g. Almeida et al. 2011; Mateos et al. 2016). An outer tilted torus on scales ~100 pc (McLeod and Rieke 1995; Maiolino and Rieke 1995) can also be included to account for intermediate AGN types.

A critical parameter defining the properties of the torus is the covering factor (CF), which is generally defined as the fraction of the whole solid angle covered by the obscuring structure ($\Omega/4\pi$, e.g. Hamann et al. 1993). Although the definition of the covering factor is purely geometrical, on a practical level there are different routes to estimate this parameter, taking advantage of several techniques across different wave-bands.

In the X-ray surveys, the fraction of obscured sources (generally those with $\log(N_{\rm H}/cm^{-2}) > 22$) is used as a proxy for the mean covering factor at a given luminosity, given a sample with a high enough completeness level and under the hypothesis of randomly oriented AGN in the sky (e.g., Ueda et al. 2003, 2014; La Franca et al. 2005; Hasinger 2008; Burlon et al. 2011; Malizia et al. 2012; Merloni et al. 2014). A similar argument has been used to estimate the CF as the ratio between narrow line (Type 2) and broad line (Type 1 AGN), based on the optical spectrum (Simpson 2005; Toba et al. 2014).

In addition, by considering that the intrinsic UV luminosity of the AGN is reprocessed by the gaseous and dusty torus and re-emitted in the infrared (e.g., Maiolino et al. 2007; Treister et al. 2008; Gandhi et al. 2009), the covering factor can thus be derived as the ratio between the reprocessed infrared luminosity and the intrinsic AGN emission. Yet, this ratio does not take into account the complicated anatomy of the covering material (Granato and Danese 1994). Early analytical models employed a simplistic continuous toroidal screen (Pier and Krolik 1992), but the need for a more irregular gas and dust distribution was already clear. The strong nuclear radiation field is indeed expected to break a continuous torus into smaller clumps (Krolik and Begelman 1988) whose turbulent motion helps in stabilising a geometrically thick structure (Beckert and Duschl 2004). Deriving the CF is far less straightforward for a non-homogeneous (i.e. clumpy) distribution of the clouds composing the torus (Nenkova et al. 2008a,c; Lusso et al. 2013; Netzer 2015), and detailed radiative transfer modelling (Stalevski et al., 2016) showed that the bare infrared-to-optical luminosity ratio systematically underestimates low CFs and overestimates high CFs in case of Type 1 AGN.

Critical pieces of information about the torus properties have also been gathered by successfully applying torus models to reproduce observations of low redshift Seyferts and luminous AGN both in the infrared (e.g. Mor et al. 2009; Hönig et al. 2010; Alonso-Herrero et al. 2011, 2021; Almeida et al. 2011; Feltre et al. 2012; Zhuang et al. 2018; Ichikawa et al. 2019; González-Martín et al. 2019; García-Bernete et al. 2019, 2022) and in the X-rays (see e.g. Ricci and Paltani 2023). In the latter case, both the iron $K\alpha$ emission line and the ~ 30 keV Compton hump have been used to constrain the geometry of the circumnuclear material (Ricci et al. 2014; Gandhi et al. 2015).

In a dynamical picture, the properties of the torus are expected to vary according to the accretion parameters of the AGN (i.e. the bolometric luminosity L_{bol}, the black hole mass M_{BH} and the Eddington ratio λ_{Edd}). A simple evolutionary scenario predicts that its covering factor should decrease with increasing luminosity, i.e. the idea of the "receding torus" (Lawrence 1991), or a "luminosity-dependent Unified Model" (Ueda et al. 2003). In this picture, the radiation field produced in the innermost regions of the AGN is capable of directly shaping the morphology of the gaseous and dusty surrounding material. At the same time, efficient accretion and high luminosity are expected to be conducive conditions for the launch of powerful accretion-disc winds, directly driven by the nuclear activity (e.g. Proga 2005; Zubovas and King 2013; Nardini et al. 2015; King and Pounds 2015; Tombesi et al. 2015; Nardini et al. 2019b), which could be equally able to shape the circumnuclear environment in episodic events rather than on galactic timescales. A dependence on the accretion rate is also supported by recent studies (see e.g. Ricci et al. 2023 and references therein) arguing that the actual driver of the covering factor decrease might be the Eddington ratio rather than the bare bolometric luminosity, with the former being equivalent to an effective (mass-normalized) luminosity.

Although the properties of the torus, dominating the infrared SED of AGN, are expected to vary with the luminosity and/or the Eddington ratio, its possible evolution with redshift has not yet found credible evidence. From a cosmological standpoint, there is growing evidence that the UV and optical SED properties in quasars do not appreciably evolve with redshift. Luminous blue AGN shining at high redshift are indeed remarkably similar to those observed locally, both in terms of continuum (e.g. Kuhn et al. 2001; Mortlock et al. 2011; Hao et al. 2013a; Shen et al. 2019; Yang et al. 2021; Trefoloni et al. 2024c) and line (e.g. Croom et al. 2002; Fan et al. 2004; Nagao et al. 2006; Stepney et al. 2023) properties. These findings are echoed in the infrared where several works showed that the average SEDs made of samples over wide redshift intervals, up to $z \sim 4$, exhibit quite similar shapes also in the NIR and MIR ranges (e.g. Elvis et al. 1994; Richards et al. 2006; Krawczyk et al. 2013, but see also Bianchini et al. 2019 for recent updates from a larger MIR sample). This evidence is confirmed also by other sparse samples at $z \gtrsim 5$, which exhibit NIR properties closely resembling those of the bulk of the quasar population at lower redshifts (Leipski et al. 2014), although with the noticeable exception of hot dust deficient quasars (e.g. Jiang et al. 2010; Hao et al. 2011). Yet, a systematic investigation of the NIR properties, and their interplay with the main optical and UV continuum, separately analysing the effects of luminosity and redshift over wide intervals, has not yet been undertaken for a large sample of blue unobscured AGN.

In this part of my thesis, my aim is to investigate separately the possible evolution of the NIR SED in a sample of blue Type 1 AGN with the accretion parameters (L_{bol}, λ_{Edd}) and the redshift, taking advantage of a large complete dataset purposefully assembled. In particular, I employed this large sample to address the following issues: i) investigate the evolution with L_{bol} and z of the NIR SED in blue quasars; ii) investigate how the covering factor in quasars evolves separately with z and with L_{bol}; iii) explore the tentative anti-correlation between CF and λ_{Edd}.

4.3 The data-set

With the aim of building a dataset covering the rest-frame emission from the UV to the IR for a large sample, I gathered and cross-matched photometric data from different surveys. Here I briefly highlight the building blocks of the final sample.

The starting sample is the Sloan Digital Sky Survey (SDSS) DR7 (Shen et al. 2011), which samples the rest-frame optical and UV wavelengths, where the AGN SED is dominated by the disc emission. This contains ~106,000 quasars with both photometric and spectral data in the five SDSS bands (Fukugita et al. 1996) brighter than $M_i < -22.0$. Although newer releases have been produced, for this analysis I opted for the SDSS DR7 catalogue as it offers a subsample of roughly 50,000 objects which abide by a uniform selection criterion, defined using the final quasar target selection algorithm described in Richards et al. (2002b), identified by the flag UNIFORM=1 in the catalogue. This avoids the uneven sampling along the redshift axis, and the selection criteria optimised to map the large-scale structure traced by the Ly-α forest, that instead characterises the later BOSS (Dawson et al. 2012) and EBOSS (Dawson et al. 2016) surveys. At the same time, the SDSS selection algorithm claims a completeness close to $\sim 90\%$ below $m_i < 19.1$ at $z < 2.9$ (see Sec 4.1 in Richards et al. 2002a for the related caveats), and this protects this work from incompleteness biases. With the aim of further increasing the quality of the sample I eventually opted for a magnitude cut at $m_i \leq 19.0$. Data in the u and z filters were corrected for the reported shifts in their zeropoints[1].

The near-infrared band ($\sim$ 1–10 μm) is crucial when investigating the emission of the innermost hot region of the torus, which dominates the SED of luminous AGN in this band. At these wavelengths the AllWISE catalogue (Cutri et al. 2021) is the largest dataset available. This catalogue was produced from the collection of the Wide Infrared Survey Explorer (WISE, Wright et al. 2010) observations. I cross-matched this sample with the SDSS one adopting an optimal $2''$ matching radius (see Sec. 2.2 in Krawczyk et al. 2013), which gives $\sim 97\%$ of matches. For a typical quasar SED, the WISE filters have effective wavelengths 3.36 μm ($W1$), 4.61 μm ($W2$), 11.82 μm ($W3$) and 22.13 μm ($W4$). To improve the quality of the NIR data, I also required at least SNR=2 in W3 band, a requirement easily met in both W1 and W2. More details about the reliability of the WISE photometry and the NIR quality cuts can be found in Supplementary Material 4.8.1. Although the features of the AGN SED crucial for this analysis are already well covered by these two surveys, I complemented the sample with other near-infrared and UV data. In particular, I added the UV points from the Galaxy Evolution Explorer (GALEX, Martin et al. 2005). The observed-frame reference wavelengths of the GALEX filters are 1528 Å (FUV) and 2271 Å (NUV), yielding respectively 38,000 and 45,000 detections which helped to probe the peak of the disc emission especially in the low redshift regime. In the near-infrared (NIR) band the main contributions to the SED come from the low-energy tail of the disc and the stellar emission from the host galaxy, which was covered using NIR photometry from both the UKIRT (United Kingdom Infrared Telescope) Infrared Deep Sky Survey (UKIDSS; Lawrence et al. 2007) and the Two Micron All Sky Survey (2MASS; Skrutskie et al. 2006).

---

[1] https://www.sdss4.org/dr17/algorithms/fluxcal/

These two supplementary datasets provided photometric data for roughly 11,300 and 10,000 sources in the $YJHK$ and JHK bandpasses, respectively.

All the available photometry was also corrected for Galactic extinction adopting the Fitzpatrick (1999) extinction curve and the extinction values from Schlafly and Finkbeiner (2011).

4.3.1 Accounting for selection effects

Since one of the goals of this work is to estimate if any evolution with z of CF exists, starting from the cross-match of flux-limited surveys, it is extremely important to take into account to what extent selection effects can affect these results. These can come basically in two forms: incompleteness and inclination. The first effect is produced whenever the optical detection is not matched by the IR counterpart in a substantial fraction of objects. This implies that only the most IR-bright objects are selected because of the IR flux sensitivity, thus biasing the CF towards higher-than-average values. In this case this issue is not critical, as the IR-to-optical cross-match fraction ($\sim 97\%$) guarantees a high degree of completeness with respect to the optical survey, which also claims to be $\sim 90\%$ complete.

The second effect has a subtler impact on the observations. I assume that the optical/UV emission comes from an accretion disc, while the IR radiation is isotropically emitted by the torus (see e.g. Treister and Urry 2006 and references therein). In flux-limited surveys, at higher redshifts increasingly fainter objects fall below the flux limit of the survey. Assuming that the intrinsic luminosity is diminished because of the projection effect as $L_{\rm bol,obs} = L_{\rm bol,int}\,\cos\theta$, with θ being the angle between the line of sight and the axis of the accretion disc, the same observed luminosity can be obtained by intrinsically brighter sources observed at higher inclination or vice-versa. Even assuming that all the quasars in the Universe had the same intrinsic luminosity (which is obviously not true) and random inclinations of the line of sight, the combined effect of the flux limit and the increasing distance with z would imply the selection of preferentially face-on objects. This, in turn translates into a relatively higher contribution of the optical/UV with respect to the IR (i.e. lower CF) for increasing z.

Such an effect, would produce an anti-correlation between the CF and z at a given intrinsic luminosity, but in the following I will demonstrate that, within the ranges of parameters explored in this work, it does not produce any statistically appreciable trend. Another, likely overly fine-tuned possibility is that the effect of increasingly face-on objects combines with intrinsically higher CF so that the two effects cancel out. Similarly, the anti-correlation observed in the data-set between between CF and $\rm L_{bol}$ at constant z (see Sec. 4.5.1, 4.5.2), under the reasonable assumption of random inclinations of the line of sight at the same redshift, cannot be ascribed to inclination effects. Therefore this anti-correlation between CF and $\rm L_{bol}$ that observed in the data, as I will show shortly, is likely a genuine feature rather than one induced by observational effects.

To quantify the impact of the inclination angle at increasing redshifts on the observed CF I took advantage of a simulation. The basic idea here is to simulate a population of quasars whose intrinsic bolometric luminosity and covering factor distribution are known and see how the effect of inclination and flux limit propagate in the observed CF in the parameter space defined by $\mathrm{L_{bol}}$ and z. To this end, I produced a mock sample of 100,000 objects uniformly distributed in the parameter space. The limits of the z and $\log(\mathrm{L_{bol}})$ distributions overlap with those spanned by the actual sample, i.e. z=[0.1,2.9] and $\log(\mathrm{L_{bol}})$=45.0–48.5 (the upper limit of the luminosity was chosen to be slightly higher so as to include very luminous, yet inclined objects). I assumed a normal intrinsic CF distribution with mean value $\langle CF\rangle = 0.5$ and standard deviation $\sigma_{CF} = 0.05$, with the underlying assumption that there is no physical connection between the torus CF and the AGN luminosity. For each object I drew a random value of $\cos\theta$ from a uniform distribution between $[\cos 0°, \cos 90°]$, representing random line of sights to the AGN of the sample, and derived the projected bolometric luminosity accordingly. This allowed us to produce the observed $CF_{\mathrm{obs}} = CF/\cos\theta$.

Additionally, I produced the simulated photometry by assuming a 3000 Å luminosity $L_{3000\text{Å}}$=$\mathrm{L_{bol}}$/5.15 from the bolometric corrections from Richards et al. (2006) and matching a quasar template (VB01) to $L_{3000\text{Å}}$. Finally, I discarded all the objects whose i photometry fell above $m_i \geq 19.0$ (the magnitude limit chosen for this work, see Sec.4.3) and whose inclination angle was above 65°, assuming an infinitely optically thick torus. Above this level of inclination, the broad lines would not be detected and the optical/UV SED would not exhibit the blue colours of unobscured quasars and would not be consequently included in the survey.

In Fig. 4.1 I show the result of this procedure. There are several details to be noted here: the first and foremost is that the combined effects of inclination and flux limit are not capable of producing any appreciable trend in the two sections of the parameter space. Secondly, the average observed covering factor CF_{obs} is ~0.7, while the intrinsic one set in the simulation was CF=0.5. This can be explained as the effect of the average inclination by which $CF_{\mathrm{obs}} = CF/\langle\cos\,\theta\rangle \simeq CF/0.7 \simeq 0.7$. Lastly, it is possible to spot that the data in the brightest bin hint at a tentative decrease in CF. This is because the most luminous objects in the distribution cannot be interpreted in terms of some even more luminous sources observed under high viewing angles. Therefore, the observed luminosity is close to the intrinsic one, and CF_{obs} tends to CF. I also explored other combinations for the simulation parameters within reasonable values, but in no case a clear trend emerged.

There are obviously several over-simplifications in this approach, such as the flux limit selection which is much more complex than a bare magnitude cut. Also the assumption of a completely optically thick torus is at odds with the patchy torus models, which admit a non-zero probability of seeing directly through the torus. Lastly, the isotropic and perfectly efficient re-irradiation of the primary continuum by the torus in the infrared is another very simplistic zero-th order assumption. Yet, the lack of a clear decreasing trend, especially in the moderate- to high-luminosity regime, motivates the search for some additional correlation between the CF of the torus and the disc emission.

4.4 Methods

Here I describe the methods employed to correct the sample photometry for systematic effects and explain the subsequent analyses.

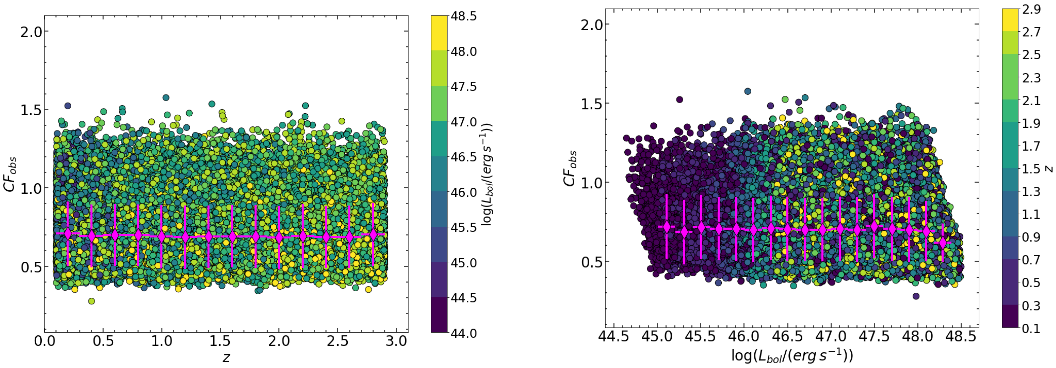

Figure 4.1. *Left:* z–CF (left) and $\log(\mathrm{L_{bol}})$–CF (right) section of the simulated parameter space. The CF and $\log(\mathrm{L_{bol}})$ values presented here are the observed (i.e. projected) quantities. Magenta diamonds represent the median CF values in bins 0.2-dex wide. The y-axis uncertainties represent the standard error on the mean CF in the bin. The third axis is colour-coded.

4.4.1 The parameter space

The key point of this study is the effort to disentangle the effects of the luminosity and the redshift in shaping the NIR emission coming from the dusty torus of quasars. To achieve this goal, the sample was analysed in the $\log(\mathrm{L_{bol}})$–z plane[2], as shown in Fig. 4.2, using the reference values for each object tabulated in Wu and Shen (2022). When referring to $\log(\mathrm{L_{bol}})$ I mean the luminosity evaluated via some bolometric correction in the form $k_{bol}\,\lambda L_\lambda$. In the following, I will introduce further quantities designating the integrated accretion disc luminosity. In order to study the evolution of the torus emission in the parameter space, the sample was divided in bins of width Δz=0.20 and $\Delta\log(\mathrm{L_{bol}})$=0.20. The width of the bins is much larger than the typical uncertainty on the redshift, which is of the order of 0.1%, while it is similar to the typical uncertainty on $\mathrm{L_{bol}}$, computed adopting monochromatic bolometric corrections (Richards et al. 2006).

4.4.2 Colour selection

The importance of the colour cut when aiming to isolate the intrinsic (i.e. not biased by extinction) quasar emission has been discussed in several works (see for instance Lusso et al., 2020, and references therein). I chose to apply a colour cut to address two main issues: 1) strong contamination from the host galaxy, which is also addressed in Sec. 4.4.3, and 2) dust reddening. Both these effects concur to make the observed SED of a quasar flatter than the intrinsic, polluting the broadband information about the relative importance of the torus emission. To tackle these issues I adopted an analogous procedure to that used to select blue quasars for the cosmological sample described in Sec.1.3. In brief, for each object I computed the slope Γ_1 of a $\log(\nu)$–$\log(\nu L_\nu)$ power law in the rest frame 0.3–1 μm range, and the analogous slope Γ_2 in the 1450–3000 Å range. I selected all the objects in the

---

[2] For the sake of a lighter notation, I adopt $\log(\mathrm{L_{bol}})$ instead of the more correct $\log(\mathrm{L_{bol}}/(\mathrm{erg\,s^{-1}}))$.

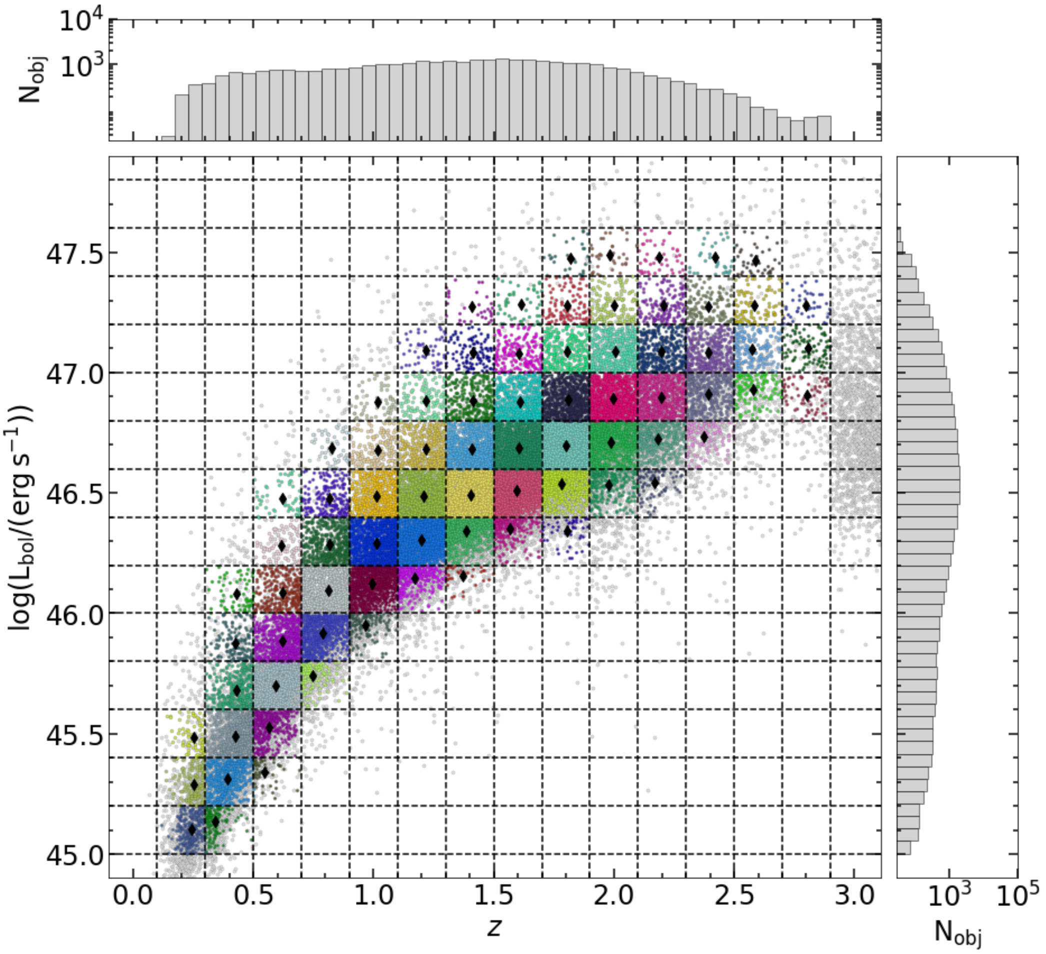

Figure 4.2. $\log L_{bol}$-z plane for the sources surviving the binning selection and the colour cut (see text for details). The final sample spans roughly 2.5 decades in bolometric luminosity and covers up to $z \sim 2.9$. Data are randomly coloured if the bin contains more than 30 objects to make the binning clearer. The black diamonds mark the average z and $\log L_{bol}$ values.

Γ_1–Γ_2 plane residing in the circle with center in the reference values for a typical quasar (Γ_1=0.82, Γ_2=0.40; Richards et al., 2006) and a reddening corresponding to E(B-V)$\lesssim$0.1 assuming an SMC extinction curve (Prevot et al. 1984). The colour selection retained 90% of the sources, and it is shown in Fig. 4.3. This selection, aimed at avoiding the effects of extinction, does not affect any of the conclusions, as shown in Supplementary Material 4.8.2. The sources surviving this final cut represent the starting sample for the analyses described here, and amount to 36,000 objects.

4.4.3 Photometric corrections

Photometric data convolve the spectral information through band-pass filters. This causes the individual features, easily recognizable in a moderate-quality spectrum, to be instead mixed up in photometric points. Since my concern here is to build

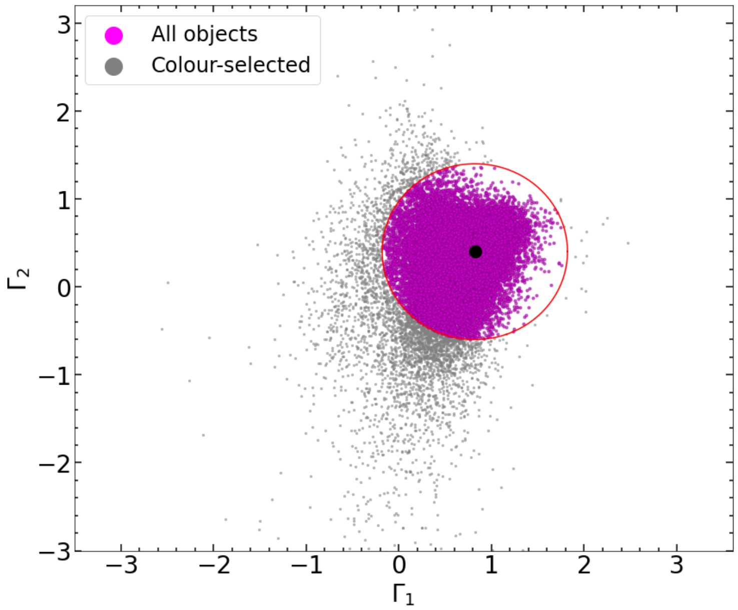

Figure 4.3. Γ_1–Γ_2 plane for the sources satisfying the colour cut (magenta dots within the red circle). The black dot marks the average values reported in Richards et al. (2006) for blue unobscured quasars.

the SED of the bare AGN disc and torus emission for each source of the sample, several corrections accounting for observational effects were needed. In detail, I estimated 1) the contribution from emission lines, 2) the host galaxy emission, 3) the inter-galactic medium (IGM) extinction. I accounted for each of these effects independently.

Generally speaking, the corrections α applied to each photometric point have the following expression:

$$L_{f,\,\mathrm{corr}} = \alpha L_f \tag{4.1}$$

where $L_f = \int_f \lambda L_\lambda\big|_{\lambda=\lambda_{\mathrm{obs}}} S_{\lambda_{\mathrm{obs}}}\, d\lambda_{\mathrm{obs}}$ is the total luminosity (i.e. λL_λ) integrated through the observed-frame normalised pass-band of the filter f. The filter transmission curve $S_{\lambda_{\mathrm{obs}}}$ was simulated using the PYPHOT[3] Python package[4].

Line emission

The line emission is produced in the gas clumps rapidly moving around the SMBH on pc scales in the BLR in the case of broad permitted lines or on galactic scales in the case of narrow forbidden lines. These features act as contaminants in the photometric data when trying to isolate the AGN continuum emission. In order to subtract the emission line contribution in each filter, I considered the emission of a typical blue quasar, based on the VB01 template T_λ. I built a model containing the

---

[3] `https://github.com/mfouesneau/pyphot`

[4] The PYPHOT package does not include UKIDSS filters response curves. The Y, J, H, K-band responses were simulated adopting the transmission curves available at the Spanish Virtual Observatory (SVO) online facility `http://svo2.cab.inta-csic.es/theory/fps3/index.php?mode=browse&gname=UKIRT&gname2=UKIDSS&asttype=`.

bare power-law continuum (T_λ^c) and another one containing the power-law continuum plus the emission lines, the UV and optical iron pseudo-continua and the Balmer continuum (T_λ^{c+l}). I only corrected for the effect of the emission lines between 1200–7000 Å, where the strongest line contribution is expected, while I did not correct for the 9.7 μm feature (expected to be in emission in case of Type 1 AGN) in the IR as this falls outside of the wavelength of interest for estimating the CF (see Sec. 4.4.5). For each photometric filter f the emission lines correction $\alpha_{\rm EL}$ was evaluated as

$$\alpha_{\rm EL} = \frac{\int_f \lambda T_\lambda^c\big|_{\lambda=\lambda_{\rm obs}} S_{\lambda_{\rm obs}} d\lambda_{\rm obs}}{\int_f \lambda T_\lambda^{c+l}\big|_{\lambda=\lambda_{\rm obs}} S_{\lambda_{\rm obs}} d\lambda_{\rm obs}} \leq 1 \tag{4.2}$$

The resulting luminosity in each filter is lower than or equal to the uncorrected one after applying this correction. An example of the result of this correction for a $z = 1.0$ quasar is shown in Fig. 4.4. Here I opted for not performing a luminosity-dependent emission line correction that would take into account the anti-correlation between the emission line equivalent width and the luminosity (i.e. the Baldwin effect). Yet, I note that with respect to these results, this is a conservative approach. Indeed, on a qualitative basis, assuming weaker emission lines at higher $\rm L_{bol}$ (and z), smaller corrections would be implied and, consequently, intrinsically brighter disc luminosities. This, in turn, would translate into even lower torus-to-disc ratios at high $\rm L_{bol}$, thus strengthening the forthcoming conclusions (see Sec. 4.5.2).

Host galaxy emission

The observed flux in each filter comes from the combination of the host galaxy and the AGN emission. Luminous AGN ($\rm L_{bol} \gtrsim 10^{46}$ erg s^{-1}) are expected to completely outshine their host galaxy. Although the importance of the host-galaxy contamination should have already been minimised by the colour cut (see Sec. 4.4.2) and the choice of $\log(\rm L_{bol})$=45 as the minimum bolometric luminosity, I aimed at removing any possible residual contamination. I performed this task by subtracting the emission from a typical galaxy, assuming a correction with the form:

$$\alpha_{\rm HGC} = 1 - \frac{L_{5100\text{Å},\rm tot} \times f_{\rm HGC} \times \int_f \lambda G_\lambda\big|_{\lambda=\lambda_{\rm obs}} S_{\lambda_{\rm obs}} d\lambda_{\rm obs}}{L_f} \leq 1 \tag{4.3}$$

where $L_{5100\text{Å},\rm tot}$ is the total luminosity at rest-frame 5100 Å evaluated by interpolating the available photometry, $f_{\rm HGC}$ is the host-galaxy fraction evaluated at 5100 Å , G_λ is the spectrum of a typical galaxy and L_f is the photometric luminosity through the filter f. As for the galaxy spectrum I chose an elliptical galaxy template from Assef et al. (2010), scaled by its 5100 Å luminosity. The host-galaxy fraction is a function of the AGN luminosity: to account for this I took advantage of the prescription described in Shen et al. (2011), which parameterises $f_{\rm HGC}$, here adapted as:

$$\frac{L_{5100,\rm host}}{L_{5100,\rm QSO}} = 0.8052 - 1.5502x + 0.9121x^2 - 0.1577x^3 \tag{4.4}$$

where x=$\log(L_{5100\text{Å},\rm tot}/(\rm erg\,s^{-1})) - 44$. No correction was applied for objects with $x > 1.053$, that represent 80% of the sample. Although Shen et al. (2011) evaluated their correction using only $x \geq 0$, I extrapolated their parameterisation also below this value. I note that the fraction of quasars below this value is negligible ($\sim 0.03\%$) and these objects are mostly discarded as residing in low counts bins in the subsequent analysis. It is therefore safe to expect that this effect does not seriously hamper these results. In a few cases (~1% of the objects suitable for the host-galaxy correction) the optical photometric data presented a steep decline towards redder wavelengths, incompatible with the adopted galaxy template. In these cases the AGN emission would be outshined by the host, giving $\alpha_{\mathrm{HGC}} < 0$. Whenever this condition occurred, no correction was applied. Although, for the sake of completeness, this correction was included, it is to be noted that this was applied only to ~20% of the sources in the sample, which reside in the low-$\mathrm{L_{bol}}$ low-z corner of the parameter space, and will not be included in the following analyses due to the lack of faint counterparts at high z.

IGM extinction

At wavelengths shorter than the Lyman α the rest frame emission of each quasar is attenuated by the intergalactic H I absorption, creating both the so-called Lyman α forest in line absorption and a drop in the continuum below the Lyman limit at $\lambda < 912\,\text{Å}$ (e.g. Møller and Jakobsen 1990). Because of the IGM absorption, the observed luminosity $\lambda L_{\lambda,\mathrm{obs}}$ is lower than the intrinsic $\lambda L_{\lambda,\mathrm{int}}$ by a wavelength- and redshift-dependent transmission factor $T(\lambda, z)$, so that $\lambda L_{\lambda,\mathrm{obs}} = T(\lambda, z) \times \lambda L_{\lambda,\mathrm{int}}$. The transmission is linked to the effective H I Lyman series and Lyman continuum photons optical depth $\tau(\lambda, z)$ by $T_\lambda(z) = e^{-\tau(\lambda,z)}$. The goal of this correction is to increase the flux in the photometric bands affected by absorption by the IGM ($\alpha_{\mathrm{IGM}} \geq 1$), in order to recover the intrinsic ultraviolet (UV) and extreme ultraviolet (EUV) flux. The IGM absorption correction α_{IGM} can thus be evaluated by assuming the knowledge of the shape of the EUV continuum as:

$$\alpha_{\mathrm{IGM}} = \frac{\int_f \lambda L_\lambda \big|_{\lambda=\lambda_{\mathrm{obs}}} S_{\lambda_{\mathrm{obs}}} d\lambda_{\mathrm{obs}}}{\int_f \lambda L_\lambda T_\lambda(z) \big|_{\lambda=\lambda_{\mathrm{obs}}} S_{\lambda_{\mathrm{obs}}} d\lambda_{\mathrm{obs}}} \geq 1 \tag{4.5}$$

Here I assumed the intrinsic EUV continuum to follow the behaviour described in Lusso et al. (2015), i.e. $L_\lambda \sim \lambda^{\alpha_\lambda}$ with $\alpha_\lambda = -0.3$. The effect of the IGM absorption at different redshifts was estimated by taking advantage of the calculations described in Inoue et al. (2014). There, the absorption is considered to be delivered mainly by two components, the Lyα forest component and the damped Lyα systems, acting on different column density regimes. With the aim of a conservative approach, and apply the minimal correction, I only included the Lyα forest in this corrections. Examples of the transmission curves are reported in the right panel of Fig. 4.4.

4.4.4 Building the average SEDs

Here I describe the technique adopted to build the average SEDs employed in this part of my work. The bottom line closely resembles the one employed to build the spectral stacks in Sec.2.4.2. The procedure is the same for building both the average SED in each bin of the $\mathrm{L_{bol}} - \mathrm{z}$ parameter space and those obtained along rows or columns of the parameter space. After performing the mentioned corrections and

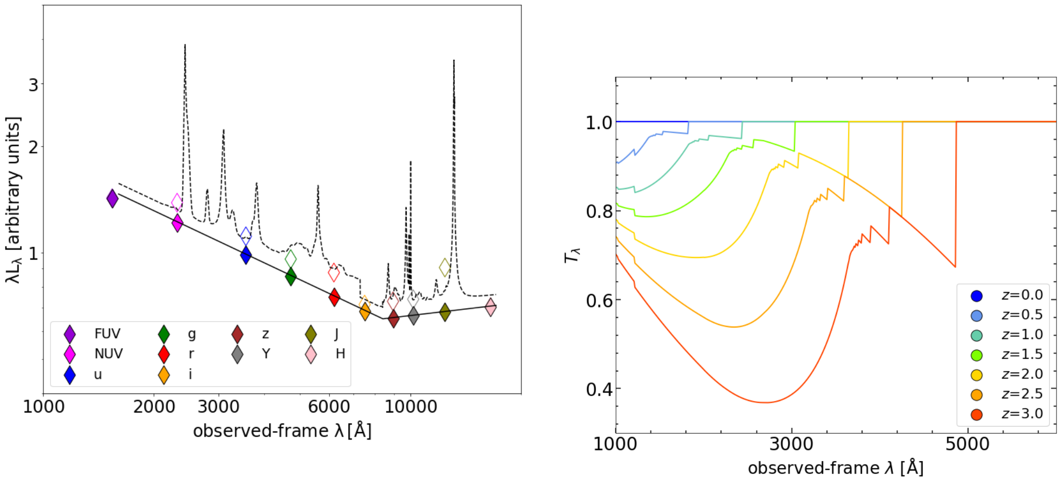

Figure 4.4. *Left:* pass-band integrated luminosity of the template with (empty diamonds) and without (filled diamonds) emission lines for a $z = 1.0$ quasar, according to the VB01 template. *Right:* IGM transmission curves at different redshifts, colour-coded as described in the legend.

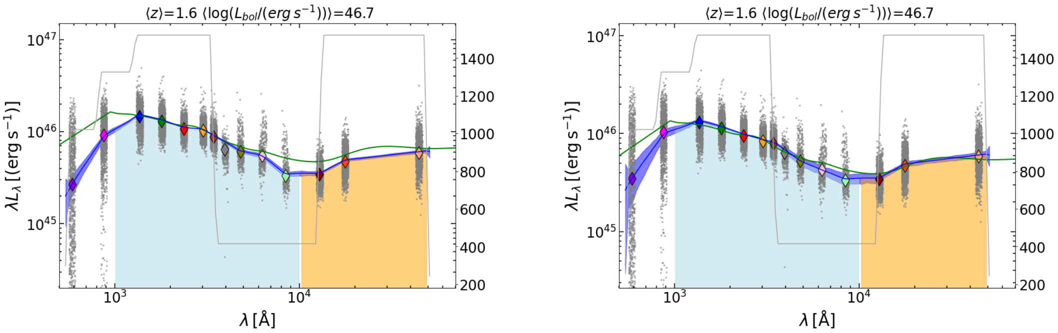

Figure 4.5. Example of average SEDs produced employing the uncorrected (left) and corrected (right) photometry (blue). The effect of the corrections applied is to increase the flux bluewards of the Lyα, mitigate the dip around 1 μm and reduce the optical and UV Fe II bumps. Also the strong Hα emission in the observed-frame H band (pink) is reduced in the corrected data-set. The grey clouds of points are made of the photometric data used to produce the SED, the coloured diamonds (same colour-code as in left panel of Fig. 4.4) are the median luminosities. The solid grey line represents the number of objects contributing to each spectral channel. The average quasar SED from Krawczyk et al. (2013), scaled to the 3000 Å total luminosity, is shown in green as a comparison. The azure and orange shaded areas represent the regions where the $L_{\rm opt}$ and the $L_{\rm NIR}$ terms in the covering factor proxy R are respectively evaluated (see Sec.4.4.5). The average z and log(L$_{\rm bol}$) of the parameter space represented by the SED are denoted in the top string.

quality cuts, I proceeded to gather all the photometric information in the selected region of the parameter space. For each source the photometric pairs ($\log \lambda_{\rm rest}$, $\log \lambda L_\lambda$) were rebinned onto a common wavelength grid made of 300 logarithmically equispaced points between $10^{1.5} - 10^6$ Å , building a *photo-array* for each object.

Not all the objects have photometric coverage between the Y and the K band. A direct interpolation between the SDSS-z and the WISE-$W1$ bands could overestimate the actual SED which generally shows a dip around $1\mu m$ (see e.g. Richards et al., 2006; Elvis et al., 2012; Krawczyk et al., 2013). Because of this, in each composite SED the flux between the last SDSS filter and W1 was computed using only sources with actual UKIDSS and/or 2MASS data, rather than by interpolation.

The average SED and the relative uncertainty in each bin were then produced by adopting a bootstrap resampling. In brief, a number of *photo-arrays* equal to the total number of objects in the bin is randomly drawn. The *photo-arrays* were scaled by the monochromatic 3000 Å luminosity and an average stack is produced by considering the median luminosity in each spectral channel. This scaling wavelength was chosen for being covered by SDSS photometry in most cases. This procedure is repeated with new random draws until the desired number of stacks (N=100) is reached. The final composite SED is made by the median of the 3σ-clipped distribution of fluxes in each spectral channel, while the uncertainty is set by the standard deviation. The final SED is scaled so that the average luminosity and the relative uncertainty at 3000 Å ($\lambda L_\lambda|_{\lambda=3000\text{Å}}$) are respectively equal to the mean and the standard error on the mean $L_{3000\text{Å}}$ in the bin. An example of the result of this procedure, also including the effect of the corrections to the photometry, is shown in Fig. 4.5.

4.4.5 Defining a proxy for the covering factor

The emission of the dusty torus in AGN is expected to peak between ~3–30 μm, with noticeable differences depending on the covering factor (CF), the optical depth (τ) and the inclination of the line of sight (see e.g. Nenkova et al., 2008b; Shi et al., 2014; García-González et al., 2017). In order to precisely define the covering factor, a complete description of the SED, representing the whole accretion disc and torus emission from the extreme UV to the far infrared, is needed. Unfortunately, this is not generally feasible, especially for large samples like the one described here.

Several past works have adopted different infrared and UV/optical proxies, respectively, for the torus and AGN luminosity terms in the CF expression. Traditionally, the ratio R between the monochromatic luminosities at some infrared and UV/optical wavelengths (e.g. Maiolino et al. 2007; Treister et al. 2008) or integrated over the available wave-bands (e.g. Cao 2005; Gu 2013; Rałowski et al. 2023) has been widely employed.

A more refined approach to the problem of evaluating the covering factor requires taking into account other factors such as the optical thickness of the torus and its shape. For instance, an optically thick torus is expected to have a lower CF (see e.g. Section 6 in Lusso et al. 2013). Moreover, it has been shown by Stalevski et al. (2016) that the clumpiness of the dusty torus in combination with the anisotropic emission of the accretion disc leads to the underestimate (overestimate) of low (high) CF in Type 1 AGN. To correct for these effects, they propose a polynomial expansion of CF in terms of R.

The wavelengths covered by the data gathered here do not consent to properly sample the mid- and far-infrared tail of the torus emission. Similarly, the low coverage in the far-UV combined with the effect of possible residual (and redshift-dependent) IGM absorption, not completely corrected by the procedure described in Sec. 4.4.3, does not guarantee a complete description of the disc emission. Because of this, I decided to rely on observational proxies for the CF based on different combinations of UV/optical and near-infrared (NIR) luminosities. Throughout this investigation, I adopted the ratio $R = L_{\rm NIR}/L_{\rm opt}$[5] as a proxy for the intrinsic CF, with $L_{\rm NIR}$ being the integrated luminosity of the average SEDs between 1–5 μm and $L_{\rm opt}$ that between 1,000 Å and 1 μm.

In the NIR, the WISE coverage at the redshifts sampled here only allows to access the hot dust emitting in the range between roughly 1–5 μm. This spectral region can be affected by stellar emission within the host galaxy (e.g. Podigachoski et al. 2016), the infrared tail of the accretion disc and/or sources with strong contributions by hot graphite dust (e.g. Mor et al. 2009). In this case, the selection of luminous AGN (the sample mean is $\log(\rm L_{bol})$ is 46.4 erg s^{-1}), as well as the correction for the host galaxy emission, help in mitigating the effect of the possible stellar light contribution. In addition, all the average SEDs were visually inspected to check that the 1 μm emission was dominated by the disc, rather than by the peak of the stellar bulge in the host, thus minimising the possible mixing of the components. On the other hand, Stalevski et al. (2016) showed that, within their model, the 1–5 μm band has the favourable aspect of having almost no dependence on optical depth, and on the other parameters explored therein, such as the clumpiness of the torus and the inclination angle.

For what concerns the AGN term in the CF definition I employed $L_{\rm opt}$, defined as the integrated UV/optical disc emission from 1,000 Å emission up to 1 μm in the average SEDs, including only the bins where the peak of the disc emission was clearly observed in the data. If the UV/optical SEDs peaked at significantly different wavelengths at different redshfits and luminosities, this choice would provide unreliable results. I here rely on the evidence that the SED of quasars in different ranges of luminosity and redshift appear to universally peak around 1,000 Å (see e.g. Zheng et al. 1997b; Telfer et al. 2002; Shull et al. 2012; Stevans et al. 2014; Cai and Wang 2023). In Supplementary Material 4.8.2 I also tested how a variable lower integration limit, following the peak of the disc emission, could affect these results, but found no significant differences. Furthermore, I present the results obtained also adopting other proxies for CF, obtained with different combinations of $L_{\rm NIR}$ and $L_{\rm opt}$ as well as with alternative datasets. In all the cases, the anti-correlation between R and $\rm L_{bol}$ and the non correlation between R and z are recovered.

The uncertainty on R was evaluated by producing 100 mock SEDs for each object, by randomizing the flux in each spectral channel adding a Gaussian deviate using the uncertainty on the final SEDs.

4.4.6 Reaching the rest-frame 5 μm

In this work, I limited my analysis to $z < 3$ so that the sample reaches a high degree of completeness at $i < 19.0$. This implies that the rest-frame 5 μm falls within the W3 filter up to $z \sim 2.3$. Above this value, an increasing portion of the rest-frame 1–5 μm

---

[5] Here I highlight the difference between $\rm L_{bol}$ and $L_{\rm opt}$. The former is evaluated via a bolometric correction, and is only used to place every source in the parameter space. The latter is instead computed by directly integrating the SED between 1,000 Å and 1 μm and is adopted to estimate the proxies of CF.

emission is sampled in the observed-frame by the W4 filter, which has been shown to be prone to overestimating the intrinsic flux when compared with instruments with similar passbands (e.g. Spitzer MIPS24, Rałowski et al. 2023). I confirmed this issue by cross-matching the W4 photometry with that of Spitzer MIPS 24 μm for a sample of common sources. In agreement with the previous findings I confirm that W4 systematically overestimates the flux in the low SNR regime. A more quantitative discussion on this issue is presented in Supplementary Material 4.8.2. Nonetheless, at $z < 3$ the emission between 1–5 μm is mostly covered by W1, W2, W3. In the cases where the rest-frame 5-μm emission falls redwards of the W3 filter I extrapolated the SED using the W2 and W3 photometric points using a power law. I estimated how much this prescription could underestimate the actual value of $\boldsymbol{CF}$ by performing the following exercise. I considered the average SEDs where 5 μm falls redwards of the central wavelength of W3 (12.3 μm). I assumed a typical NIR quasar spectrum represented by the template built in Hernán-Caballero et al. (2016), and matched it to the average SED at the rest-frame W3 wavelength, using it to cover the rest 5-μm emission. I then evaluated $\boldsymbol{R}$ from the template-matched and from the extrapolated SED. The typical difference is at the per cent level. Notably, this is a conservative approach, because of the actual width of the W3 filter. For instance, at 16.3 μm the filter response is still about ~50%.

4.5 Results

In this Section I report the results of the analysis regarding the evolution of NIR SED and $\boldsymbol{R}$ with z, $L_{\rm bol}$ and $\lambda_{\rm Edd}$. Additionally, I compare the average SED built upon the whole sample with others in literature, and present how the information about the dusty torus gathered in this part of my work can give constrains on the mechanism responsible for obscuration in the X-rays.

4.5.1 Evolution of the average SED with z and $L_{\rm bol}$

A key question when trying to understand the observed properties of the obscuring torus in AGN is whether and how they change as a function of the AGN parameters ($L_{\rm bol}$, $M_{\rm BH}$) and of the cosmic epoch. For what concerns the luminosity evolution, the sub-linear relations claimed by different authors (e.g. Maiolino et al. 2007; Ma and Wang 2013; Gu 2013) between the optical and infrared luminosities evaluated at several pairs of wavelengths, imply a relative decrease of the NIR luminosity for increasing optical and UV luminosity. This feature, as already mentioned, fits in the physical picture where the torus recedes for increasing accretion disc luminosity. From a cosmological perspective, the IR SED of high-redshift, non dust-deficient quasars (Leipski et al. 2014) has been shown to closely resemble, on average, that of more local samples (e.g. Elvis et al. 1994; Richards et al. 2006), thus hinting at the fact that a non-evolution of the IR SED is actually possible. Here my aim is to explore systematic changes in the shape of the NIR SED as a function of both $L_{\rm bol}$ and z separately.

For this purpose, I performed the following exercise: I considered all sources residing in the region of the parameter space comprised between $46.4 \leq \log(L_{\rm bol}) \leq 47.4$ and $1.0 \leq z \leq 2.8$ (~21,000/36,000 quasars) and proceeded to produce composite

SEDs for each luminosity or redshift bin while integrating along the other axis, following the procedure described in Sec. 4.4.4. I chose this subspace because, within this region, the coverage of the parameter space is fairly homogeneous, although the luminosity tends to slightly increase with redshift. For example, the average $\log(L_{\rm bol})$ at $z \sim 1.0$ is 46.58, while it reaches 47.06 in the highest redshift bin at $z \sim 2.8$. However, including also sources below z=1.0, the mismatch in terms of luminosity between the low- and the high-redshift composites, would be even worse, becoming as high as ∼1.5 dex. I then employed these average SEDs (shown in Fig. 4.6) to test the evolution of the NIR SED shape with z and $L_{\rm bol}$ separately. I also highlight in the inset panels of Fig. 4.6 the values of $\boldsymbol{R}$ derived from these composite SEDs. It is easy to assess the receding NIR SED with increasing luminosity, a feature also testified by the decreasing $\boldsymbol{R}$ shown in the inset plot, albeit the limited dynamical range of only one order of magnitude. The composite SEDs in z bins exhibit slightly more pronounced SED to SED variations, particularly at ∼2 μm where a turnover appears, mostly in the data at $z \lesssim 1.6$. Yet, the values of $\boldsymbol{R}$ derived from these SEDs do not show any clear trend with z. It should also be noted here that producing average SEDs at different z introduces the technical issue given by the uneven sampling of the rest-frame spectrum, which, in the NIR, is exacerbated by two factors: the first is the scarce sampling due to the presence of only the three WISE filters W1, W2, W3, and the second being the non-power law shape of the continuum. The combination of these factors likely leads to the seeming differences in the NIR of the average SEDs at different z. However, such effect is not present in the SEDs at fixed luminosity where, instead, the wide range of redshifts allows for a finer sampling of the rest-frame spectra.

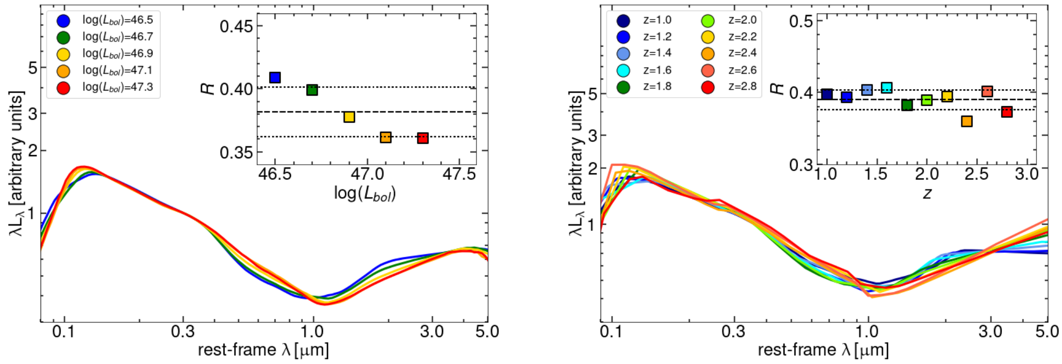

Figure 4.6. *Left:* Sequence of average SEDs for increasing luminosity, scaled by their total luminosity between 1,000 Å and 1 μm. The trend of decreasing NIR luminosity for increasing optical luminosity is apparent, although the small dynamical range, and it is testified by the decreasing $\boldsymbol{R}$ shown in the inset. Here the mean value (standard deviation) is shown as a black solid (dashed) line. *Right:* Sequence of average SEDs for increasing redshift, scaled by their total luminosity between 1,000 Å and 1 μm. The different sampling of the rest-frame emission leads to slightly different SEDs. However, on average $\boldsymbol{R}$ does not show any evolutionary trend, as no systematic departures from the mean value are observed.

With the end of verifying whether the SEDs in bins of fixed z are really consistent with an intrinsically constant NIR SED not varying with the redshift, I performed an additional test: I created an intrinsic FUV-to-NIR SED by joining three spectral templates, namely the Zheng et al. (1997b) template for the FUV, the Selsing et al. (2016) for the optical and the Hernán-Caballero et al. (2016) for the NIR. The choice of the Selsing et al. (2016) template, rather than the Berk et al. (2001) one, was mainly driven by the fact that the former is based on luminous quasars, hence the optical band is almost unaffected by the host galaxy, as it likely is for the objects in the subsample considered here. In this case I opted for a NIR spectral template, rather than a photometric SED, in order to include the effect of the emission lines at different z, as I did not subtract NIR emission line features from the photometric data set. As done for each of the sources in the parent sample, I removed the contribution from prominent broad emission lines, as well as the UV and optical Fe II pseudo-continua. I then shifted the spectral template to the same redshifts where the average SEDs had been produced, and convolved it with the filters of the surveys employed in this work. Lastly, I evaluated R in the same way as it was estimated from the actual SEDs. In the cases where the observed-frame photometry did not cover the rest-frame 5 μm, I resorted to extrapolation. The result of this further test is shown in Fig. 4.7. Here I highlight two noticeable features: the first is that the turnover at ~2 μm, present in the composite SEDs below z ~1.6, is also observed in the simulated SEDs at the same redshift, where both the rising and the flat regions of the NIR bump (consistent with a blackbody emission at $T \sim 1200$ K, Hernán-Caballero et al. 2016) are sampled by W1, W2 and W3. As the redshift increases, only the rising part of this bump is sampled by the WISE filters, hence the power-law extrapolation. This effect is shown in detail in Supplementary Material 4.8.3, where I demonstrate how the interpolation (and extrapolation) across the filters of the template varies with the redshift. Secondly, I note that, although R is slightly different in absolute value with respect to that observed in the actual data[6], it does not show any conspicuous trend, notwithstanding the different sampling wave-bands. The dispersion in R is close to consistency with a single NIR SED at all redshifts: the standard deviation of R estimated in the simulated SEDs (0.010) is indeed remarkably similar to that of actual SEDs (0.012), thus leaving little room for further effects causing the observed dispersion. As a comparison term, the standard deviation of R at different $L_{\rm bol}$ reaches 0.021 in just one order of magnitude, while also showing an obvious decreasing trend (see the inset plot of the left panel in Fig. 4.7).

To sum up, the average SEDs produced at fixed $L_{\rm bol}$ confirm the trend of a weaker NIR emission for increasing optical luminosity. This is clearly observed even employing a relatively small dynamical range (1 dex). I also argue that, although some SED-to-SED variations, the average SEDs at different z are consistent with an intrinsically similar rest-frame NIR SED sampled at different observed-frame wave-bands, rather than with an actual evolution with z. There are obviously other effects, here not taken into account, which might contribute to the SED-to-SED differences. For instance, in the real data, the average luminosity increases slightly in each redshift bin, as already noted, therefore influencing the NIR emission accordingly.

---

[6] This difference might be due to the fact that the one or more of the templates joined to build the total composite spectrum are not fully representative of the subsample under analysis. Nonetheless, the main concern here is not about the absolute value of R, but rather how the wave-bands shifts affect its estimates.

Furthermore, the differences in luminosity are likely accompanied by minor changes in the emission line strength, which are not taken into account by the fixed NIR template used here.

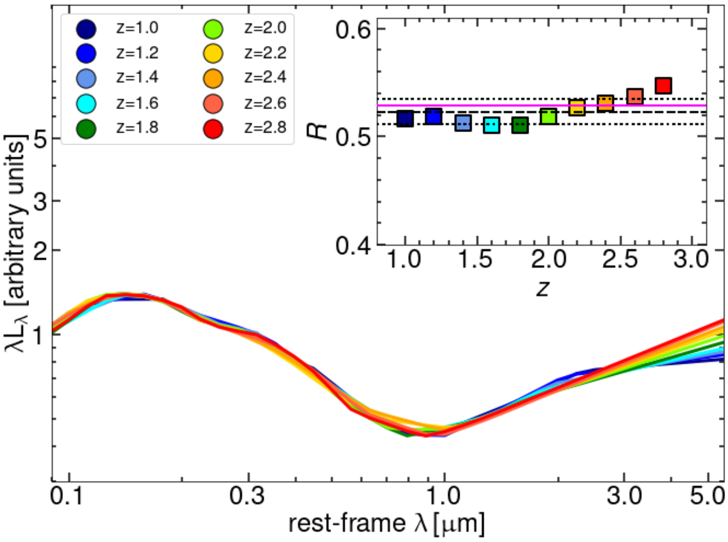

Figure 4.7. The composite SEDs from the simulated photometry of the template in the same redshift bins of the actual data. Here the magenta line marks the actual R value estimated using the total spectral template, rather than the photometry.

4.5.2 Analysis of the correlation between CF, $L_{\rm bol}$ and z

The evolution of the NIR SEDs with $L_{\rm bol}$ can be epitomised in the (sub-linear) anti-correlation between the CF and the AGN luminosity. The fraction of the solid angle covered by the obscuring torus diminishes for increasing luminosity. Here I aim at quantifying the respective effects of the luminosity and redshift in driving the evolution of CF.

The main axes of the parameter space, i.e. the bolometric luminosity and the redshift are correlated for both physical and observational reasons. Indeed, more luminous AGN, or quasars, are generally observed at redshifts corresponding to the so-called "quasar epoch" at $z \sim 2-3$, while, observationally the SDSS is a flux limited survey. I therefore aimed at employing statistical tools to assess the degree of correlation between the proxies of the CF and the main parameters that could account for this effect. In particular, I adopted a methodology similar to that used in Croom et al. (2002), who studied the independent effects of luminosity and redshift on the evolution of the equivalent width in the quasar population. In particular they used both a partial correlation analysis (PCA, which I will introduce shortly), and performed linear fits between the parameter of interest and the equivalent width, while keeping the other fixed.

The first approach in this analysis was to estimate the degree of correlation between R and the main parameters via a PCA. This tool allows us to disjointly evaluate the degree of correlation between R and one of the main parameters, while keeping the other fixed (see e.g. Bluck et al. 2022; Baker et al. 2023). This kind of analysis requires a monotonic dependence of R on both the main parameters. This is the case for the $\log(\mathrm{L_{bol}}) - \mathrm{R}$ relation, while the correlation between R and z appears weaker, as also testified by the correlation indices explored below. In particular, given the three or more quantities (A, B, C) one whishes to test the correlation on, the partial correlation coefficient between A and B while keeping C fixed can be expressed as:

$$\rho_{\mathrm{AB|C}} = \frac{\rho_{\mathrm{AB}} - \rho_{\mathrm{AC}}\,\rho_{\mathrm{BC}}}{\sqrt{1-\rho^2_{\mathrm{AC}}}\,\sqrt{1-\rho^2_{\mathrm{BC}}}}, \tag{4.6}$$

where ρ_{XY} denotes the Spearman rank correlation index between quantity X and Y. The PCA values are used to define a gradient arrow in Fig. 4.8, whose inclination is defined as:

$$\tan\theta = \frac{\rho_{R\,\mathrm{L_{bol}|z}}}{\rho_{R\,z|\mathrm{L_{bol}}}} \tag{4.7}$$

The arrow shows the direction of strongest variation in the tested parameter. The more aligned the arrow with an axis, the stronger the correlation with that quantity. The PCA arrow is almost completely ($\theta = -87°$) inclined towards lower $\log \mathrm{L_{bol}}$ values, signifying that the increasing bolometric luminosity is ultimately responsible for the decrease of the covering factor. This analysis was performed in the region marked by a thick black rectangle in Fig. 4.8, which is made of 56 bins with more than 30 sources per bin. This choice avoids the low-luminosity tail at redshift below z =0.7, where R reaches its maximum values. I note, however, that the inclusion of these points would not alter any of the results presented here. The uncertainty on this parameter was evaluated via a bootstrap resampling of the values of R. I computed θ 1,000 times, each time using a random subsample made of only 30/56 bins in the PCA region, allowing for re-immission. The uncertainty on the PCA inclination was ultimately set as the standard deviation of the distribution of $\mid \theta \mid$. For the sake of completeness I also report in Table 4.1 the partial correlation coefficients and the respective p-values associated to the null hypothesis that there is no correlation between the variables. In Fig. 4.8 I show R derived from the SED in each bin of the parameter space in colour-code superimposed to the whole sample. I also plot the arrow representing the main direction of the PCA, which clearly indicates $\mathrm{L_{bol}}$ as the main driver of the evolution of R.

As a further test, I also employed a similar procedure based on the use the Kendall τ index of correlation (Kendall 1938) instead of the Spearman one, as it provides more robust results in case of outliers. The partial correlation evaluated using the Kendall τ has the same form highlighted in Eq. 4.6 with ρ being substituted by τ (Akritas and Siebert 1996). In this case, I adopted a permutation test to compute the associated p-value (see e.g. Tibshirani and Efron 1993). In brief, given three parameters, the correlation is to be tested on (A, B, C), the array containing the parameter A is shuffled, to simulate a non correlation (random association) between both A and B as well as A and C, while keeping the relation between B and C unaltered. Then, the partial correlation coefficient $\tau_{AB|C}$ for this simulated dataset was evaluated. This procedure was repeated 10,000 times, producing the test distribution, and the p-value was estimated as the two-tailed fraction of simulated datasets where $\tau_{AB|C}$ exceeded the observed value. The resulting values are reported in Table 4.1.

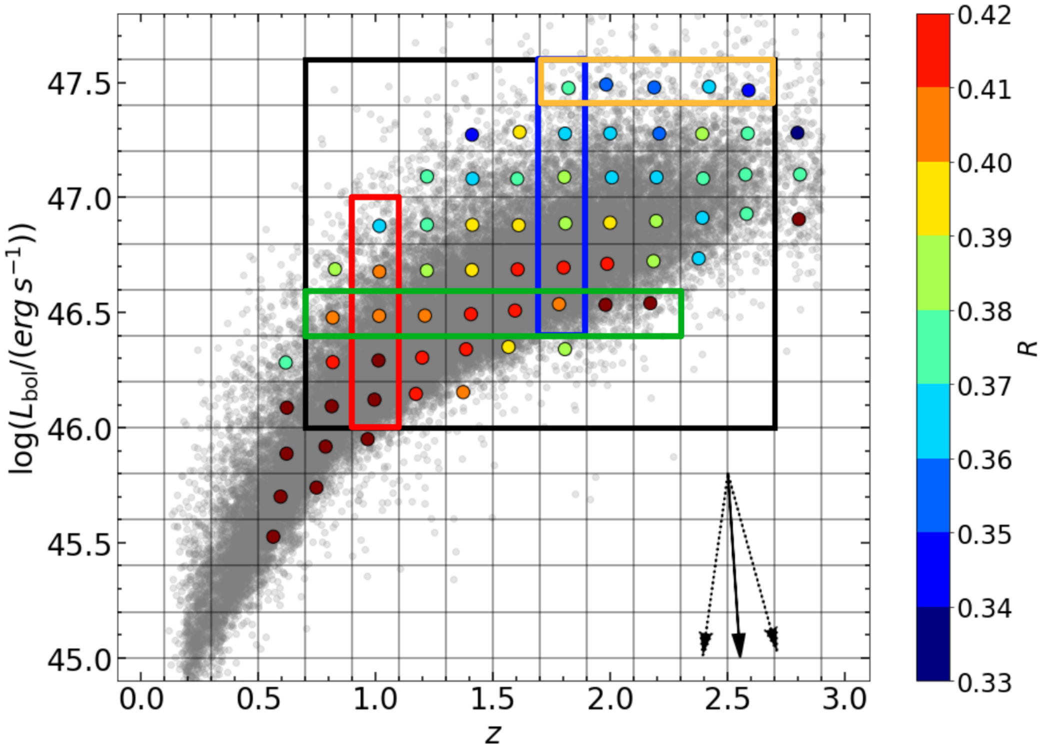

Figure 4.8. log($L_{\rm bol}$)–z plane with R in colour-code. The black arrow points in the direction given by the PCA, evaluated in the bins within the black rectangle, while the dashed arrows show the uncertainty on the direction. The coloured rectangles highlight the bins of the parameter space shown in Fig. 4.9.

Additionally, as another independent check on the correlation strength, I performed the regression of linear forms between R and one of the two parameters, while keeping the other fixed. Again, this was performed in the rows or columns of the parameter space within the same region where the PCA was evaluated. Also in this case, the inclusion of the high R bins at log($L_{\rm bol}$) < 46.0 would make the R-log($L_{\rm bol}$) anti-correlation even stronger. In more detail, I adopted functional forms as:

$$i)\ R = a_0 + a_1\,(z - z_0) \tag{4.8}$$

$$ii)\ R = a_0 + a_1\,[\log(\mathrm{L_{bol}}) - \mathrm{L_0}], \tag{4.9}$$

respectively for the $R - z$ and the $R - \log(\mathrm{L_{bol}})$ relations, with z_0 and L_0 being the mean of the z or log($L_{\rm bol}$) values upon which the regression was performed. In this case the slope of the line gives information about the strength of the correlation between R and one of the two parameters while keeping the other fixed. I report the average slopes and offsets of the best fit relations in Table 4.2. I remark that both the relations are merely empirical efforts to describe the correlation between the parameters of the parameter space and the proxy adopted for the actual covering factor. These results are used as statistical tools of comparison, while a physical description of the evolution of the covering factor with any of these parameters would require a detailed modelling, beyond the scope of this work.

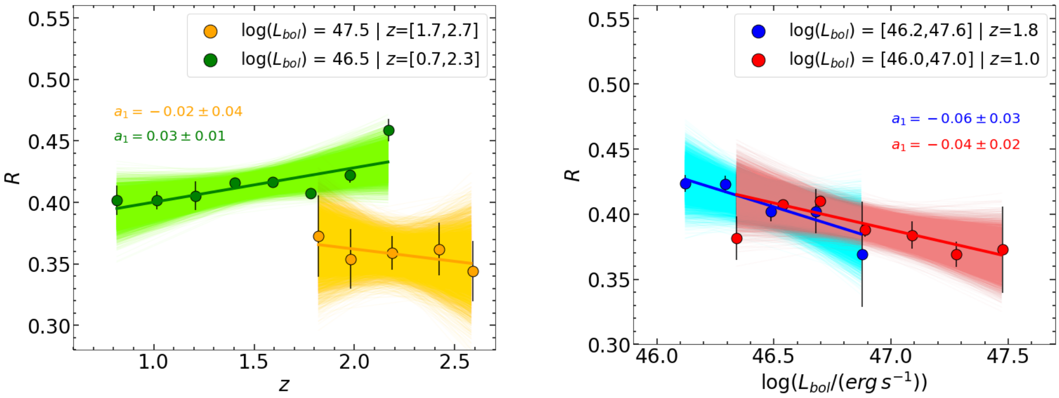

Figure 4.9. *Left:* z–R (left) and log(L$_{\rm bol}$)–R (right) section of the parameter space for the bins denoted by rectangles in Fig. 4.8. The solid lines represent the best linear fits to the data, while the shaded areas, obtained by resampling the posterior distributions of the best fit parameters, mark the 95% confidence intervals.

In Fig. 4.9 I show, as an example, the $z - R$ and the log(L$_{\rm bol}$) − R projections of the parameter space highlighted as rectangles in Fig. 4.8, together with the best-fit relations. In brief, although the best fit slopes for the $R - z$ relation along the different sections of the parameter space can be significantly different from zero, the average of the overall distribution is consistent with zero.

In general, the partial correlation coefficients clearly indicate L$_{\rm bol}$ as the main driver of the correlation ($\rho = -0.734$, p-value=1×10^{-10}, $\tau = -0.537$, p-value=$< 10^{-4}$), while at fixed luminosity z plays no role in the evolution of R ($\rho = 0.048$, p-value=0.726, $\tau = -0.099$, p-value=0.222). The same finding is independently testified by the average slopes of the linear regressions: the anti-correlation between L$_{\rm bol}$ and R is systematically detected at all redshifts with the average slope of the linear regressions being $\langle a_{1,L}\rangle = -0.051 \pm 0.012$. On the other hand, the average slope of the $z - R$ relation is on average consistent with zero within 1 σ, being $\langle a_{1,z}\rangle = -0.007 \pm 0.007$.

Parameters (1)	$\rho_{R\,x\|y}$ (p-value) (2)	$\tau_{R\,x\|y}$ (p-value) (3)
$z - R$	0.048 (0.726)	−0.099 (0.222)
log(L$_{\rm bol}$) − R	−0.734 (10^{-10})	−0.537 ($< 10^{-4}$)

Table 4.1. Correlation parameters between z, log(L$_{\rm bol}$) and R. Columns represent respectively: correlated parameters (1), partial correlation index between R and parameter x keeping y fixed and associated p-value using the Spearman correlation index (2), partial correlation index between R and parameter x keeping y fixed and associated p-value using the Kendall τ correlation index (3).

These results suggest that the covering factor, here parametrised by its proxy R, does not evolve with redshift, and its evolution is only driven by the AGN luminosity.

Parameters (1)	$\langle a_0 \rangle$ (2)	$\langle a_1 \rangle$ (3)
$z - R$	0.388 ± 0.008	-0.007 ± 0.007
$\log(\mathrm{L_{bol}}) - \mathrm{R}$	0.392 ± 0.004	-0.051 ± 0.012

Table 4.2. Best fit parameters of the relations between z , $\log(\mathrm{L_{bol}})$ and R. Columns represent respectively: fitted parameters (1) mean coefficients of the best-fit polynomial and relative standard errors of the means (2, 3).

A direct consequence of this finding, on which I will come back when discussing these results, is the self similarity of the innermost region of the AGN throughout all cosmic times, at fixed luminosity.

4.5.3 The full sample SED

In Fig. 4.10 I show the comparison between the total composite obtained using the full sample with other SED templates in the literature (Richards et al. 2006; Krawczyk et al. 2013; Saccheo et al. 2023). Additionally, I show in black the spectral composite from Lusso et al. (2023) to compare this photometric SED to Euclid NIR spectroscopy. The SEDs are scaled by their integrated luminosity between 1,000 Å and 1 μm for a proper comparison. In the optical, the global SED built here resembles those from Richards et al. (2006) and Krawczyk et al. (2013), as expected since also these works were based on SDSS samples. In the IR the WISSH average SED from Saccheo et al. 2023 outshines the SDSS-based samples, again unsurprisingly, being the WISSH quasars IR-selected. The small blue bump associated with the Fe II UV pseudo-continuum between 2250–3300 Å (e.g. Grandi 1982), visible in the other average SEDs, instead appears to have been well subtracted in this global SED.

4.5.4 Evolution of *CF* with the Eddington ratio

The Eddington ratio expresses the efficiency of the accretion process in AGN, with sources emitting close or above the Eddington ratio having reached their maximal radiative emission under the assumption of spherical accretion. Despite this simplistic approximation, this parameter represents a reasonable proxy for the normalised accretion rate. By scaling the emitted luminosity by the black hole mass (which sets the black hole sphere of influence), the Eddington ratio is a *scale invariant* quantity, in contrast with the bare $\mathrm{L_{bol}}$. Tori with similar covering factors possibly share similar accretion properties (see e.g. Ricci et al. 2023 and references therein).

With the aim of investigating this possibility, I explored the evolution of the covering factor within the accretion parameter space, i.e. the parameter space given by $\log(\mathrm{M_{BH}})$ and $\log(\mathrm{L_{bol}})$[7]. Since I just showed that the seeming dependence of the covering factor on z actually derives from the effect of the luminosity, here I do not take into account any redshift effect. For this analysis, I basically repeated the same

---

[7] Although the axes of this parameter space are physically not correlated, I highlight that from an observational standpoint they are. Both the estimators for $\mathrm{M_{BH}}$ -computed via the virial calibrations- and $\mathrm{L_{bol}}$ -obtained through bolometric corrections- depend generally on the same continuum monochromatic luminosity.

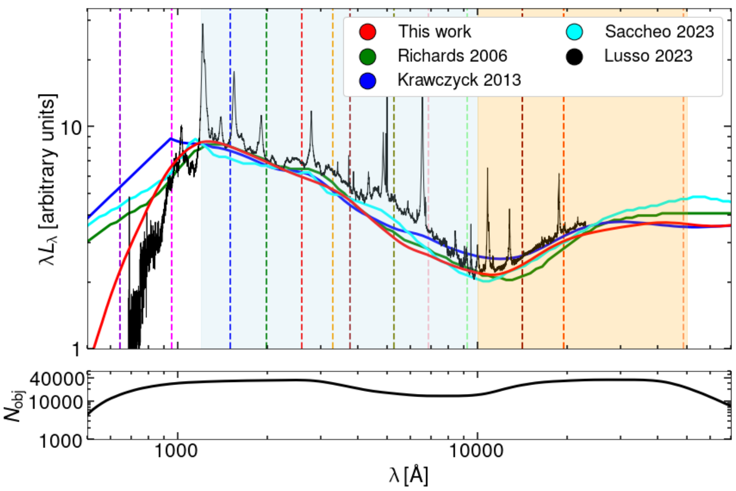

Figure 4.10. Our full sample SED and others from literature (see text). The vertical dashed lines represent the effective wavelengths of the photometric filters used in this work, adopting the same colour code as in Fig. 4.4 blue-shifted to the mean redshift of the sample. All the SEDs are normalized by their integrated luminosity between 1,000 Å and 1 μm. The AGN spectral composite from Lusso et al. (2023) is scaled to match the full sample SED (red solid line) at 2,200 Å. The black line in the bottom panel shows the number of sources contributing per spectral channel in the average SED.

steps adopted to build the log($L_{\rm bol}$)-z parameter space, keeping the same binning width. I then proceeded to produce the average SEDs and evaluate R accordingly. I also computed in each bin the average $\lambda_{\rm Edd}$. This alternative parameter space, together with the R parameter in colour-code, is shown in Fig. 4.11. Considering the values of the log($L_{\rm bol}$)–R and the log($\lambda_{\rm Edd}$)–R standard correlations (i.e. non partial) significant correlations for both the relations, as expected, are found. In particular, for log($L_{\rm bol}$)–R I report ρ=−0.895 with p-value$< 10^{-20}$ and for log($\lambda_{\rm Edd}$)–R ρ=−0.465 with p-value 10^{-4}. Although both anti-correlations are statistically significant, the face values suggest that the stronger driver of the two, in the evolution of the covering factor, is the luminosity. Similar conclusions were reached by employing the τ index of correlation, which gives τ=−0.708 (p-value = 8×10^{-17}) and τ=−0.346 (p-value = 5×10^{-5}) respectively for $L_{\rm bol}$–R and $\lambda_{\rm Edd}$–R. A more informative way to tackle this question is to perform again a PCA, this time within the accretion parameter space, and check *a posteriori* the direction of the strongest correlation. I performed this test on the bins residing in the region quite uniformly populated, marked as a black rectangle in Fig. 4.11. As described in Sec. 4.5.2, I evaluated the PCA between log($L_{\rm bol}$) and R, while keeping log($M_{\rm BH}$) fixed and vice-versa. I also evaluated the uncertainty on the direction of the strongest correlation by performing a bootstrap resampling. The PCA arrow aligns almost completely ($\theta = -84°$) with the direction of decreasing log($L_{\rm bol}$). In Fig. 4.11 I show the PCA direction of increasing R as a black arrow. As a comparison, I also mark as a magenta arrow the direction of decreasing $\lambda_{\rm Edd}$, which should be followed by an increase of the covering factor if the Eddington ratio were the main driver of the CF evolution. Clearly, the effect of $L_{\rm bol}$ is stronger than that of the Eddington ratio in driving the evolution of CF.

Again, $L_{\rm bol}$ appears as the main driver in the evolution of CF, despite the large

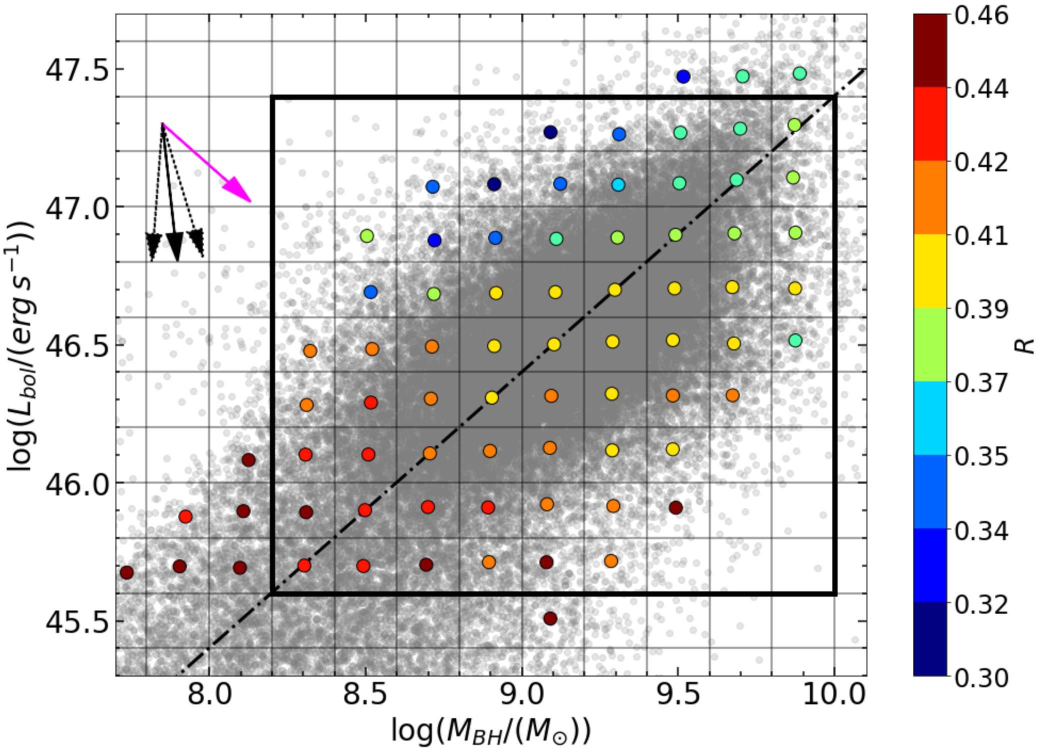

Figure 4.11. log(M_{BH})–log(L_{bol}) plane with R in colour-code. The black rectangle shows the region where the PCA was evaluated. The black solid and dotted arrows represent the direction of the strongest correlation as in Fig. 4.8. The dot-dashed line marks a constant λ_{Edd}=0.2, representing the average value of the sample, while the magenta arrow shows the direction of decreasing λ_{Edd}.

systematic uncertainties on the black hole masses of the current calibrations (0.3–0.5 dex, see e.g. Vestergaard and Peterson 2006), which do not provide reliable estimates of λ_{Edd}, thus possibly diluting any correlation with λ_{Edd}.

4.5.5 The non-evolution with z of the torus in AGN: implications for the X-ray obscured fraction

The analyses carried out so far strongly suggest a non-evolution with z of the torus properties, at least in its innermost region for the blue Type 1 AGN included in this sample. When this evidence is coupled with the seeming non-evolution of the optical/UV SED between local and high redshift quasars, it appears that the nuclear structure in blue quasars only depends on the (mass-normalised) luminosity of the nucleus, regardless of the cosmic epoch. Within the Unified Model, a redshift-independent torus geometry translates into a constant fraction of optical Type 1 AGN at fixed luminosity (see e.g. Fig. 6 in Merloni 2003) at all cosmic times. As an application of this result, it is possible to employ the covering factor derived from L_{NIR}/L_{opt} to set a lower limit for the X-ray obscuration. X-ray obscuration can be indeed delivered on different scales (nuclear/circumnuclear and galactic), and by dusty and/or dust-free gas. If the amount of obscuration imparted by the torus does not vary with redshift, any kind of evolution in the obscuring medium should occur elsewhere.

I thus aimed at comparing the covering factor here derived via the $L_{\rm NIR}/L_{\rm opt}$ ratio with that estimated in several X-ray surveys. I achieved this by converting the proxy into the actual covering factor adopting standard prescriptions. In particular, I show that, adopting reasonable assumptions regarding the disc emission and the torus opening angle, it is possible to reproduce the X-ray obscured fraction at $z \sim 0$, and set a lower limit for the X-ray obscuration.

To assess the degree of obscuration ascribable to the torus and compare it with other samples in literature, I selected all the bins in the $\log(\rm L_{bol}) - z$ plane between $46.8 \leq \log(\rm L_{bol}) \leq 47.2$ and $0.9 \leq z \leq 2.9$. This region of the parameter space is densely populated and allows to sample a wide redshift interval also covered by the X-ray samples. I then converted the observed $R = L_{\rm NIR}/L_{\rm opt}$ into the covering factor CF by scaling these observed quantities respectively to the total torus and disc luminosities following this procedure. First, I assumed that the disc emission comes from a standard optically thick and geometrically thin accretion disc (Shakura and Sunyaev 1973). I evaluated its SED in each bin using the average $\rm M_{BH}$ and converting the observed $\rm L_{bol}$ into the accretion rate assuming a standard mass-to-luminosity conversion efficiency of 0.1. I also explored other values for the efficiency, but the variations in the plausible range of opening angles were of the order of some degrees. I then scaled the far infrared quasar template from Lyu and Rieke (2017) to match the 1-μm emission of the accretion disc. This allowed to consider also the FIR torus emission up to 1,000 μm. Lastly, I computed the total disc luminosity between 10 Å and 1 μm and the total torus luminosity between 1 μm and 1,000 μm, and used these quantities to scale the observed luminosities which are instead integrated between ~1,000 Å–1 μm, and 1–5μm. In order to explore the effect of the anisotropy of the radiation field of the accretion disc and the clumpiness of the torus, I also employed the total disc and torus luminosities to evaluate the CF adopting the Stalevski et al. (2016) prescriptions.

I show the result of this approach in Fig. 4.12. There, I compare the CF values derived here to the fraction of X-ray obscured objects (with column density $N_{\rm H} > 10^{22}$ cm^{-2}) according to different literature samples (Aird et al. 2015; Buchner et al. 2015; Ananna et al. 2019; Peca et al. 2023). When the AGN sample included only Compton-thin objects, I adjusted the obscured AGN fractions by assuming an equal number of Compton-thin and Compton-thick sources (e.g. Gilli et al. 2007; Ananna et al. 2019). The chosen X-ray luminosity regime is $L_X \sim 10^{45}$ erg s^{-1}, which roughly corresponds to $\rm L_{bol} \sim 10^{47}$ erg s^{-1} adopting the Duras et al. (2020) X-ray to bolometric conversion. Here the obscured fractions of the reference samples were corrected for the effect of the Malmquist bias, which reduces the fraction of observed obscured sources, by assuming intrinsically equal amounts of obscured and unobscured sources (i.e. p=0.5 in Eq. 1 in Signorini et al. 2023a).

In the plot are also highlighted the curves from the analytical model described in Gilli et al. (2022) accounting for both the ISM and the torus absorption in the X-rays, corresponding to $\delta = 3.3$, $\gamma = 2.0$, and $\theta = 60°$ (black solid line), and $\theta = 70°$ (black dotted line), which encompass the possible range of CF values. Here δ is the exponent in the relation between the column density ($N_{\rm H}$) and z, i.e. $N_{\rm H} \propto (1+z)^{\delta}$, γ is the exponent in the relation describing the evolution of the surface density of the molecular clouds (Σ) with z, that is $\Sigma \propto (1+z)^{\gamma}$ and θ is the torus half-opening angle evaluated from its vertical axis. I also display as shaded rectangles the inferred *CF* directly estimated as the infrared-to-optical luminosity ratio (salmon) as well as according to the Stalevski et al. (2016) recipe (maroon). The lines guide the eye at the redshifts not actually sampled by the $L_{\rm bol} \sim 10^{47}$ erg s^{-1} bins.

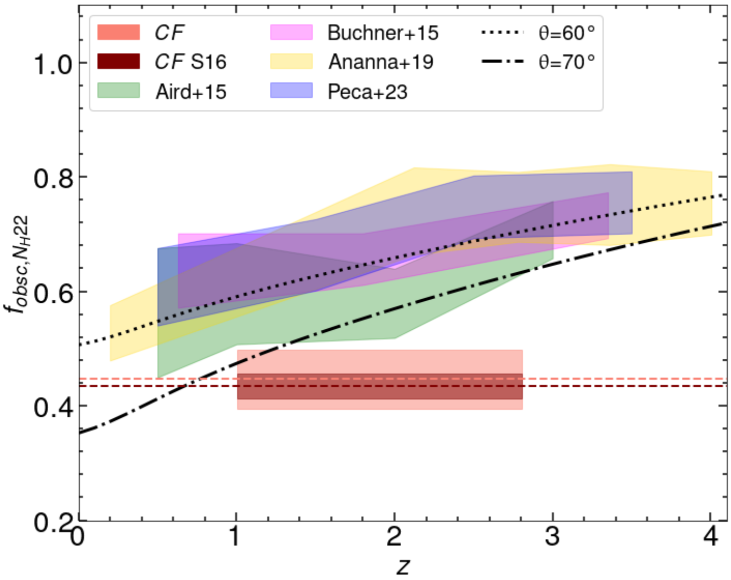

Figure 4.12. Obscured AGN fraction with $N_{\rm H} > 10^{22}$ cm^{-2} as a function of redshift in different literature samples (Aird et al. 2015; Buchner et al. 2015; Ananna et al. 2019; Peca et al. 2023, including a correction for Compton thick sources, see text for details. The horizontal shaded areas represent the different inferred ratios between the torus and the disc luminosities, as well as the intrinsic *CF* according to the Stalevski et al. (2016) prescriptions. These values are extrapolated at the redshifts not directly covered by the bins at $\log(L_{\rm bol}) \sim 47$ accordingly to the dashed lines. The black dotted and dot-dashed lines correspond respectively to the Gilli et al. (2022) models for δ=3.3, γ=2.0 and θ=60°, and 70°.

Assuming a plausible range of opening angles, the model curves manage to reproduce the X-ray obscured fraction, which at $z = 0$ can be explained by the torus alone. The resulting opening angles implied by the model are consistent with other independent estimates derived from modelling of the infrared emission in Type 1 AGN (e.g. Almeida et al. 2011; Ichikawa et al. 2015). Interestingly, also studies not directly aimed at investigating the torus properties provided evidence for similar values. For instance, Signorini et al. (2024), while attempting to explain the remarkably small intrinsic dispersion of the $L_X - L_{UV}$ relation, thoroughly discussed in 1.3, found – in a completely independent way – the need for the presence of a toroidal structure obscuring the accretion disc with an opening angle $\gtrsim$65° from the disc axis.

Although the obscuration provided by the torus does not appear to vary with z, the X-ray obscured fraction does instead appear to increase. This observational trend calls for some sort of redshift-dependent absorber. Yet, the nature of this additional component is not clear, nor are the scales where the absorption of the

X-rays should happen. In principle, an increase of dust-free gas in the micro-scale (i.e. the BLR) and/or dust and gas in the macro-scale (i.e. the ISM scale) towards earlier cosmic times could go in the direction of bridging between the degree of obscuration derived in optical/infrared and X-ray surveys.

4.6 Discussion

Understanding the evolution of the covering factor and its dependence on the parameters regulating the accretion process is a crucial step towards unveiling the complicated and dynamic structure of AGN. In this effort, valuable information can be gathered by exploring the broadband correlations between the main emission from the accretion disc and the reprocessed emission by the dusty torus in the infrared. The large photometric dataset presented here, spanning roughly two and a half orders of magnitude in terms of bolometric luminosity, has been purposefully assembled to explore these correlations up to $z \sim 3$, when the Universe was about 2 Gyr old.

Here, I showed that the disc luminosity acts as the main driver in the evolution of the NIR properties in the sample, representative of blue unobscured Type 1 AGN. This results in an anti-correlation between the AGN luminosity and the torus covering factor, here parameterised via the ratio R between the NIR and the UV/optical luminosity. Conversely, the redshift does not play a significant role, as the CF does not evolve between low- and high-z objects at fixed luminosity.

The large sample analysed in this part of my work provides compelling evidence against a redshift evolution of the dusty torus geometry, at least in its innermost, hottest region. The NIR SED does not exhibit any evolution with z, once the dependence on the luminosity is considered and the effect of the shifting wavebands is taken into account. The most likely driver in the covering factor appears to be the AGN luminosity, whose intensity directly shapes the circumnuclear surroundings. In a broader perspective, the similarity of the SEDs between low- and high-redshift quasars is remarkable. As already mentioned, the optical/UV SEDs of blue unobscured AGN are barely sensitive to the passing of cosmic time since $z \sim 7$ (e.g. Kuhn et al. 2001; Mortlock et al. 2011; Hao et al. 2013b; Shen et al. 2019; Yang et al. 2021; Trefoloni et al. 2024c). Similar considerations apply to the interplay between the accretion disc and the X-ray coronal emission. Their coupling, epitomised in the $L_{\mathrm{X}} - L_{\mathrm{UV}}$ relation (Tananbaum et al. 1979), does not exhibit any appreciable redshift evolution up to $z \sim 7$ (Lusso et al. 2015; Risaliti and Lusso 2019; Salvestrini et al. 2019; Nardini et al. 2019b; Lusso et al. 2020) once observational biases have been removed. Again, it is important to stress that the similarity between low- and high-redshift quasars also holds in terms of broad emission line properties. Several works investigating the evolution of the broad lines in large samples of quasars have indeed demonstrated the absence of significant redshift trends at fixed luminosity (Croom et al. 2002; Nagao et al. 2006; Stepney et al. 2023). Analogue results have been obtained when investigating the chemical enrichment of the BLR, parameterised, for instance, via the UV Fe II to Mg IIλ2798 ratio, which, as discussed in Sec.3.4.1, does not evolve up to $z \sim 7$ (Dietrich et al. 2003a; Mazzucchelli et al. 2017; Sameshima et al. 2020; Wang et al. 2022b; Trefoloni et al. 2023; Jiang et al. 2024). Putting together these pieces of evidence, what follows is that the quasar nuclear environment, i.e. the ensemble made of corona, accretion disc, BLR, and torus, is barely sensitive to the redshift, once the accretion parameters are fixed. The striking similarity between high- and low-redshift AGN goes in the direction of an early assembly of the nuclear region in luminous AGN, with the BLR of high-redshift quasars being already enriched by $z \sim 7$ and the circumnuclear torus shaped according to the quasar radiation field.

A direct comparison with other works exploring the correlations between the CF and the accretion parameters is not straightforward. There are indeed several technical limitations on the available wavebands at different redshifts, as well as different proxies adopted in literature to estimate the covering factor. For instance, earlier works on the PG quasars (Cao 2005) adopted the 3–10 μm interval to estimate $L_{\rm IR}$, while both Gu (2013) and Rałowski et al. (2023) adopted the 1–7 μm interval and, more recently, Wu et al. (2023) took advantage of the 1–10 μm band. Conversely, Lusso et al. (2013) and Ichikawa et al. (2019) performed a torus–galaxy decomposition first, and then integrated the best-fit torus model between 1–1,000 μm. Similar considerations apply to the choice of $L_{\rm opt}$. Despite these minor differences in the adopted proxies to the covering factor, the results highlighted here follow the trend generally observed in studies using $L_{\rm IR}/L_{\rm opt}$ as a proxy to CF, which find an anti-correlation between CF and both the disc luminosity and the Eddington ratio (Treister et al. 2008; Maiolino et al. 2007; Calderone et al. 2012; Ma and Wang 2013; Ezhikode et al. 2017; Toba et al. 2021; Rałowski et al. 2023, although there are also claims of non-correlations e.g. Gu 2013; Zhuang et al. 2018). It is also important to remark that the choice of the IR integration interval does not only play a role in the comparison between different literature works, but is also key when it comes to assessing the strength of the anti-correlation between the disc and the torus luminosities. For example, when the MIR wavelengths ($\gtrsim$ 10 μm) are included in the torus luminosity estimate, the cooler polar dust emission can add up to that coming from the torus, hence diluting the correlation (Wu et al. 2023).

An update of the canonical unification paradigm, the so-called "radiation-regulated Unification Model" (Ricci et al. 2017), adds the accretion rate as a further parameter playing a crucial role in the classification of an AGN. In this framework, highly accreting sources are more efficient in clearing their close environment and shaping the circumnuclear toroidal structure, by means of radiation pressure (Pier and Krolik 1992; Fabian et al. 2008) and outflows (Fabian et al. 2009). The correlation observed between CF and $\lambda_{\rm Edd}$ in the data presented here supports this scenario. Yet, the degree of correlation between R–$\rm L_{bol}$ and R–$\lambda_{\rm Edd}$ favours the former as a stronger driver of the CF evolution. There are several explanations for this result: if the luminosity were the actual stronger driver, expressing the correlation in terms of observed quantities for the bulk of the sample, $\rm L_{bol} \propto L_{3000Å}$ and $\lambda_{\rm Edd} \propto L_{3000Å}/(\rm FWHM^2_{MgII}\, L^{1/2}_{3000Å}) \propto L^{1/2}_{3000Å}$, the lower degree of correlation would come from the lower exponent of the luminosity term. Conversely, it is also possible that the Eddington ratio is the actual parameter driving the evolution of the CF, but the large systematic uncertainties on the $\rm M_{BH}$ estimates reduce the degree of correlation. Lastly, it is also possible that the Eddington ratio is actually an important factor in shaping the dusty torus, but not in the λ_{Edd} range covered by the sample. This is what has been shown in recent studies, parameterising the

CF as the fraction of X-ray obscured sources. These works argued that the strongest decrease in the CF for increasing λ_{Edd} occurs between $\log(\lambda_{\text{Edd}}) \simeq -3$ and -1 (Ricci et al. 2017; Mizukoshi et al. 2024). As a comparison, the bulk of the sample has $\lambda_{\text{Edd}} \gtrsim -1.2$.

Once the redshift evolution of the torus covering factor is abandoned in favour of the accretion parameters being the sole drivers in the torus shape, any redshift-dependent obscuration, such that reported in X-ray surveys, must be delivered elsewhere. Generally speaking, X-ray obscuration can occur on different scales, ranging from nuclear to galactic scales. Although there is strong evidence in favour of X-ray obscuration happening also because of dust-free gas within the BLR (Maiolino et al. 2001; Risaliti et al. 2002; Goulding et al. 2012; Ichikawa et al. 2019; Ricci et al. 2022), there are not observational clues about gas richer BLR with increasing redshift: as already mentioned, luminosity-matched samples of Type 1 AGN at low and high redshift display on average broad emission lines with comparable strength (e.g. Croom et al. 2002; Stepney et al. 2023). However, on galactic scales, the combination of increasing ISM mass (e.g. Scoville et al. 2017) and decreasing galactic sizes with redshift (e.g. Allen et al. 2017) naturally implies the increase in the ISM density. This, in turn, could provide an additional source of X-ray opacity (Gilli et al. 2022; Alonso-Tetilla et al. 2024), whose relevance is expected to increase with z, thus going in the direction of increasing the fraction of X-ray obscured sources.

4.7 Summary and conclusions

In this part of my thesis, I gathered a large photometric dataset containing ~36,000 blue quasars to analyse separately the evolution of the NIR properties of blue Type 1 AGN with the redshift and the bolometric luminosity. The main conclusions for this chapter are listed below:

- The average NIR emission in different luminosity bins clearly shows a decreasing trend for increasing L_{bol}. Once the effect of the shift of the sampling wavebands at different redshifts is taken into account, the average NIR SEDs at different z are mostly consistent with an intrinsic standard torus SED. This finding, coupled with the other pieces of evidence of non evolution of accretion disc, BLR and coronal emission in blue quasars, goes in the direction of a universal (but luminosity-dependent) quasar SED.

- All the explored proxies for the covering factor do not correlate with the redshift, once the bolometric luminosity is kept fixed.

- The ratio, R, between the NIR and optical/UV luminosities, chosen as a proxy to the intrinsic CF, anti-correlates with the bolometric luminosity ($\rho = -0.734$) regardless of the redshift. This finding fits within the so-called "receding torus" scenario, where the radiation field from the inner AGN is capable of shaping the structure of the dusty torus.

- R also significantly anti-correlates with the Eddington ratio, but this trend is likely due to the dependence of λ_{Edd} on L_{bol}. This is confirmed by the fact that the direction of strongest variation of R in the accretion parameter space aligns with L_{bol} rather than with λ_{Edd}.

- A direct consequence of the non-evolution of the torus covering factor with z is that any increase in the X-ray obscuration with redshift, if systematically detected, should occur by means of some other mechanism, either on nuclear or galactic scales.

This systematic investigation of the interplay between the optical and infrared broadband properties of Type 1 AGN provides evidence for a standard NIR torus SED. The properties of the torus seem to be mostly governed by the luminosity of the nucleus, regardless of the redshift. In spite of the wide sample gathered here, a key step forward will be the detection of a statistically significant number of faint high-redshift objects in the rest-frame infrared, to test whether this behaviour also holds in the low-luminosity tail of the AGN population at high z. As far-infrared missions such as the Origins Space Telescope (Battersby et al. 2018) still stand out in a not so near future, most of the efforts should be directed in two main directions. A thorough theoretical understanding of the interplay between the disc emission and the patchy torus, taking into account also the action of a disc wind in the process of shaping the circumnuclear environment (e.g. Chan and Krolik 2016 and references therein), would prove of utmost importance. At the same time, a panchromatic effort involving both new and archival X-ray data would definitively deepen our knowledge in the canonical classifications between optical and X-ray Type 1/2 AGN.

4.8 Supplementary Material

4.8.1 On the reliability of WISE photometry

During its primary mission WISE measured the full sky in four mid infrared bands centered on 3.4, 4.6, 12, and 22 μm, but the exhaustion of the solid hydrogen cryogen made W4 unusable. After this, the survey continued another half-sky scan in W1, W2, and W3. For the sake of comparison, before the reactivation of the WISE survey (NEOWISE, Mainzer et al. 2014), the median coverage in the W1 and W2 bands was 33 exposures, 24 in W3 and only 16 in W4 (Lang et al. 2016). This, combined with the lower relative response made the W4 WISE survey significantly shallower than in the other bands.

The inclusion of these photometric data could, in theory, bias towards higher than the average IR fluxes, especially at high redshift ($z > 2$) where the 1–5 μm range becomes increasingly contained within the W4 passband. In order to check whether this is the case, I compared the Spitzer First Look Field (FLS, PID: 26; PI: B. T. Soifer) observed by the SPITZER Multiband Imaging Photometer for SPITZER (MIPS) photometry at 24 μm (M24) with that of WISE W4. To this purpose, I cross-matched the SPITZER FLS MIPS24 (16,905 sources) and the AllWISE point source catalogues adopting a 2" matching radius, obtaining 11,253 matches. In Fig. 4.13 I show the result of the comparison, colour-coding the W4 SNR. It is evident that at low fluxes (and SNR) the W4 photometry, including also upper limits which amount to ~75% of the matches, overestimates the actual flux. The high incidence of the upper limits is likely due to the low sensitivity in the W4 band, while the large fraction of overestimates likely resulting from the larger aperture (16.5") adopted for the W4 filter. Because of this systematic overestimation at low fluxes, I refrained from using W4 photometry. I show as solid and dotted lines the median and lowest 5^{th} percentile of the flux distribution for the sample adopting the quality cuts described in the main text, i.e. mag$i$<19.0, the colour selection and the choice of the $0.1 \leq z \leq 2.9$ redshift interval. The red lines represent the same values after adding also the SNR≥2 criterion on W3 photometry.

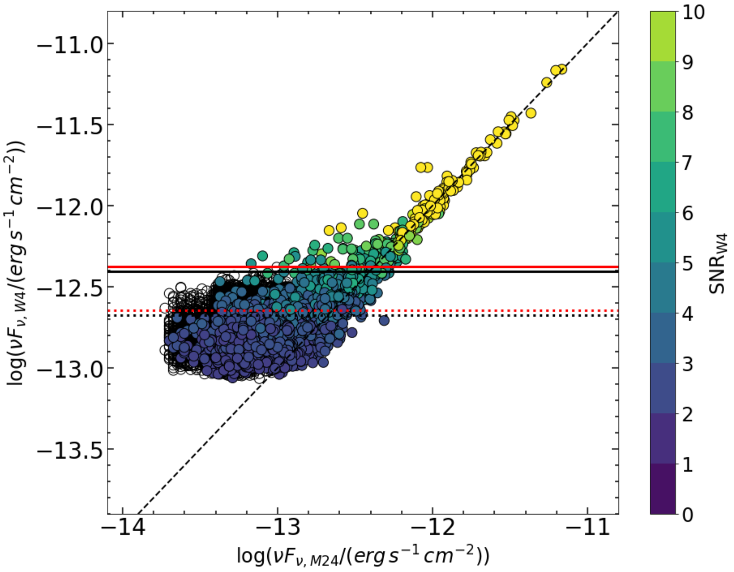

Figure 4.13. Comparison between SPITZER MIPS24 and W4 photometry as a function of W4 SNR in colour-code. Empty circles in the background denote upper limits. W4 measurements are systematically overestimating the actual fluxes at low SNR. The black solid (dotted) horizontal line marks the median (lowest 5^{th} percentile) flux for the objects in the sample without performing the quality cuts described in the text. The same holds for the red lines where also the SNR≥2 cut is applied. A significant amount of the sources in the sample would have systematically overestimated W4 fluxes.

I also performed the same exercise to check the reliability of the W3 measurements. However, this check was only possible on a much smaller (557 sources) sample of targets, obtained by cross-matching the Spitzer/IRAC and Spitzer/IRS data in the GOODS North and South fields (Giavalisco et al. 2004) with the AllWISE catalogue. In order to evaluate the monochromatic flux at the W3 reference wavelength (12 μm), I logarithmically interpolated the flux of the two closest Spitzer bands, namely IRAC 8 μm and IRS 16 μm. I show the result of this match in Fig. 4.14. Also in this case it is possible to observe a trail detaching from the one-to-one relation, although the average difference between the $\log F_\nu$ for Spitzer and WISE is lower than in the W4 vs. MIPS24 comparison (−0.22 dex after selecting sources with SNR W3 ≥2 against −0.42). Also in this case the lowest SNR points are increasingly more offset from the identity line. Yet, in this case even the lowest 5^{th} percentile of the flux distribution for the SDSS-WISE sample lies above the flux value where W3 starts to systematically overestimate the actual flux with respect to Spitzer. This implies that, within the sample employed here, the effect of overestimating the W3 fluxes has a negligible impact.

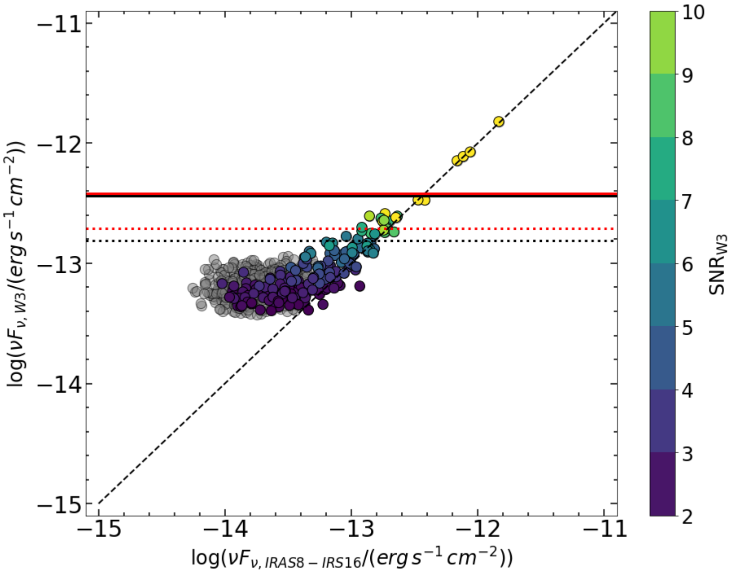

Figure 4.14. Comparison between the 12-μm fluxes interpolated between SPITZER IRAC 8 μm and IRS 16 μm and W3, with the W3 SNR in colour-code. The grey dots denote sources below the W3 SNR=2 threshold chosen in this work. The black solid (dotted) horizontal line marks the median (lowest 5^{th} percentile) flux for the objects in the sample without performing the quality cuts described in the text. The same holds for the red lines where also the SNR≥2 cut is applied. Although there is a trail of points detaching from the one-to-one relation at low SNR W3 (~4–5), roughly 95% of the sample has fluxes higher than the threshold where W3 starts to systematically overestimate the Spitzer measurements. The colour-code of the lines is the same as in Fig.4.13.

4.8.2 Consistency checks

The selection of 5 μm as the longest wavelength to sample the torus emission was chiefly dictated by the trade-off between choosing a wavelength well within the IR regime and the maximal observability throughout the sample. At the same time, the choice of employing the ratio $L_{\rm NIR}/L_{\rm opt}$, evaluated respectively between 1–5 μm and 1,000 Å − 1 μm, as a proxy for the intrinsic CF was mainly due to the data-driven approach employed here. As consistency checks, I performed the same analyses described in the main text adopting different proxies for the NIR term of the CF and alternative data sets.

- I explored the adoption of the 2–5 μm interval for estimating the IR term contained in R (subset $R_{2-5\,\mu m}$ in Table 4.3). A longer wavelength for the lower end of the IR term is more reliable when it comes to estimate the torus emission, being less prone to stellar emission within the host galaxy. The price for this choice is, however, the narrowing of the integration interval and the consequent lowering of the R value.

Subset (1)	Parameters (2)	$\rho_{R\,x\|y}$ (p-value) (3)	$\tau_{R\,x\|y}$ (p-value) (4)	$\langle a_0 \rangle$ (5)	$\langle a_1 \rangle$ (6)
$R_{2-5\mu m}$	$z-R$	0.459 (4×10^{-4})	0.133 (0.100)	0.247 ± 0.003	0.009 ± 0.005
$R_{2-5\mu m}$	$\log(\mathrm{L_{bol}})-\mathrm{R}$	-0.737 (10^{-10})	-0.465 $(<10^{4})$	0.250 ± 0.001	-0.031 ± 0.009
$R_{1-5\mu m\,peak}$	$z-R$	-0.028 (0.836)	-0.104 (0.196)	0.425 ± 0.013	-0.003 ± 0.017
$R_{1-5\mu m\,peak}$	$\log(\mathrm{L_{bol}})-\mathrm{R}$	-0.448 (6×10^{-4})	-0.328 $(<10^{4})$	0.424 ± 0.007	-0.074 ± 0.019
R_{S16}	$z-R$	0.048 (0.726)	-0.099 (0.219)	0.580 ± 0.005	-0.005 ± 0.004
R_{S16}	$\log(\mathrm{L_{bol}})-\mathrm{R}$	-0.740 (10^{-10})	-0.537 $(<10^{4})$	0.583 ± 0.002	-0.031 ± 0.008
CF_{L13}	$z-R$	0.048 (0.726)	-0.099 (0.222)	0.279 ± 0.004	-0.004 ± 0.003
CF_{L13}	$\log(\mathrm{L_{bol}})-\mathrm{R}$	-0.740 (10^{-10})	-0.537 $(<10^{4})$	0.282 ± 0.002	-0.026 ± 0.006
no-corr	$z-R$	0.155 (0.260)	-0.0459 (0.572)	0.331 ± 0.006	-0.002 ± 0.005
no-corr	$\log(\mathrm{L_{bol}})-\mathrm{R}$	-0.746 (7×10^{-11})	-0.533 $(<10^{4})$	0.334 ± 0.002	-0.043 ± 0.011
no-col	$z-R$	0.011 (0.937)	-0.142 (0.077)	0.371 ± 0.008	-0.011 ± 0.010
no-col	$\log(\mathrm{L_{bol}})-\mathrm{R}$	-0.726 (4×10^{-10})	-0.531 $(<10^{4})$	0.375 ± 0.004	-0.055 ± 0.013

Table 4.3. Correlation parameters between z , $\log(\mathrm{L_{bol}})$ and alternative CF proxies also considering alternative data sets. Columns represent respectively: alternative CF proxy or alternative data-set (1) described in 4.8.2, correlated/fitted parameters (2), Spearman partial correlation index between CF and parameter x keeping y fixed and relative p-value (3). Kendall τ partial correlation index between CF and parameter x keeping y fixed and relative p-value (4). Mean coefficients of the best-fit polynomial and relative uncertainties (5, 6).

- I explored the possibility of integrating the accretion disc SED between its peak and 1 μm rather than in the fixed 1,000 Å–1 μm interval (subset $R_{1-5\mu m\,\mathrm{peak}}$).
- With the aim of taking into account the effect of the anisotropy of the accretion disc radiation field, as well as the clumpiness of the torus, I tested the parameterisation described in Stalevski et al. 2016. To this end, I scaled R to the total ratio between the 1–1,000 μm infrared luminosity and the disc luminosity. Thiw was achieved by adopting the quasar template SED built in Sec.4.5.1 (subset CF_{S16}).
- I also explored the CF the expression described in Lusso et al. (2013), i.e. $CF = R/(1+(1-p)R)$, where the p parameter takes into account the optical depth of the torus to its own radiation. An optically thin torus has p=0, whereas an optically thick torus has p=1 (subset R_{L13}).
- As additional checks to make sure that the corrections made to the photometry, as well as the colour selection criterion, have not altered the results, I also present the same results obtained without including these corrections (respectively the subsets "no-corr" and "no-col").

The results evaluated adopting these alternative prescriptions and data sets are shown in Table 4.3. The structure of the table is the same as that of Table 4.1 and 4.2.

Although the absolute value of the CF proxy obviously depends on the parameterisation and the wavelength interval for the L_{NIR} and L_{opt} terms, the trends described in the main text are confirmed adopting all the other possible choices. In the data set where the 2–5 μm interval was adopted a significant correlation appears in between R and z according to the Spearman index. Yet, such trend is not confirmed by neither the Kendall correlation index, nor by the average slope of the fitted regression lines.

4.8.3 The shift of the NIR bump across WISE filters

The appearance of the NIR bump depends on its sampling in the observed-frame filters. As the redshift increases from z=1.0 to z=2.9, the NIR bump is sampled only in its rising part, thus leading to the loss of information about its real shape. Here I show this effect at work on the Hernán-Caballero et al. (2016) template, and how the interpolated/extrapolated SED gets affected.

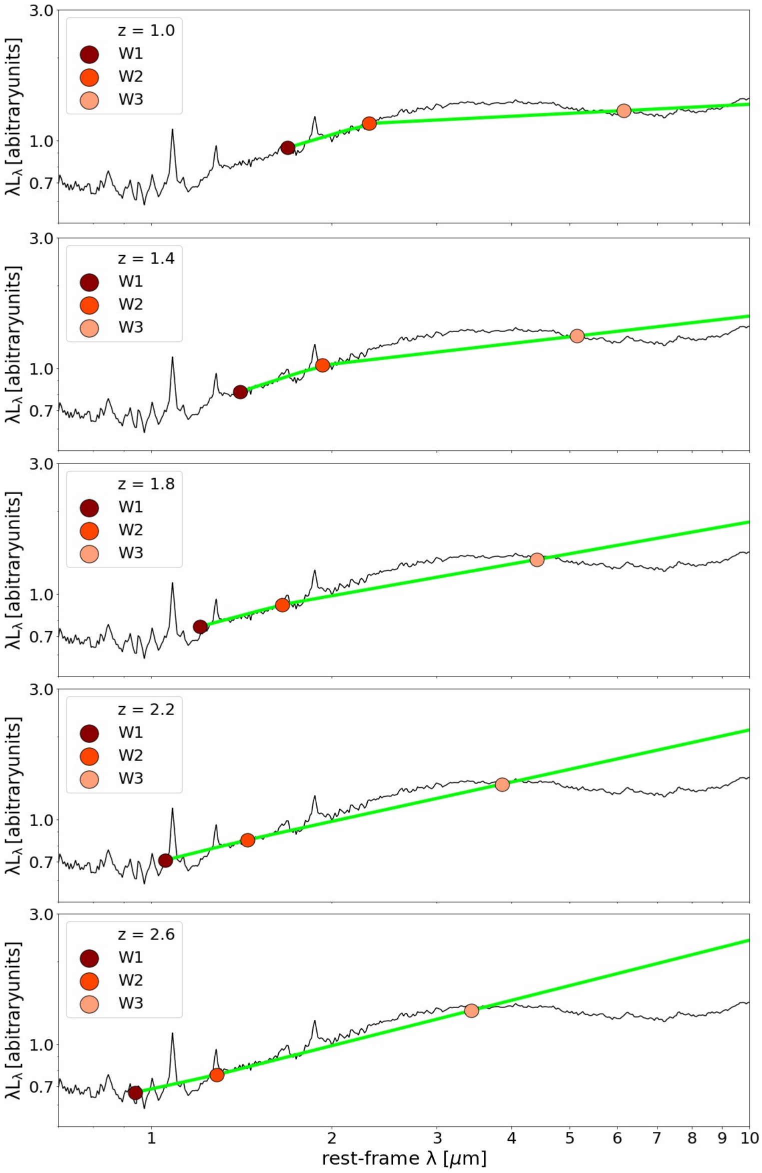

Figure 4.15. The shift of the NIR bump, here represented by the Hernán-Caballero et al. (2016) template (black), across the WISE W1, W2 and W3 filters for increasing z. The green line represents the interpolated/extrapolated SED through the WISE photometric points.

Chapter 5

The missing Fe II bump in faint *JWST* AGN

5.1 Outline

Recent *JWST* observations have revealed a large population of intermediate/low-luminosity AGN at early times with peculiar properties, different from local AGN or luminous quasars. To better understand the physical conditions in the BLRs of these early AGN, I used the optical Fe II (4434–4684 Å) and broad Hβ emission, and the ratio between their equivalent widths $R_{\rm Fe}$, as a probe on a purposefully assembled sample. Specifically, I gathered a sample of 26 high redshift ($\langle z \rangle$=6.4) AGN, observed by *JWST*, with broad Hβ detection both in the high and low luminosity regimes (respectively 14 faint AGN and 12 quasars), to investigate their optical Fe II emission properties. In addition, I carefully selected control samples at lower z. I found that the population of faint AGN ($\log(\mathrm{L}_{\mathrm{H}\beta}/(\mathrm{erg\,s^{-1}})) \lesssim 44$) exhibits a significantly lower Fe II emission than their local counterparts ($R_{\rm Fe}$ <0.24 versus $R_{\rm Fe}$ ≃0.85 in the control sample), while the quasars at the epoch of reionisation observed by *JWST* present a Fe II emission profile that closely resembles that observed at $z < 3$. I argue that the weakness of the Fe II bump in the faint *JWST* AGN might be due to the reduced metallicity of their broad line region ($\lesssim 0.5\ Z_\odot$), while luminous quasars have already reached chemical maturity ($\gtrsim Z_\odot$). Lastly, I highlight an intriguing similarity between the spectral properties of the high redshift population of faint AGN with those harboured in local metal poor dwarf galaxies. The analyses described here are discussed in Trefoloni et al. (2024b).

5.2 Context and aims of the work

The relevance of AGN in the process of shaping galaxies has been already discussed in 1.1.2. Most notably, the energy released from gas accretion onto SMBHs powering the AGN has been shown capable of significantly affecting the star-formation processes within their host galaxies by heating and/or depleting the interstellar medium (ISM, e.g. King 2005; Fabian 2012; Costa et al. 2015; King and Pounds 2015). As a consequence, repeatedly injecting energy into the surrounding ISM, AGN can ultimately lead to the quenching of the galactic star formation. Tracking their ubiquity and investigating their properties through the cosmic ages offers the possibility to follow the assembly history of the Universe.

Recently, our knowledge of the high-redshift ($z \sim 5-11$) Universe has been dramatically expanded through the observations obtained with the *James Webb Space Telescope* (JWST; Gardner et al. 2006). Several deep surveys (down to $mag_{F444W} = 30.65$) carried out within the first *JWST* cycles have indeed revealed a large population of intermediate/low bolometric luminosity ($L_{\rm bol} \sim 10^{42}-10^{45}\,{\rm erg\,s^{-1}}$) AGN with black hole masses (M_{BH}) already grown up to $10^6-10^8\,M_\odot$ within $z \sim$ 6-8 (Kocevski et al. 2023; Harikane et al. 2023; Maiolino et al. 2023; Larson et al. 2023; Onoue et al. 2023; Übler et al. 2023; Greene et al. 2024; Übler et al. 2024) undetected by the previous optical and X-ray surveys of high-z quasars (see e.g. Yang et al. 2023a and references therein).

Most of these new AGN at high-z are identified through the detection of a broad component of Hα or Hβ without a counterpart in [O III], hence excluding an outflow scenario and leaving the Broad Line Region around an accreting black hole as the main plausible explanation (Kocevski et al. 2023; Übler et al. 2023; Maiolino et al. 2023; Matthee et al. 2024; Kocevski et al. 2024; Übler et al. 2024; Kokorev et al. 2023; Greene et al. 2024; Taylor et al. 2024), although some more exotic scenarios have been proposed (Kokubo and Harikane 2024; Baggen et al. 2024). Type 2, narrow line AGN have also been searched, although with the caveat that standard BPT diagrams seem to lose their capability of discriminating between star forming galaxies and AGN at such early epochs (likely because of the low metallicity, Übler et al. 2023; Maiolino et al. 2023), prompting the exploration of other Narrow Line diagnostics (Scholtz et al. 2023; Chisholm et al. 2024; Mazzolari et al. 2024). Interestingly, a number of these newly discovered AGN have peculiar colors, with red optical slopes and blue UV slopes (Labbé et al. 2023; Barro et al. 2023; Greene et al. 2024; Kocevski et al. 2024) and have been dubbed Little Red Dots, although they contribute to only 10–30% of the population of newly discovered AGN (Maiolino et al. 2023; Hainline et al. 2024; Kocevski et al. 2024)

Interestingly, the photometric colours are not the only peculiarities observed in these sources. For instance, their black holes appear to be overmassive with respect to the stellar mass contained within the host galaxy, when compared to the expectations from scaling relations in the local Universe (Maiolino et al. 2023; Übler et al. 2023; Harikane et al. 2023; Kokorev et al. 2023; Furtak et al. 2024; Juodžbalis et al. 2024b; Parlanti et al. 2024; Marshall et al. 2024). Such high-redshift overmassive BHs are predicted by several theoretical models as a direct consequence of super-Eddington accretion and/or direct-collapse black holes (Trinca et al. 2022; Koudmani et al. 2022; Schneider et al. 2023).

Another noticeable feature of faint *JWST* AGN is their X-ray weakness. These sources are systematically undetected even in the X-ray stacks of the deepest *Chandra* fields, such as GOODS-N and GOODS-S (Maiolino et al. 2024; Yue et al. 2024; Kocevski et al. 2024; Wang et al. 2024). Yet, it is still a matter of debate whether the observed X-ray weakness is actually intrinsic (i.e. due to an inefficient or beamed coronal emission, expected in some models, Pacucci and Narayan 2024; Madau and Haardt 2024; Maiolino et al. 2024; King 2024) or rather caused by Compton-thick absorption along the line of sight (for a more detailed discussion see Maiolino et al. 2024).

In addition, low-luminosity *JWST* AGN seem to lack the signature of prominent large-scale ionised winds, which are instead observed even in the low-luminosity tail of the local AGN population (Shen and Ho 2014; Bisogni et al. 2017). This could be explained, at least qualitatively, by considering that the low gas metallicity observed in the NLR of these sources implies lower dust content and consequently lower radiation pressure powering the outflow (Maiolino et al. 2024).

However, a physical picture embracing all the peculiarities featured by this new, elusive population is still far from being formulated. In this framework, valuable pieces of information can be gathered by a careful comparison with typical local AGN, matched in terms of accretion parameters (i.e. luminosity and black hole mass).

In the more local Universe ($z < 1$), AGN are generally observed to share an ensemble of correlations between spectral properties which define the so-called Eigenvector 1, firstly discovered on a sample of 80 Palomar-Green AGN by Boroson and Green (1992b). Several following studies aimed at consolidating the observational trends on more sound statistical basis, and arranged the spectral diversity of local AGN into a four-dimensional correlation space, the so-called 4DE1 (e.g. Sulentic et al. 2000a; Zamfir et al. 2010; Marziani and Sulentic 2014, see also Marziani et al. 2018 for a more comprehensive review). These properties include, among the other features, the anti-correlation between the strength of the narrow [O III] and of the Fe II (e.g. Shen and Ho 2014), the anti-correlation between the full width at half maximum (FWHM) of the Hβ emission line and the ratio between the equivalent width (EW) of the Hβ and that of the Fe II (R_{Fe}; see e.g. Deconto-Machado et al. 2023 and references therein), and the anti-correlation between the modulus of the C IV emission line offset and its EW (e.g., Richards et al. 2011; Rivera et al. 2022; Stepney et al. 2023). Additionally, other noticeable correlations have been observed across different wavebands, with the strength of the Fe II anti-correlating with both the Radio intensity (Miley and Miller 1979) and compactness (Osterbrock 1977). In a similar fashion, generally steeper X-ray spectra (i.e. larger photon indices Γ) are found in objects with stronger R_{Fe} (Wang et al. 1996; Laor et al. 1997; Shen and Ho 2014).

Although the ultimate physical driver(s) of the 4DE1 has not been fully understood, it is generally believed that the Eddington ratio and the inclination of the accretion disc along the line of sight play a crucial role in producing the observed diversity in terms of spectral shapes (Shen and Ho 2014; Sun and Shen 2015, but see also Panda et al. 2018 for a discussion on the effect of the Eddington ratio). Also, a more thorough understanding of the mechanism underlying the optical 4DE1 trends is hampered by a meagre comprehension of the physical details of the Fe II emission. In particular, the modelling of the Fe II emission is still not quite satisfactory. This is mostly due to the complexity of a detailed treatment of the Fe II ion and the fact that an accurate set of radiative and collisional atomic data is necessary to deal with the selective excitation, the continuum pumping and the fluorescence, which are relevant for the Fe II (see e.g. Sarkar et al. 2021 and references therein). Additionally, the physical mechanism responsible for the micro-turbulence (i.e. the effective turbulent motions within the line-forming region of the cloud), which is required to reproduce the strength of Fe II emission in observations (Netzer and Wills 1983; Baldwin et al. 2004; Bruhweiler and Verner 2008), is still far from being understood.

Although a theoretical framework explaining all the 4DE1 details has not been developed, this observational parameter space offers the possibility to track systematic differences and similarities between low- and high-redshift objects in a common (and model independent) parameter space.

In this part of my thesis my aim is to characterise the strength of the optical Fe II bump between 4434–4684 Å , whose intensity is commonly included among the 4DE1 parameters. In particular I show that, despite faint *JWST* AGN share the locus occupied by their low-redshift counterparts in terms of Hβ parameters, their Fe II emission is extremely low. Here I also aim at pinning down the possible causes of this Fe II weakness.

5.3 Sample

The main goal of this study is to investigate the emission line properties in the rest-frame optical region including both the Fe II [1] and the Hβ emission for high-z AGN. Therefore, the sample of AGN was tailored by adopting the following criteria:

- Previous identification as a broad line AGN.
- Presence of a broad component in the Hβ profile.
- *JWST* observations[2] covering of the Fe II 4434–4684 Å range.

For most of the sample I included high-z sources ($z > 5$), yet in three cases (namely JADES-028074, J-209777, XID-2028) I relaxed this criterion, as these sources offer the possibility to track the properties of low-luminosity AGN at intermediate redshifts. Relevant information about the objects in the sample is listed in Table 5.1. In addition to the already known AGN with broad Hβ , I included three sources from the RUBIES survey (GO-4233; PI: A. de Graaff, de Graaff et al. 2024) identified as broad line AGN. Lastly, with the aim of enriching the high-luminosity tail of this sample, I added the eight quasars from the ASPIRE survey (ID 2078, PI: F. Wang; Wang et al. 2023) whose rest-frame optical properties have recently been analysed in Yang et al. (2023b).

To sum up, the sample described in this Chapter is made of 26 high-redshift sources ($\sim$ 90% of the sample is at $z > 6$) out of which 14 have Hβ luminosity $\log(\mathrm{L}_{\mathrm{H}\beta,\mathrm{br}}/(\mathrm{erg\,s^{-1}})) < 43.8$. For the sake of simplicity, I will refer to these sources as the low-luminosity (or faint) AGN. The remaining 12 have instead $\log(\mathrm{L}_{\mathrm{H}\beta,\mathrm{br}}/(\mathrm{erg\,s^{-1}})) > 43.8$ and I will refer to them as the high-luminosity subsample (or quasars). Although the $\log(L_{\mathrm{H}\beta,\mathrm{br}}/(\mathrm{erg\,s^{-1}}) = 43.8$ threshold is quite arbitrary, the two samples are fairly separated in terms of Hβ luminosity, as shown in Fig.5.1. The only object somewhat in-between the high- and the low-luminosity samples is XID-2028, having $\log(\mathrm{L}_{\mathrm{H}\beta,\mathrm{br}}/(\mathrm{erg\,s^{-1}}) = 43.6$. Yet, its inclusion in either

---

[1] Throughout this Chapter, when referring to Fe II , I mean the Fe II blend in the range 4434–4684 Å.

[2] As the Hβ line moves out of the K band at $z \gtrsim 4$ it becomes effectively inaccessible from the ground, thus the analysis in the high-redshift regime is mostly limited to objects observed with JWST.

of the two samples does not significantly alter the average properties later discussed in the Chapter.

As a complement to the sample, I also introduce some reference samples at lower z that were purposefully chosen in order to compare the properties of the sample selected here. In particular, for what concerns the low-luminosity sub-sample, I chose the sources from the already mentioned latest SDSS quasar catalogue, whose properties are described in Wu and Shen (2022). I selected sources below z=0.8 with reliable Hβ measurements, by applying the quality cuts suggested in Wu and Shen (2022) (see their Sec. 4 for details).

For what regards the high-luminosity regime, a complication for finding suitable reference samples is given by the prevalence of quasars at redshift $z \sim 2-3$, the so-called "quasar epoch" (see Sec. 1.1.2). At these redshifts, the Hβ region falls in the $\boldsymbol{H}$ band which is not covered by large optical surveys. For this reason, I opted for objects targeted by near-infrared surveys. In particular, I adopted the samples described respectively in Shen (2016), Matthews et al. (2023) and Deconto-Machado et al. (2023)[3]. The Shen (2016) sample comprises 74 luminous quasars ($\mathrm{L_{bol}} = 10^{46.2-48.2}\mathrm{erg\,s^{-1}}$) between $1.5 < z < 3.5$, observed with near-infrared (JHK) slit spectroscopy covering the rest-frame Hβ, Fe II and [O III] region. The catalogue described in Matthews et al. (2021) constitutes the Gemini Near Infrared Spectrograph-Distant Quasar Survey (GNIRS), containing a sample of 226 quasars between $1.5 < z < 3.5$ with infrared data covering the rest-frame optical/UV range. Lastly, the Deconto-Machado et al. (2023) sources are a similar sample of luminous ($\log(\mathrm{L_{bol}}/(\mathrm{erg\,s^{-1}}))$ ~47.0-48.5) objects at $2.3 < z < 3.8$, with spectral coverage in the rest-frame optical band, purposefully observed with the goal of describing the Fe II and Hβ properties at intermediate z.

---

[3] Since it was not reported in their work, I derived $L_{H\beta,br}$ for the sources in Deconto-Machado et al. (2023) using the Hβ equivalent width and the 5100 Å luminosity, assuming a standard ratio between the luminosity of the continuum at the Hβ location and at 5100 Å of 1.05 (e.g. Berk et al. 2001).

ID (1)	RA (2)	DEC (3)	z (4)	Instrument (5)	Configuration (6)	ref. (7)
GS_3073	57.078	-27.884	5.555	NIRSpec/IFS	G395M/F290LP - 0.25"	Übler et al. (2023)
COS-ZS7	150.099	2.3436	7.145	NIRSpec/IFS	G395M/F290LP - 0.50"	Übler et al. (2024)
CEERS-01019	215.035	52.890	8.681	NIRSpec/MSA	G395M/F290LP	Larson et al. (2023)
JADES-000954	189.152	62.260	6.762	NIRSpec/MSA	G395M/F290LP	Maiolino et al. (2023)
JADES-028074	189.065	62.234	2.261	NIRSpec/MSA	G395M/F290LP	Juodžbalis et al. (2024a)
JADES-209777	53.156	27.776	3.711	NIRSpec/MSA	235M/F170LP	Juodžbalis et al. in prep
RUBIES-CEERS-49140	214.892	52.878	6.687	NIRSpec/MSA	G395M/F290LP	Kocevski et al. (2024)
RUBIES-CEERS-55604	214.982	52.956	6.985	NIRSpec/MSA	G395M/F290LP	Kocevski et al. (2024)
UNCOVER-20466	3.640	-30.386	8.502	NIRSpec/MSA	PRISM/CLEAR	Kokorev et al. (2023)
Abell2744-QSO1	3.604	-30.382	7.045	NIRSpec/MSA	PRISM/CLEAR	Furtak et al. (2024)
XID-2028	150.547	1.619	1.593	NIRSpec/IFS	G140H/F100LP - 0.25"	Cresci et al. (2023)
DELS J0411–0907	62.869	-9.130	6.820	NIRSpec/IFS	G395M/F290LP - 0.35"-0.45"	Marshall et al. (2023)
VDES J0020–3653	5.131	-36.895	6.855	NIRSpec/IFS	G395M/F290LP - 0.35"-0.45"	Marshall et al. (2023)
PJ308-21	308.042	-21.234	6.234	NIRSpec/IFS	G395M/F290LP - 0.30"	Loiacono et al. (2024)
J0100+2802	15.054	28.041	6.327	NIRCam/WFSS	F356W	Eilers et al. (2023)
J010953.13-304726.30	17.471	-30.791	6.790	NIRCam/WFSS	F356W	Yang et al. (2023b)
J021847.04+000715.20	34.696	0.121	6.770	NIRCam/WFSS	F356W	Yang et al. (2023b)
J022426.54-471129.40	36.111	-47.192	6.522	NIRCam/WFSS	F356W	Yang et al. (2023b)
J022601.87+030259.28	36.508	3.050	6.541	NIRCam/WFSS	F356W	Yang et al. (2023b)
J024401.02-500853.70	41.004	-50.148	6.731	NIRCam/WFSS	F356W	Yang et al. (2023b)
J030516.92-315056.00	46.320	-30.791	6.614	NIRCam/WFSS	F356W	Yang et al. (2023b)
J200241.59-301321.69	300.673	-30.223	6.688	NIRCam/WFSS	F356W	Yang et al. (2023b)
J223255.15+293032.04	338.230	29.509	6.666	NIRCam/WFSS	F356W	Yang et al. (2023b)
RUBIES-EGS-8488	215.035	52.891	6.68	NIRSpec/MSA	G395M/F290LP	This work
RUBIES-EGS-948917	214.893	52.857	6.73	NIRSpec/MSA	G395M/F290LP	This work
RUBIES-CEERS-966623‡	214.876	52.881	8.35	NIRSpec/MSA	G395M/F290LP	This work
SBS_0335-052E	54.434	-5.044	0.014	FORS1	600B, 600R	Izotov et al. (2009)
J102530.29+140207.3	156.376	14.035	0.101	SDSS	–	Izotov and Thuan (2008)
J104755.92+073951.2	161.983	7.664	0.168	SDSS	–	Izotov and Thuan (2008)

Table 5.1. Relevant information for the objects in the sample. Identifier (1), coordinates (2,3) and redshift (4). Column 5 reports the instrument employed for these observations. Column 6 described the configuration adopted for each observation. In the case of NIRSpec multi-shutter array (MSA) I report the disperser/filter coupling. In the case of integral field spectroscopy (IFS) I also report the radius of the circular extraction region in arcseconds. In the case of Wide Field Slitless Spectrocopy (WFSS) I report the filter employed for the observations analysed here. Column 7 highlights the reference papers for the spectral data employed in this work for each source. I also report the instrument and configuration for the spectra of AGN in dwarf galaxies.

‡: already reported in Kocevski et al. (2024), but without the broad component in Hβ.

Lastly, alongside the main sample of low-luminosity *JWST* objects, I also consider three extremely metal poor dwarf galaxies hosting a Type 1 AGN, identified by the presence of broad Hα emission lines. These are SBS_0335-052E (Izotov et al. 1990), J102530.29+140207.3 and J104755.92+073951.2 (Izotov and Thuan 2008) whose properties are extensively described in Sec.5.3.1. I included these sources as tentative very local analogues of the faint *JWST* AGN since, as I will show briefly, they share a substantial set of similarities, in terms of optical lines and X-ray properties, with the high redshift sources.

In order to put these sources in the broader context of the emission line and accretion properties of local AGN, in Fig. 5.1 I show this sample, together with the control samples on the $\log(\mathrm{FWHM}_{\mathrm{H}\beta,\mathrm{br}})$–$\log(\mathrm{L}_{\mathrm{H}\beta,\mathrm{br}})$[4] plane. The choice of this parameter space presents several advantages. First, since the parameters describing the accretion process, such as the black hole mass and the bolometric luminosity, can be derived from these quantities (see e.g. Vestergaard and Peterson 2006; Dalla Bontà et al. 2020b), it is natural to expect objects residing in the same region of this parameter space to also share similar accretion parameters. Therefore, it is straightforward to consistently define the control samples. Secondly, since the parameter space is defined on the basis of observed quantities, the position of these sources therein is not subject to systematic uncertainties affecting the calibrations.

5.3.1 Metal-poor X-ray weak local analogues of faint *JWST* AGN

For comparison with galaxies in the local Universe, I included three metal-poor dwarf galaxies hosting low-luminosity Type 1 AGN (DG-T1AGN). The identification of the AGN in these sources has been first confirmed by the presence of a broad (FHWM > 1000 km s^{-1}) Hα emission line in Izotov and Thuan (2008). In addition, more recent observations, 15 yr after the first ones (Burke et al. 2021), confirmed the presence of the broad components in J102530.29+140207.3 and J104755.92+073951.2, thus excluding the supernovae shock scenario (Baldassare et al. 2016). Here I also report a secure detection of a broad component in the Hβ profile.

From an observational perspective, there are several similarities between the known properties of the faint *JWST* AGN and DG-T1AGN. Both these classes of objects have remarkably low NLR heavy element abundance with the highest measured oxygen abundance values in DG-T1AGN spanning $12 + \log(\mathrm{O/H})$ 7.3 and 8.0 (Izotov et al. 1999; Burke et al. 2021), and similar values having been detected in low-luminosity *JWST* AGN (e.g. Harikane et al. 2023; Übler et al. 2023; Kocevski et al. 2023; Maiolino et al. 2023). Another noticeable feature of these objects is the X-ray weakness of the AGN they harbour (Thuan et al. 2004; Burke et al. 2021). Additionally, there is also tentative evidence that the fraction of DG-T1AGN exhibiting absorption features in Balmer lines is higher than what is generally found in typical SDSS local AGN, just as reported in faint *JWST* AGN (Matthee et al. 2024; Kocevski et al. 2024; Juodžbalis et al. 2024a). However, the current sample size is limited for solid conclusions. As I will show in the following Sections, and discuss more thoroughly in Sec.5.7, these properties, often observed also in the faint

---

[4] When dealing with these parameters, for the sake of a lighter notation, I will simply report $\log(\mathrm{FWHM}_{\mathrm{H}\beta,\mathrm{br}})$ and $\log(\mathrm{L}_{\mathrm{H}\beta,\mathrm{br}})$, rather than to the more correct notation $\log(\mathrm{FWHM}_{\mathrm{H}\beta,\mathrm{br}}/(\mathrm{km\,s^{-1}}))$ and $\log(\mathrm{L}_{\mathrm{H}\beta,\mathrm{br}}/(\mathrm{erg\,s^{-1}}))$.

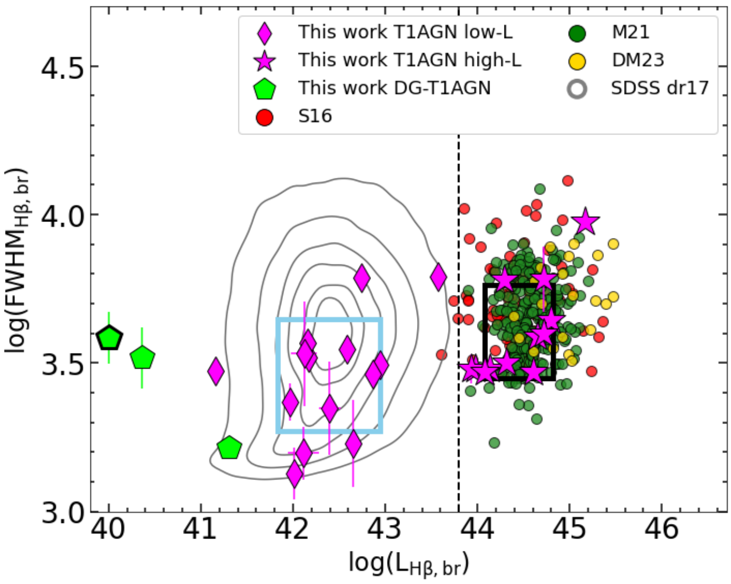

Figure 5.1. The log(FWHM$_{H\beta,br}$) – log(L$_{H\beta,br}$) parameter space for the broad line AGN (T1AGN) and the reference samples (SDSS dr17, Shen 2016 S16, Matthews et al. 2021 M21, Deconto-Machado et al. 2023 DM23), where the SDSS dr17 galaxies are shown with contours. I also includethe three broad line AGN in metal-poor dwarf galaxies (DG-T1AGN). The dashed line marks the threshold luminosity dividing the high- and the low-luminosity sub-samples. The actual log(L$_{H\beta,br}$) of SBS_0335-052E (black thick edge) is 38.3, but it was shifted to 40.0 for the sake of a tighter image layout. The azure and black rectangles mark the regions adopted to define the control samples (Sec.5.5).

JWST AGN, make AGN in metal poor dwarf galaxies an intriguing class of local analogues to compare the properties observed at remote cosmic distances.

5.4 Methods

In this section, I describe the techniques adopted to quantify the spectral properties of the sources in the sample.

5.4.1 Spectral fits

In order to access the spectral information embedded in the *JWST* spectra, I performed a detailed spectroscopic analysis, focusing on a reliable determination of the Fe II and Hβ properties. To this end, I adopted a custom-made Python code, based on the IDL MPFIT package (Markwardt, 2009), which takes advantage of the Levenberg-Marquardt technique (Moré, 1978) to solve the least-squares problem. The main emission lines were modelled by adopting different line profiles (Gaussian, Lorentzian). In the case of the broad Hβ line in quasars, I also use a broken power-law profile convolved with a Gaussian (e.g. Nagao et al. 2006), as it proves more effective in describing the asymmetry often observed in the red side of the Hβ (see e.g. Deconto-Machado et al. 2023). The kinematics of [O III] has been tied to that of the narrow Hβ component, and the flux ratio between the 5007 Å and the 4959 Å components was fixed to three to one (Osterbrock and Ferland 2006). With the aim of reproducing the diversity of the Fe II emission, I included several spectral templates produced within the CLOUDY environment (Ferland et al. 2013). Specifically, employed models spanning a wide range of physical parameters in order to broadly cover the parameter space of the Fe II emission. In particular, the models span the cloud Hydrogen density (n_H) range between $10^8 \leq n_e \leq 10^{14}$ cm^{-3}, photon ionising flux (ϕ) between $10^{17} \leq \phi \leq 10^{23}$ cm^{-2} s^{-1}, microturbulence velocity values v_{turb} fixed to 0 and 100 km s^{-1} and solar metal abundances. The continuum adopted is the default AGN continuum from Mathews and Ferland (1987). These models are then convolved with a Gaussian profile (the same for all the models as they are thought to represent co-spatial emission), shifted, and weighted during the fitting process. The parameters ultimately fitted for the Fe II templates are then the velocity dispersion and the shift of the Gaussian kernel as well as the weights of each template.

Since here I adopted a non-linear least square approach to perform the fit, the weights of the Fe II templates are constrained to be > 0. This implies that, in the case of low signal and/or low Fe II emission, positive spikes of noise could be interpreted as actual iron emission, leading to an overestimate of the actual Fe II flux. In order to mitigate this issue I also adopted a non-parametric approach to estimate the Fe II contribution in the 4434–4684 Å bump. In brief, I performed the spectral fit without the Fe II templates and focused on faithful modelling of the emission lines included in or close to this wavelength range (chiefly He Iλ4471 and He IIλ4686). I then subtracted the best-fit models of these lines from the observed spectrum and considered the remaining emission to be ascribable to Fe II . If the integrated flux estimated by this second method was < 0, I marked the measurement obtained via the Fe II templates (the parametric approach) as an upper limit.

I estimated the uncertainty on the best-fit parameters by adopting a Monte Carlo approach as already described in Sections 2.4.3 and 3.3.1. Specifically, I performed the fit for 100 mock spectra for each source: the flux in every spectral channel was simulated by randomising the measured flux adopting a Gaussian noise whose amplitude was set by the uncertainty value in that spectral channel. After fitting every mock sample, I computed the distribution of the best-fit parameters and set the uncertainty as the standard deviation of the distribution, after applying a 3σ clipping.

Examples of the spectral fits of both a low- and a low-luminosity object are shown in Fig.5.2. A complete gallery of all the fits is presented in Supplementary Material 5.9.3.

I report the spectral quantities of interest for the broad components, namely FWHM$_{\mathrm{H}\beta}$, R_{Fe} and $\log \mathrm{L}_{\mathrm{H}\beta}$ [5] for each object in the sample in Table 5.2.

---

[5] I note that the logL$_{\mathrm{H}\beta}$ are not corrected for intrinsic reddening within the BLR, yet this also applies to the control samples.

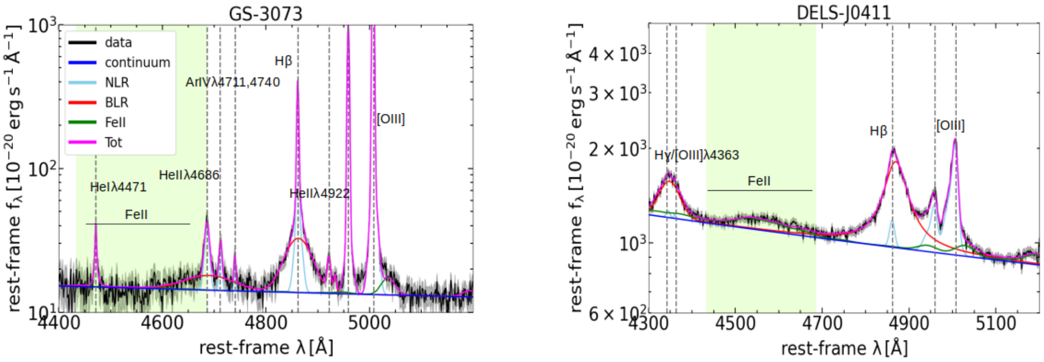

Figure 5.2. Examples of the spectral fits of a low-luminosity (left) and a high-luminosity (right) AGN of the sample. The different components are colour-coded as stated in the legend. The uncertainty on the data is shown as a shaded area. The Fe II pseudo-continuum is highlighted in green. The vertical grey dashed lines mark the most prominent emission lines. All the spectral fits are shown in 5.12.

ID	FWHM $H\beta_{br}$ [$km\,s^{-1}$]	$\log(L_{H\beta,br})$ [$erg\,s^{-1}$]	R_{Fe} [$H\beta$/Fe II_{opt}]	$\log(L_{5100Å})$ [$erg\,s^{-1}$]	EW$H\beta$, br [Å]	[OIII]/$H\beta_{na}$	O32	EW[O III] [Å]	12+log(O/H)
GS_3073	3525 ± 339	42.58 ± 0.04	0.03 ± 0.03	44.55	84	6.6 ± 0.2	12.8 ± 0.4	1084 ± 268	8.0*
COS-ZS7	3289 ± 299	42.17 ± 0.04	0.09 ± 0.02	44.30	41	8.3 ± 0.2	14.4 ± 0.6	597 ± 11	8.0 ± 0.2
CEERS-01019	1571 ± 311	42.11 ± 0.17	0.22 ± 0.35	43.09	302	9.6 ± 1.4	-	3251 ± 2499	8.1 ± 0.2
JADES-000954	2338 ± 341	41.96 ± 0.06	0.19 ± 0.22	43.79	74	7.3 ± 0.8	13.3 ± 3.0	389 ± 23	-
JADES-028074	3685 ± 136	42.16 ± 0.01	0.10 ± 0.01	43.45	62	5.0 ± 0.1	15.1 ± 0.4	254 ± 3	7.4 ± 0.2
JADES-20977	6145 ± 692	42.74 ± 0.03	1.10 ± 0.05	44.75	42	1.8 ± 0.3	-	20 ± 1	-
RUBIES-EGS-8488	1695 ± 506	42.65 ± 0.07	0.28 ± 0.04	43.82	87	9.1 ± 0.6	19.0 ± 5.0	1692 ± 165	-
RUBIES-CEERS-49140	3108 ± 135	42.95 ± 0.01	0.08 ± 0.03	44.44	154	26.9** ± 22.3	-	99 ± 4	-
RUBIES-CEERS-55604	2905 ± 187	42.86 ± 0.02	0.14 ± 0.03	44.41	144	10.2 ± 2.1	-	146 ± 6	-
RUBIES-EGS-948917	1344 ± 257	42.01 ± 0.06	0.41 ± 0.17	43.71	116	7.0 ± 0.6	-	791 ± 123	-
RUBIES-CEERS-966323	2226 ± 972	42.40 ± 0.12	0.24 ± 0.19	43.87	98	4.2 ± 0.5	-	218 ± 31	-
UNCOVER-20466	3395 ± 1175	42.12 ± 0.14	0.02 ± 0.09	43.62	211	4.3 ± 3.2	-	426 ± 153	-
Abell2744-QSO1	2982 ± 267	41.16 ± 0.05	0.01 ± 0.03	43.25	45	14.8 ± 1.1	-	4 ± 2	-
XID-2028	6175 ± 218	43.57 ± 0.01	0.44 ± 0.05	45.35	93	11.4 ± 0.9	-	80 ± 1	-
DELS J0411–0907	3887 ± 76	44.65 ± 0.15	0.01 ± 0.05	46.38	87	-	-	-	-
VDES J0020–3653	6058 ± 1083	44.71 ± 0.41	0.09 ± 0.05	46.24	139	-	-	-	-
PJ308-21	4402 ± 22	44.79 ± 0.00	0.33 ± 0.00	46.41	113	-	-	-	-
J0100+2802	9477 ± 240	45.17 ± 0.01	0.26 ± 0.03	47.27	35	-	-	-	-
J010953.13-304726.30	3033 ± 117	43.98 ± 0.01	0.93 ± 0.05	45.81	-	-	-	-	-
J021847.04+000715.20	3030 ± 117	44.14 ± 0.02	1.45 ± 0.11	45.83	-	-	-	-	-
J022426.54-471129.40	3936 ± 78	44.72 ± 0.04	0.45 ± 0.05	46.47	-	-	-	-	-
J022601.87+030259.28	3131 ± 129	44.32 ± 0.01	1.11 ± 0.04	46.24	-	-	-	-	-
J024401.02-500853.70	2969 ± 158	44.60 ± 0.08	0.30 ± 0.05	46.18	-	-	-	-	-
J030516.92-315056.00	3020 ± 314	43.93 ± 0.03	1.78 ± 0.12	45.84	-	-	-	-	-
J200241.59-301321.69	2951 ± 79	44.07 ± 0.01	2.34 ± 0.08	46.14	-	-	-	-	-
J223255.15+293032.04	6044 ± 201	44.29 ± 0.01	1.61 ± 0.08	45.63	-	-	-	-	-
SBS_0335-052E	3845 ± 804	38.31 ± 0.02	0.05 ± 0.09	41.13	7	2.8 ± 0.2	14.8 ± 1.0	1044 ± 66	7.3 ± 0.2
J102530.29+140207.3	3287 ± 559	40.37 ± 0.07	0.28 ± 0.07	42.79	20	4.8 ± 0.2	8.9 ± 0.7	268 ± 5	7.5 ± 0.2
J104755.92+073951.2	1638 ± 100	41.30 ± 0.02	0.05 ± 0.02	43.23	57	6.4 ± 0.1	8.4 ± 0.2	869 ± 11	8.2 ± 0.2

Table 5.2. The broad lines spectral properties estimated from the spectral fits of the sample. All the FWHM have been corrected for the instrumental resolution. The uncertainty on log L_{5100} and EW$H\beta$ are negligible with respect to the others involved.

* The [O III]λ4363 is only marginally covered by the R2700 data. Here I report the value quoted in Übler et al. (2023), where [O III]λ4363 kinematics had been tied to other narrow lines.

** RUBIES-CEERS-49140 presents an absorption feature close to the location of the narrow $H\beta$, which hampers a reliable measurement of the narrow component flux. Therefore, I mark this value as unreliable.

5.4.2 Spectral stacks

In order to provide an immediate term of comparison at lower redshifts for the *JWST* samples, I built spectral templates from the comparison samples described in Sec.5.3.

Since the SDSS low-redshift sample covers a region of the adopted parameter space much wider than that spanned by the low-luminosity sample, I tailored a sample analogue to the *JWST* one in the $\mathrm{FWHM}_{\mathrm{H}\beta}$-$\log(\mathrm{L}_{\mathrm{H}\beta,\mathrm{br}})$ space. I therefore selected a sample of SDSS AGN in the region of the parameter space defined as $[\langle\log(\mathrm{L}_{\mathrm{H}\beta,\mathrm{br}})\rangle \pm \sigma_{\mathrm{L}_{\mathrm{H}\beta,\mathrm{br}}}, \langle\log(\mathrm{FWHM}_{\mathrm{H}\beta})\rangle \pm \sigma_{\mathrm{FWHM}_{\mathrm{H}\beta,\mathrm{br}}}]$, with the quantities in brackets being the mean values and the respective standard deviations for the low-luminosity sub-sample. The same selection was applied in the high-luminosity regime, with the only difference that here I only combined in the average spectrum the sources from Matthews et al. (2021) and Deconto-Machado et al. (2023), as Shen (2016) already provided a spectral composite of their full sample.

I then proceeded to produce the composite spectra for the samples adopting the same procedure explained in 2.4.2. In brief:

- Each spectrum was corrected for Galactic absorption assuming the value for the colour excess E(B-V) available in the Wu and Shen (2022) catalogue according to the Schlafly and Finkbeiner 2011 extinction maps and a Fitzpatrick (1999) extinction curve. Then, the de-reddened spectra were shifted to the rest frame.

- All the spectra in the same sample were resampled, by means of linear interpolation, onto a fixed wavelength grid. Successively all the spectra were scaled by their 5100Å monochromatic flux, in order not to bias the stack towards the most luminous objects in each subsample.

- The final composite spectrum is obtained by taking the median value of the flux distribution in each spectral channel. The uncertainty on the median value was evaluated as the standard deviation in each spectral channel divided by the square root of the number of sources contributing to that channel.

The same recipe was also adopted to produce the composite spectrum of the three DG-T1AGN. The composite spectra produced as a result of this procedure, scaled by their broad Hβ fluxes and continuum-subtracted are shown in Fig.5.3. There are several features clearly arising from this comparison. For what concerns the Fe II emission, the low-luminosity sample at high redshift exhibits a faint Fe II emission which translates into a R_{Fe} significantly lower than the local AGN counterparts. At the same time, the high-z quasars present a slightly fainter Fe II than the other samples, yet their R_{Fe} is on average consistent with the other reference samples. The differences in terms of the R_{Fe} ratio are more quantitatively assessed in Section 5.5. The lack of prominent Fe II in the low-luminosity objects can also be assessed by inspecting the fits of the composite spectra, as well as the spectral fit of each source in Appendices 5.9.2 and 5.9.3.

In particular, in Fig. 5.10 and 5.11 I show the spectral fits of the composite spectra presented in Fig. 5.3. For what regards the faint-AGN stack, I point out

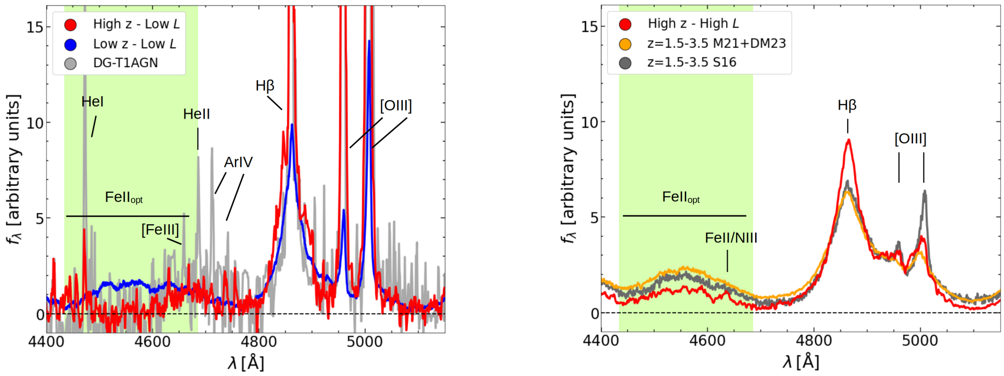

Figure 5.3. Continuum-subtracted spectral composites of the low-luminosity (left) and high-luminosity (right) subsamples. The Hβ and [O III] narrow components have been cut for visualisation purposes. In the right panel I also show the composite quasar spectrum described in Shen 2016, made of 74 luminous quasars at $1.5 < z < 3.5$. The iron bump between 4434–4684 Å (green shaded area) is evidently weaker in the *JWST* low-luminosity sample than in the local AGN. However, the strength of the Fe II bump in the high-luminosity sample is comparable to the lower redshift analogue sample.

that the spectral fit reveals the presence of a significant[6] broad (~1000 km s^{-1}, ΔBIC = -67) component in the [O III] profile. This component is particularly interesting as it shows remarkable differences with respect to that observed in the SDSS control sample stacked spectrum. Firstly, this component is much fainter compared to the narrow component than that detected in the SDSS stack. The broad-to-narrow ratio in the SDSS composite is ~0.45, while it is almost three times smaller in the *JWST* one. Additionally, while the broad [O III] component is significantly blueshifted with respect to the core component in the SDSS stack, by ~300 km s^{-1}, the shift between the narrow and broad components in the faint *JWST* AGN is consistent with zero within the uncertainties. Lastly, I also mention that the FWHM of the broad [O III] component is much smaller than the broad Hβ (3731 ± 133 km s^{-1}). Notably, this finding can be viewed as a clue against the interpretation of broad lines observed in these AGN as produced by star formation driven outflows (see e.g. Yue et al. 2024; Kokubo and Harikane 2024). As a matter of fact, this sample of AGN was selected only on the basis of the presence of broad lines, without any other kind of emission line diagnostic. If the mechanism producing the observed broad Hβ were star formation driven outflows, it is reasonable to expect the Hβ and [O III] broad components to share similar kinematics. Although the high density might lead to suppression of [O III], causing the weakness of the broad component, the broad Hβ and the broad [O III] have significantly different kinematics (at 15σ). Therefore, this evidently points in the direction of a different origin for these two components.

---

[6] The significance of the inclusion of a broad component is assessed via the variation in the Bayesian Information Criterion (BIC). I consider as significant a decrease in the BIC by at least $|\Delta\mathrm{BIC}| > 10$

sub-samples	KS	W	MW
J low-L / J high-L (1)	2×10^{-4}	5×10^{-3}	10^{-4}
J low-L / CS low-L (2)	4×10^{-9}	9×10^{-7}	10^{-8}
J high-L / CS high-L $z=2-3$ (3)	0.120	0.154	0.279
J low-L / CS low-L de-red (4)	3×10^{-9}	2×10^{-6}	4×10^{-8}
J low-L / [O III] CS (5)	0.035	0.050	0.011

Table 5.3. p-values of the statistical tests performed on the *JWST* low- and high-luminosity samples (J) against their respective control samples (CS; 1,2,3). Rows 4 and 5 denote respectively the same tests performed on the samples matching the de-reddened $L_{H\beta}$ and the [O III] control sample described in 5.6.1.

5.5 Results

With the aim of understanding the Fe II properties observed in the sample, in Fig. 5.4 I show again the FWHM$_{H\beta,br}$ vs L$_{H\beta,br}$ parameter space, adding this time the $R_{\rm Fe}$ in colour code. For a clearer visualisation of the surface, I binned the control samples in cells containing at least 30 objects. When the *JWST* subsamples are compared to their control samples a clear dichotomy can be spotted, already foreseen in Fig. 5.3. The low-luminosity sample displays $R_{\rm Fe}$ much weaker than that observed for the same regions in the parameter space for the local control sample; the only notable exceptions are JADES-209777 and XID-2028, whose peculiarities will be discussed in Sec. 5.6. At the same time, the luminous quasars subsample is consistent, albeit with some scatter, with the expectations from the control sample at high luminosity.

Quantitatively, I estimated the significance of the difference in the $R_{\rm Fe}$ ratios using different statistical tests to assess what is the probability that the $R_{\rm Fe}$ distributions of the *JWST* and control samples actually come from the same parent distribution as a null-hypothesis. In particular, I took advantage of the Kolmogorov-Smirnov test (KS; Hodges Jr 1958), the Welch's t-test (W; Welch 1947) suited for cases of small samples with unequal variances, and the Mann-Whitney U Test (MW; Mann and Whitney 1947). The results of these tests are reported in Table 5.3.

When the *JWST* samples are matched to their respective control samples in the parameter space, all the tests confirm the different behaviour already seen in Fig.5.3. The difference in the $R_{\rm Fe}$ ratios for the low-luminosity sample is extremely significant, with p-values $\lesssim 10^{-6}$. On the other hand, the $R_{\rm Fe}$ measured in the *JWST* quasars is fully consistent with those measured at cosmic noon. In order to further strengthen these results against the possible effect of dust reddening within the BLR, I performed the same tests on a control sample chosen in order to match the average values of the de-reddened $L_{\rm H\beta,br}$. Again, the difference proved extremely significant (p-value$< 10^{-6}$).

To conclude, I highlight that in the low-luminosity regime, I conservatively included also the X-ray detected AGN JADES-20977 and XID-2028, and considered the upper limits as actual measurements estimated via the parametric fits. The exclusion of these values would make the difference even stronger.

As a more straightforward way to notice the region occupied by the *JWST* sources with respect to the bulk of the lower z samples, I also present two side views on the FWHM-L$_{\rm H\beta}$-$R_{\rm Fe}$ parameter space in Fig. 5.5. Specifically, the left panel

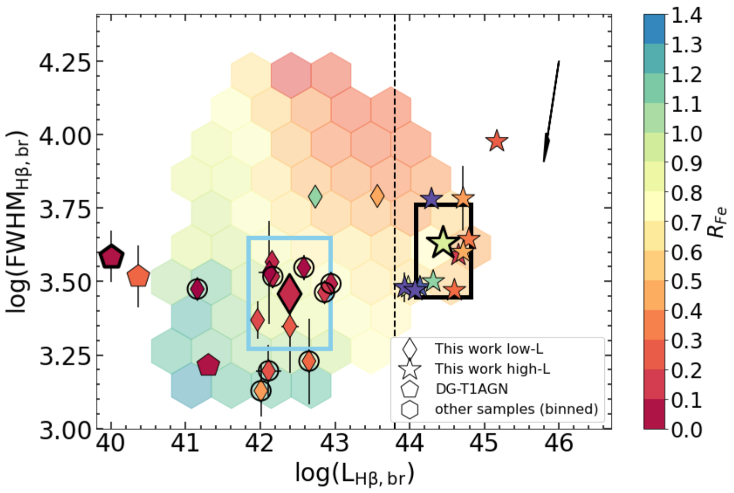

Figure 5.4. R_{Fe}-log(FWHM$_{\mathrm{H}\beta}$) – log(L$_{\mathrm{H}\beta,\mathrm{br}}$) diagram; specifically: log(FWHM$_{\mathrm{H}\beta}$) versus log(L$_{\mathrm{H}\beta,\mathrm{br}}$) color-coded by R_{Fe}. Objects marked with a circle represent R_{Fe} upper limits as defined in the text. The background 2D histogram is obtained by binning the control sample (with a minimum of 30 objects per bin); individual objects from *JWST* are colour-coded with the same scale in R_{Fe}. Due to the large number of upper limits in the low-luminosity region, I also include the values derived from the composite spectra as symbols with thicker black edges. The coloured rectangles mark the regions where the control samples were drawn. The black solid arrow marks the direction of the PCA, as described in Sec. 5.6.2. SBS_0335-052E (black thick edge pentagon) has been shifted for a tighter image layout.

shows R_{Fe} versus L$_{\mathrm{H}\beta}$ in (color-coded) bins of FWHM, while the right panel shows R_{Fe} versus FWHM in (color-coded) bins of L$_{\mathrm{H}\beta}$. It is clear that the low-luminosity sample exhibits systematically lower R_{Fe} than that expected for the corresponding region in the parameter space based on lower-z data.

5.6 Possible causes of the observed differences

There is no consensus about the main drivers of the correlations involving the strength of the R_{Fe} ratio falling in the ensemble of the 4DE1.

It is generally thought that the R_{Fe}-FWHM$_{\mathrm{H}\beta,\mathrm{br}}$ anti-correlation results from the combined effect of the accretion rate and inclination of the line of sight with respect to the axis of the accretion disc powering the AGN. Yet, it is unlikely that the λ_{Edd} is *per se* the main driver of the 4DE1 correlation. The λ_{Edd} increases perpendicularly to the main sequence, and objects with low Eddington ratios produce very different R_{Fe} ratios. The same spread in terms of R_{Fe} is observed in samples allegedly made of sources accreting at high-Eddington ratios such as the SEAMBH sample (see e.g. Du et al. 2018). Also, from a theoretical perspective, the inclusion of a physically motivated warm X-ray corona has been observed to loosen the dependence of the R_{Fe} with the λ_{Edd} (Panda et al. 2019).

Lastly, it should be kept in mind that both the FWHM$_{\mathrm{H}\beta}$ and the Eddington ratio are easy to estimate parameters, useful when it comes to roughly describing the accretion properties of the sample, but they are not the physical quantities

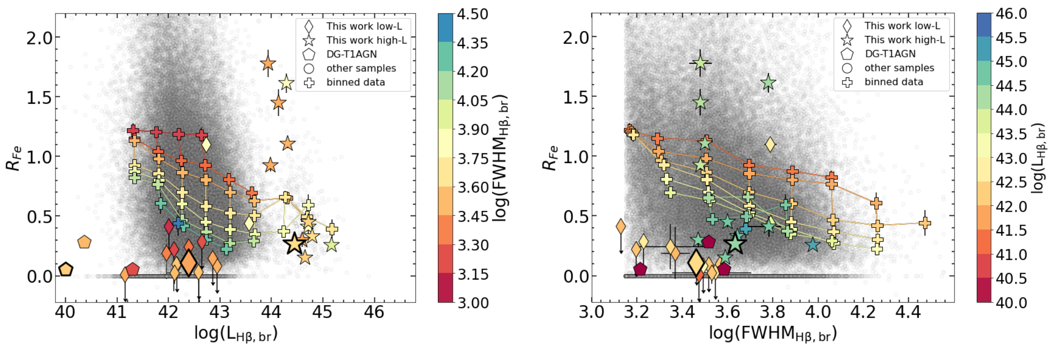

Figure 5.5. Orthogonal sections of the log(FWHM$_{H\beta}$) − log(L$_{H\beta}$)−$R_{\rm Fe}$ parameter space; specifically (left) $R_{\rm Fe}$ versus log($L_{H\beta}$) in (colour-coded) bins of FWHM$_{H\beta}$, and (right) $R_{\rm Fe}$ versus FWHM$_{H\beta}$ in (colour-coded) bins of log($L_{H\beta}$). The thick-edged diamond and star represent the values derived from the composite spectra. The colour-coded lines represent the third quantity evaluated on the binned sources of the control samples. SBS_0335-052E (black thick edge pentagon) has been shifted for a tighter image layout. It is clear that, while the high-luminosity objects of the sample reside -albeit with some scatter- in the expected locus of the parameter space according to the control sample, the low-luminosity objects display far lower $R_{\rm Fe}$. Interestingly, two low-luminosity objects (JADES-029777 and XID-2028) detach from the bulk of the faint sample, being close to the $R_{\rm Fe}$ expected. As discussed further in Sec.5.6.5, these are the two only faint AGN which are X-ray detected.

ultimately governing the micro-physics of Fe II and Hβ emissivity. Their effect on the $R_{\rm Fe}$ ratio comes more subtly in the form, for instance, of a dependence of the $R_{\rm Fe}$ on the SED, which, in turn depends on the accretion properties of the AGN.

In this section, I present a series of tests aiming at exploring the possible drivers of the observed properties, in both the main sample and the reference samples.

5.6.1 Are we probing an extreme tail of the 4DE1?

Within the 4DE1 set of correlations, it is well known that objects with stronger $R_{\rm Fe}$ exhibit weaker [O III] emission lines and vice-versa (Boroson and Green 1992b). Since the faint AGN show quite strong [O III] emission ($\sim \langle 600 \rangle$ Å), it is therefore legitimate to question whether the $R_{\rm Fe}$ weakness detected in these sources might be interpreted as the high-EW[O III] and low-$R_{\rm Fe}$ end of the eigenvector 1. I explored this possibility and here I present several arguments against this interpretation.

Firstly, it should be noted that the faint *JWST* AGN are not consistent with the expectations for local (i.e. SDSS) sources in the same region of the log(EW[O III])–$R_{\rm Fe}$ plane. This can be seen in Fig.5.7. There I highlight in pink the local sources -this time not selected from the log(FWHM$_{H\beta}$) − log(L$_{H\beta,\rm br}$) control sample- within 0.2 dex from the mean value of the *JWST* low-luminosity sources. I tested whether the $R_{\rm Fe}$ estimated from the *JWST* and the SDSS EW[O III]-matched sources could be compatible with coming from the same parent distribution, adopting the same statistical tests described in Sec.5.5. The $R_{\rm Fe}$ distribution for the *JWST* sources resulted significantly different (at $\gtrsim$95% confidence level, depending on the test, see Table 5.3) from the SDSS one. Here I also note that I made the very conservative assumption of considering the upper limits as actual measurements. Also the choice of the 0.2 dex interval in EW[O III] is conservative. The combination of lower $R_{\rm Fe}$ values with increasing EW[O III], and high EW[O III] sources becoming increasingly rarer, would produce an higher mean value of $\log(R_{Fe})$ for the control sample and therefore a stronger discrepancy if I considered sources between $[\langle\log(\mathrm{EW[OIII]})\rangle \pm \sigma_{\mathrm{EW[OIII]}}]$. In Fig.5.7 I also show that the average $R_{\rm Fe}$ values for the faint *JWST* sources are far below ($> 2.5\sigma$) the best-fit relation for the SDSS full sample. There I estimated the average $R_{\rm Fe}$ in multiple ways: including the upper limits as actual measurements (maroon), extracting the non-detected values from a uniform distribution between the SDSS lowest 1^{st} percentile and the upper limits (red), and using the value derived from the spectral fit of the stack (magenta).

Furthermore, other arguments can be brought against the faint *JWST* sources fitting within the 4DE1 framework, which are the average Eddington ratio and the inclination. The Eddington ratio, albeit the already mentioned caveats, is generally observed to correlate, with $R_{\rm Fe}$ (e.g. Shen and Ho 2014). These sources exhibit, on average, the same Eddington ratio as their low-z counterparts, having $\langle\lambda_{\rm Edd}\rangle \sim 0.14$ ($\langle\lambda_{\rm Edd}\rangle_{\rm SDSS} \sim 0.11$) adopting the Vestergaard and Peterson (2006) calibration for the black hole mass and the Shen et al. (2011) for the bolometric luminosity. Although the validity of the local calibrations in these so different environments is questionable, the $R_{\rm Fe}$ is far lower than the expectations. The other mechanism classically invoked to explain the 4DE1 trends is the inclination of the line of sight. Objects with large [O III] are thought to be observed under large viewing angles (e.g. Risaliti et al. 2011; Bisogni et al. 2017), while a more face-on inclination decreases the [O III] EW while increasing $R_{\rm Fe}$. However, the large fraction of *JWST* low-luminosity objects with large (EW[O III]$\gtrsim$ 100 Å) does not seem reconcilable with the local one ($\sim 4\%$ in Fig. 5.7). At the same time, the inclination hypothesis to explain the large [O III] would leave room for the other -perhaps even more striking- question: where are all the low-inclination, low EW[O III] sources at these redshifts?

Lastly, I mention that all the considerations made so far subsumed the AGN nature of the [O III] emission. This could be not the case, as for these sources a significant fraction of the [O III] emission could be ascribable to star formation. Indeed, star-forming galaxies and the AGN discovered at these redshifts overlap in the classical BPT diagrams (see e.g. Maiolino et al. 2023; Kocevski et al. 2023; Harikane et al. 2023). Therefore, the EWs computed here would only be an upper limit to those actually coming from the AGN. Disentangling the AGN contribution from the star-formation would result in a shift leftwards of the average [O III] values in Fig. 5.7, thus making the inconsistency with the SDSS 4DE1 even stronger.

5.6.2 Accretion parameters

The black hole mass and the accretion rate (or its closely related observable, the luminosity) are thought to ultimately rule, with a few other parameters, the shape and the emissivity of the accretion disc in AGN. These quantities are expected to be, therefore, the strongest drivers in the changes of the AGN SED, mainly responsible for the photoionisation in these sources. Hence, an obvious point is to assess whether the observed difference in $R_{\rm Fe}$ could be ascribed to changes in one or both of these parameters.

Nonetheless, there are some complications: the first is the fact that the evaluation

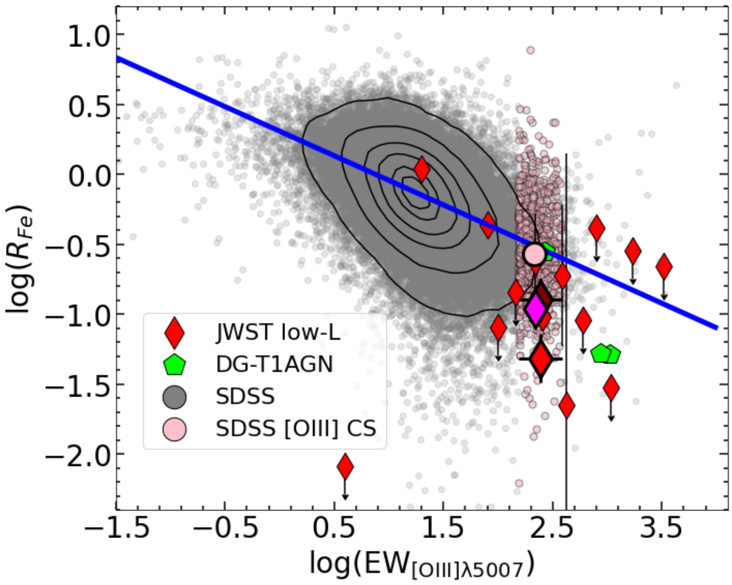

Figure 5.6. The log(EW[O III])–log($R_{\rm Fe}$) section of the 4DE1. The pink dots mark the SDSS objects selected as a control sample. The blue line highlights the best linear fit to the SDSS data. The thick-edged diamonds represent the average values for the faint *JWST* AGN as described in the text.

of the M_{BH} comes with a significant systematic uncertainty due to single-epoch calibrations (between 0.3-0.5 dex, see e.g. Shen 2013; Dalla Bontà et al. 2020b). In this work, I adhered to the Vestergaard and Peterson 2006 prescription, also employed in Wu and Shen (2022) for a fair comparison with the control sample.

Moreover, there is not a well-defined relation between the $R_{\rm Fe}$ and any of the accretion parameters, but the λ_{Edd}, with which there is a correlation, although Panda et al. (2019) argued that this is more observational rather than due to an intrinsic effect. In the effort to understand the evolution of the $R_{\rm Fe}$ within this parameter space, I took advantage of a partial correlation analysis, already introduced in 4.5.2. In particular, this analysis showed that the correlation with the $\rm FWHM_{H\beta}$ is significantly stronger than with the $\rm L_{H\beta,br}$. Nonetheless, both of them yield low, yet significant, partial correlation coefficients ($\rho_{\rm R_{Fe}\,L_{H\beta,br}|FWHM_{H\beta,br}} = -0.166$ with p-value $< 10^{-6}$ and $\rho_{\rm R_{Fe}\,FWHM_{H\beta}|L_{H\beta,br}} = -0.281$ with p-value $< 10^{-6}$). At fixed $\rm L_{H\beta,br}$, the increase in $\rm FWHM_{H\beta}$ can be readily interpreted as an increase in M_{BH}, as a consequence of the Hβ virial relation (see e.g. Dalla Bontà et al. 2020b and references therein). At the same time, $\rm L_{H\beta,br}$ is tightly related to the 5100 Å luminosity (see e.g. Kaspi et al. 2005; Dalla Bontà et al. 2020b) which in turn is a good proxy to the bolometric luminosity (Richards et al. 2006). Yet, none of these two parameters seems to be a strong driver of the observed changes in $R_{\rm Fe}$. Additionally, it is useful to recall that the difference evaluated in Section 5.5 has been computed between the *JWST* low-luminosity objects and their local counterparts in the parameter space, which is tightly related to the accretion parameters. Therefore, it is reasonable to expect that neither the black hole mass nor the luminosity are driving the observed difference, under the non-trivial assumption that the local calibrations apply also for this class of AGN. The same consideration applies to the

Eddington ratio as well.

5.6.3 The effect of metallicity

A trivial factor which could be responsible for the weakness of the Fe II bump is the metallicity. Here I explore what it is possible to infer about the gas-phase metallicity for the low-luminosity sources by employing line diagnostic ratios.

Extensive work based on CLOUDY simulations showed that it is possible to reproduce the diversity in the optical R_{Fe} of the low-z SDSS sample allowing for a super-solar metallicity [1 $Z_{\odot}$-10 $Z_{\odot}$] while keeping the other BLR parameters, such as the density and the column density, within typical values (Panda et al. 2018). However, there is evidence for the faint objects in this early stages of the Universe not to have reached the chemical maturity observed in more local sources, at least in the NLR (Curti et al. 2023; Isobe et al. 2023; Maiolino et al. 2023; Übler et al. 2023, 2024; Kocevski et al. 2024). This points in the direction of low metallicity as a possible driver of the low R_{Fe} ratios observed in the sample.

Preliminary considerations

The most straightforward way to estimate the metallicity of the BLR gas in these sources would be to employ high ionisation line ratios such as N V/C IV or (Si IV+O IV)/C IV (see e.g. Lai et al. 2022 and references therein). Unfortunately, this wavelength range is not accessible within the spectra described here. Alternatively, it would be possible to infer the metallicity from the readily available rest-optical lines in the NLR, but translating this measurement into a BLR metallicity would require a model of the chemical enrichment and of the interplay between these two spatially different regions at these early cosmic epochs.

From an observational point of view, it is well known that the BLR and NLR metallicities are linked, with the former reaching generally higher metallicity (e.g. Wang et al. 2022b) at early cosmic epochs. However, this link between the NLR and BLR metallicities implies that even managing to get reliable estimates of the NLR metallicity for the low-luminosity objects, these would only set a *lower limit* to the corresponding BLR metallicity.

In addition, estimating the metallicity of the NLR in AGN is not a well-established procedure (see e.g. Dors et al. 2020a for a compilation of the few attempts made in this direction) and efforts in this field have been mainly directed towards Type 2 AGN (Thomas et al. 2019; Dors et al. 2020b; Li et al. 2024). An example of complications in estimating the AGN metallicity is the higher fraction of O^{3+} (whose corresponding transitions are undetectable in the optical range). This is associated with the harder AGN continuum and the effect of temperature inhomogeneities in the NLRs (Riffel et al. 2021).

For the faint objects in the sample, the most straightforward way to estimate the metallicity of the NLR would be via the electron temperature method (Smith 1975), which is based on the use of the [O III]λ4363 auroral line. Unfortunately, this line is detected above 2σ in only 4 out of 14 low-luminosity AGN. In comparison, strong-line methods would usually require detection of low ionization lines such as [N II]$\lambda\lambda$6548,6584, which are outside of the wavelength coverage for most of the sample, or barely detectable as outshined by the broad H α. Here, I also recall that it is quite challenging to detect the [O III]λ4363 line in local Type 1 AGN to compare to the *JWST* results, as it is generally faint and not easy to deblend from the narrow and broad H γ and the Fe II pseudo-continuum (Baskin and Laor 2005b). This leads to the additional complication of having a comparison sample (the SDSS local AGN catalogue) where metallicity measurements would be biased towards high [O III]λ4363 emitters. In addition, it is well known that the metallicity of H II regions and star-forming galaxies, directly estimated via this method, are systematically lower than those produced adopting calibrations from photoionisation modelling by 0.1-0.4 dex (see e.g. Kennicutt Jr et al. 2003; Dors and Copetti 2005; López-Sánchez et al. 2007; Kewley and Ellison 2008; Marconi et al. 2024). This difference is even exacerbated in the case of AGN with the oxygen abundance being underestimated on average by 0.6–0.8 dex (Dors Jr et al. 2015; Dors et al. 2020a).

Lastly, I note that the oxygen abundance estimated via the T_e method or other calibrations (e.g. Storchi-Bergmann et al. 1998; Castro et al. 2017) does not necessarily trace the actual iron abundance, unless a chemical enrichment model is assumed. Indeed, high-redshift objects have been observed to display gas-phase oxygen abundances consistent with those observed locally (e.g. Arellano-Córdova et al. 2022; Jones et al. 2023). This follows as a consequence of the enrichment by core-collapse supernovae, while the total Fe abundance is expected to be significantly lower, having this element a delayed enrichment contribution from Type Ia SNe. An additional complication is the fact that Fe is heavily depleted onto dust grains (see e.g. Jenkins 2009; Shields et al. 2010). Although, within the standard evolutionary picture, the effect of depletion onto dust grains in the redshift range spanned by the sources described here is not expected to be a crucial channel to suppress the Fe II emission, as it might happen at lower redshift (Shields et al. 2010), more detailed studies are definitely needed to assess this possibility.

Oxygen abundance

Notwithstanding all these considerations, for 4/14 objects [O III]λ4363 was detected with SNR$\geq$2. Assuming Gaussian noise, and the redshift of each source being well determined, the 1-tailed probability of a false 2-sigma detection of [O III]λ4363 is 0.022. Supposing, in the worst case scenario, that the [O III]λ4363 line were actually absent in all sources, the joint probability of having 4 or more detections only due to positive statistical fluctuations would be $\simeq 1 \times 10^{-4}$. In the following, I assume all detections to be real, and proceed to estimate the gas-phase oxygen abundance.

I derived the electron temperature (T_e) using the PYNEB *getTemDen* routine (Luridiana et al. 2015). In most of these objects, it was not possible to access the typical optical density indicators such as the [O II]$\lambda\lambda$3726,3729 or the [S II]$\lambda\lambda$6716,6731 doublets. Actually, the spectral fit of the [O II]$\lambda\lambda$3726,3728 (unresolved) doublet was successfully carried out only in five objects, and in two cases (COS-ZS7 and JADES-028074) this happened with simultaneous detection of the [O III]λ4363 line. This ratio is an excellent tracer of the NLR density and temperature, and is virtually independent from the actual SED producing the ionisation. To compensate for this, I computed the electron temperature using an equispaced grid of densities from 10^1 cm^{-3} to 10^5 cm^{-3}. For each density value I evaluated the corresponding temperature of the high ionisation region (t_3) using the ratio between the [O III]λ5007 and the [O III]λ4363 emission lines (the O33 ratio) using the *getTemDen* routine[7]. Finally, I computed the oxygen abundances employing the PYNEB *getIonAbundance* routine. The uncertainty associated with the abundance measurements was derived as the 16th − 84th semi-interpercentile range of the abundance distribution obtained by varying the density. For the objects without [O II]λ3728 detection I assumed the average [O III]λ5007/[O II]λ3728 ratio (O32) derived from the sources where it was instead detected, i.e. 16.7.

I estimated the electron temperature for the low ionisation zone (t_2), adopting the relation $t_2^{-1} = 0.693\, t_3^{-1} + 0.281$[8] (see e.g. Dors et al. 2020a). Additionally, the total oxygen abundance was corrected for the unobserved ions adopting an average ionic correction factor (ICF) equal to the mean value of those measured in the Seyfert 2 sample described in Dors et al. (2020b), that is ICF(O^{2+})=1.21. For three out of four objects, this procedure yielded reasonable results with sub-solar oxygen abundances ranging between $Z = 12 + \log(O/H)$=7.5-8.1 and electron temperatures between 16,000 K and 24,000 K. In the case of RUBIES-CEERS-55604, adopting the A_V reported in Kocevski et al. (2024), the electron temperature inferred from the O33 ratio was unreasonably high ($T_e > 10^5$ K). At the same time, the combination of a narrow absorption bluewards of the Hβ and the low SNR of the Hγ hampered the possibility of estimating the Balmer decrement via the Hβ/Hγ ratio. For these reasons, I precautionarily excluded this value from the results. The values obtained via this procedure are reported alongside other narrow emission line ratios for the low-luminosity sample in Table 5.2.

With the aim of comparing the narrow-line properties between all the *JWST* low-luminosity sources and their local counterparts, in Fig. 5.7 I show $R_{\rm Fe}$ against the [O III]/Hβ ratio, while in colour-code I highlight the O32 ratio for the comparison sample. It is well known that there are several parameters influencing the [O III]/Hβ, namely the ionisation parameter, the metallicity, the shape of the ionising continuum, and the density (e.g. Veilleux and Osterbrock 1987). The dependence on all these parameters makes this ratio a suitable tool for interpreting observations of the nebular emission from active and inactive galaxies. In this case, the selection of a homogeneous control sample in terms of black hole mass and luminosity helps in narrowing down the parameter space. Indeed, assuming that the optical/UV region of the SED is dominated by an accretion disc, it is reasonable to expect that the ionising continua are not dramatically different as the average accretion parameters should be, by sample construction, close. In more quantitative terms, the difference in average $\log(M_{BH})$ and $\log(L_{5100\text{Å}})$ between the local sample and the *JWST* low-luminosity one amounts respectively to 0.15 and 0.25 dex, which is fairly close or even lower than the typical systematic uncertainty 0.3 dex and 0.2 dex. I therefore expect the shape of the continuum to be similar between these two samples as well as within the local sample itself. Similar considerations concerning how the shape of the SED should be limited by construction, apply to the diversity

---

[7] Line fluxes were corrected for the reddening (if present), evaluated from the Balmer ratio, assuming the SMC extinction curve from Gordon et al. (2016).

[8] Here I adopted a $t_2 - t_3$ relation calibrated for an AGN continuum. I repeated the same procedure adopting a different relation suited for a star-forming continuum (Pilyugin et al. 2009), but found that the average difference in the metallicity was negligible.

along the $R_{\rm Fe}$ axis in Fig.5.7.

Additional information can be gained employing the O32 ratio, colour-coded in Fig. 5.7 for the SDSS control sample, which serves as a useful proxy for the ionisation parameter. In the low-luminosity sample the [O II]$\lambda\lambda$3726,3728 doublet was reliably detected, albeit unresolved, in only a handful of *JWST* objects, while it was clearly measured in all the DG-T1AGN. For this reason, I only colour-code accordingly these few sources in Fig. 5.7.

It is thus interesting to observe that, from the main anti-correlation trend between $R_{\rm Fe}$ and [O III]/Hβ, which is basically a shallower version of the well-known $R_{\rm Fe}$-[O III] anti-correlation, an even steeper anti-correlation branch detaches (see dashed lines in Fig.5.7). Notably, the *JWST* low-luminosity objects sit nicely on this secondary branch. The nature of this secondary branch is not clear, but a speculative hypothesis is that this sample is a low metallicity trail. This interpretation seems favoured by the fact that the trail detaching at low values of $R_{\rm Fe}$ displays similar O32 values to those following the main trend. The same roughly holds for the faint AGN where this ratio was estimated. Indeed, once the shape of the ionising SED and the ionisation parameter (O32) are roughly fixed, [O III]/Hβ would increase with increasing metallicity at low metallicities and decrease with increasing metallicities at high metallicities (Groves et al., 2006; Curti et al., 2016; Dors Jr et al., 2015)[9]. Thus, it is possible to interpret the lower left branch occupied by the low-luminosity sample as having lower metallicities compared to the SDSS sources at similar ionisation parameters, even though it was not possible to have access to O32 for all of the low-luminosity sources.

If this scenario proved consistent, the weakness of the $R_{\rm Fe}$ in these sources could well be an effect of the reduced metal content, as this seems also the case for the three DG-T1AGN, whose metallicities are notoriously low. Still, I caution that the metallicities and ionisation parameters inferred from narrow lines only reflect the properties of NLRs. Indeed, BLRs can have chemical abundances enriched earlier than NLRs and their ionisation parameters are not necessarily connected to each other. Regardless, confirmations of metal-poor NLRs in low-luminosity sources would have room for the existence of metal-poor BLRs. In contrast, the more metal-rich NLRs in SDSS sources would likely indicate even more metal-rich BLRs. To understand more quantitatively what might be driving the difference in $R_{\rm Fe}$, I took advantage of theoretical photoionisation models to predict $R_{\rm Fe}$ under different physical conditions in the next section.

5.6.4 Photoionisation models

To better understand the difference in $R_{\rm Fe}$ between the low-z SDSS sample and the high-z *JWST* sample, I took advantage of theoretical photoionisation models computed with CLOUDY (v17.03, Ferland et al., 2017). During the computation of the models, I turned on all levels available for $\rm Fe^+$ with atomic data sets implemented by Sarkar et al. (2021), from Bautista et al. (2015), Tayal and Zatsarinny (2018), and Smyth et al. (2019). The theoretical computation of the strength of Fe II has been investigated by many previous works, which showed that $R_{\rm Fe}$ broadly depends on

---

[9] The threshold metallicity is roughly $\sim Z/Z_\odot \sim 0.15$ for SF regions but can be as high as $Z/Z_\odot \sim 1$ for NLRs of AGN due to the harder ionizing SED.

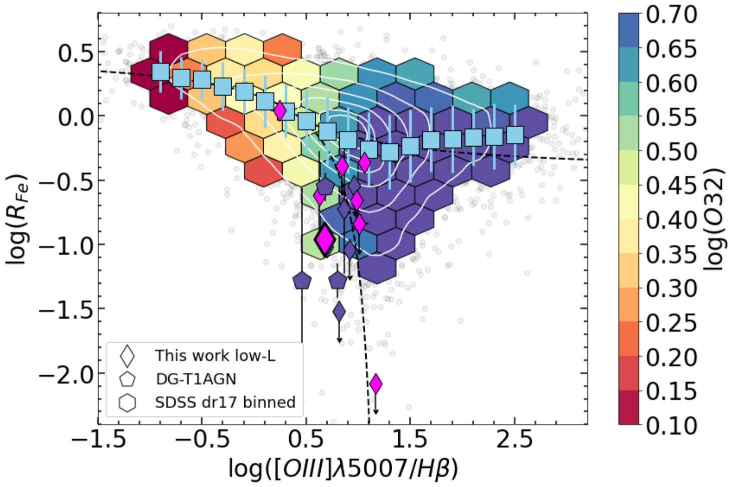

Figure 5.7. Distributions of the SDSS analogues and the *JWST* faint AGN sample in the log([O III]/Hβ])-log($R_{\rm Fe}$) plane with the O32 ratio colour-coded (except for the faint AGN where the [O II] was not detected). White contours show the distribution of SDSS AGN. The diamond with thicker black edges represents the value derived from the low-luminosity composite spectrum. Alongside the main anti-correlation, a secondary branch of SDSS objects detaches (the dashed lines guide the eye along the two branches), which still shares O32 values similar to those of the main trend. Notably, the *JWST* low-luminosity sources follow this steeper anti-correlation trail, likely driven by low metallicity as explained in the text.

parameters such as the Fe abundance, the gas volume density, the gas column density, the ionizing photon flux, the shape of the ionizing SED, and the microturbulent velocity (e.g., Baldwin et al., 2004; Ferland et al., 2009; Panda et al., 2018; Temple et al., 2020; Sarkar et al., 2021). For the purpose of this work, I make and justify the following assumptions and simplifications during photoionisation modelling, with the model parameters summarized in Table 5.4.

First, I restrict the comparison between the low-z and high-z samples to a region within the observed parameter space with similar broad Hβ luminosities and FWHM (see Fig. 5.1). Based on this selection criterion, I assume both samples of AGN share similar accretion properties and thus do not differ significantly in their ionising SED produced by the accretion discs. Specifically, I assume the shape of the SED to follow the functional form

$$F_\nu = \nu^{\alpha_{\rm uv}} \exp(-h\nu/kT_{\rm BB}) \exp(0.01\ {\rm Ryd}/h\nu) + a\nu^{\alpha_{\rm x}}, \tag{5.1}$$

where by default I set the temperature of the cutoff of the "Big Blue Bump" component to $T_{\rm BB} = 10^6$ K, the UV-to-X-ray slope to $\alpha_{\rm ox} = -1.4$ (by adjusting a in the equation above), the UV slope to $\alpha_{\rm uv} = -0.5$, and the X-ray slope to $\alpha_{\rm x} = -1.0$. It is worth noting that this assumption might not hold over the full energy range of the SED, as the majority of the *JWST* identified AGN in the sample is clearly X-ray weak. Recently, Maiolino et al. (2024) suggested two potential reasons for the lack of hard X-ray detections in early AGN, one being the intrinsic lack of the hard X-ray component due to the missing hot corona, the other being the presence of Compton-thick and dust-free clouds within the BLRs. To take into account these

Table 5.4. Input parameters for CLOUDY photoionisation models.

Parameter	Values
$Z/Z_\odot$	0.1, 0.2, 0.5, 1, 2
$\log U$	−3.5, −3, −2.5, −2, −1.5, −1
$\log(n_\mathrm{H}/\mathrm{cm}^{-3})$	11 (see Supplementary Material for more values)
$\log(N_\mathrm{H}/\mathrm{cm}^{-2})$	24, 25
Microturbulence	$v_\mathrm{turb} = 100$ km s^{-1}
AGN SED	$T_\mathrm{BB} = 10^6$ K; $\alpha_\mathrm{ox} = -1.4, -5$
Solar abundance set	Grevesse et al. (2010) abundance set
Dust	No dust
Fe II atomic data	Bautista et al. (2015), Tayal and Zatsarinny (2018), Smyth et al. (2019)

effects, I performed two additional tests by computing models with suppressed X-ray components and models with different hydrogen column densities.

Second, I assumed a fixed gas density and a fixed microturbulence velocity. Specifically, I adopted a hydrogen density of $n_\mathrm{H} = 10^{11}$ cm^{-3}, a value encompassed by those explored in many previous Fe II modelling works and is typical for BLR regions (e.g., Joly 1987; Netzer 1990; Collin and Joly 2000; Sigut and Pradhan 2003; Baldwin et al. 2004; Ferland et al. 2009; Panda et al. 2018; Sarkar et al. 2021). While there is evidence that the ISM density in galaxies is gradually increasing with redshift, there is neither observational evidence nor theoretical expectation that a similar evolution should exist in the BLR surrounding supermassive black holes. Systematic studies about the evolution of the broad line strength with redshift point in the direction of no evolution with cosmic time (Croom et al. 2002; Stepney et al. 2023). The same consideration applies to the ionisation parameter, which is observed to increase with redshift in the ISM, but its redshift evolution within BLRs is not clear and its value strongly depends on the geometry. I further discuss the effect of the ionisation parameter together with that of the metallicity later in this section. Nonetheless, I checked the effect of the density variation by computing models with $n_\mathrm{H} = 10^{10}$ cm^{-3} and $n_\mathrm{H} = 10^{12}$ cm^{-3}, respectively. In general, at lower density, R_Fe is enhanced at low ionisation parameters but suppressed at high ionisation parameters. At the high density, the opposite effect of the ionisation parameter on R_Fe is seen. This can be understood as the fact that Fe II is optimally emitted by clouds with certain combinations of densities and ionising fluxes (e.g., Baldwin et al., 2004), and the latter is simply the product of the ionisation parameter and the density. In Supplementary Material 5.9.4, I further discuss the effect of density variations.

The microturbulence is usually included in the photoionisation modelling of BLRs as a source for producing large Doppler broadening of line profiles within the photoionisation mean free path for line productions. The microturbulence strengthens the continuum pumping and line fluorescence that produce Fe II emission, and reduces the optical depths of Fe II lines (e.g. Netzer and Wills 1983; Baldwin et al. 2004). Although the origin of the microturbulence in BLRs remains debated (see Sec. 8.1 in Baldwin et al. 2004 for a review of possible mechanisms), it is generally

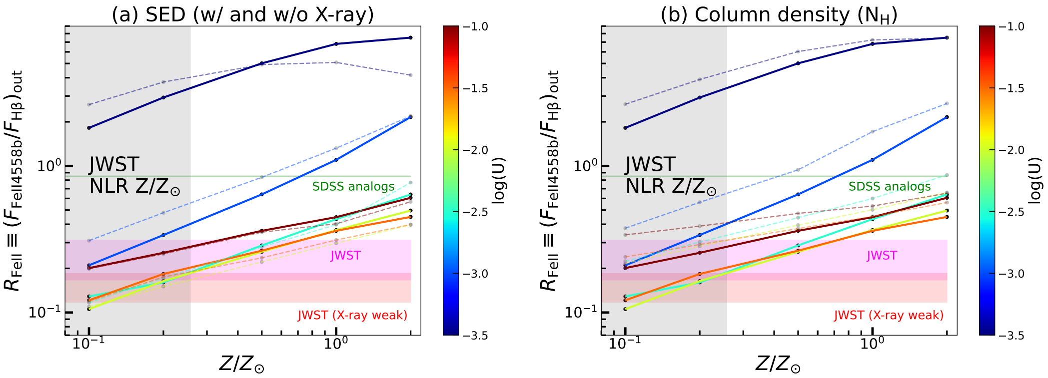

Figure 5.8. Comparisons between R_{Fe} predicted by photoionisation models with different input parameters and R_{Fe} measured in the sample. In each panel, the green shaded band indicates the mean R_{Fe} and its 1σ uncertainty found in the SDSS sample that matches the *JWST* sample in terms of Hβ luminosities and FWHM; the magenta shaded region corresponds to the value found in the *JWST* sample; the red shaded region corresponds to the value found in the *JWST* sample excluding sources with X-ray detections. The grey shaded region indicates the plausible range of metallicities in the NLRs of the *JWST* sources based on the T_e method for a subset of the *JWST* sample. Photoionsation model predictions are plotted as a function of the metallicity, $Z/Z_{\odot}$, and are colour-coded by the ionisation parameter. *Left:* solid lines and dashed lines correspond to models with and without a hard X-ray component representing the hot corona contribution to the SED, respectively, *Right:* solid lines and dashed lines correspond to models having $N_{\mathrm{H}} = 10^{24}$ cm^{-2} and $N_{\mathrm{H}} = 10^{25}$ cm^{-2}, respectively.

agreed among the previous modelling works that a microturbulent velocity of at least $v_{\mathrm{turb}} = 100$ km s^{-1} is needed to correctly predict Fe II emission (Panda et al. 2019), which is also what I adopted in these models. One potential way to connect the microturbulence to the other peculiar features of this sample, in particular the X-ray weakness, is to consider the magneto-hydrodynamic (MHD) wave explanation, where the microturbulence comes from non-dissipative waves generated by magnetic fields (Bottorff and Ferland, 2000). If the hot corona producing the hard X-ray emission ($E \gtrsim 2$ keV) is missing in these low-luminosity AGN due to the absence of the magnetic field lifting the corona from the accretion disc, it might be reasonable that the microturbulence is also suppressed and even vanishing in these early AGN, leading to reduced emergent Fe II emission. The issue with this explanation is that the reason for the vanishing magnetic fields is not clear and it is also not clear whether the microturbulence should rise from the MHD waves.

I note that it is still possible that the density and microturbulence play a role in producing the observed difference in R_{Fe} . This choice of not varying these parameters is mainly motivated by the fact that their redshift evolution is neither expected nor observed. The main parameters inspected here are the metallicity (or, more precisely, the iron abundance), the power-law X-ray component of the SED, and the hydrogen column density. Although previous works on BLR metallicities of bright quasars suggest fast chemical evolution within BLRs (e.g., Dietrich et al., 2003a; Maiolino et al., 2003; Wang et al., 2022b), the sample mainly consists of lower luminosity Type 1 AGN and it is not unreasonable to speculate they are more metal-poor compared to the local AGN. Checking the effect of the X-ray component and the hydrogen column density, as I have explained, is motivated by the fact that the *JWST* identified Type 1 AGN are mostly X-ray weak. One potential explanation is the lack of hot coronae in these AGN, meaning the absence of the power-law X-ray component in their SEDs, an occurrence verified for instance in Ricci et al. (2020) to explain the drastic transformation of the X-ray properties following a changing-look event. The other potential explanation is the presence of Compton-thick ($N_{\rm H} \gtrsim 1.5 \times 10^{24}$ cm^{-2}) and dust-free clouds within their BLRs. While such clouds might not be uncommon for line-emitting clouds within BLRs (Netzer, 2009b), to significantly obscure X-ray emission, they need to have a large covering fraction near unity. This might also explain the high EWs of broad Hα in early AGN (Maiolino et al. 2023; Wang et al. 2024) and could be caused by the metal-poor environments and the consequent ineffective removal of dense gas through radiation pressure. Regardless, I computed additional models with $N_{\rm H} = 10^{25}$ cm^{-2} to check the potential effect with a further increase in the column densities of BLR clouds (compared to $N_{\rm H} = 10^{24}$ cm^{-2} by default).

In Fig. 5.8, I compare the Cloudy model predictions with $R_{\rm Fe}$ measured in the sample. Specifically, from the sample, I plot the mean $R_{\rm Fe}$ of the whole *JWST* sample, the X-ray weak *JWST* sample, and the SDSS analogues matched in Hβ luminosities and FWHM, together with the corresponding 1σ uncertainties. The mean $R_{\rm Fe}$ of the SDSS sample is roughly 3.5 times that of the whole *JWST* sample, which is roughly 1.6 times that of the X-ray weak *JWST* sample. I plot the model predicted $R_{\rm Fe}$ as a function of the metallicity and the ionisation parameter. At fixed ionisation parameters, $R_{\rm Fe}$ generally increases with increasing metallicities. Although Fe II transitions are important cooling channels in the partially ionised zones within the BLR clouds, meaning their strengths are largely determined by the heating and cooling equilibrium rather than the Fe abundance, this effect is stronger for the UV Fe II transitions, while the optical Fe II transitions have a stronger metallicity dependence (Shields et al., 2010). At fixed metallicity, on the other hand, $R_{\rm Fe}$ does not exhibit a strong dependence on the ionisation parameter for $\log U > -2.5$ and only starts to significantly increase with decreasing ionisation parameters for $\log U < -2.5$. At low ionisation parameters, the intensity of Hβ drops significantly due to the drop in the ionisation rate. In contrast, due to the low ionisation potential of Fe, the intensity of Fe II from the partially ionised zone decreases more gradually than the Hβ.

Focusing on the high ionisation parameter branch, the mean $R_{\rm Fe}$ of the SDSS sample is consistent with $Z/Z_\odot \gtrsim 2$, and the mean $R_{\rm Fe}$ of the *JWST* sample can be explained by $0.1 \lesssim Z/Z_\odot \lesssim 0.5$. In comparison, I mark the potential range of the NLR metallicities for the *JWST* sample with the shaded region. I note that the BLR metallicities could be well above the NLR metallicities, and the abundance ratio of Fe/O could also be different. Regardless, from these models, the metallicity difference appears as a plausible explanation for the much lower $R_{\rm Fe}$ in the *JWST* sample.

On the left panel of Fig. 5.8, I simulate the effect of an intrinsic X-ray weakness by virtually removing the corona. I achieved this by computing a set of models with $\alpha_{\rm ox} = -5$, which effectively makes the power-law X-ray component contributed by the hot corona negligible compared to the emission from the accretion disc. The resulting models are plotted as dashed lines, which do not predict very different $R_{\rm Fe}$ compared to the fiducial models with $\alpha_{\rm ox} = -1.4$ at given metallicities and ionisation parameters. This is expected as the hard X-ray does not play a crucial role in the heating and ionization at the optical depths where most of the Fe II is produced. In addition, compared to the accretion disc emission, the hot corona contributes little to the total soft X-ray emission that is responsible for creating the partially ionised zone where Fe II originates from. I emphasise again that I assumed no significant difference in the shape of the accretion disc emission between the SDSS analogues and low-luminosity sources, given their accretion parameters are empirically constrained to be similar by their broad Hβ luminosities and FWHM. On the right panel of Fig. 5.8, I checked the effect of thicker BLR clouds with larger column densities reaching $N_{\rm H} = 10^{25}$ cm^{-2}. As expected, increasing the column density increases $R_{\rm Fe}$. This is because Hβ is mainly produced by the ionised layer of the clouds, whereas Fe II becomes the major coolant at large cloud depths, and thus increasing the cloud depths tends to boost $R_{\rm Fe}$. However, this trend is opposite to what is observed, that is, a decrease in $R_{\rm Fe}$ at early times.

To summarise, neither the hot corona emission nor the column density seems to cause the observed difference in $R_{\rm Fe}$. The metallicity is likely the most important factor governing the $R_{\rm Fe}$ in the sample, consistent with the interpretations based on $R_{\rm Fe}$ versus narrow-line ratios in Fig. 5.7. These analyses point towards the picture where, unlike luminous quasars at early times, the low-luminosity AGN in the sample have less chemically evolved BLRs or, at least, less Fe-enriched BLRs. I further discuss the implications for the chemical evolution of these systems in Section 5.7.

5.6.5 An X-ray perspective

The low luminosity AGN population discovered by *JWST* is prevalently undetected in the X-ray surveys (Yue et al. 2024; Maiolino et al. 2024) with the detection efficiency being below the percent level (see e.g. Kocevski et al. 2024). This sample makes no exception, with all (but two) of the low luminosity sources being undetected in the X-rays in their respective fields. This also applies for the three newly discovered RUBIES objects where no X-ray counterpart was found in the 800 ks of the Chandra Aegis-X Deep survey catalogue (Nandra et al. 2015). The only two non quasar sources which escape this picture are XID-2028 and JADES-209777, both of them reliably X-ray detected as reported in Brusa et al. (2010) and Juodžbalis et al. in prep. Intriguingly, these sources are the objects with the highest $R_{\rm Fe}$ below the quasar luminosity regime (respectively $R_{\rm Fe} = 1.10$ and $R_{\rm Fe} = 0.44$), and in line or even above the $R_{\rm Fe}$ expectations for the local sources in the corresponding region of the parameter space (see the colour-code in Fig.5.4). Although it is certainly risky to draw conclusions based on such a small-number statistics, it is interesting to notice that the only two X-ray detected sources of the sample are also those on the high end of the $R_{\rm Fe}$ distribution for the *JWST* low-luminosity objects.

From a theoretical perspective, it is not straightforward to link the X-ray properties with the $R_{\rm Fe}$ strength. As I showed in Sec.5.6.4, the intensity of the optical iron does not strongly correlate with the hard X-rays component. This is due to the fact that the Fe II is mostly produced at optical depths where the heating and the ionisation are due to lower energy soft X-ray photons rather than hard

X-ray photons. Indeed, from an observational standpoint, R_{Fe} does instead seem to positively correlate with the so-called soft excess, i.e. the low-energy ($\lesssim 0.5$ keV) extrapolation of the hard X-ray power law (Wilkes et al. 1987; Wang et al. 1996; Shastri et al. 1993). This broadly agrees with the findings on narrow-line Seyfert 1 galaxies, whose X-ray spectra on average steep, being generally stronger optical iron emitters. Here I mention two possible scenarios to link X-ray and R_{Fe} weaknesses. In the first case, the accretion parameters characterising the local and the high-z sources are systematically disparate because of different $\mathrm{M_{BH}}$ and $\mathrm{L_{bol}}$ calibrations between these two populations. Therefore, these classes of sources have intrinsically distinct soft X-ray SEDs that lead to the observed R_{Fe} difference. Secondly, it is possible that the low metallicity of the BLR clouds causes both the X-ray and the R_{Fe} weakness. I already showed in 5.6.4 that the R_{Fe} observed in the faint *JWST* AGN are consistent with metal-poor BLR. Qualitatively, it is possible to speculate that this effect might also lead to the BLR clouds lingering close to the innermost AGN engine because of the low effective radiation pressure. Therefore, the reduced metal content devoids the BLR clouds of the metal line transitions which helps reaching the dynamical equilibrium.

I also highlight that both these X-ray detected sources have substantially lower redshifts than the bulk of the low luminosity sample ($\langle z\rangle$=6.34), in particular $z = 1.59$ for XID-2028 and $z = 3.71$ for JADES-209777 against. The only other object at a somewhat lower redshift from the bulk of the redshift distribution of the low luminosity sample is JADES-028074 (Juodžbalis et al. 2024a) at z=2.26. This object is of utmost interest as it encapsulates some of the typicalities of the faint *JWST* AGN, such as the X-ray (and Radio) weakness, the lack of ionised outflows, and hereby we also add the R_{Fe} weakness, at the same time showing correlated absorptions in the Hβ, Hα and He I. Within an evolutionary framework, sources akin to JADES-028074, could be experiencing the transitioning phase between an AGN with the characteristics of the faint *JWST* AGN and those of Seyfert 1 AGN observed at lower z exemplified by JADES-209777 and XID-2028. In a wider perspective, the significant fraction of JWST-detected AGN with absorption features in the broad lines (Matthee et al. 2024; Kocevski et al. 2024; Wang et al. 2024; Maiolino et al. 2024; Juodžbalis et al. 2024a) could be experiencing the "blow-out" phase bridging between the obscured and unobscured stages of the AGN cycle (Hickox and Alexander 2018). Yet, the outflow velocities reported in this case are significantly lower than those seen in the nuclear region of quasars measured from broad absorption lines or in X-ray spectra (a few hundred versus tens of thousands km s^{-1}).

5.7 Discussion

The first years of *JWST* observations have revolutionised our understanding of the high-redshift Universe, in particular by sheding a new light on an enigmatic population of faint AGN. These sources have been discovered to generally share a set of observational characteristics that distinguish them from local counterparts of similar luminosity and hosting black holes of comparable mass. Examples of these observational features are the weakness of the ionised outflows, routinely observed in low-z sources as blue wings in the [O III] profile, the incidence of absorption features in Balmer lines, and their remarkable X-ray and radio weakness. Hereby I also demonstrated the weakness of their $R_{\rm Fe}$ ratios when compared to a sample of local Type 1 AGN with similar Hβ properties.

The strength of the $R_{\rm Fe}$ ratio is influenced by multiple factors (see e.g., Netzer and Wills, 1983; Joly, 1987; Verner et al., 1999; Baldwin et al., 2004), such as the shape and the intensity of the incident continuum, the cloud density, the column density, the metallicity, and the microturbulence, which concur to produce the optical spectral diversity of Type 1 AGN (e.g. Panda et al. 2019). Although it is not possible to directly infer the density and the turbulent velocity, I could narrow down the parameter space in terms of the incident SED, by selecting a local Type 1 control sample with comparable $\rm M_{BH}$ and $\rm L_{H\beta,br}$ (and likely $\rm L_{bol}$). This under the hypothesis that the shape of the accretion disc SED only depends on $\rm M_{BH}$ and $\rm L_{bol}$ with the exception of the hard X-rays that, as I showed, are not crucial for the Fe II production. Here, my main finding is that, on average, the *JWST* low-luminosity sources exhibit significantly (p-value$\lesssim 10^{-6}$) lower $R_{\rm Fe}$ than their local counterparts.

The same, instead, does not apply to the more luminous objects of the sample, which closely resemble their lower redshift counterparts. The similarity in terms of continuum shape and emission lines -albeit some known trends with the luminosity, e.g. the Baldwin effect (Baldwin 1977)- is not surprising, since high-redshift quasars have often been observed to match the spectral properties of typical sources at $z \lesssim 1$ (e.g. Kuhn et al. 2001; Mortlock et al. 2011; Hao et al. 2013b; Banados et al. 2018; Fan et al. 2023; Trefoloni et al. 2024c). This implies that, at least for the bright end of the AGN distribution, no signs of clear evolution in the spectral properties can be observed up to $z \sim 7$.

Similar considerations have been drawn from the chemical enrichment of the BLR of luminous quasars which, parametrised for instance in the UV Fe II/Mg II, does not even show any evolutionary trends up to redshift 7.5 (see e.g. Dietrich et al. 2003a; Mazzucchelli et al. 2017; Onoue et al. 2020; Sameshima et al. 2020; Wang et al. 2022b; Trefoloni et al. 2023; Jiang et al. 2024), although the dependence on the Fe and Mg abundances of this ratio is quite weak (Sarkar et al. 2021).

The most straightforward explanation for this lack of evolution resides in the fact that quasars are expected (e.g. Costa et al. 2014) and observed (e.g. Cantalupo et al. 2014; Mignoli et al. 2020; Overzier 2022) to reside in overdense regions of the cosmic web, and therefore likely represent the most advanced stage of the chemical evolution at all the cosmic times. This effect has often been epitomised in the so-called luminosity-metallicity relation ($L-Z$ relation; Hamann and Ferland 1993, 1999; Dietrich et al. 2003b). In these spots, the first generation of low- and intermediate-mass evolved stars might have been able to promptly produce heavy elements even at $z \gtrsim 6$, following the rapid enrichment of α-elements owing to type II supernovae.

All the luminous sources in the sample are X-ray detected (or X-ray observations are ongoing), while the low-luminosity AGN are mostly not (12/14). Notwithstanding the nature of the X-ray weakness (intrinsic or rather due to absorption) in these sources has not been understood, the overwhelming fraction of X-ray weak objects in this redshift and luminosity regime calls for an explanation. Although several mechanisms involving, for instance, a systematic increase in the ISM density have been proposed to explain the increasing X-ray obscured fraction (e.g. Gilli et al. 2022; Alonso-Tetilla et al. 2024), such a large amount seems hardly reconcilable with those observed at lower redshift. As a term of comparison, the X-ray weak fraction ranges between 2% in optically selected samples (e.g. Gibson et al. 2009) to ~20% in samples of broad absorption line objects such as that in Liu et al. 2018, reaching as high as ~25% for the most luminous blue quasars at z~3 (Nardini et al. 2019b). Yet, even the highest of these X-ray weak fractions is far below the non-detection rate of the faint *JWST* AGN.

An obvious question is how these sources relate to the local population of AGN and how the transition between these apparently different classes of sources might take place. Some clues about a tentative evolutionary path bridging between the population of faint high redshift and local AGN, could be embedded in the fraction of sources displaying blueshifted Balmer absorption features, which the latest compilations report to be at least 10% (see Section 7 in Juodžbalis et al. 2024a for a more complete discussion). In this case, I detected significant absorption features in 2/14 low-luminosity AGN. This fraction is significantly larger than the 0.1% found in the SDSS Type 1 compilation at lower redshift (Juodžbalis et al. 2024a). Yet, this value could be somewhat underestimated, given that the typical SDSS resolution is lower than the high-resolution *JWST* grating, that the SDSS spectra have generally lower SNR, and that a systematic search for Balmer absorptions in a large sample of SDSS Type 1 AGN has not yet been undertaken.

Balmer lines absorption requires peculiar conditions of the gas along the line of sight, in particular a substantial amount of mostly neutral gas with a significant fraction of hydrogen pumped to the n = 2 level. Due to the short lifetime of H(n = 2), it is quite challenging to have prominent absorption in hydrogen lines without the presence of high-density gas with column densities of the order of $N_{\mathrm{H}} \sim 10^{21-23}$ cm $^{-2}$ (the interested reader may consult Sec 5.2 in Juodžbalis et al. 2024a for a more complete discussion of the gas properties required for Balmer absorption). The large column densities required to produce Balmer absorption, combined with the recent findings of larger H α equivalent widths in *JWST* low-luminosity objects (Maiolino et al. 2024; Wang et al. 2024), could fit in the scenario where the BLR has both a high column density and a high covering factor. These factors, could also be key in producing the extremely high fraction of X-ray non-detections, by means of dust-free absorption.

In Sec. 5.6.4 I explored which physical parameters could be the most conducive to driving the observed R_{Fe} weakness, by means of photoionisation modelling. In doing so, I adopted observationally educated guesses, while, at the same time, narrowing down the parameter space of the control sample. I employed the strong observational constraints about the X-ray emission in the *JWST* low-luminosity AGN to test whether an intrinsic lack of the hard X-ray coronal emission could play any role in producing the low R_{Fe} observed within the sample, but I found none. This is in line with several other works reporting the irrelevance or even the anti-correlation between the strength of the hard X-ray component (parametrised via the spectral index) and the R_{Fe} ratio (see e.g. Shastri et al. 1993; Wang et al. 1996; Laor et al. 1997; Wilkes et al. 1999; Shen and Ho 2014). As a consequence, I argue that the X-ray weakness cannot account for the observed R_{Fe} weakness.

At the same time, I also excluded systematic differences in the ionising SED as the drivers of the observed difference between the *JWST* low-luminosity and the local AGN, under the hypothesis that the spectra of accretion discs with similar M_{BH} and L_{bol} do not vary greatly with redshift. Such non-evolution seems to hold, at least, for the UV/optical regions of the accretion disc SED in quasars which show a remarkable similarity between low and high-z (e.g. Trefoloni et al. 2024c). Although there is evidence for an increase of both the ISM ionising parameter (see e.g. Reddy et al. 2023 and references therein) and electron density (see e.g. Isobe et al. 2023), little however is known about the redshift evolution of these properties in the BLR. Even less is known about the causes for the microturbulence invoked to give the higher Fe II multiplets access to a greater range of exciting continuum photons, thus increasing the Fe II equivalent width (Netzer and Wills 1983; Baldwin et al. 2004; Bruhweiler and Verner 2008). Under the hypothesis that these quantities are not systematically different between the low-luminosity *JWST* and the local AGN, I showed that the most likely responsible for the low $R_{\rm Fe}$ measured is the BLR metallicity, as already pointed out for local sources in Floris et al. (2024), although it not is possible to directly probe it in the sample.

The low metallicity could be the keystone to explain the exotic properties in both the NLR and BLR of *JWST* low-luminosity objects. Indeed, as the low metal (or at least Fe) content seems the most viable explanation for the weakness of the $R_{\rm Fe}$, the reduced metal abundance in the BLR gas could, at least qualitatively, imply significantly fewer line transitions to provide radiation pressure support. This in turn, would translate into a closer, and hence more covering, BLR. A low-metallicity framework also goes in the direction of explaining the scarcity of prominent [O III] outflows, which struggle to develop on galactic scales due to the reduced radiation pressure, as already pointed out in Maiolino et al. 2023. If this were the case, the scarcity of metals would also naturally explain the several similarities between the faint *JWST* AGN and those observed in local metal poor dwarf galaxies.

Valuable insights on the physical properties of these high-redshift sources could be gathered, if the analogy between the faint *JWST* AGN and those in metal poor dwarf galaxies actually holds. Recently, Doan et al. (2024) proposed that SDSS J1201+0211, a compact metal-poor dwarf galaxy, possibly hosting an AGN, could represent a local analogue to the primordial galaxies. Here the authors focus on the locus occupied by this object in the BPT diagram, which is also populated by low-metallicity star forming (dwarf) galaxies, as well as high-z AGNs recently discovered by *JWST* (e.g. Maiolino et al. 2023; Harikane et al. 2023; Übler et al. 2023). Although a more quantitative and systematic assessment of the similarities between the faint high-redshift AGN population and that in metal poor dwarf galaxies has not yet been undertaken, some commonalities are apparent. For instance, weak ionised outflows (if any), mostly detectable in the [O III], the X-ray weakness and the scarcity of heavy elements characterise both these classes of objects (although I report a faint outflow component in J1025+1402). Hereby, I also highlight the $R_{\rm Fe}$ weakness revealed by the analysis on the three DG-T1AGN with broad Hβ, which this analysis proved consistent with a reduced iron content. Additionally, I also remark, as a further similarity, the high incidence of Balmer absorption features encountered in the dwarf galaxies hosting broad line AGN. Indeed, one out of the four DG-T1AGN described in Burke et al. (2021) (J1025+1402), also included in the sample, shows a clear absorption in the H α profile. Moreover, I also report a significant absorption in the Hβ profile of SBS_0335-052E (ΔBIC=-44), thus yielding a 40% detection rate, although on a fairly small sample.

To summarise, evidence is growing in favour of metallicity as being the ultimate responsible for the observed differences between the local and the high-redshift AGN populations. Yet, additional observations and modelling will prove key in constraining the physical properties of this newly discovered, intriguing class of AGN.

5.8 Summary and conclusions

I assembled a sample of high-redshift AGN observed by *JWST* spanning a wide range in terms of luminosity and black hole mass with the aim of characterising the strength of the $R_{\rm Fe}$. To this end, I performed a detailed spectroscopic analysis and selected control subsamples at lower redshift to compare their properties and assess possible differences. I remark that the control samples are selected to match the *JWST* AGN in both Hβ FWHM and luminosity, which are the direct observables that best capture the black hole properties and accretion parameters. Additionally, I also included as a separate comparison sample three metal-poor dwarf galaxies hosting low-luminosity AGN as tentative super local counterparts. Here I summarise my findings:

- The strength in the ratio between optical Fe II and the Hβ equivalent widths ($R_{\rm Fe}$) in the *JWST* low-luminosity AGN is significantly lower (p-value $< 10^{-6}$) than in their local SDSS counterparts with similar BH accretion parameters. This $R_{\rm Fe}$ weakness is not compatible with the expectations from known sets of correlations such as the 4DE1.

- The strength in the $R_{\rm Fe}$ of the high-luminosity (quasar) subsample is instead consistent with the expectations derived in a comparison sample of quasars between $1.5 < z < 3.5$.

- The photoionisation modelling explored here suggests the weakness of the $R_{\rm Fe}$ in faint AGN is consistent with low metal content in their BLRs. In contrast, high luminosity sources likely reached the chemical maturity at early cosmic times.

- The faint AGN hosted in local metal poor dwarf galaxies (DG-T1AGN) also exhibit strikingly low $R_{\rm Fe}$. Also in this case, the driver for the observed weakness is expected to be the lack of metals.

- In all the parameter spaces explored, faint AGN in dwarf metal-poor galaxies (DG-T1AGN) occupy the same locus as the low-luminosity *JWST* AGN. Additionally, they also seem to share other characteristics such as X-ray weakness, faint or absent ionised outflows and a tentative high incidence of absorption features in Balmer lines. These findings go in the direction of DG-T1AGN being close local analogues to the faint high-redshift AGN population, barring a potential difference in their host galaxy properties to be verified by follow-up studies.

The launch of the *JWST* space telescope three years ago opened a new era for astronomy, astrophysics and cosmology. It made possible, for the first time, not only to observe the brightest objects shining only a few hundred Myr after the Big Bang, but even to start collecting a census of the elusive populations of faint sources already in place at that time.

The results elaborated here point in the direction that the realm of AGN shows hints of bimodality. If luminous quasars at redshift $\gtrsim 6$ seem to exhibit features broadly consistent with those observed at lower redshifts, the same does not apply to faint sources which display quite peculiar features. A comprehensive model capable of explaining such exotic behaviours (such as the X-ray and $R_{\rm Fe}$ weakness, the faint ionised outflows, the incidence of Balmer absorption) is still far from being designed. Yet, pieces of evidence in favour of the metallicity playing a key role are being collected.

Obtaining new (possibly large) panchromatic datasets will be key to consolidate our knowledge on a more solid base, as well as to infer many new details still overlooked. To this end, a crucial role will be played by the new generation of optical and infrared ground based telescopes such as Extremely Large Telescope (ELT; Gilmozzi and Spyromilio 2007), the Giant Magellan Telescope (GMT; Sanders et al. 2007) and the Thirty Meter Telescope (TMT; Skidmore et al. 2015). This new class of observing facilities will allow us to investigate the Universe up to the dark ages with unprecedented sensitivity. Another viable way to strengthen our knowledge about the faint *JWST* AGN population is a more thorough assessment of their similarity with AGN in local dwarf metal poor galaxies. If these sources were confirmed to be reliable very local counterparts of the high-redshift population, this would enable us to get a deeper understanding of the high-redshift Universe with unparalleled sensitivity and spatial resolution.

5.9 Supplementary Material

5.9.1 Systematic $R_{\rm Fe}$ differences due to the fitting technique

Here I explore the possible differences in the $R_{\rm Fe}$ measurements between the low-luminosity AGN and the SDSS ones, whose properties are described in Wu and Shen (2022). To this aim, I compared the $R_{\rm Fe}$ values reported in the catalogue estimated through the PYQSOFIT code (Guo et al. 2018) to those measured via the spectral fitting code used here, adopting the same Gaussian line deconvolution for the Hβ complex adopted in the catalogue. The most noticeable difference here is that the PYQSOFIT code employs the Boroson and Green (1992b) Fe II template, while I rely on CLOUDY models of Fe II emission. To ensure a test sample with data of decent quality, I performed the following selection process. I started from the control sample (~26,600 sources), and selected all those with low $R_{\rm Fe}$ ($\leq$0.15) and $R_{\rm Fe}/\sigma_{\rm R_{Fe}} \geq 3$. I sorted these sources by their average continuum SNR and picked the top 50. I then performed a spectral fit on these sources using the fitting code employed here. In Fig.5.9 I show the distribution of the residuals defined as $\Delta R_{\rm Fe} = (R_{\rm Fe\,SDSS} - R_{\rm Fe\,ours})/R_{\rm Fe\,SDSS}$. Although there is quite a significant spread (the standard deviation approaches 100%), I note that the mean is close to zero ($\langle \Delta R_{\rm Fe} \rangle$=-0.04). This highlights that the fitting technique used here is not biasing on average the R_{Fe} measurements with respect to the control sample. Additionally, the tail of negative values, implies that in the cases of highest inconsistency these measurements tend to overestimate R_{Fe} with respect to the SDSS. Therefore, in these cases, the adoption of the alternative recipe for evaluating R_{Fe} , would result in even lower R_{Fe} values, thus going in the direction of even strengthening the observed difference.

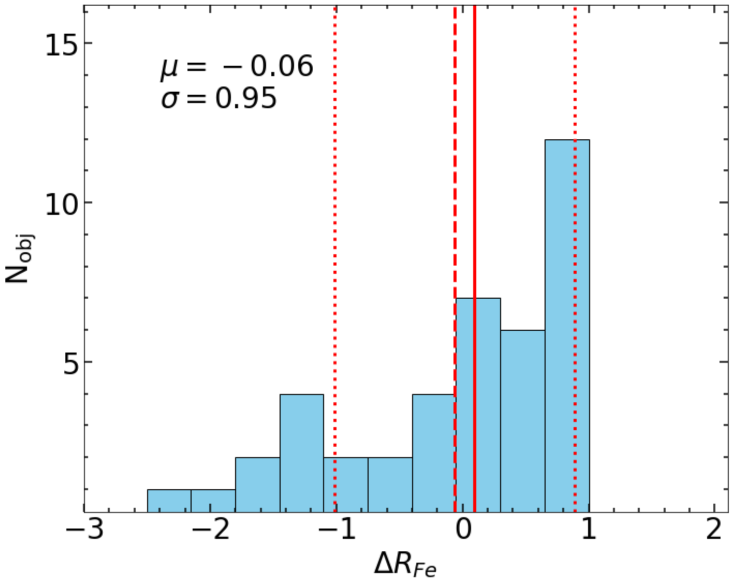

Figure 5.9. The ΔR_{Fe} distribution. Although the fairly large spread, the mean relative difference is close to zero, thus these estimates are not systematically offset with respect to the SDSS control sample.

5.9.2 Spectral fits of the composite spectra

In this Section I show the spectral fits of the composite spectra shown in Fig. 5.3. The colour-coding is the same as in Fig. 5.2. In particular, in Fig. 5.10, I present the fit of the low-luminosity composite spectrum. In the top panel I show the fit without the broad component for the [O III] doublet, while in the bottom figure it is included. There, I also report the values of the broad Hβ (red) and [O III] (azure) FWHM values, which are significantly different. In Fig. 5.11 I show also the spectral fits of the other composite spectra built employing the control samples as well as the AGN in metal-poor dwarf galaxies.

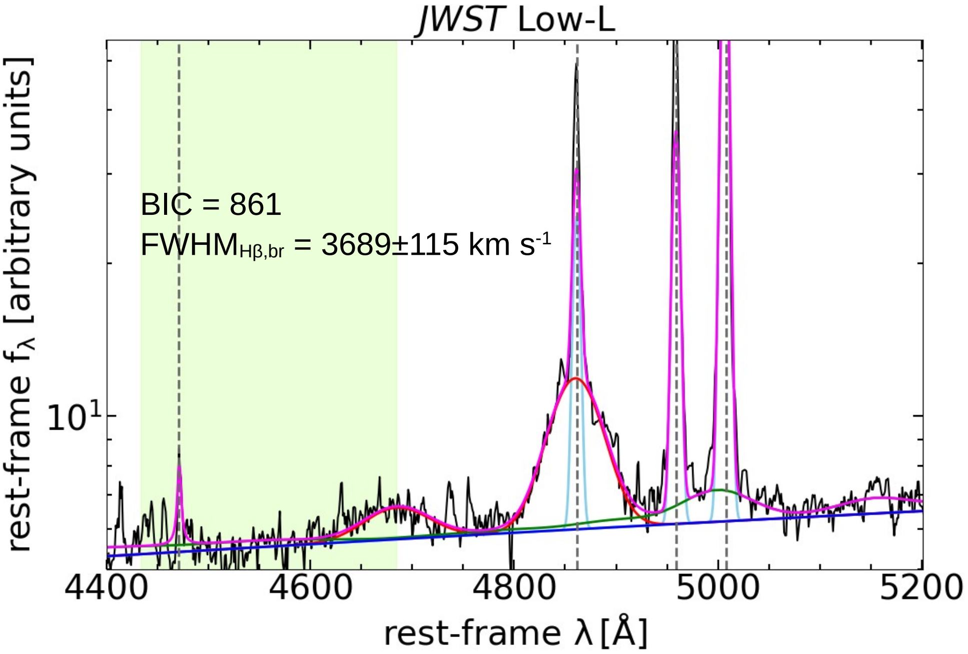

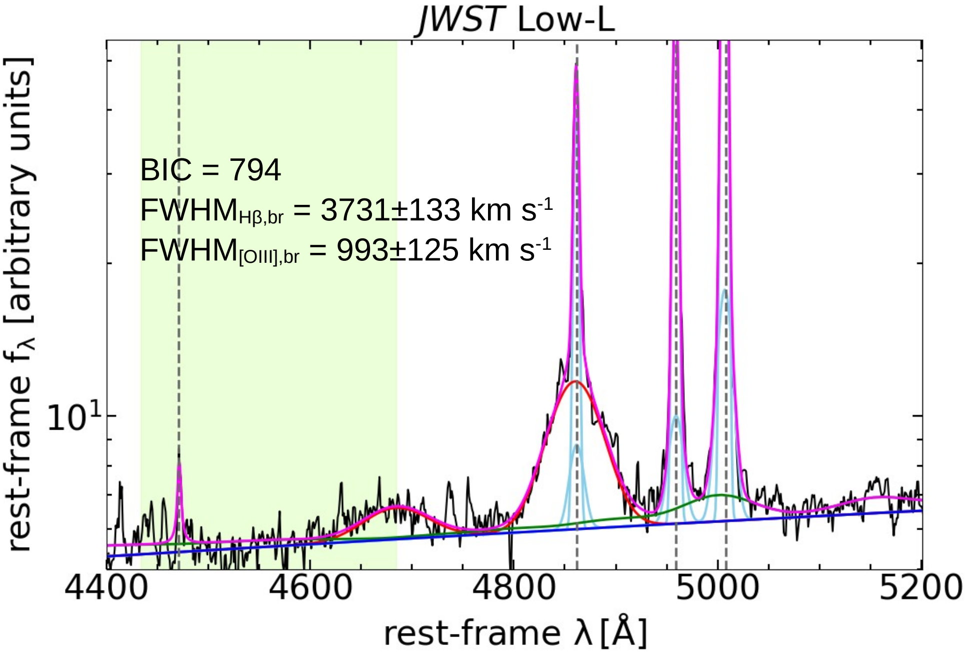

Figure 5.10. The spectral modelling of the Hβ region of the low-luminosity composite spectrum. The colour-coding is the same as in Fig.5.12. In the top panel I show the fit where only one NLR narrow component is included. In the bottom panel a narrow and a broad outflow component are included for the NLR. The improvement in the best fit BIC is significant (ΔBIC=-67). The FWHM of the broad [O III] (azure) is significantly smaller than that of the broad Hβ supposedly tracing the BLR (red).

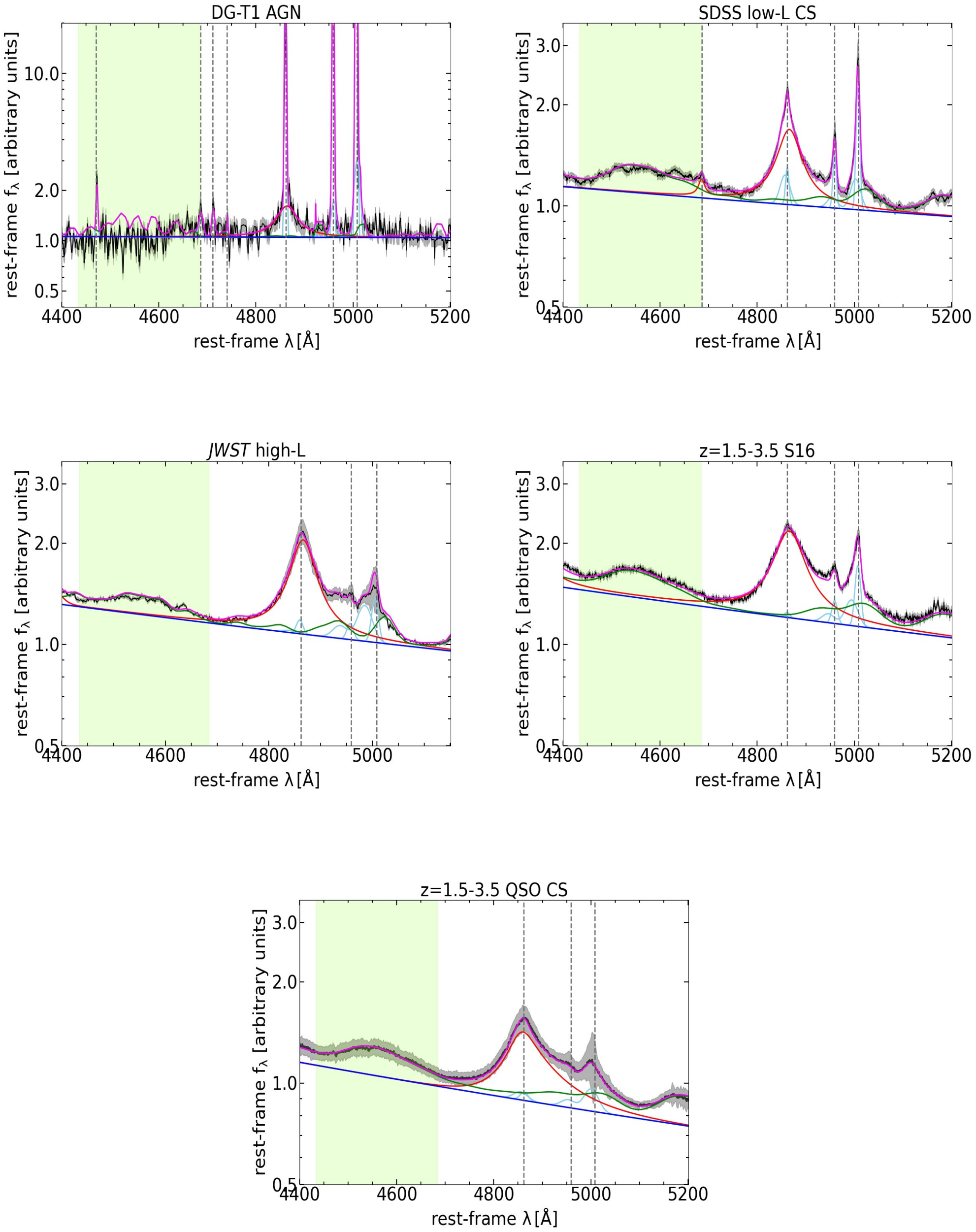

Figure 5.11. The spectral modelling of the Hβ–[O III] region for the composite spectra shown in Fig.5.3. The colour-coding is the same as in Fig.5.2.

5.9.3 Fits atlas

Here I present the complete atlas of the spectral fits described in 5.4.1, together with the rest-frame spectra. Lines produced in the BLR are highlighted in red, those arising from the NLR in light blue, the Fe II is marked in green, while the power-law continuum is shown in blue. The various component are labelled as described in the top left plot. I also highlight in green the region where the Fe II EW is evaluated.

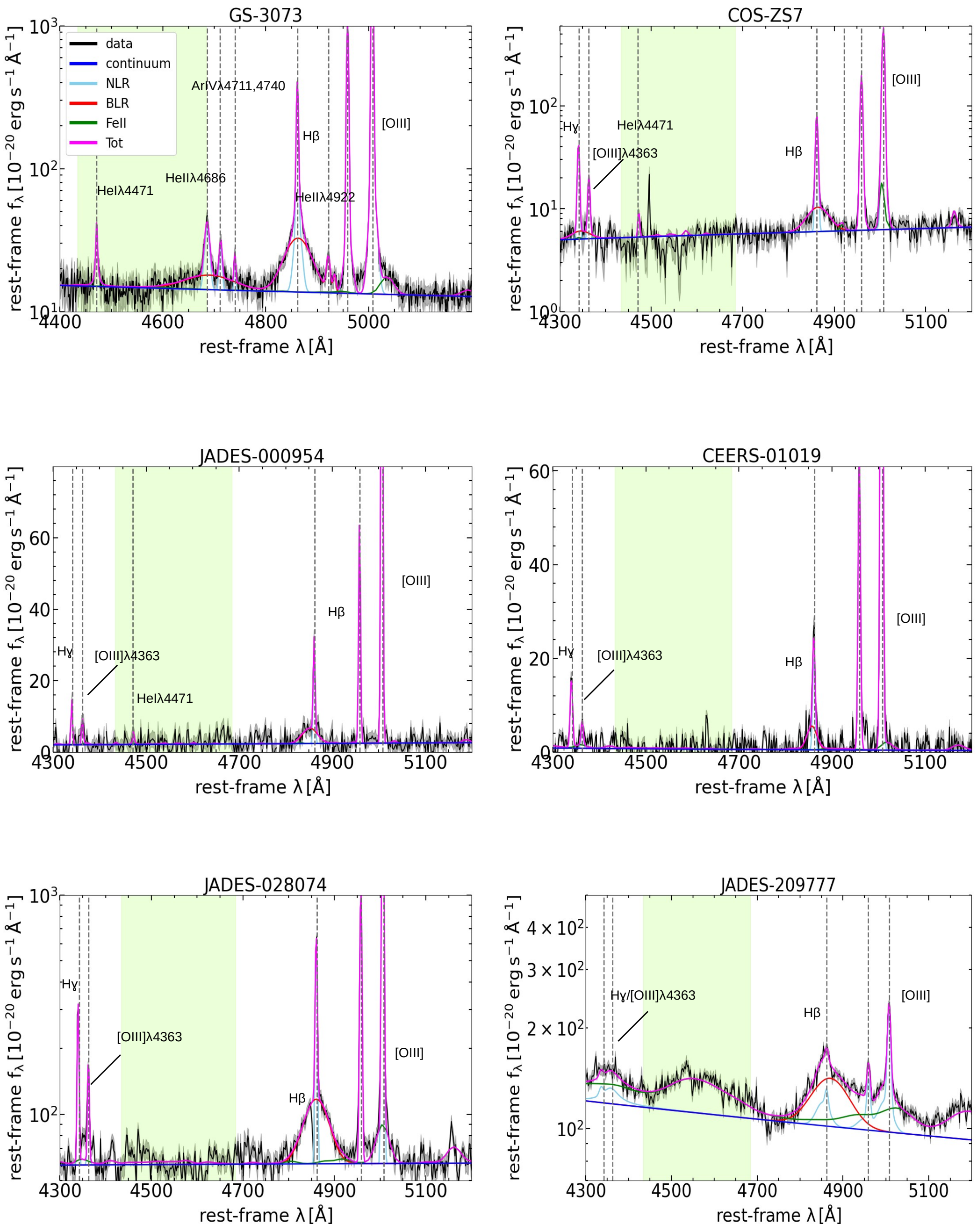

Figure 5.12. Fits atlas.

5.9.4 Photoionisation models with varying densities

In this Supplementary Material I present additional photoionisation models with a range of hydrogen densities from 10^8 cm^{-3} to 10^{16} cm^{-3}. In Figure 5.13 I show two sets of AGN BLR models with subsolar and supersolar metallcities. Apart from the hydrogen density and the metallicity, all other parameters are set to be the same as described in Table 5.4. It is clear that for both sets of models, local maxima of $R_{\rm Fe}$ are found for certain combinations of U and $n_{\rm H}$, a phenomenon already noted by previous modelling works (e.g., Baldwin et al., 2004; Ferland et al., 2009).

As a comparison, I also show the contours corresponding to the means of JWST-identified Type 1 AGN and SDSS Type 1 AGN with similar $\rm FWHM_{H\beta,br}$ and $\rm L_{H\beta,br}$, respectively. Compared to the subsolar metallicity models ($Z = 0.2\ Z_\odot$), the *JWST* AGN mean is found for 10^{10} cm^{-3} $< n_{\rm H} <$ 10^{12} cm^{-3}. In contrast, the supersolar metallicity models ($Z = 2\ Z_\odot$) only match the *JWST* AGN mean when $n_{\rm H} \gtrsim 10^{16}$ cm^{-3}. The SDSS mean can be found at 10^{10} cm^{-3} $< n_{\rm H} <$ 10^{12} cm^{-3}, $n_{\rm H} \lesssim 10^9$ cm^{-3}, or $n_{\rm H} \gtrsim 10^{15}$ cm^{-3} compared to the supersolar metallicity models depending on the value of U, or a broader density range compared to the subsolar metallicity models.

While Figure 5.13 illustrates the complex degeneracies between model parameters, discussed in Sec. 5.6.4, based on the current observational evidence it might be more natural to assume redshift evolution in the metallicity rather than other model parameters for high-redshift BLRs. A scenario invoking the redshift evolution in the gas density, for example, would require ultra-dense environments for JWST-identified AGN assuming they are similarly metal enriched as SDSS AGN. At extremely high densities, the strength of permitted UV lines from the BLR would change significantly (Temple et al., 2021), which could be tested observationally using medium-to-high resolution UV follow-ups of less obscured early AGN with *JWST*. However, this is beyond the scope of the current work and I leave it for future investigations.

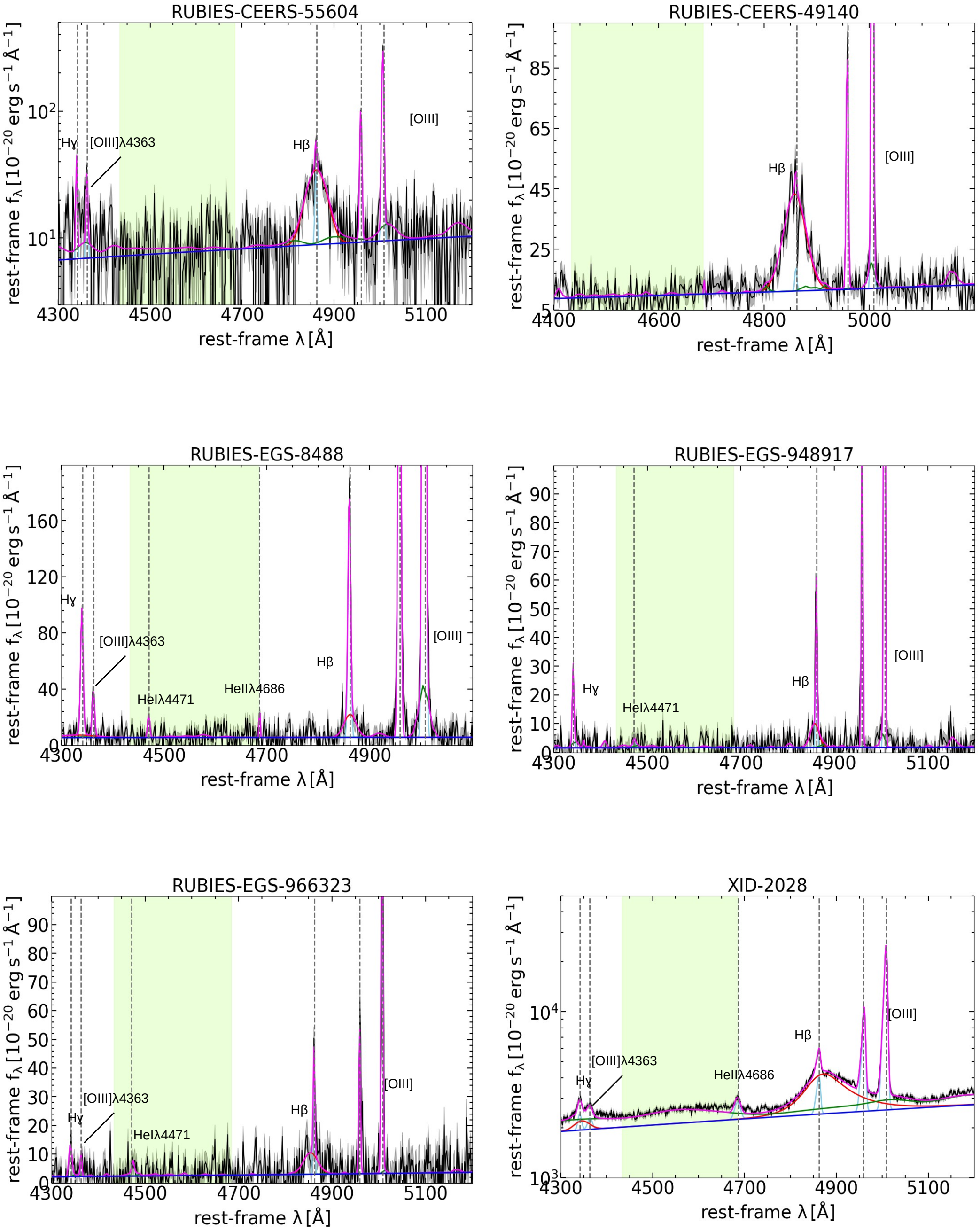

Figure 5.12. Fits atlas, continued.

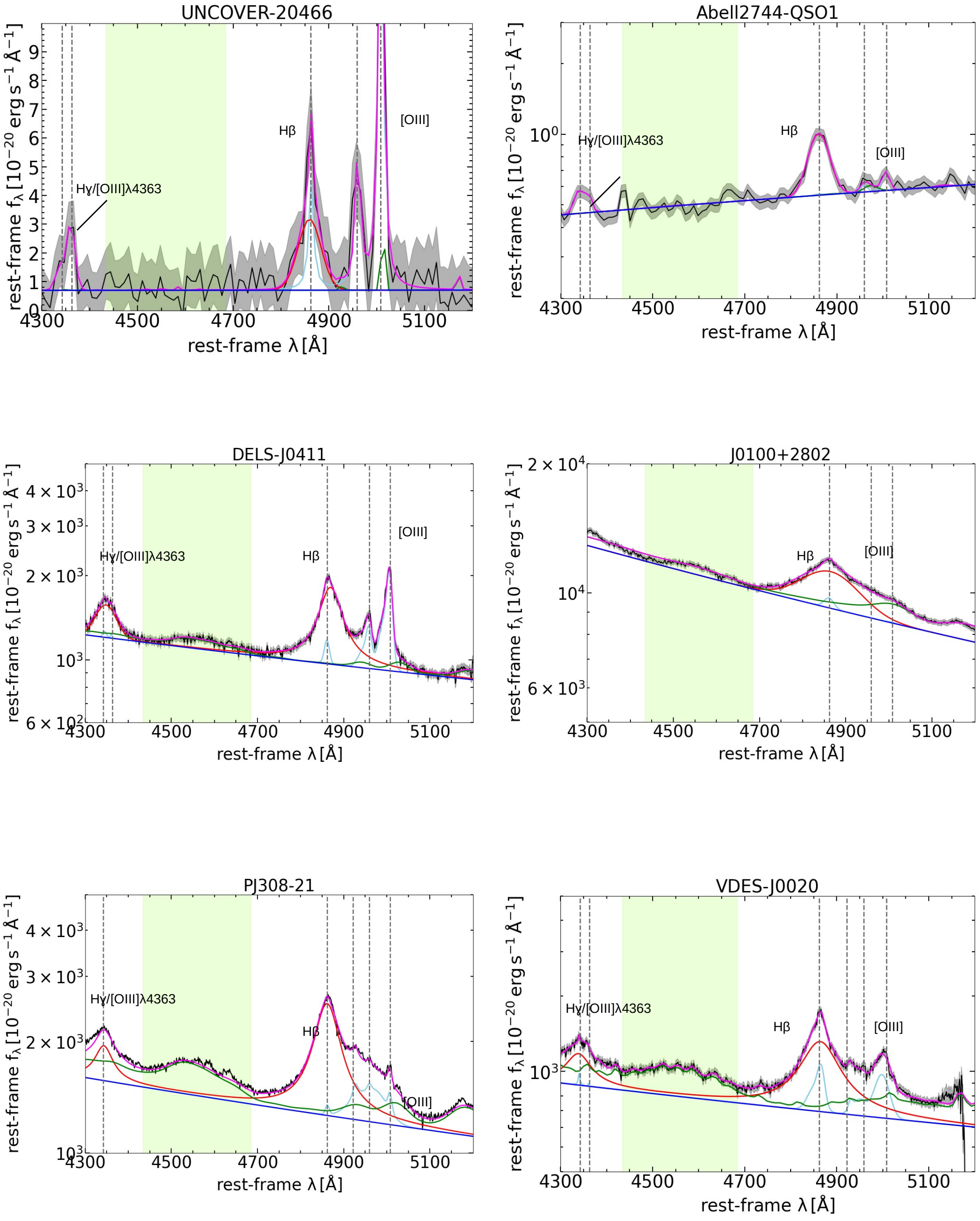

Figure 5.12. Fits atlas, continued.

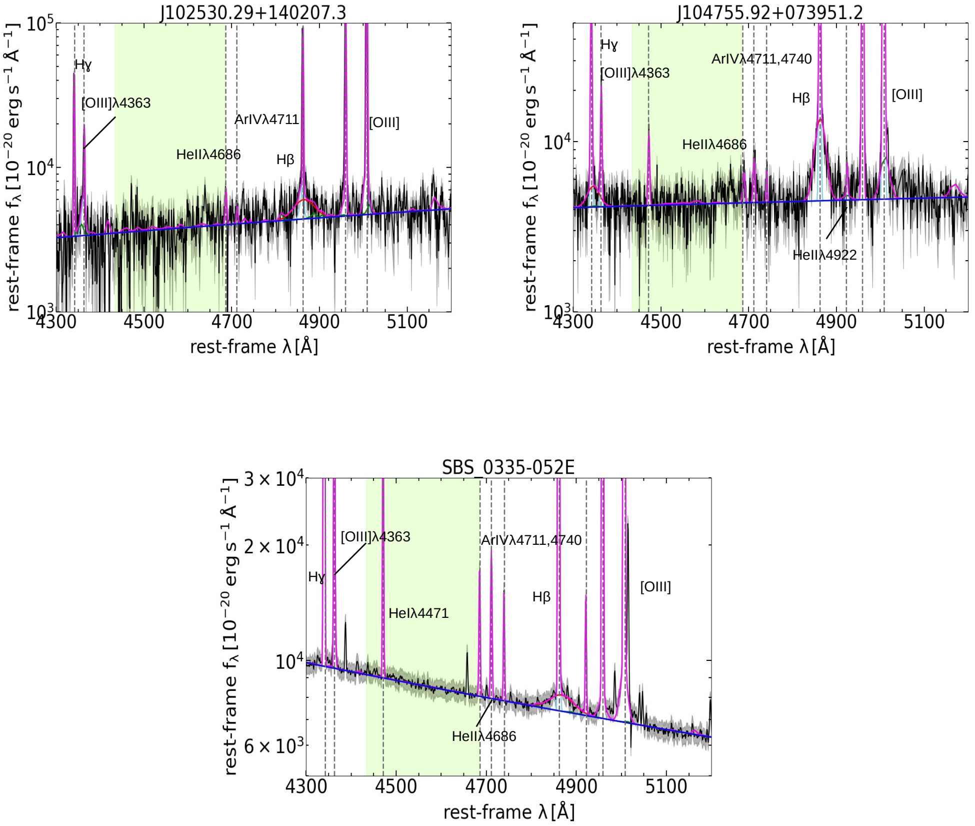

Figure 5.12. Fits atlas, continued.

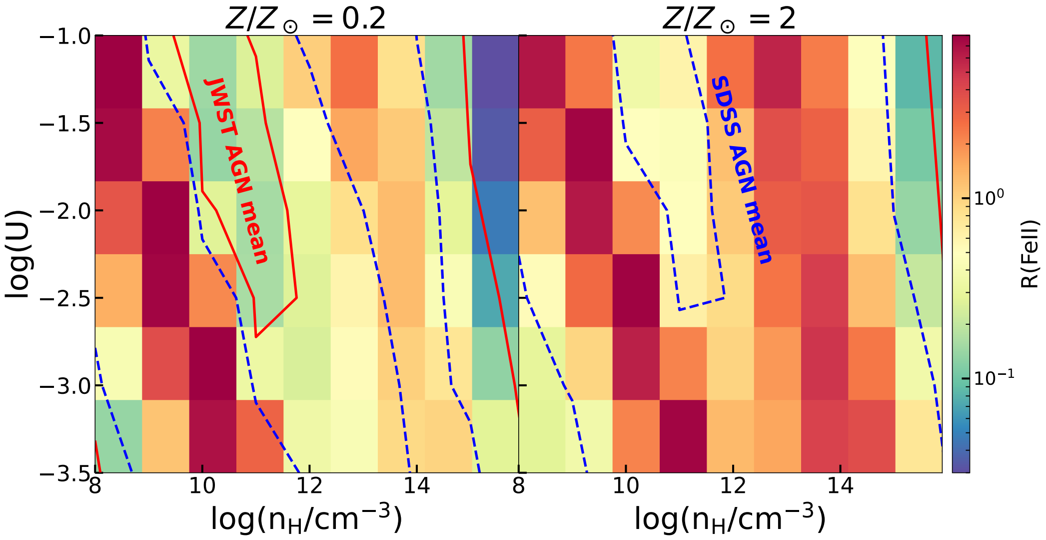

Figure 5.13. Photoionisation models predicted $R_{\rm Fe}$ as a function of the ionisation parameter and hydrogen density. *Left:* Models with a subsolar metallicity of $Z/Z_\odot = 0.2$ plausible for BLRs of low-luminosity AGN observed by *JWST*. *Right:* Models with a super solar metallicity of $Z/Z_\odot = 2$ plausible for BLRs of local AGN as well as high-luminosity quasars observed in SDSS. In both figures, the mean $R_{\rm Fe}$ of *JWST*-identified AGN is indicated by the solid red contour, and the mean $R_{\rm Fe}$ of SDSS AGN is indicated by the dashed blue contour.

Chapter 6

Conclusions and future prospects

The work collected in this thesis has been mainly devoted to understanding the mechanism powering AGN at different cosmic times, and the interplay between the components of the nuclear environment. This because the luminosity and prevalence of these fascinating objects makes them relevant both in the process of shaping their host galaxies, as well as cosmological probes. A more detailed comprehension of the physical mechanisms at work in these sources and a multi-wavelength charaterisation of the interplay between the physical regions of AGN, only began here, will be key to assess their role in a cosmological context and their suitability as *standardised candles*.

For what concerns the use of quasars as cosmological probes, in Chapter 2 I explained how my work was chiefly dedicated to dispelling possible observational biases (dust reddening, host galaxy contamination and/or evolution with z of the spectral properties) in the cosmological sample assembled by my group via a spectroscopic analysis. The analysis carried out in Trefoloni et al. (2024c) suggests that the latest quasar compilation employed for cosmological purposes is free from the aforementioned biases, as the average spectral properties closely resemble those of typical blue, unobscured quasars. This result has two major consequences: first and foremost, the results obtained by employing quasars as cosmological probes are corroborated by the absence of these possible biases. In second instance, the spectroscopic confirmation of the reliability of the photometric cuts implies that these criteria will still be valid for selecting forthcoming larger samples, without the need for a time-consuming spectroscopic analysis. Additionally, the rest-frame UV and optical spectra built using the cosmological sample do not show any kind of appreciable evolution with z, apart from the emission lines properties which correlate with the luminosity. This remarkable similarity in different bins of black hole mass and luminosity hints to some kind of universal quasar spectral energy distribution. For what concerns the cosmological implementation of quasars, the $\mathrm{L_X - L_{UV}}$ relation proved robust in turning quasars into *standardised candles*. Building an Hubble–Lemaître diagram by joining SNeIa and quasars revealed a 4σ significant deviation from the prediction of the standard cosmological model (Risaliti and Lusso 2019).

Subsequent tests were performed, employing model-independent methods, such as a Neural Network regression on the Hubble Diagram of SNeIa+quasars to reconstruct its shape without relying on any cosmological assumption (Giambagli et al. 2023). These investigations confirmed the strong tension with the flat ΛCDM model and showed hints towards Interactive Dark Sector models. Interestingly, the high-redshift data are essential in both driving the tension with the current cosmological model as well as for distinguishing between different cosmological models. This in particular, highlights the relevance of quasars for the Hubble–Lemaître Diagram. If on the one hand, there is a relative abundance of high-redshift ($z \gtrsim 4$) quasars whose UV spectra can be obtained through ground-based facilities, it is much harder to obtain good-quality X-ray data for these sources. Therefore, it is my aim to apply for new X-ray observations on tailored samples of high-redshift quasars with the goal of testing whether the deviation already observed at $z \sim 3$ (Sacchi et al. 2022) is confirmed when adding high quality data at higher z.

Furthermore, the similarity of the UV and optical spectra demonstrated by this work, at different redsfhits and accretion parameters also raises the question on why all the SEDs of blue quasars appear so similar. In a wider picture, it is possible that the self-regulating mechanism behind the $L_X - L_{UV}$ relation could also be responsible for the apparent similarity of the quasar spectra. In this context, my aim is to gather large samples with spectroscopic data to test different accretion disc models in order to achieve a self-consistent estimate of the accretion parameters, which ultimately determine the SED. This will also allow to test the reliability of the virial calibrations for the black hole masses against those derived from accretion disc modelling.

The strong coupling between the disc and the corona, abundantly discussed in this thesis, has a useful corollary: broad line AGN falling below the $L_X - L_{UV}$ relation (X-ray weak) are experiencing a phase of "non-standard" X-ray emission. This can be chiefly caused by obscuration by gas within the broad line region (or gas and dust outside it) or by an intrinsic dimming of the X-ray emission.

The X-ray weak phase can be echoed by peculiar line properties in the optical and UV emission lines. In Chapter 3, which summarises the work described in Trefoloni et al. (2023), I explored this possibility, by analysing the rest-frame UV and optical LBT spectra of a sample of 30 quasars at $z = 3.0 - 3.3$ with dedicated X-ray observations (Nardini et al. 2019b). This sample, assembled by picking 30 of the most luminous blue quasars in this redshift range, showed an unexpected X-ray bi-modality, with 3/4 of the sample exhibiting typical X-ray properties, while the remaining part being X-ray weak. In this context, there are notable differences between the optical lines, mimicking the X-ray dichotomy. In particular, X-ray weak quasars exhibit Fe II/Mg II ratios higher than the X-ray normal ones, a feature possibly enhanced by shocks and microturbulence within the BLR (Sameshima et al. 2020; Temple et al. 2020). At the same time, they also exhibit weaker [O III] lines, while still abiding the X-ray/[O III] luminosity correlation, thus hinting at an intrinsically weak X-ray and [O III] emission, rather than due to some kind of X-ray obscuration. The reason for the intrinsically faint X-ray and [O III] emission could be ascribable to some differences in the far-UV ionising SED between the two samples. At the same time, a previous analysis of the UV archival spectra confirmed that X-ray weak sources displayed systematically weaker CIV emission lines and flatter UV continua (Lusso

et al. 2021). These pieces of evidence can be framed within a disc wind scenario, where a strong -nearly equatorial- disc wind diminishes the local accretion rate of the innermost region of the accretion disc. The net effect of this outflowing phase is thus to starve the corona and reduce the strength of the emission lines. This possibility was also tested on other samples in Trefoloni (2023) where an enhanced fraction of outflow signatures was reported in X-ray weak sources with respect to the global blue quasar population.
With the aim of systematically investigating the UV/optical spectral properties of X-ray weak quasars, and to more tightly constrain their accretion properties, I embarked on the QUasar BElow the X-ray to UV luminosity relation (QUBEX) survey as a co-PI. This project, which so-far was awarded 17 hr at LBT, aims at building the first systematic data-set to study the relation between accretion disc and corona in X-ray weak objects. My plan is to expand this sample applying for new multi-wavelength (and possibly simultaneous) observations, both employing X-ray and optical facilities. At the same time, a more comprehensive photoionisation modelling, including the optical lines and constrained by the forthcoming observations will be key to provide a physically consistent scenario.

Despite being a fundamental ingredient within the Unified Model, the evolution of the torus properties with both redshift and luminosity of the AGN are still not thoroughly understood. In particular, it is still not clear whether the covering factor of the torus evolves over time and how it relates with the accretion parameters of the nucleus. In Chapter 4, with the aim of investigating how the NIR ($\sim 1-5\mu$m) properties of the dusty torus evolve independently according to the bolometric luminosity and redshift, I undertook a statistical study on a large sample of blue quasars, whose results are discussed in Trefoloni et al. (2024a). There, I assembled a large dataset of ~36,000 Type 1 AGN between $0.5 < z < 2.9$ and $45.0 < \log(\mathrm{L_{bol}}/(\mathrm{erg/s})) < 48.0$ with UV, optical and near-infrared photometry. This sample showed that the NIR luminosity decreases for increasing $\mathrm{L_{bol}}$ at any redshift, a feature that can be interpreted within the so-called framework of the "receding torus", while the NIR SED is consistent with a non-evolution with z. These results translate into the non-evolution with z of the torus covering factor, which can be expressed in terms of different proxies. It is also interesting to see that, when the evolution of the CF is tested within the accretion parameter space (i.e. that described by $\mathrm{M_{BH}}$ and $\mathrm{L_{bol}}$), it appears that $\mathrm{L_{bol}}$ is the strongest driver in the CF evolution, rather than the mass-normalised accretion rate (i.e. the Eddington ratio, λ_{Edd}), although the latter quantity suffers from larger systematic uncertainties carried by the M_{BH} term. In a wider picture, again, there is evidence for the nuclear environment to be ultimately shaped by the luminosity of the accretion disc, regardless of the cosmic time.
The collection of such a large sample was possible only restricting the analysis to the NIR region of the quasar SED. A key development of this work is therefore the extension of this kind of analysis towards the mid-infrared (MIR). Here the contribution of the colder polar dust, possibly lifted as a result of the shaping of the torus by winds/outflows (e.g. Wada 2012) becomes increasingly important. Therefore, the collection of a statistically meaningful sample to test the interplay between the accretion parameters and the MIR band properties, will be key to test the evolutionary picture describing the dynamical nature of the torus and of the

circum-nuclear environment. At the same time, the new unprecedented IR imaging capabilities offered by JWST/MIRI unlocked the possibility to directly observe the spatial extent of the polar dust (Haidar et al. 2024). Thus, it is my plan to apply for *JWST* imaging on a sample of local AGN with the aim of directly imaging the polar component, as well as getting the NIR spectrum of the innermost hot torus. This effort will be crucial in constraining torus models, which, for instance, predict the development of a polar component during the radiation-driven phase which shapes the torus.

During the final year of my PhD, I have been a Visiting Graduate Researcher at KAVLI Institute for Cosmology in Cambridge, working on the spectral properties of high-redshift AGN observed with JWST. There, I had the chance to analyse cutting-edge *JWST* data. The new observational capabilities offered by *JWST* raised the veil on an enygmatic population of faint AGN at high z (e.g. Matthee et al. 2024). These sources exhibit peculiar spectral features, different from local AGN or luminous quasars. Examples of these observational features are the weakness of the ionised outflows, routinely observed in low-z sources as blue wings in the [O III] profile (e.g. Maiolino et al. 2023), the incidence of absorption features in Balmer lines (e.g. Juodžbalis et al. 2024a), and their remarkable X-ray and radio weakness (e.g. Maiolino et al. 2024). In Chapter 5 I summarise the work described in Trefoloni et al. (2024b). There, with the end of better understanding the physical conditions in the BLR of these early AGN, I used the optical Fe II (4434–4684 Å), the broad Hβ emission, and the ratio between their equivalent widths R_{Fe}, as a probe on a purposefully assembled sample, made of both faint AGN and quasars. The population of faint AGN exhibits a significantly lower Fe II emission than a sample of carefully selected local counterparts (R_{Fe} <0.24 against R_{Fe} ≃0.85 in the control sample), while the $z \gtrsim 6$ quasars observed by *JWST* display a Fe II emission profile that closely resembles that observed at $z < 3$. Detailed photionisation modelling points in the direction of the weakness of the Fe II bump in the faint *JWST* AGN to be due to the reduced metallicity of their BLR gas ($\lesssim 0.5\ Z_\odot$), while luminous quasars have already reached chemical maturity ($\gtrsim Z_\odot$). Another notable feature revealed by the spectroscopy of these faint sources is an intriguing similarity with the faint AGN harboured in local metal poor dwarf galaxies. These two classes of objects indeed behave similarly in all the diagnostic diagrams explored, hinting at the possibility that the physical reason behind the peculiarities of the high-z sources could also be found in these local tentative counterparts.

The new elusive population of AGN revealed by *JWST* severely challenged our understanding of the AGN environment, displaying features that differ remarkably from those routinely observed in the local Universe. In this task, my aim is to take advantage of spectroscopic surveys recently carried out (e.g. RUBIES, de Graaff et al. 2024) to fully characterise the BLR (and NLR) kinematics as well as to constrain the source of the potoionisation in these objects. For what concerns the luminous quasars, other questions should be raised: up to which redshift can we observe such massive BH shining at the center of galaxies? Can we spot any kind of evolution in the BLR properties of primordial quasars? How do these sources affect their close environment? These are questions which I plan to address requesting new *JWST* IFU observations on thoughtfully selected sources. Lastly, the possibility that AGN hosted in metal-poor dwarf galaxies could actually be local analogues of the high redshift faint AGN, should be concretely tested. To this aim, IFU observations on local AGN harboured in metal-poor dwarf galaxies could be decisive for several scientific goals, such as the detection of coronal lines, testing the incidence and size of possible outflows, and spatially resolved diagnostic line ratios, just to mention some. These spectral properties should then be compared to those measured in faint *JWST* objects, to quantify how similar these two classes of sources really are.

Bibliography

Abazajian, K. N., Adelman-McCarthy, J. K., Agüeros, M. A., Allam, S. S., Prieto, C. A., An, D., Anderson, K. S., Anderson, S. F., Annis, J., Bahcall, N. A., et al. (2009). The seventh data release of the sloan digital sky survey. *The Astrophysical Journal Supplement Series*, 182(2):543.

Abdurro'uf, N., Accetta, K., Aerts, C., Silva Aguirre, V., Ahumada, R., Ajgaonkar, N., Filiz Ak, N., Alam, S., Allende Prieto, C., Almeida, A., et al. (2022). The seventeenth data release of the sloan digital sky surveys: Complete release of manga, mastar, and apogee-2 data. *The Astrophysical Journal. Supplement Series*, 259(2).

Abramowicz, M., Czerny, B., Lasota, J., and Szuszkiewicz, E. (1988). Slim accretion disks. *Astrophysical Journal, Part 1 (ISSN 0004-637X), vol. 332, Sept. 15, 1988, p. 646-658. Research supported by Observatoire de Paris and NASA.*, 332:646–658.

Adelman-McCarthy, J. (2008). Ma ag ueros, ss allam, et al. *Astrophys. J. Suppl. Ser*, 175:297.

Ageorges, N., Seifert, W., Jütte, M., Knierim, V., Lehmitz, M., Germeroth, A., Buschkamp, P., Polsterer, K., Pasquali, A., Naranjo, V., Gemperlein, H., Hill, J., Feiz, C., Hofmann, R., Laun, W., Lederer, R., Lenzen, R., Mall, U., Mandel, H., Müller, P., Quirrenbach, A., Schäffner, L., Storz, C., and Weiser, P. (2010). LUCIFER1 commissioning at the LBT. In McLean, I. S., Ramsay, S. K., and Takami, H., editors, *Ground-based and Airborne Instrumentation for Astronomy III*, volume 7735 of *Society of Photo-Optical Instrumentation Engineers (SPIE) Conference Series*, page 77351L.

Ahumada, R., Prieto, C. A., Almeida, A., Anders, F., Anderson, S. F., Andrews, B. H., Anguiano, B., Arcodia, R., Armengaud, E., Aubert, M., et al. (2020). The 16th data release of the sloan digital sky surveys: first release from the apogee-2 southern survey and full release of eboss spectra. *The Astrophysical Journal Supplement Series*, 249(1):3.

Aird, J., Coil, A. L., Georgakakis, A., Nandra, K., Barro, G., and Pérez-González, P. G. (2015). The evolution of the x-ray luminosity functions of unabsorbed and absorbed agns out to z 5. *Monthly Notices of the Royal Astronomical Society*, 451(2):1892–1927.

Aird, J., Nandra, K., Laird, E., Georgakakis, A., Ashby, M., Barmby, P., Coil, A., Huang, J.-S., Koekemoer, A., Steidel, C., et al. (2010). The evolution of the hard x-ray luminosity function of agn. *Monthly Notices of the Royal Astronomical Society*, 401(4):2531–2551.

Akritas, M. G. and Siebert, J. (1996). A test for partial correlation with censored astronomical data. *Monthly Notices of the Royal Astronomical Society*, 278(4):919–924.

Allen, R. J., Kacprzak, G. G., Glazebrook, K., Labbé, I., Tran, K.-V. H., Spitler, L. R., Cowley, M., Nanayakkara, T., Papovich, C., Quadri, R., et al. (2017). The size evolution of star-forming galaxies since z 7 using zfourge. *The Astrophysical Journal Letters*, 834(2):L11.

Almeida, C. R., Levenson, N., Alonso-Herrero, A., Ramos, A. A., Espinosa, J. R., García, A. P., Packham, C., Mason, R., Radomski, J., and Díaz-Santos, T. (2011). Testing the unification model for active galactic nuclei in the infrared: are the obscuring tori of type 1 and 2 seyferts different? *The Astrophysical Journal*, 731(2):92.

Alonso-Herrero, A., Almeida, C. R., Mason, R., Ramos, A. A., Roche, P. F., Levenson, N. A., Elitzur, M., Packham, C., Espinosa, J. M. R., Young, S., et al. (2011). Torus and active galactic nucleus properties of nearby seyfert galaxies: Results from fitting infrared spectral energy distributions and spectroscopy. *The Astrophysical Journal*, 736(2):82.

Alonso-Herrero, A., García-Burillo, S., Hönig, S., García-Bernete, I., Almeida, C. R., González-Martín, O., López-Rodríguez, E., Boorman, P., Bunker, A., Burtscher, L., et al. (2021). The galaxy activity, torus, and outflow survey (gatos)-ii. torus and polar dust emission in nearby seyfert galaxies. *Astronomy & Astrophysics*, 652:A99.

Alonso-Tetilla, A. V., Shankar, F., Fontanot, F., Menci, N., Valentini, M., Buchner, J., Laloux, B., Lapi, A., Puglisi, A., Alexander, D. M., et al. (2024). Probing the roles of orientation and multiscale gas distributions in shaping the obscuration of active galactic nuclei through cosmic time. *Monthly Notices of the Royal Astronomical Society*, 527(4):10878–10896.

Ananna, T. T., Treister, E., Urry, C. M., Ricci, C., Kirkpatrick, A., LaMassa, S., Buchner, J., Civano, F., Tremmel, M., and Marchesi, S. (2019). The accretion history of agns. i. supermassive black hole population synthesis model. *The Astrophysical Journal*, 871(2):240.

Antonucci, R. (1993). Unified models for active galactic nuclei and quasars. *Annual review of astronomy and astrophysics*, 31(1):473–521.

Antonucci, R., Kinney, A., and Ford, H. (1989). The lyman edge test of the quasar emission mechanism. *Astrophysical Journal, Part 1 (ISSN 0004-637X), vol. 342, July 1, 1989, p. 64-82.*, 342:64–82.

Antonucci, R. and Miller, J. (1985). Spectropolarimetry and the nature of ngc 1068. *Astrophysical Journal, Part 1 (ISSN 0004-637X), vol. 297, Oct. 15, 1985, p. 621-632.*, 297:621–632.

Aoyama, S., Hou, K.-C., Hirashita, H., Nagamine, K., and Shimizu, I. (2018). Cosmological simulation with dust formation and destruction. *Monthly Notices of the Royal Astronomical Society*, 478(4):4905–4921.

Arcodia, R., Merloni, A., Nandra, K., and Ponti, G. (2019). Testing the disk-corona interplay in radiatively-efficient broad-line agn. *Astronomy & Astrophysics*, 628:A135.

Arellano-Córdova, K. Z., Berg, D. A., Chisholm, J., Haro, P. A., Dickinson, M., Finkelstein, S. L., Leclercq, F., Rogers, N. S., Simons, R. C., Skillman, E. D., et al. (2022). A first look at the abundance pattern—o/h, c/o, and ne/o—in z> 7 galaxies with jwst/nirspec. *The Astrophysical Journal Letters*, 940(1):L23.

Arnaud, K. A. (1996). *XSPEC: The First Ten Years*, volume 101 of *Astronomical Society of the Pacific Conference Series*, page 17.

Assef, R., Kochanek, C., Brodwin, M., Cool, R., Forman, W., Gonzalez, A., Hickox, R., Jones, C., Le Floc'h, E., Moustakas, J., et al. (2010). Low-resolution spectral templates for active galactic nuclei and galaxies from 0.03 to 30 μm. *The Astrophysical Journal*, 713(2):970.

Avni, Y. and Tananbaum, H. (1982). On the cosmological evolution of the x-ray emission from quasars. *Astrophysical Journal, Part 2-Letters to the Editor, vol. 262, Nov. 15, 1982, p. L17-L21.*, 262:L17–L21.

Baggen, J. F., van Dokkum, P., Brammer, G., de Graaff, A., Franx, M., Greene, J., Labbé, I., Leja, J., Maseda, M. V., Nelson, E. J., et al. (2024). The small sizes and high implied densities oflittle red dots' with balmer breaks could explain their broad emission lines without an agn. *arXiv preprint arXiv:2408.07745*.

Baker, W. M., Maiolino, R., Belfiore, F., Bluck, A. F., Curti, M., Wylezalek, D., Bertemes, C., Bothwell, M., Lin, L., Thorp, M., et al. (2023). The molecular gas main sequence and schmidt–kennicutt relation are fundamental, the star-forming main sequence is a (useful) byproduct. *Monthly Notices of the Royal Astronomical Society*, 518(3):4767–4781.

Baldassare, V. F., Reines, A. E., Gallo, E., Greene, J. E., Graur, O., Geha, M., Hainline, K., Carroll, C. M., and Hickox, R. C. (2016). Multi-epoch spectroscopy of dwarf galaxies with agn signatures: identifying sources with persistent broad hα emission. *The Astrophysical Journal*, 829(1):57.

Baldwin, J., Ferland, G. J., Korista, K., Hamann, F., and LaCluyzé, A. (2004). The origin of fe ii emission in active galactic nuclei. *The Astrophysical Journal*, 615(2):610.

Baldwin, J. A. (1977). Luminosity indicators in the spectra of quasi-stellar objects. *Astrophysical Journal, Vol. 214, pp. 679-684 (1977).*, 214:679–684.

Baldwin, J. A., Phillips, M. M., and Terlevich, R. (1981). Classification parameters for the emission-line spectra of extragalactic objects. *Publications of the Astronomical Society of the Pacific*, 93(551):5.

Banados, E., Venemans, B. P., Mazzucchelli, C., Farina, E. P., Walter, F., Wang, F., Decarli, R., Stern, D., Fan, X., Davies, F. B., et al. (2018). An 800-million-solar-mass black hole in a significantly neutral universe at a redshift of 7.5. *Nature*, 553(7689):473–476.

Bargiacchi, G., Benetti, M., Capozziello, S., Lusso, E., Risaliti, G., and Signorini, M. (2022). Quasar cosmology: dark energy evolution and spatial curvature. *Monthly Notices of the Royal Astronomical Society*, 515(2):1795–1806.

Bargiacchi, G., Dainotti, M., and Capozziello, S. (2023). Tensions with the flat λcdm model from high-redshift cosmography. *Monthly Notices of the Royal Astronomical Society*, 525(2):3104–3116.

Bargiacchi, G., Risaliti, G., Benetti, M., Capozziello, S., Lusso, E., Saccardi, A., and Signorini, M. (2021). Cosmography by orthogonalized logarithmic polynomials. *Astronomy & Astrophysics*, 649:A65.

Barro, G., Perez-Gonzalez, P. G., Kocevski, D. D., McGrath, E. J., Trump, J. R., Simons, R. C., Somerville, R. S., Yung, L., Haro, P. A., Bagley, M. B., et al. (2023). Extremely red galaxies at $z = 5 - 9$ with miri and nirspec: dusty galaxies or obscured agns? *arXiv preprint arXiv:2305.14418*.

Barth, A. J., Martini, P., Nelson, C. H., and Ho, L. C. (2003). Iron emission in the z= 6.4 quasar sdss j114816. 64+ 525150.3. *The Astrophysical Journal*, 594(2):L95.

Baskin, A. and Laor, A. (2005a). What controls the c iv line profile in active galactic nuclei? *Monthly Notices of the Royal Astronomical Society*, 356(3):1029–1044.

Baskin, A. and Laor, A. (2005b). What controls the [o iii] λ5007 line strength in active galactic nuclei? *Monthly Notices of the Royal Astronomical Society*, 358(3):1043–1054.

Bassani, L., Dadina, M., Maiolino, R., Salvati, M., Risaliti, G., Della Ceca, R., Matt, G., and Zamorani, G. (1999). A three-dimensional diagnostic diagram for seyfert 2 galaxies: probing x-ray absorption and compton thickness. *The Astrophysical Journal Supplement Series*, 121(2):473.

Battersby, C., Armus, L., Bergin, E., Kataria, T., Meixner, M., Pope, A., Stevenson, K. B., Cooray, A., Leisawitz, D., Scott, D., et al. (2018). The origins space telescope. *Nature Astronomy*, 2(8):596–599.

Bautista, M. A., Fivet, V., Ballance, C., Quinet, P., Ferland, G., Mendoza, C., and Kallman, T. R. (2015). Atomic data and spectral model for fe ii. *The Astrophysical Journal*, 808(2):174.

Beckert, T. and Duschl, W. (2004). The dynamical state of a thick cloudy torus around an agn. *Astronomy & Astrophysics*, 426(2):445–454.

Beckmann, V. and Shrader, C. (2012). *Active galactic nuclei*. John Wiley & Sons.

Berk, D. E. V., Richards, G. T., Bauer, A., Strauss, M. A., Schneider, D. P., Heckman, T. M., York, D. G., Hall, P. B., Fan, X., Knapp, G., et al. (2001). Composite quasar spectra from the sloan digital sky survey. *The Astronomical Journal*, 122(2):549.

Bianchi, S., Fonseca Bonilla, N., Guainazzi, M., Matt, G., and Ponti, G. (2009). CAIXA: a Catalogue of AGN In the XMM-Newton Archive II. Multiwavelength correlations. *ArXiv e-prints*.

Bianchi, S., Guainazzi, M., Matt, G., Bonilla, N. F., and Ponti, G. (2009). Caixa: a catalogue of agn in the xmm-newton archive-i. spectral analysis. *Astronomy & Astrophysics*, 495(2):421–430.

Bianchini, F., Fabbian, G., Lapi, A., Gonzalez-Nuevo, J., Gilli, R., and Baccigalupi, C. (2019). Broadband spectral energy distributions of sdss-selected quasars and of their host galaxies: intense activity at the onset of agn feedback. *The Astrophysical Journal*, 871(2):136.

Bisogni, S., Marconi, A., and Risaliti, G. (2017). Orientation effects on spectral emission features of quasars. *Monthly Notices of the Royal Astronomical Society*, 464(1):385–397.

Bluck, A. F., Maiolino, R., Brownson, S., Conselice, C. J., Ellison, S. L., Piotrowska, J. M., and Thorp, M. D. (2022). The quenching of galaxies, bulges, and disks since cosmic noon-a machine learning approach for identifying causality in astronomical data. *Astronomy & Astrophysics*, 659:A160.

Bongiorno, A., Maiolino, R., Brusa, M., Marconi, A., Piconcelli, E., Lamastra, A., Cano-Díaz, M., Schulze, A., Magnelli, B., Vignali, C., et al. (2014). The m bh-m* relation for x-ray-obscured, red qsos at 1.2< z< 2.6. *Monthly Notices of the Royal Astronomical Society*, 443(3):2077–2091.

Boroson, T. A. and Green, R. F. (1992a). The emission-line properties of low-redshift quasi-stellar objects. *Astrophysical Journal Supplement Series (ISSN 0067-0049), vol. 80, no. 1, May 1992, p. 109-135.*, 80:109–135.

Boroson, T. A. and Green, R. F. (1992b). The emission-line properties of low-redshift quasi-stellar objects. *Astrophysical Journal Supplement Series (ISSN 0067-0049), vol. 80, no. 1, May 1992, p. 109-135.*, 80:109–135.

Bottorff, M. and Ferland, G. J. (2000). Magnetic confinement, magnetohydrodynamic waves and smooth line profiles in active galactic nuclei. *Monthly Notices of the Royal Astronomical Society*, 316(1):103–106.

Brightman, M., Silverman, J., Mainieri, V., Ueda, Y., Schramm, M., Matsuoka, K., Nagao, T., Steinhardt, C., Kartaltepe, J., Sanders, D., et al. (2013). A statistical relation between the x-ray spectral index and eddington ratio of active galactic nuclei in deep surveys. *Monthly Notices of the Royal Astronomical Society*, 433(3):2485–2496.

Brotherton, M., Tran, H. D., Becker, R., Gregg, M. D., Laurent-Muehleisen, S., and White, R. (2001). Composite spectra from the first bright quasar survey. *The Astrophysical Journal*, 546(2):775.

Bruhweiler, F. and Verner, E. (2008). Modeling fe ii emission and revised fe ii (uv) empirical templates for the seyfert 1 galaxy i zw 1. *The Astrophysical Journal*, 675(1):83.

Brusa, M., Civano, F., Comastri, A., Miyaji, T., Salvato, M., Zamorani, G., Cappelluti, N., Fiore, F., Hasinger, G., Mainieri, V., et al. (2010). The xmm-newton wide-field survey in the cosmos field (xmm-cosmos): demography and multiwavelength properties of obscured and unobscured luminous active galactic nuclei. *The Astrophysical Journal*, 716(1):348.

Buchner, J., Georgakakis, A., Nandra, K., Brightman, M., Menzel, M.-L., Liu, Z., Hsu, L.-T., Salvato, M., Rangel, C., Aird, J., et al. (2015). Obscuration-dependent evolution of active galactic nuclei. *The Astrophysical Journal*, 802(2):89.

Burke, C. J., Liu, X., Chen, Y.-C., Shen, Y., and Guo, H. (2021). On the agn nature of broad balmer emission in four low-redshift metal-poor galaxies. *Monthly Notices of the Royal Astronomical Society*, 504(1):543–550.

Burlon, D., Ajello, M., Greiner, J., Comastri, A., Merloni, A., and Gehrels, N. (2011). Three-year swift–bat survey of active galactic nuclei: Reconciling theory and observations? *The Astrophysical Journal*, 728(1):58.

Cai, Z.-Y. and Wang, J.-X. (2023). A universal average spectral energy distribution for quasars from the optical to the extreme ultraviolet. *Nature Astronomy*, 7(12):1506–1516.

Calderone, G., Sbarrato, T., and Ghisellini, G. (2012). The wide-field infrared survey explorer view of the disc-torus connection in z 0.6 active galactic nuclei. *Monthly Notices of the Royal Astronomical Society: Letters*, 425(1):L41–L45.

Cantalupo, S., Arrigoni-Battaia, F., Prochaska, J. X., Hennawi, J. F., and Madau, P. (2014). A cosmic web filament revealed in lyman-α emission around a luminous high-redshift quasar. *Nature*, 506(7486):63–66.

Cao, X. (2005). On the dust tori in palomar-green quasars. *The Astrophysical Journal*, 619(1):86.

Casebeer, D. A., Leighly, K. M., and Baron, E. (2006). Fuse observation of the narrow-line seyfert 1 galaxy re 1034+ 39: dependence of broad emission line strengths on the shape of the photoionizing spectrum. *The Astrophysical Journal*, 637(1):157.

Castro, C. S., Dors, O. L., Cardaci, M. V., and Hägele, G. F. (2017). New metallicity calibration for seyfert 2 galaxies based on the n 2 o 2 index. *Monthly Notices of the Royal Astronomical Society*, 467(2):1507–1514.

Chan, C.-H. and Krolik, J. H. (2016). Radiation-driven outflows from and radiative support in dusty tori of active galactic nuclei. *The Astrophysical Journal*, 825(1):67.

Chen, L.-H. and Wang, J.-M. (2004). Slim disks with transition regions and applications to microquasars and narrow-line seyfert 1 galaxies. *The Astrophysical Journal*, 614(1):101.

Chisholm, J., Berg, D., Endsley, R., Gazagnes, S., Richardson, C., Lambrides, E., Greene, J., Finkelstein, S., Flury, S., Guseva, N., et al. (2024). [ne v] emission from a faint epoch of reionization-era galaxy: evidence for a narrow-line intermediate-mass black hole. *Monthly Notices of the Royal Astronomical Society*, 534(3):2633–2652.

Cicone, C., Maiolino, R., Sturm, E., Graciá-Carpio, J., Feruglio, C., Neri, R., Aalto, S., Davies, R., Fiore, F., Fischer, J., et al. (2014). Massive molecular outflows and evidence for agn feedback from co observations. *Astronomy & Astrophysics*, 562:A21.

Coatman, L., Hewett, P. C., Banerji, M., Richards, G. T., Hennawi, J. F., and Prochaska, J. X. (2017). Correcting c iv-based virial black hole masses. *Monthly Notices of the Royal Astronomical Society*, 465(2):2120–2142.

Collin, S. and Joly, M. (2000). The fe ii problem in nls1s. *New Astronomy Reviews*, 44(7-9):531–537.

Costa, T., Sijacki, D., and Haehnelt, M. G. (2015). Fast cold gas in hot agn outflows. *Monthly Notices of the Royal Astronomical Society: Letters*, 448(1):L30–L34.

Costa, T., Sijacki, D., Trenti, M., and Haehnelt, M. G. (2014). The environment of bright qsos at z 6: star-forming galaxies and x-ray emission. *Monthly Notices of the Royal Astronomical Society*, 439(2):2146–2174.

Cresci, G., Tozzi, G., Perna, M., Brusa, M., Marconcini, C., Marconi, A., Carniani, S., Brienza, M., Giroletti, M., Belfiore, F., et al. (2023). Bubbles and outflows: The novel jwst/nirspec view of the z= 1.59 obscured quasar xid2028. *Astronomy & Astrophysics*, 672:A128.

Cristiani, S., Trentini, S., La Franca, F., Aretxaga, I., Andreani, P., Vio, R., and Gemmo, A. (1995). The optical variability of qso's. *arXiv preprint astro-ph/9506140*.

Croom, S., Rhook, K., Corbett, E., Boyle, B., Netzer, H., Loaring, N., Miller, L., Outram, P., Shanks, T., and Smith, R. (2002). The correlation of line strength with luminosity and redshift from composite quasi-stellar object spectra. *Monthly Notices of the Royal Astronomical Society*, 337(1):275–292.

Curti, M., Cresci, G., Mannucci, F., Marconi, A., Maiolino, R., and Esposito, S. (2016). New fully empirical calibrations of strong-line metallicity indicators in star forming galaxies. *Monthly Notices of the Royal Astronomical Society*, page stw2766.

Curti, M., d'Eugenio, F., Carniani, S., Maiolino, R., Sandles, L., Witstok, J., Baker, W. M., Bennett, J. S., Piotrowska, J. M., Tacchella, S., et al. (2023). The chemical enrichment in the early universe as probed by jwst via direct metallicity measurements at z 8. *Monthly Notices of the Royal Astronomical Society*, 518(1):425–438.

Cutri, R. e., Wright, E., Conrow, T., Fowler, J., Eisenhardt, P., Grillmair, C., Kirkpatrick, J., Masci, F., McCallon, H., Wheelock, S., et al. (2021). Vizier online data catalog: Allwise data release (cutri+ 2013). *VizieR Online Data Catalog*, pages II–328.

Czerny, B., Beaton, R., Bejger, M., Cackett, E., Dall'Ora, M., Holanda, R., Jensen, J. B., Jha, S. W., Lusso, E., Minezaki, T., et al. (2018). Astronomical distance determination in the space age: Secondary distance indicators. *Space Science Reviews*, 214:1–69.

Dalla Bontà, E., Peterson, B. M., Bentz, M. C., Brandt, W., Ciroi, S., De Rosa, G., Alvarez, G. F., Grier, C. J., Hall, P., Santisteban, J. V. H., et al. (2020a). The sloan digital sky survey reverberation mapping project: estimating masses of black holes in quasars with single-epoch spectroscopy. *The Astrophysical Journal*, 903(2):112.

Dalla Bontà, E., Peterson, B. M., Bentz, M. C., Brandt, W., Ciroi, S., De Rosa, G., Alvarez, G. F., Grier, C. J., Hall, P., Santisteban, J. V. H., et al. (2020b). The sloan digital sky survey reverberation mapping project: estimating masses of black holes in quasars with single-epoch spectroscopy. *The Astrophysical Journal*, 903(2):112.

Davies, R. I. (2007). A method to remove residual oh emission from near-infrared spectra. *Monthly Notices of the Royal Astronomical Society*, 375(3):1099–1105.

Dawson, K. S., Kneib, J.-P., Percival, W. J., Alam, S., Albareti, F. D., Anderson, S. F., Armengaud, E., Aubourg, É., Bailey, S., Bautista, J. E., et al. (2016). The sdss-iv extended baryon oscillation spectroscopic survey: overview and early data. *The Astronomical Journal*, 151(2):44.

Dawson, K. S., Schlegel, D. J., Ahn, C. P., Anderson, S. F., Aubourg, É., Bailey, S., Barkhouser, R. H., Bautista, J. E., Beifiori, A., Berlind, A. A., et al. (2012). The baryon oscillation spectroscopic survey of sdss-iii. *The Astronomical Journal*, 145(1):10.

de Graaff, A., Brammer, G., Weibel, A., Lewis, Z., Maseda, M. V., Oesch, P. A., Bezanson, R., Boogaard, L. A., Cleri, N. J., Cooper, O. R., et al. (2024). Rubies: a complete census of the bright and red distant universe with jwst/nirspec. *arXiv preprint arXiv:2409.05948*.

De Rosa, G., Decarli, R., Walter, F., Fan, X., Jiang, L., Kurk, J., Pasquali, A., and Rix, H.-W. (2011). Evidence for non-evolving fe ii/mg ii ratios in rapidly accreting z 6 qsos. *The Astrophysical Journal*, 739(2):56.

De Rosa, G., Venemans, B. P., Decarli, R., Gennaro, M., Simcoe, R. A., Dietrich, M., Peterson, B. M., Walter, F., Frank, S., McMahon, R. G., et al. (2014). Black hole mass estimates and emission-line properties of a sample of redshift z> 6.5 quasars. *The Astrophysical Journal*, 790(2):145.

Deconto-Machado, A., del Olmo Orozco, A., Marziani, P., Perea, J., and Stirpe, G. (2023). High-redshift quasars along the main sequence. *Astronomy & Astrophysics*, 669:A83.

Delvecchio, I., Gruppioni, C., Pozzi, F., Berta, S., Zamorani, G., Cimatti, A., Lutz, D., Scott, D., Vignali, C., Cresci, G., et al. (2014). Tracing the cosmic growth of supermassive black holes to z 3 with herschel. *Monthly Notices of the Royal Astronomical Society*, 439(3):2736–2754.

Denney, K. D. (2012). Are outflows biasing single-epoch c iv black hole mass estimates? *The Astrophysical Journal*, 759(1):44.

Dietrich, M., Hamann, F., Appenzeller, I., and Vestergaard, M. (2003a). Fe ii/mg ii emission-line ratio in high-redshift quasars. *The Astrophysical Journal*, 596(2):817.

Dietrich, M., Hamann, F., Shields, J., Constantin, A., Heidt, J., Jäger, K., Vestergaard, M., and Wagner, S. (2003b). Quasar elemental abundances at high redshifts. *The Astrophysical Journal*, 589(2):722.

Doan, S., Satyapal, S., Matzko, W., Abel, N. P., Böker, T., Bohn, T., Canalizo, G., Cann, J. M., Fischer, J., LaMassa, S., et al. (2024). Local analogs of primordial galaxies: In search of intermediate mass black holes with jwst nirspec. *arXiv preprint arXiv:2408.04774*.

Dong, X., Wang, T., Wang, J., Yuan, W., Zhou, H., Dai, H., and Zhang, K. (2007). Broad-line balmer decrements in blue active galactic nuclei. *Monthly Notices of the Royal Astronomical Society*, 383(2):581–592.

Dong, X.-B., Wang, J.-G., Ho, L. C., Wang, T.-G., Fan, X., Wang, H., Zhou, H., and Yuan, W. (2011). What controls the fe ii strength in active galactic nuclei? *The Astrophysical Journal*, 736(2):86.

Dong, X.-B., Zhou, H.-Y., Wang, T.-G., Wang, J.-X., Li, C., and Zhou, Y.-Y. (2005). Partially obscured quasars in the sloan digital sky survey early data release. *The Astrophysical Journal*, 620(2):629.

Dors, O. and Copetti, M. (2005). Abundance gradients in a sample of barred spiral galaxies. *Astronomy & Astrophysics*, 437(3):837–847.

Dors, O. L., Freitas-Lemes, P., Amôres, E., Pérez-Montero, E., Cardaci, M. V., Hägele, G. F., Armah, M., Krabbe, A., and Faúndez-Abans, M. (2020a). Chemical abundances of seyfert 2 agns–i. comparing oxygen abundances from distinct methods using sdss. *Monthly Notices of the Royal Astronomical Society*, 492(1):468–479.

Dors, O. L., Maiolino, R., Cardaci, M. V., Hägele, G. F., Krabbe, A., Pérez-Montero, E., and Armah, M. (2020b). Chemical abundances of seyfert 2 agns–iii. reducing the oxygen abundance discrepancy. *Monthly Notices of the Royal Astronomical Society*, 496(3):3209–3221.

Dors Jr, O., Cardaci, M. V., Hägele, G. F., Rodrigues, I., Grebel, E., Pilyugin, L., Freitas-Lemes, P., and Krabbe, A. (2015). On the central abundances of active galactic nuclei and star-forming galaxies. *Monthly Notices of the Royal Astronomical Society*, 453(4):4102–4111.

Du, P., Zhang, Z.-X., Wang, K., Huang, Y.-K., Zhang, Y., Lu, K.-X., Hu, C., Li, Y.-R., Bai, J.-M., Bian, W.-H., et al. (2018). Supermassive black holes with high accretion rates in active galactic nuclei. ix. 10 new observations of reverberation mapping and shortened hβ lags. *The Astrophysical Journal*, 856(1):6.

Duras, F., Bongiorno, A., Ricci, F., Piconcelli, E., Shankar, F., Lusso, E., Bianchi, S., Fiore, F., Maiolino, R., Marconi, A., et al. (2020). Universal bolometric corrections for active galactic nuclei over seven luminosity decades. *Astronomy & Astrophysics*, 636:A73.

Eilers, A.-C., Simcoe, R. A., Yue, M., Mackenzie, R., Matthee, J., Ďurovčíková, D., Kashino, D., Bordoloi, R., and Lilly, S. J. (2023). Eiger. iii. jwst/nircam observations of the ultraluminous high-redshift quasar j0100+ 2802. *The Astrophysical Journal*, 950(1):68.

Eisenstein, D. J., Weinberg, D. H., Agol, E., Aihara, H., Prieto, C. A., Anderson, S. F., Arns, J. A., Aubourg, É., Bailey, S., Balbinot, E., et al. (2011). Sdss-iii: Massive spectroscopic surveys of the distant universe, the milky way, and extra-solar planetary systems. *The Astronomical Journal*, 142(3):72.

Elvis, M., Hao, H., Civano, F., Brusa, M., Salvato, M., Bongiorno, A., Capak, P., Zamorani, G., Comastri, A., Jahnke, K., et al. (2012). Spectral energy distributions of type 1 active galactic nuclei in the cosmos survey. i. the xmm-cosmos sample. *The Astrophysical Journal*, 759(1):6.

Elvis, M. and Karovska, M. (2002). Quasar parallax: a method for determining direct geometrical distances to quasars. *The Astrophysical Journal*, 581(2):L67.

Elvis, M. S., Wilkes, B. J., McDowell, J. C., Green, R. F., Bechtold, J., Willner, S. P., Oey, M., Polomski, E., and Cutri, R. (1994). Atlas of quasar energy distributions. *The Astrophysical Journal Supplement Series.*

Evans, D. (1989). Photometric calibration of the apm proper motion project. *Astronomy and Astrophysics Supplement Series (ISSN 0365-0138), vol. 78, no. 2, May 1989, p. 249-268. Research supported by SERC.*, 78:249–268.

Evans, I. N., Primini, F. A., Glotfelty, K. J., Anderson, C. S., Bonaventura, N. R., Chen, J. C., Davis, J. E., Doe, S. M., Evans, J. D., Fabbiano, G., et al. (2010). The chandra source catalog. *The Astrophysical Journal Supplement Series*, 189(1):37.

Ezhikode, S. H., Gandhi, P., Done, C., Ward, M., Dewangan, G. C., Misra, R., and Philip, N. S. (2017). Determining the torus covering factors for a sample of type 1 agn in the local universe. *Monthly Notices of the Royal Astronomical Society*, 472(3):3492–3511.

Fabian, A., Vasudevan, R., and Gandhi, P. (2008). The effect of radiation pressure on dusty absorbing gas around active galactic nuclei. *Monthly Notices of the Royal Astronomical Society: Letters*, 385(1):L43–L47.

Fabian, A., Vasudevan, R., Mushotzky, R., Winter, L., and Reynolds, C. (2009). Radiation pressure and absorption in agn: results from a complete unbiased sample from swift. *Monthly Notices of the Royal Astronomical Society: Letters*, 394(1):L89–L92.

Fabian, A. C. (2012). Observational evidence of active galactic nuclei feedback. *Annual Review of Astronomy and Astrophysics*, 50(1):455–489.

Fan, X., Bañados, E., and Simcoe, R. A. (2023). Quasars and the intergalactic medium at cosmic dawn. *Annual Review of Astronomy and Astrophysics*, 61(1):373–426.

Fan, X., Hennawi, J. F., Richards, G. T., Strauss, M. A., Schneider, D. P., Donley, J. L., Young, J. E., Annis, J., Lin, H., Lampeitl, H., et al. (2004). A survey of z> 5.7 quasars in the sloan digital sky survey. iii. discovery of five additional quasars. *The Astronomical Journal*, 128(2):515.

Faucher-Giguere, C.-A., Lidz, A., Hernquist, L., and Zaldarriaga, M. (2008). Evolution of the intergalactic opacity: implications for the ionizing background, cosmic star formation, and quasar activity. *The Astrophysical Journal*, 688(1):85.

Feltre, A., Hatziminaoglou, E., Fritz, J., and Franceschini, A. (2012). Smooth and clumpy dust distributions in agn: a direct comparison of two commonly explored infrared emission models. *Monthly Notices of the Royal Astronomical Society*, 426(1):120–127.

Ferland, G., Chatzikos, M., Guzmán, F., Lykins, M., Van Hoof, P., Williams, R., Abel, N., Badnell, N., Keenan, F., Porter, R., et al. (2017). The 2017 release of cloudy. *Revista mexicana de astronomía y astrofísica*, 53(2).

Ferland, G. J., Hu, C., Wang, J.-M., Baldwin, J. A., Porter, R. L., Van Hoof, P. A., and Williams, R. (2009). Implications of infalling fe ii-emitting clouds in active galactic nuclei: anisotropic properties. *The Astrophysical Journal*, 707(1):L82.

Ferland, G. J., Porter, R., Van Hoof, P., Williams, R., Abel, N., Lykins, M., Shaw, G., Henney, W. J., and Stancil, P. (2013). The 2013 release of cloudy. *Revista mexicana de astronomía y astrofísica*, 49(1):137–163.

Ferrarese, L. and Merritt, D. (2000). A fundamental relation between supermassive black holes and their host galaxies. *The Astrophysical Journal*, 539(1):L9.

Feruglio, C., Maiolino, R., Piconcelli, E., Menci, N., Aussel, H., Lamastra, A., and Fiore, F. (2010). Quasar feedback revealed by giant molecular outflows. *Astronomy & Astrophysics*, 518:L155.

Fiore, F., Gaspari, M., Luminari, A., Tozzi, P., and De Arcangelis, L. (2023). Dynamical complexity in micro-scale disk-wind systems. *arXiv e-prints*, page arXiv:2304.12696.

Fitzpatrick, E. L. (1999). Correcting for the effects of interstellar extinction. *Publications of the Astronomical Society of the Pacific*, 111(755):63.

Floris, A., Marziani, P., Panda, S., Sniegowska, M., D'Onofrio, M., Deconto-Machado, A., Del Olmo, A., and Czerny, B. (2024). Chemical abundances along the quasar main sequence. *arXiv preprint arXiv:2405.04456*.

Foreman-Mackey, D., Hogg, D. W., Lang, D., and Goodman, J. (2013). emcee: The mcmc hammer. *PASP*, 125:306–312.

Fossati, G. a., Maraschi, L., Celotti, A., Comastri, A., and Ghisellini, G. (1998). A unifying view of the spectral energy distributions of blazars. *Monthly Notices of the Royal Astronomical Society*, 299(2):433–448.

Francis, P., Hewett, P. C., Foltz, C. B., Chaffee, F. H., Weymann, R. J., Morris, S. L., et al. (1991). A high signal-to-noise ratio composite quasar spectrum.

Freudling, W., Corbin, M. R., and Korista, K. T. (2003). Iron emission in z$\simeq$ 6 qsos. *The Astrophysical Journal*, 587(2):L67.

Fukugita, M., Shimasaku, K., Ichikawa, T., Gunn, J., et al. (1996). The sloan digital sky survey photometric system. Technical report, SCAN-9601313.

Furtak, L. J., Labbé, I., Zitrin, A., Greene, J. E., Dayal, P., Chemerynska, I., Kokorev, V., Miller, T. B., Goulding, A. D., de Graaff, A., et al. (2024). A high black-hole-to-host mass ratio in a lensed agn in the early universe. *Nature*, 628(8006):57–61.

Gallagher, S., Brandt, W., Chartas, G., and Garmire, G. (2002). X-ray spectroscopy of quasi-stellar objects with broad ultraviolet absorption lines. *The Astrophysical Journal*, 567(1):37.

Gallerani, S., Maiolino, R., Juarez, Y., Nagao, T., Marconi, A., Bianchi, S., Schneider, R., Mannucci, F., Oliva, T., Willott, C., et al. (2010). The extinction law at high redshift and its implications. *Astronomy & Astrophysics*, 523:A85.

Gandhi, P., Hönig, S. F., and Kishimoto, M. (2015). The dust sublimation radius as an outer envelope to the bulk of the narrow fe kα line emission in type 1 agns. *The Astrophysical Journal*, 812(2):113.

Gandhi, P., Horst, H., Smette, A., Hönig, S., Comastri, A., Gilli, R., Vignali, C., and Duschl, W. (2009). Resolving the mid-infrared cores of local seyferts. *Astronomy & Astrophysics*, 502(2):457–472.

García-Bernete, I., González-Martín, O., Almeida, C. R., Alonso-Herrero, A., Martínez-Paredes, M., Ward, M., Roche, P., Acosta-Pulido, J., López-Rodríguez, E., Rigopoulou, D., et al. (2022). Torus and polar dust dependence on active galactic nucleus properties. *Astronomy & Astrophysics*, 667:A140.

García-Bernete, I., Ramos Almeida, C., Alonso-Herrero, A., Ward, M., Acosta-Pulido, J., Pereira-Santaella, M., Hernán-Caballero, A., Asensio Ramos, A., González-Martín, O., Levenson, N., et al. (2019). Torus model properties of an ultra-hard x-ray selected sample of seyfert galaxies. *Monthly Notices of the Royal Astronomical Society*, 486(4):4917–4935.

García-González, J., Alonso-Herrero, A., Hönig, S., Hernán-Caballero, A., Ramos Almeida, C., Levenson, N., Roche, P., González-Martín, O., Packham, C., and Kishimoto, M. (2017). A mid-infrared statistical investigation of clumpy torus model predictions. *Monthly Notices of the Royal Astronomical Society*, 470(3):2578–2598.

Gardner, J. P., Mather, J. C., Clampin, M., Doyon, R., Greenhouse, M. A., Hammel, H. B., Hutchings, J. B., Jakobsen, P., Lilly, S. J., Long, K. S., et al. (2006). The james webb space telescope. *Space Science Reviews*, 123:485–606.

Gargiulo, A., Fumana, M., Bisogni, S., Franzetti, P., Cassarà, L., Garilli, B., Scodeggio, M., and Vietri, G. (2022). Sipgi: an interactive pipeline for spectroscopic data reduction. *Monthly Notices of the Royal Astronomical Society.*

Gaskell, C. M. and Ferland, G. J. (1984). Theoretical hydrogen-line ratios for the narrow-line regions of active galactic nuclei. *Publications of the Astronomical Society of the Pacific*, 96(580):393.

Gaskell, C. M., Goosmann, R. W., Antonucci, R. R., and Whysong, D. H. (2004). The nuclear reddening curve for active galactic nuclei and the shape of the infrared to x-ray spectral energy distribution. *The Astrophysical Journal*, 616(1):147.

Gebhardt, K., Bender, R., Bower, G., Dressler, A., Faber, S., Filippenko, A. V., Green, R., Grillmair, C., Ho, L. C., Kormendy, J., et al. (2000). A relationship between nuclear black hole mass and galaxy velocity dispersion. *The Astrophysical Journal*, 539(1):L13.

Gehrels, N., Chincarini, G., Giommi, P. e., Mason, K., Nousek, J., Wells, A., White, N., Barthelmy, S., Burrows, D., Cominsky, L., et al. (2004). The swift gamma-ray burst mission. *The Astrophysical Journal*, 611(2):1005.

Giambagli, L., Fanelli, D., Risaliti, G., and Signorini, M. (2023). Nonparametric analysis of the hubble diagram with neural networks. *Astronomy & Astrophysics*, 678:A13.

Gianolli, V., Kim, D., Bianchi, S., Agís-González, B., Madejski, G., Marin, F., Marinucci, A., Matt, G., Middei, R., Petrucci, P., et al. (2023). Uncovering the geometry of the hot x-ray corona in the seyfert galaxy ngc 4151 with ixpe. *Monthly Notices of the Royal Astronomical Society*, 523(3):4468–4476.

Giavalisco, M., Ferguson, H., Koekemoer, A., Dickinson, M., Alexander, D., Bauer, F., Bergeron, J., Biagetti, C., Brandt, W., Casertano, S., et al. (2004). The great observatories origins deep survey: initial results from optical and near-infrared imaging. *The Astrophysical Journal*, 600(2):L93.

Gibson, R. R., Jiang, L., Brandt, W., Hall, P. B., Shen, Y., Wu, J., Anderson, S. F., Schneider, D. P., Berk, D. V., Gallagher, S., et al. (2009). A catalog of broad absorption line quasars in sloan digital sky survey data release 5. *The Astrophysical Journal*, 692(1):758.

Gilli, R., Comastri, A., and Hasinger, G. (2007). The synthesis of the cosmic x-ray background in the chandra and xmm-newton era. *Astronomy & Astrophysics*, 463(1):79–96.

Gilli, R., Norman, C., Calura, F., Vito, F., Decarli, R., Marchesi, S., Iwasawa, K., Comastri, A., Lanzuisi, G., Pozzi, F., et al. (2022). Supermassive black holes at high redshift are expected to be obscured by their massive host galaxies' inter stellar medium. *arXiv preprint arXiv:2206.03508.*

Gilmozzi, R. and Spyromilio, J. (2007). The european extremely large telescope (e-elt). *The Messenger*, 127(11):3.

González-Martín, O., Masegosa, J., García-Bernete, I., Almeida, C. R., Rodríguez-Espinosa, J. M., Márquez, I., Esparza-Arredondo, D., Osorio-Clavijo, N., Martínez-Paredes, M., Victoria-Ceballos, C., et al. (2019). Exploring the mid-infrared seds of six agn dusty torus models. i. synthetic spectra. *The Astrophysical Journal*, 884(1):10.

Goodrich, R. W. (1990). Pa-beta measurements and reddening in seyfert 1.8 and 1.9 galaxies. *Astrophysical Journal, Part 1 (ISSN 0004-637X), vol. 355, May 20, 1990, p. 88-93.*, 355:88–93.

Gordon, K. D., Fouesneau, M., Arab, H., Tchernyshyov, K., Weisz, D. R., Dalcanton, J. J., Williams, B. F., Bell, E. F., Bianchi, L., Boyer, M., et al. (2016). The panchromatic hubble andromeda treasury. xv. the beast: Bayesian extinction and stellar tool. *The Astrophysical Journal*, 826(2):104.

Goulding, A., Alexander, D., Bauer, F., Forman, W., Hickox, R., Jones, C., Mullaney, J., and Trichas, M. (2012). Deep silicate absorption features in compton-thick active galactic nuclei predominantly arise due to dust in the host galaxy. *The Astrophysical Journal*, 755(1):5.

Granato, G. and Danese, L. (1994). Thick tori around active galactic nuclei: a comparison of model predictions with observations of the infrared continuum and silicate features. *Monthly Notices of the Royal Astronomical Society*, 268(1):235–252.

Grandi, S. A. (1982). The 3000 a bump in quasars. *Astrophysical Journal, Part 1, vol. 255, Apr. 1, 1982, p. 25-38.*, 255:25–38.

Green, P. J. (1998). Differences between the optical/ultraviolet spectra of x-ray bright and x-ray faint qsos. *The Astrophysical Journal*, 498(1):170.

Greene, J. E. and Ho, L. C. (2005). Estimating black hole masses in active galaxies using the hα emission line. *The Astrophysical Journal*, 630(1):122.

Greene, J. E., Labbe, I., Goulding, A. D., Furtak, L. J., Chemerynska, I., Kokorev, V., Dayal, P., Volonteri, M., Williams, C. C., Wang, B., et al. (2024). Uncover spectroscopy confirms the surprising ubiquity of active galactic nuclei in red sources at z> 5. *The Astrophysical Journal*, 964(1):39.

Grevesse, N., Asplund, M., Sauval, A., and Scott, P. (2010). The chemical composition of the sun. *Astrophysics and Space Science*, 328(1-2):179–183.

Groves, B. A., Heckman, T. M., and Kauffmann, G. (2006). Emission-line diagnostics of low-metallicity active galactic nuclei. *Monthly Notices of the Royal Astronomical Society*, 371(4):1559–1569.

Gu, M. (2013). The evolution of the dusty torus covering factor in quasars. *The Astrophysical Journal*, 773(2):176.

Guo, H., Shen, Y., and Wang, S. (2018). Pyqsofit: Python code to fit the spectrum of quasars. *Astrophysics Source Code Library*, pages ascl–1809.

Haidar, H., Rosario, D. J., Alonso-Herrero, A., Pereira-Santaella, M., García-Bernete, I., Campbell, S., Hönig, S. F., Ramos Almeida, C., Hicks, E., Delaney, D., et al. (2024). Dust beyond the torus: revealing the mid-infrared heart of local seyfert eso 428-g14 with jwst/miri. *Monthly Notices of the Royal Astronomical Society*, 532(4):4645–4660.

Hainline, K. N., Maiolino, R., Juodzbalis, I., Scholtz, J., Ubler, H., D'Eugenio, F., Helton, J. M., Sun, Y., Sun, F., Robertson, B., et al. (2024). An investigation into the selection and colors of little red dots and active galactic nuclei. *arXiv preprint arXiv:2410.00100.*

Halpern, J. and Steiner, J. (1983). Low-ionization active galactic nuclei-x-ray or shock heated? *Astrophysical Journal, Part 2-Letters to the Editor (ISSN 0004-637X), vol. 269, June 15, 1983, p. L37-L41.*, 269:L37–L41.

Hamann, F. and Ferland, G. (1993). The chemical evolution of qsos and the implications for cosmology and galaxy formation. *Astrophysical Journal v. 418, p. 11*, 418:11.

Hamann, F. and Ferland, G. (1999). Elemental abundances in quasistellar objects: star formation and galactic nuclear evolution at high redshifts. *Annual Review of Astronomy and Astrophysics*, 37(1):487–531.

Hamann, F., Korista, K. T., and Morris, S. L. (1993). On the geometry, covering factor, and scattering-emission properties of qso broad absorption-line regions. *The Astrophysical Journal*, 415:541.

Hamuy, M., Phillips, M., Schommer, R. A., Suntzeff, N. B., Maza, J., and Aviles, R. (1996). The absolute luminosities of the calan/tololo type ia supernovae. *arXiv preprint astro-ph/9609059.*

Hao, H., Elvis, M., Bongiorno, A., Zamorani, G., Merloni, A., Kelly, B. C., Civano, F., Celotti, A., Ho, L. C., Jahnke, K., et al. (2013a). A quasar–galaxy mixing diagram: quasar spectral energy distribution shapes in the optical to near-infrared. *Monthly Notices of the Royal Astronomical Society*, 434(4):3104–3121.

Hao, H., Elvis, M., Civano, F., and Lawrence, A. (2011). Hot-dust-poor quasars in mid-infrared and optically selected samples. *The Astrophysical Journal*, 733(2):108.

Hao, H., Elvis, M., Civano, F., Zamorani, G., Ho, L. C., Comastri, A., Brusa, M., Bongiorno, A., Merloni, A., Trump, J. R., et al. (2013b). Spectral energy distributions of type 1 agn in xmm-cosmos–ii. shape evolution. *Monthly Notices of the Royal Astronomical Society*, 438(2):1288–1304.

Harikane, Y., Zhang, Y., Nakajima, K., Ouchi, M., Isobe, Y., Ono, Y., Hatano, S., Xu, Y., and Umeda, H. (2023). A jwst/nirspec first census of broad-line agns at z= 4–7: Detection of 10 faint agns with m bh $10^6 - 10^8 m_{\odot}$ and their host galaxy properties. *The Astrophysical Journal*, 959(1):39.

Harris, D. W., Jensen, T. W., Suzuki, N., Bautista, J. E., Dawson, K. S., Vivek, M., Brownstein, J. R., Ge, J., Hamann, F., Herbst, H., et al. (2016). The composite spectrum of boss quasars selected for studies of the lyα forest. *The Astronomical Journal*, 151(6):155.

Harrison, C. (2014). *Observational constraints on the influence of active galactic nuclei on the evolution of galaxies*. PhD thesis, Durham University, UK.

Harrison, C., Costa, T., Tadhunter, C., Flütsch, A., Kakkad, D., Perna, M., and Vietri, G. (2018). Agn outflows and feedback twenty years on. *Nature Astronomy*, 2(3):198–205.

Hasinger, G. (2008). Absorption properties and evolution of active galactic nuclei. *Astronomy & Astrophysics*, 490(3):905–922.

Heger, A., Fryer, C. L., Woosley, S. E., Langer, N., and Hartmann, D. H. (2003). How massive single stars end their life. *The Astrophysical Journal*, 591(1):288.

Hernán-Caballero, A., Hatziminaoglou, E., Alonso-Herrero, A., and Mateos, S. (2016). The near-to-mid infrared spectrum of quasars. *Monthly Notices of the Royal Astronomical Society*, 463(2):2064–2078.

Hickox, R. C. and Alexander, D. M. (2018). Obscured active galactic nuclei. *Annual Review of Astronomy and Astrophysics*, 56(1):625–671.

Hirano, S., Hosokawa, T., Yoshida, N., Omukai, K., and Yorke, H. W. (2015). Primordial star formation under the influence of far ultraviolet radiation: 1540 cosmological haloes and the stellar mass distribution. *Monthly Notices of the Royal Astronomical Society*, 448(1):568–587.

Hodges Jr, J. (1958). The significance probability of the smirnov two-sample test. *Arkiv för matematik*, 3(5):469–486.

Hönig, S., Kishimoto, M., Gandhi, P., Smette, A., Asmus, D., Duschl, W., Polletta, M., and Weigelt, G. (2010). The dusty heart of nearby active galaxies-i. high-spatial resolution mid-ir spectro-photometry of seyfert galaxies. *Astronomy & Astrophysics*, 515:A23.

Hopkins, P. F., Strauss, M. A., Hall, P. B., Richards, G. T., Cooper, A. S., Schneider, D. P., Berk, D. E. V., Jester, S., Brinkmann, J., and Szokoly, G. P. (2004). Dust reddening in sloan digital sky survey quasars. *The Astronomical Journal*, 128(3):1112.

Hu, J., Yu, H., and Wang, F. (2017). Investigating the effect of cosmic opacity on standard candles. *The Astrophysical Journal*, 836(1):107.

Ichikawa, K., Packham, C., Almeida, C. R., Ramos, A. A., Alonso-Herrero, A., González-Martín, O., Lopez-Rodriguez, E., Ueda, Y., Díaz-Santos, T., Elitzur, M., et al. (2015). The differences in the torus geometry between hidden and non-hidden broad line active galactic nuclei. *The Astrophysical Journal*, 803(2):57.

Ichikawa, K., Ricci, C., Ueda, Y., Bauer, F. E., Kawamuro, T., Koss, M. J., Oh, K., Rosario, D. J., Shimizu, T. T., Stalevski, M., et al. (2019). Bat agn spectroscopic survey. xi. the covering factor of dust and gas in swift/bat active galactic nuclei. *The Astrophysical Journal*, 870(1):31.

Inayoshi, K., Visbal, E., and Haiman, Z. (2020). The assembly of the first massive black holes. *Annual Review of Astronomy and Astrophysics*, 58:27–97.

Inoue, A. K., Shimizu, I., Iwata, I., and Tanaka, M. (2014). An updated analytic model for attenuation by the intergalactic medium. *Monthly Notices of the Royal Astronomical Society*, 442(2):1805–1820.

Isobe, Y., Ouchi, M., Nakajima, K., Harikane, Y., Ono, Y., Xu, Y., Zhang, Y., and Umeda, H. (2023). Redshift evolution of electron density in the interstellar medium at z 0–9 uncovered with jwst/nirspec spectra and line-spread function determinations. *The Astrophysical Journal*, 956(2):139.

Ivezić, Ž., Kahn, S. M., Tyson, J. A., Abel, B., Acosta, E., Allsman, R., Alonso, D., AlSayyad, Y., Anderson, S. F., Andrew, J., et al. (2019). Lsst: from science drivers to reference design and anticipated data products. *The Astrophysical Journal*, 873(2):111.

Iwamuro, F., Kimura, M., Eto, S., Maihara, T., Motohara, K., Yoshii, Y., and Doi, M. (2004). Fe ii/mg ii emission-line ratios of qsos. ii. z> 6 objects. *The Astrophysical Journal*, 614(1):69.

Iwamuro, F., Motohara, K., Maihara, T., Kimura, M., Yoshii, Y., and Doi, M. (2002). Fe ii/mg ii emission-line ratios of qsos within 0< z< 5.3. *The Astrophysical Journal*, 565(1):63.

Izotov, Y., Guseva, N., Fricke, K., and Papaderos, P. (2009). Sbs 0335-052e+ w: deep vlt/fors+ uves spectroscopy of the pair of the lowest-metallicity blue compact dwarf galaxies. *Astronomy & Astrophysics*, 503(1):61–72.

Izotov, Y. I., Chaffee, F. H., Foltz, C. B., Green, R. F., Guseva, N. G., and Thuan, T. X. (1999). Helium abundance in the most metal-deficient blue compact galaxies: I zw 18 and sbs 0335–052. *The Astrophysical Journal*, 527(2):757.

Izotov, Y. I., Lipovetskii, V., Guseva, N., Kniazev, A. Y., and Stepanian, J. (1990). Unusually low heavy-element abundance found in the blue compact dwarf galaxy sbs0335–052. *Nature*, 343(6255):238–240.

Izotov, Y. I. and Thuan, T. X. (2008). Active galactic nuclei in four metal-poor dwarf emission-line galaxies. *The Astrophysical Journal*, 687(1):133.

Jalan, P., Rakshit, S., Woo, J.-J., Kotilainen, J., and Stalin, C. (2023). An empirical relation to estimate host galaxy stellar light from agn spectra. *Monthly Notices of the Royal Astronomical Society: Letters*, 521(1):L11–L16.

Jenkins, E. B. (2009). A unified representation of gas-phase element depletions in the interstellar medium. *The Astrophysical Journal*, 700(2):1299.

Jiang, D., Onoue, M., Jiang, L., Lai, S., Banados, E., Becker, G. D., Bischetti, M., Bosman, S. E., Davies, R. L., DOdorico, V., et al. (2024). No redshift evolution in the fe ii/mg ii flux ratios of quasars across cosmic time. *arXiv preprint arXiv:2409.06174*.

Jiang, L., Fan, X., Brandt, W., Carilli, C. L., Egami, E., Hines, D. C., Kurk, J. D., Richards, G. T., Shen, Y., Strauss, M. A., et al. (2010). Dust-free quasars in the early universe. *Nature*, 464(7287):380–383.

Jiang, L., Fan, X., Vestergaard, M., Kurk, J. D., Walter, F., Kelly, B. C., and Strauss, M. A. (2007). Gemini near-infrared spectroscopy of luminous z 6 quasars: chemical abundances, black hole masses, and mg ii absorption. *The Astronomical Journal*, 134(3):1150.

Jiang, Y.-F., Blaes, O., Stone, J. M., and Davis, S. W. (2019). Global radiation magnetohydrodynamic simulations of sub-eddington accretion disks around supermassive black holes. *The Astrophysical Journal*, 885(2):144.

Jiang, Y.-F., Davis, S. W., and Stone, J. M. (2016). Iron opacity bump changes the stability and structure of accretion disks in active galactic nuclei. *The Astrophysical Journal*, 827(1):10.

Jiang, Y.-F., Stone, J. M., and Davis, S. W. (2014). Radiation magnetohydrodynamic simulations of the formation of hot accretion disk coronae. *The Astrophysical Journal*, 784(2):169.

Jin, C., Done, C., Ward, M., Panessa, F., Liu, B., and Liu, H.-Y. (2023). The extreme super-eddington nls1 rx j0134. 2-4258–ii. a weak-line seyfert linking to the weak-line quasar. *Monthly Notices of the Royal Astronomical Society*, 518(4):6065–6082.

Jin, C., Lusso, E., Ward, M., Done, C., and Middei, R. (2024). Wavelength dependences of the optical/uv and x-ray luminosity correlations of quasars. *Monthly Notices of the Royal Astronomical Society*, 527(1):356–373.

Jin, C., Ward, M., and Done, C. (2012). A combined optical and x-ray study of unobscured type 1 active galactic nuclei–iii. broad-band sed properties. *Monthly Notices of the Royal Astronomical Society*, 425(2):907–929.

Joly, M. (1987). Formation of low ionization lines in active galactic nuclei. *Astronomy and Astrophysics (ISSN 0004-6361), vol. 184, no. 1-2, Oct. 1987, p. 33-42.*, 184:33–42.

Jones, T., Sanders, R., Chen, Y., Wang, X., Morishita, T., Roberts-Borsani, G., Treu, T., Dressler, A., Merlin, E., Paris, D., et al. (2023). Early results from glass–jwst. xxi. rapid asembly of a galaxy at z= 6.23 revealed by its c/o abundance. *The Astrophysical Journal Letters*, 951(1):L17.

Juarez, Y., Maiolino, R., Mujica, R., Pedani, M., Marinoni, S., Nagao, T., Marconi, A., and Oliva, E. (2009). The metallicity of the most distant quasars. *Astronomy & Astrophysics*, 494(2):L25–L28.

Juodžbalis, I., Ji, X., Maiolino, R., D'Eugenio, F., Scholtz, J., Risaliti, G., Fabian, A. C., Mazzolari, G., Gilli, R., Prandoni, I., et al. (2024a). Jades–the rosetta stone of jwst-discovered agn: deciphering the intriguing nature of early agn. *arXiv preprint arXiv:2407.08643*.

Juodžbalis, I., Maiolino, R., Baker, W. M., Tacchella, S., Scholtz, J., D'Eugenio, F., Schneider, R., Trinca, A., Valiante, R., DeCoursey, C., et al. (2024b). A dormant, overmassive black hole in the early universe. *arXiv preprint arXiv:2403.03872*.

Just, D. W., Brandt, W., Shemmer, O., Steffen, A., Schneider, D., Chartas, G., and Garmire, G. (2007). The x-ray properties of the most luminous quasars from the sloan digital sky survey. *The Astrophysical Journal*, 665(2):1004.

Kakkad, D., Mainieri, V., Vietri, G., Carniani, S., Harrison, C., Perna, M., Scholtz, J., Circosta, C., Cresci, G., Husemann, B., et al. (2020). Super-ii. spatially resolved ionised gas kinematics and scaling relations in z 2 agn host galaxies. *Astronomy & Astrophysics*, 642:A147.

Kaspi, S., Maoz, D., Netzer, H., Peterson, B. M., Vestergaard, M., and Jannuzi, B. T. (2005). The relationship between luminosity and broad-line region size in active galactic nuclei. *The Astrophysical Journal*, 629(1):61.

Kauffmann, G., Heckman, T. M., Tremonti, C., Brinchmann, J., Charlot, S., White, S. D., Ridgway, S. E., Brinkmann, J., Fukugita, M., Hall, P. B., et al. (2003). The host galaxies of active galactic nuclei. *Monthly Notices of the Royal Astronomical Society*, 346(4):1055–1077.

Kawakatu, N., Umemura, M., and Mori, M. (2003). Protoquasars: physical states and observable properties. *The Astrophysical Journal*, 583(1):85.

Kawara, K., Murayama, T., Taniguchi, Y., and Arimoto, N. (1996). Infrared spectroscopy of the gravitationally lensed quasar b1422+ 231: Mg ii λ2798 and fe ii emission from the broad-line gas at z= 3.62. *The Astrophysical Journal*, 470(2):L85.

Kellermann, K., Sramek, R., Schmidt, M., Shaffer, D., and Green, R. (1989). Vla observations of objects in the palomar bright quasar survey. *Astronomical Journal (ISSN 0004-6256), vol. 98, Oct. 1989, p. 1195-1207.*, 98:1195–1207.

Kendall, M. G. (1938). A new measure of rank correlation. *Biometrika*, 30(1-2):81–93.

Kennicutt Jr, R. C., Bresolin, F., and Garnett, D. R. (2003). The composition gradient in m101 revisited. ii. electron temperatures and implications for the nebular abundance scale. *The Astrophysical Journal*, 591(2):801.

Kewley, L. J. and Ellison, S. L. (2008). Metallicity calibrations and the mass-metallicity relation for star-forming galaxies. *The Astrophysical Journal*, 681(2):1183.

Khadka, N., Zajaček, M., Panda, S., Martínez-Aldama, M. L., and Ratra, B. (2022). Consistency study of high-and low-accreting mg ii quasars: no significant effect of the fe ii to mg ii flux ratio on the radius–luminosity relation dispersion. *Monthly Notices of the Royal Astronomical Society*, 515(3):3729–3748.

Khadka, N., Zajaček, M., Prince, R., Panda, S., Czerny, B., Martínez-Aldama, M. L., Jaiswal, V. K., and Ratra, B. (2023). Quasar uv/x-ray relation luminosity distances are shorter than reverberation-measured radius–luminosity relation luminosity distances. *Monthly Notices of the Royal Astronomical Society*, 522(1):1247–1264.

King, A. (2005). The agn-starburst connection, galactic superwinds, and mbh-σ. *The Astrophysical Journal*, 635(2):L121.

King, A. (2024). The black hole masses of high-redshift qsos. *Monthly Notices of the Royal Astronomical Society*, 531(1):550–553.

King, A. and Pounds, K. (2015). Powerful outflows and feedback from active galactic nuclei. *Annual Review of Astronomy and Astrophysics*, 53:115–154.

Kocevski, D. D., Finkelstein, S. L., Barro, G., Taylor, A. J., Calabrò, A., Laloux, B., Buchner, J., Trump, J. R., Leung, G. C., Yang, G., et al. (2024). The rise of faint, red agn at $z > 4$: A sample of little red dots in the jwst extragalactic legacy fields. *arXiv preprint arXiv:2404.03576*.

Kocevski, D. D., Onoue, M., Inayoshi, K., Trump, J. R., Haro, P. A., Grazian, A., Dickinson, M., Finkelstein, S. L., Kartaltepe, J. S., Hirschmann, M., et al. (2023). Hidden little monsters: spectroscopic identification of low-mass, broad-line agns at z> 5 with ceers. *The Astrophysical Journal Letters*, 954(1):L4.

Kokorev, V., Fujimoto, S., Labbe, I., Greene, J. E., Bezanson, R., Dayal, P., Nelson, E. J., Atek, H., Brammer, G., Caputi, K. I., et al. (2023). Uncover: A nirspec identification of a broad-line agn at z= 8.50. *The Astrophysical Journal Letters*, 957(1):L7.

Kokubo, M. and Harikane, Y. (2024). Challenging the agn scenario for jwst/nirspec broad h α emitters/little red dots in light of non-detection of nircam photometric variability and x-ray. *arXiv preprint arXiv:2407.04777*.

Koudmani, S., Sijacki, D., and Smith, M. C. (2022). Two can play at that game: constraining the role of supernova and agn feedback in dwarf galaxies with cosmological zoom-in simulations. *Monthly Notices of the Royal Astronomical Society*, 516(2):2112–2141.

Kratzer, R. M. and Richards, G. T. (2015). Mean and extreme radio properties of quasars and the origin of radio emission. *The Astronomical Journal*, 149(2):61.

Krawczyk, C. M., Richards, G. T., Mehta, S. S., Vogeley, M. S., Gallagher, S., Leighly, K. M., Ross, N. P., and Schneider, D. P. (2013). Mean spectral energy distributions and bolometric corrections for luminous quasars. *The Astrophysical Journal Supplement Series*, 206(1):4.

Krolik, J. H. and Begelman, M. C. (1988). Molecular tori in seyfert galaxies-feeding the monster and hiding it. *Astrophysical Journal, Part 1 (ISSN 0004-637X), vol. 329, June 15, 1988, p. 702-711. Research supported by the Ball Corp., Rockwell International Corp., and Exxon Education Foundation.*, 329:702–711.

Krolik, J. H. and Kallman, T. R. (1988). The effects of thermal accretion disk spectra on the emission lines from active galactic nuclei. *The Astrophysical Journal*, 324:714–720.

Kuhn, O., Elvis, M., Bechtold, J., and Elston, R. (2001). A search for signatures of quasar evolution: comparison of the shapes of the rest-frame optical/ultraviolet continua of quasars at z> 3 and z˜ 0.1. *The Astrophysical Journal Supplement Series*, 136(2):225.

Kurk, J. D., Walter, F., Fan, X., Jiang, L., Riechers, D. A., Rix, H.-W., Pentericci, L., Strauss, M. A., Carilli, C., and Wagner, S. (2007). Black hole masses and enrichment of z˜ 6 sdss quasars. *The Astrophysical Journal*, 669(1):32.

La Franca, F., Bianchi, S., Ponti, G., Branchini, E., and Matt, G. (2014). A new cosmological distance measure using active galactic nucleus x-ray variability. *The Astrophysical Journal Letters*, 787(1):L12.

La Franca, F., Fiore, F., Comastri, A., Perola, G., Sacchi, N., Brusa, M., Cocchia, F., Feruglio, C., Matt, G., Vignali, C., et al. (2005). The hellas2xmm survey. vii. the hard x-ray luminosity function of agns up to z= 4: More absorbed agns at low luminosities and high redshifts. *The Astrophysical Journal*, 635(2):864.

Labbé, I., van Dokkum, P., Nelson, E., Bezanson, R., Suess, K. A., Leja, J., Brammer, G., Whitaker, K., Mathews, E., Stefanon, M., et al. (2023). A population of red candidate massive galaxies˜ 600 myr after the big bang. *Nature*, 616(7956):266–269.

Lai, S., Bian, F., Onken, C. A., Wolf, C., Mazzucchelli, C., Banados, E., Bischetti, M., Bosman, S. E., Becker, G., Cupani, G., et al. (2022). Chemical abundance of z˜ 6 quasar broad-line regions in the xqr-30 sample. *Monthly Notices of the Royal Astronomical Society*, 513(2):1801–1819.

Lang, D., Hogg, D. W., and Schlegel, D. J. (2016). Wise photometry for 400 million sdss sources. *The Astronomical Journal*, 151(2):36.

Laor, A., Fiore, F., Elvis, M., Wilkes, B. J., and McDowell, J. C. (1997). The soft x-ray properties of a complete sample of optically selected quasars. ii. final results. *The Astrophysical Journal*, 477(1):93.

Larson, R. L., Finkelstein, S. L., Kocevski, D. D., Hutchison, T. A., Trump, J. R., Haro, P. A., Bromm, V., Cleri, N. J., Dickinson, M., Fujimoto, S., et al. (2023). A ceers discovery of an accreting supermassive black hole 570 myr after the big bang: identifying a progenitor of massive z> 6 quasars. *The Astrophysical Journal Letters*, 953(2):L29.

Laureijs, R., Amiaux, J., Arduini, S., Augueres, J.-L., Brinchmann, J., Cole, R., Cropper, M., Dabin, C., Duvet, L., Ealet, A., et al. (2011). Euclid definition study report. *arXiv preprint arXiv:1110.3193*.

Laurenti, M., Piconcelli, E., Zappacosta, L., Tombesi, F., Vignali, C., Bianchi, S., Marziani, P., Vagnetti, F., Bongiorno, A., Bischetti, M., del Olmo, A., Lanzuisi, G., Luminari, A., Middei, R., Perri, M., Ricci, C., and Vietri, G. (2022). X-ray spectroscopic survey of highly accreting agn. *A&A*, 657:A57.

Lawrence, A. (1991). The relative frequency of broad-lined and narrow-lined active galactic nuclei: Implications for unified schemes. *Monthly Notices of the Royal Astronomical Society*, 252(4):586–592.

Lawrence, A., Warren, S., Almaini, O., Edge, A., Hambly, N., Jameson, R., Lucas, P., Casali, M., Adamson, A., Dye, S., et al. (2007). The ukirt infrared deep sky survey (ukidss). *Monthly Notices of the Royal Astronomical Society*, 379(4):1599–1617.

Leighly, K. M., Halpern, J. P., Jenkins, E. B., and Casebeer, D. (2007a). The intrinsically x-ray-weak quasar phl 1811. ii. optical and uv spectra and analysis. *The Astrophysical Journal Supplement Series*, 173(1):1.

Leighly, K. M., Halpern, J. P., Jenkins, E. B., Grupe, D., Choi, J., and Prescott, K. B. (2007b). The intrinsically x-ray weak quasar phl 1811. i. x-ray observations and spectral energy distribution. *The Astrophysical Journal*, 663(1):103.

Leipski, C., Meisenheimer, K., Walter, F., Klaas, U., Dannerbauer, H., De Rosa, G., Fan, X., Haas, M., Krause, O., and Rix, H.-W. (2014). Spectral energy distributions of qsos at z> 5: common active galactic nucleus-heated dust and occasionally strong star-formation. *The Astrophysical Journal*, 785(2):154.

Lenart, A. Ł., Bargiacchi, G., Dainotti, M. G., Nagataki, S., and Capozziello, S. (2023). A bias-free cosmological analysis with quasars alleviating h 0 tension. *The Astrophysical Journal Supplement Series*, 264(2):46.

Li, S.-L., Grasha, K., Krumholz, M. R., Wisnioski, E., Sutherland, R. S., Kewley, L. J., Chen, Y.-M., and Li, Z. (2024). The mass–metallicity and fundamental metallicity relations in non-agn and agn-host galaxies. *Monthly Notices of the Royal Astronomical Society*, 529(4):4993–5010.

Liu, H., Luo, B., Brandt, W., Brotherton, M. S., Gallagher, S., Ni, Q., Shemmer, O., and Timlin, J. (2021). On the observational difference between the accretion disk–corona connections among super-and sub-eddington accreting active galactic nuclei. *The Astrophysical Journal*, 910(2):103.

Liu, H., Luo, B., Brandt, W., Gallagher, S., and Garmire, G. (2018). The frequency of intrinsic x-ray weakness among broad absorption line quasars. *The Astrophysical Journal*, 859(2):113.

Loiacono, F., Decarli, R., Mignoli, M., Farina, E. P., Bañados, E., Bosman, S., Eilers, A.-C., Schindler, J.-T., Strauss, M. A., Vestergaard, M., et al. (2024). A quasar-galaxy merger at z∼ 6.2: Black hole mass and quasar properties from the nirspec spectrum. *Astronomy & Astrophysics*, 685:A121.

López-Sánchez, A. R., Esteban, C., García-Rojas, J., Peimbert, M., and Rodríguez, M. (2007). The localized chemical pollution in ngc 5253 revisited: results from deep echelle spectrophotometry. *The Astrophysical Journal*, 656(1):168.

Luo, B., Brandt, W., Hall, P., Wu, J., Anderson, S., Garmire, G., Gibson, R., Plotkin, R., Richards, G., Schneider, D., et al. (2015). X-ray insights into the nature of phl 1811 analogs and weak emission-line quasars: Unification with a geometrically thick accretion disk? *The Astrophysical Journal*, 805(2):122.

Luridiana, V., Morisset, C., and Shaw, R. A. (2015). Pyneb: a new tool for analyzing emission lines-i. code description and validation of results. *Astronomy & Astrophysics*, 573:A42.

Lusso, E. (2020). Cosmology with quasars: predictions for erosita from a quasar hubble diagram. *Frontiers in Astronomy and Space Sciences*, 7:8.

Lusso, E., Comastri, A., Vignali, C., Zamorani, G., Brusa, M., Gilli, R., Iwasawa, K., Salvato, M., Civano, F., Elvis, M., et al. (2010). The x-ray to optical-uv luminosity ratio of x-ray selected type 1 agn in xmm-cosmos. *Astronomy & Astrophysics*, 512:A34.

Lusso, E., Fotopoulou, S., Selwood, M., Allevato, V., Calderone, G., Mancini, C., Mignoli, M., Scodeggio, M., Bisigello, L., Feltre, A., et al. (2023). Euclid preparation tbd. spectroscopy of active galactic nuclei with nisp. *arXiv preprint arXiv:2311.12096*.

Lusso, E., Hennawi, J., Comastri, A., Zamorani, G., Richards, G., Vignali, C., Treister, E., Schawinski, K., Salvato, M., and Gilli, R. (2013). The obscured fraction of active galactic nuclei in the xmm-cosmos survey: a spectral energy distribution perspective. *The Astrophysical Journal*, 777(2):86.

Lusso, E., Nardini, E., Bisogni, S., Risaliti, G., Gilli, R., Richards, G. T., Salvestrini, F., Vignali, C., Bargiacchi, G., Civano, F., et al. (2021). The most luminous blue quasars at 3.0< z< 3.3. ii. civ/x-ray emission and accretion disc physics. *arXiv preprint arXiv:2107.02806*.

Lusso, E. and Risaliti, G. (2016). The tight relation between x-ray and ultraviolet luminosity of quasars. *The Astrophysical Journal*, 819(2):154.

Lusso, E. and Risaliti, G. (2017). Quasars as standard candles-i. the physical relation between disc and coronal emission. *Astronomy & Astrophysics*, 602:A79.

Lusso, E., Risaliti, G., Nardini, E., Bargiacchi, G., Benetti, M., Bisogni, S., Capozziello, S., Civano, F., Eggleston, L., Elvis, M., et al. (2020). Quasars as standard candles-iii. validation of a new sample for cosmological studies. *Astronomy & Astrophysics*, 642:A150.

Lusso, E., Valiante, R., and Vito, F. (2022). The dawn of black holes. *arXiv preprint arXiv:2205.15349*.

Lusso, E., Worseck, G., Hennawi, J., Prochaska, J., Vignali, C., Stern, J., and O'Meara, J. (2015). The first ultraviolet quasar-stacked spectrum at z$\simeq$ 2.4 from wfc3. *Monthly Notices of the Royal Astronomical Society*, 449(4):4204–4220.

Lyu, J. and Rieke, G. H. (2017). The intrinsic far-infrared continua of type-1 quasars. *The Astrophysical Journal*, 841(2):76.

Ma, X.-C. and Wang, T.-G. (2013). The covering factor of warm dust in quasars: a view from the wide-field infrared survey explorer all-sky data release. *Monthly Notices of the Royal Astronomical Society*, 430(4):3445–3452.

Ma, Y.-S., Li, S.-J., Gu, C.-S., Jiang, J.-X., Hou, K.-L., Qin, S.-H., and Bian, W.-H. (2023). The variability of the broad-line balmer decrement for quasars from the sloan digital sky survey reverberation mapping. *Monthly Notices of the Royal Astronomical Society*, 522(4):5680–5689.

Madau, P. (1995). Radiative transfer in a clumpy universe: The colors of high-redshift galaxies. *The Astrophysical Journal*, 441:18–27.

Madau, P. and Dickinson, M. (2014). Cosmic star-formation history. *Annual Review of Astronomy and Astrophysics*, 52(1):415–486.

Madau, P. and Haardt, F. (2024). X-ray weak agns from super-eddington accretion onto infant black holes. *arXiv preprint arXiv:2410.00417*.

Magdziarz, P. and Zdziarski, A. A. (1995). Angle-dependent compton reflection of x-rays and gamma-rays. *Monthly Notices of the Royal Astronomical Society*, 273(3):837–848.

Mainzer, A., Bauer, J., Cutri, R., Grav, T., Masiero, J., Beck, R., Clarkson, P., Conrow, T., Dailey, J., Eisenhardt, P., et al. (2014). Initial performance of the neowise reactivation mission. *The Astrophysical Journal*, 792(1):30.

Maiolino, R., Juarez, Y., Mujica, R., Nagar, N., and Oliva, E. (2003). Early star formation traced by the highest redshift quasars. *The Astrophysical Journal*, 596(2):L155.

Maiolino, R., Marconi, A., Salvati, M., Risaliti, G., Severgnini, P., Oliva, E., La Franca, F., and Vanzi, L. (2001). Dust in active nuclei-i. evidence for" anomalous" properties. *Astronomy & Astrophysics*, 365(2):28–36.

Maiolino, R. and Rieke, G. (1995). Low-luminosity and obscured seyfert nuclei in nearby galaxies. *The Astrophysical Journal*, 454:95.

Maiolino, R., Risaliti, G., Signorini, M., Trefoloni, B., Juodzbalis, I., Scholtz, J., Uebler, H., D'Eugenio, F., Carniani, S., Fabian, A., et al. (2024). Jwst meets chandra: a large population of compton thick, feedback-free, and x-ray weak agn, with a sprinkle of sne. *arXiv preprint arXiv:2405.00504*.

Maiolino, R., Scholtz, J., Curtis-Lake, E., Carniani, S., Baker, W., de Graaff, A., Tacchella, S., Übler, H., d'Eugenio, F., Witstok, J., et al. (2023). Jades. the diverse population of infant black holes at 4< z< 11: merging, tiny, poor, but mighty. *arXiv preprint arXiv:2308.01230*.

Maiolino, R., Shemmer, O., Imanishi, M., Netzer, H., Oliva, E., Lutz, D., and Sturm, E. (2007). Dust covering factor, silicate emission, and star formation in luminous qsos. *Astronomy & Astrophysics*, 468(3):979–992.

Malizia, A., Bassani, L., Bazzano, A., Bird, A., Masetti, N., Panessa, F., Stephen, J., and Ubertini, P. (2012). The integral/ibis agn catalogue—i. x-ray absorption properties versus optical classification. *Monthly Notices of the Royal Astronomical Society*, 426(3):1750–1766.

Mann, H. B. and Whitney, D. R. (1947). On a test of whether one of two random variables is stochastically larger than the other. *The annals of mathematical statistics*, pages 50–60.

Marconi, A., Amiri, A., Feltre, A., Belfiore, F., Cresci, G., Curti, M., Mannucci, F., Bertola, E., Brazzini, M., Carniani, S., et al. (2024). Homerun a new approach to photoionization modelling. i–reproducing observed emission lines with percent accuracy and obtaining accurate physical properties of the ionized gas. *arXiv preprint arXiv:2401.13028*.

Marconi, A. and Hunt, L. K. (2003). The relation between black hole mass, bulge mass, and near-infrared luminosity. *The Astrophysical Journal*, 589(1):L21.

Marconi, A., Risaliti, G., Gilli, R., Hunt, L. K., Maiolino, R., and Salvati, M. (2004). Local supermassive black holes, relics of active galactic nuclei and the x-ray background. *Monthly Notices of the Royal Astronomical Society*, 351(1):169–185.

Markwardt, C. B. (2009). Non-linear Least-squares Fitting in IDL with MPFIT. In Bohlender, D. A., Durand, D., and Dowler, P., editors, *Astronomical Data Analysis Software and Systems XVIII*, volume 411 of *Astronomical Society of the Pacific Conference Series*, page 251.

Marshall, M. A., Perna, M., Willott, C. J., Maiolino, R., Scholtz, J., Übler, H., Carniani, S., Arribas, S., Lützgendorf, N., Bunker, A. J., et al. (2023). Ga-nifs: Black hole and host galaxy properties of two z≃ 6.8 quasars from the nirspec ifu. *Astronomy & Astrophysics*, 678:A191.

Marshall, M. A., Yue, M., Eilers, A.-C., Scholtz, J., Perna, M., Willott, C. J., Maiolino, R., Übler, H., Arribas, S., Bunker, A. J., et al. (2024). Ga-nifs & eiger: A merging quasar host at z= 7 with an overmassive black hole. *arXiv preprint arXiv:2410.11035*.

Martin, D. C., Fanson, J., Schiminovich, D., Morrissey, P., Friedman, P. G., Barlow, T. A., Conrow, T., Grange, R., Jelinsky, P. N., Milliard, B., et al. (2005). The galaxy evolution explorer: a space ultraviolet survey mission. *The Astrophysical Journal*, 619(1):L1.

Marziani, P., Dultzin, D., Sulentic, J. W., Del Olmo, A., Negrete, C. A., Martínez-Aldama, M. L., D'Onofrio, M., Bon, E., Bon, N., and Stirpe, G. M. (2018). A main sequence for quasars. *Frontiers in Astronomy and Space Sciences*, 5:6.

Marziani, P., Sulentic, J., Zwitter, T., Dultzin-Hacyan, D., and Calvani, M. (2001). Searching for the physical drivers of the eigenvector 1 correlation space. *The Astrophysical Journal*, 558(2):553.

Marziani, P. and Sulentic, J. W. (2014). Quasars and their emission lines as cosmological probes. *Advances in Space Research*, 54(7):1331–1340.

Mateos, S., Carrera, F. J., Alonso-Herrero, A., Hernán-Caballero, A., Barcons, X., Ramos, A. A., Watson, M. G., Blain, A., Caccianiga, A., Ballo, L., et al. (2016). X-ray absorption, nuclear infrared emission, and dust covering factors of agns: testing unification schemes. *The Astrophysical Journal*, 819(2):166.

Mathews, W. G. and Ferland, G. J. (1987). What heats the hot phase in active nuclei? *Astrophysical Journal, Part 1 (ISSN 0004-637X), vol. 323, Dec. 15, 1987, p. 456-467.*, 323:456–467.

Matthee, J., Naidu, R. P., Brammer, G., Chisholm, J., Eilers, A.-C., Goulding, A., Greene, J., Kashino, D., Labbe, I., Lilly, S. J., et al. (2024). Little red dots: An abundant population of faint active galactic nuclei at z 5 revealed by the eiger and fresco jwst surveys. *The Astrophysical Journal*, 963(2):129.

Matthews, B. M., Dix, C., Shemmer, O., Brotherton, M. S., Myers, A. D., Andruchow, I., Brandt, W., Gallagher, S., Green, R., Lira, P., et al. (2023). Gemini near infrared spectrograph–distant quasar survey: Augmented spectroscopic catalog and a prescription for correcting uv-based quasar redshifts. *arXiv preprint arXiv:2304.09964*.

Matthews, B. M., Shemmer, O., Dix, C., Brotherton, M. S., Myers, A. D., Andruchow, I., Brandt, W., Ferrero, G. A., Gallagher, S. C., Green, R., et al. (2021). Placing high-redshift quasars in perspective: A catalog of spectroscopic properties from the gemini near infrared spectrograph–distant quasar survey. *The Astrophysical Journal Supplement Series*, 252(2):15.

Mazzolari, G., Übler, H., Maiolino, R., Ji, X., Nakajima, K., Feltre, A., Scholtz, J., D'Eugenio, F., Curti, M., Mignoli, M., et al. (2024). New agn diagnostic diagrams based on the [oiii] λ 4363 auroral line. *arXiv preprint arXiv:2404.10811*.

Mazzucchelli, C., Bañados, E., Venemans, B., Decarli, R., Farina, E., Walter, F., Eilers, A.-C., Rix, H.-W., Simcoe, R., Stern, D., et al. (2017). Physical properties of 15 quasars at z$\gtrsim$ 6.5. *The Astrophysical Journal*, 849(2):91.

McLeod, K. and Rieke, G. (1995). Near-infrared imaging of cfa seyfert galaxies. *Astrophysical Journal, Part 1 (ISSN 0004-637X), vol. 441, no. 1, p. 96-112*, 441:96–112.

Mejía-Restrepo, J. E., Trakhtenbrot, B., Koss, M. J., Oh, K., Den Brok, J., Stern, D., Powell, M. C., Ricci, F., Caglar, T., Ricci, C., et al. (2022). Bass. xxv. dr2 broad-line-based black hole mass estimates and biases from obscuration. *The Astrophysical Journal Supplement Series*, 261(1):5.

Mejía-Restrepo, J. E., Trakhtenbrot, B., Lira, P., Netzer, H., and Capellupo, D. M. (2016). Active galactic nuclei at z 1.5–ii. black hole mass estimation by means of broad emission lines. *Monthly Notices of the Royal Astronomical Society*, 460(1):187–211.

Meléndez, M., Kraemer, S., Armentrout, B., Deo, R., Crenshaw, D., Schmitt, H., Mushotzky, R., Tueller, J., Markwardt, C., and Winter, L. (2008). New indicators for agn power: The correlation between [o iv] lambda 25.89 micron and hard x-ray luminosity for nearby seyfert galaxies. *arXiv preprint arXiv:0804.1147*.

Menzel, M.-L., Merloni, A., Georgakakis, A., Salvato, M., Aubourg, E., Brandt, W. N., Brusa, M., Buchner, J., Dwelly, T., Nandra, K., et al. (2016). A spectroscopic survey of x-ray-selected agns in the northern xmm-xxl field. *Monthly Notices of the Royal Astronomical Society*, 457(1):110–132.

Merloni, A. (2003). Beyond the standard accretion disc model: coupled magnetic disc–corona solutions with a physically motivated viscosity law. *Monthly Notices of the Royal Astronomical Society*, 341(3):1051–1056.

Merloni, A., Bongiorno, A., Brusa, M., Iwasawa, K., Mainieri, V., Magnelli, B., Salvato, M., Berta, S., Cappelluti, N., Comastri, A., et al. (2014). The incidence of obscuration in active galactic nuclei. *Monthly Notices of the Royal Astronomical Society*, 437(4):3550–3567.

Merloni, A., Predehl, P., Becker, W., Böhringer, H., Boller, T., Brunner, H., Brusa, M., Dennerl, K., Freyberg, M., Friedrich, P., et al. (2012). erosita science book: mapping the structure of the energetic universe. *arXiv preprint arXiv:1209.3114*.

Mignoli, M., Gilli, R., Decarli, R., Vanzella, E., Balmaverde, B., Cappelluti, N., Cassarà, L. P., Comastri, A., Cusano, F., Iwasawa, K., et al. (2020). Web of the giant: Spectroscopic confirmation of a large-scale structure around the z= 6.31 quasar sdss j1030+ 0524. *Astronomy & Astrophysics*, 642:L1.

Miley, G. K. and Miller, J. S. (1979). Relations between the emission spectra and radio structures of quasars. *Astrophysical Journal, Part 2-Letters to the Editor, vol. 228, Mar. 1, 1979, p. L55-L58. Research supported by the Martin Kellogg Fund*, 228:L55–L58.

Mizukoshi, S., Minezaki, T., Sameshima, H., Kokubo, M., Noda, H., Kawamuro, T., Yamada, S., and Horiuchi, T. (2024). Updated picture of the active galactic nuclei with dusty/dust-free gas structures and effects of the radiation pressure. *Monthly Notices of the Royal Astronomical Society*, page stae1482.

Møller, P. and Jakobsen, P. (1990). The lyman continuum opacity at high redshifts-through the lyman forest and beyond the lyman valley. *Astronomy and Astrophysics (ISSN 0004-6361), vol. 228, no. 2, Feb. 1990, p. 299-309. Research supported by Carlsbergfondet, Rumudvalget, and ESTEC.*, 228:299–309.

Mor, R., Netzer, H., and Elitzur, M. (2009). Dusty structure around type-i active galactic nuclei: clumpy torus narrow-line region and near-nucleus hot dust. *The Astrophysical Journal*, 705(1):298.

Moré, J. J. (1978). The levenberg-marquardt algorithm: implementation and theory. In *Numerical analysis*, pages 105–116. Springer.

Mortlock, D. J., Warren, S. J., Venemans, B. P., Patel, M., Hewett, P. C., McMahon, R. G., Simpson, C., Theuns, T., Gonzáles-Solares, E. A., Adamson, A., et al. (2011). A luminous quasar at a redshift of z= 7.085. *Nature*, 474(7353):616–619.

Mulchaey, J. S., Koratkar, A., Ward, M. J., Wilson, A. S., Whittle, M., Antonucci, R. R., Kinney, A. L., and Hurt, T. (1994). Multiwavelength tests of the dusty torus model for seyfert galaxies. *Astrophysical Journal, Part 1 (ISSN 0004-637X), vol. 436, no. 2, p. 586-598*, 436:586–598.

Nagao, T., Marconi, A., and Maiolino, R. (2006). The evolution of the broad-line region among sdss quasars. *Astronomy & Astrophysics*, 447(1):157–172.

Nandra, K., Laird, E., Aird, J., Salvato, M., Georgakakis, A., Barro, G., Perez-Gonzalez, P., Barmby, P., Chary, R.-R., Coil, A., et al. (2015). Aegis-x: Deep chandra imaging of the central groth strip. *The Astrophysical Journal Supplement Series*, 220(1):10.

Nanni, R., Vignali, C., Gilli, R., Moretti, A., and Brandt, W. (2017). The x-ray properties of z˜ 6 luminous quasars. *Astronomy & Astrophysics*, 603:A128.

Nardini, E., Lusso, E., and Bisogni, S. (2019a). Towards an informed quest for accretion disc winds in quasars: the intriguing case of ton 28. *Monthly Notices of the Royal Astronomical Society: Letters*, 482(1):L134–L138.

Nardini, E., Lusso, E., Risaliti, G., Bisogni, S., Civano, F., Elvis, M., Fabbiano, G., Gilli, R., Marconi, A., Salvestrini, F., et al. (2019b). The most luminous blue quasars at 3.0< z< 3.3-i. a tale of two x-ray populations. *Astronomy & Astrophysics*, 632:A109.

Nardini, E., Reeves, J., Gofford, J., Harrison, F., Risaliti, G., Braito, V., Costa, M., Matzeu, G., Walton, D., Behar, E., et al. (2015). Black hole feedback in the luminous quasar pds 456. *Science*, 347(6224):860–863.

Nenkova, M., Sirocky, M. M., Ivezić, Ž., and Elitzur, M. (2008a). Agn dusty tori. i. handling of clumpy media. *The Astrophysical Journal*, 685(1):147.

Nenkova, M., Sirocky, M. M., Ivezić, Ž., and Elitzur, M. (2008b). Agn dusty tori. i. handling of clumpy media. *The Astrophysical Journal*, 685(1):147.

Nenkova, M., Sirocky, M. M., Nikutta, R., Ivezić, Ž., and Elitzur, M. (2008c). Agn dusty tori. ii. observational implications of clumpiness. *The Astrophysical Journal*, 685(1):160.

Netzer, H. (1990). AGN emission lines. In Blandford, R. D., Netzer, H., Woltjer, L., Courvoisier, T. J. L., and Mayor, M., editors, *Active Galactic Nuclei*, pages 57–160.

Netzer, H. (2009a). Accretion and star formation rates in low-redshift type ii active galactic nuclei. *Monthly Notices of the Royal Astronomical Society*, 399(4):1907–1920.

Netzer, H. (2009b). Radiation pressure force and black hole mass determination in low-redshift type-i and type-ii active galactic nuclei. *The Astrophysical Journal*, 695(1):793.

Netzer, H. (2015). Revisiting the unified model of active galactic nuclei. *Annual Review of Astronomy and Astrophysics*, 53:365–408.

Netzer, H. and Wills, B. J. (1983). Broad emission features in qsos and active galactic nuclei. i-new calculations of fe ii line strengths. *Astrophysical Journal, Part 1 (ISSN 0004-637X), vol. 275, Dec. 15, 1983, p. 445-460. Sponsorship: United States-Israel Binational Science Foundation.*, 275:445–460.

Neugebauer, G., Oke, J., Becklin, E., and Matthews, K. (1979). Absolute spectral energy distribution of quasi-stellar objects from 0.3 to 10 microns. *Astrophysical Journal, Part 1, vol. 230, May 15, 1979, p. 79-94.*, 230:79–94.

Ni, Q., Brandt, W., Yi, W., Luo, B., Timlin, J., Hall, P., Liu, H., Plotkin, R., Shemmer, O., Vito, F., et al. (2020). An extreme x-ray variability event of a weak-line quasar. *The Astrophysical Journal Letters*, 889(2):L37.

Nicastro, F. (2000). Broad emission line regions in active galactic nuclei: the link with the accretion power. *The Astrophysical Journal*, 530(2):L65.

Ohsuga, K. and Mineshige, S. (2011). Global structure of three distinct accretion flows and outflows around black holes from two-dimensional radiation-magnetohydrodynamic simulations. *The Astrophysical Journal*, 736(1):2.

Onoue, M., Banados, E., Mazzucchelli, C., Venemans, B. P., Schindler, J.-T., Walter, F., Hennawi, J. F., Andika, I. T., Davies, F. B., Decarli, R., et al. (2020). No redshift evolution in the broad-line-region metallicity up to z= 7.54: Deep near-infrared spectroscopy of ulas j1342+ 0928. *The Astrophysical Journal*, 898(2):105.

Onoue, M., Inayoshi, K., Ding, X., Li, W., Li, Z., Molina, J., Inoue, A. K., Jiang, L., and Ho, L. C. (2023). A candidate for the least-massive black hole in the first 1.1 billion years of the universe. *The Astrophysical Journal Letters*, 942(1):L17.

Osterbrock, D. E. (1977). Spectrophotometry of seyfert 1 galaxies. *Astrophysical Journal, Part 1, vol. 215, Aug. 1, 1977, p. 733-745.*, 215:733–745.

Osterbrock, D. E. and Ferland, G. J. (2006). *Astrophysics Of Gas Nebulae and Active Galactic Nuclei.* University science books.

Overzier, R. A. (2022). Conditions for direct black hole seed collapse near a radio-loud quasar 1 gyr after the big bang. *The Astrophysical Journal*, 926(2):114.

Pacucci, F. and Narayan, R. (2024). Mildly super-eddington accretion onto slowly-spinning black holes explains the x-ray weakness of the little red dots. *arXiv preprint arXiv:2407.15915.*

Panda, S., Czerny, B., Adhikari, T. P., Hryniewicz, K., Wildy, C., Kuraszkiewicz, J., and Śniegowska, M. (2018). Modeling of the quasar main sequence in the optical plane. *The Astrophysical Journal*, 866(2):115.

Panda, S., Czerny, B., Done, C., and Kubota, A. (2019). Cloudy view of the warm corona. *The Astrophysical Journal*, 875(2):133.

Panessa, F., Bassani, L., Cappi, M., Dadina, M., Barcons, X., Carrera, F. J., Ho, L., and Iwasawa, K. (2006). On the x-ray, optical emission line and black hole mass properties of local seyfert galaxies. *Astronomy & Astrophysics*, 455(1):173–185.

Pâris, I., Petitjean, P., Aubourg, É., Myers, A. D., Streblyanska, A., Lyke, B. W., Anderson, S. F., Armengaud, É., Bautista, J., Blanton, M. R., et al. (2018). The sloan digital sky survey quasar catalog: fourteenth data release. *Astronomy & Astrophysics*, 613:A51.

Parlanti, E., Carniani, S., Übler, H., Venturi, G., Circosta, C., D'Eugenio, F., Arribas, S., Bunker, A. J., Charlot, S., Lützgendorf, N., et al. (2024). Ga-nifs: Early-stage feedback in a heavily obscured active galactic nucleus at z= 4.76. *Astronomy & Astrophysics*, 684:A24.

Peca, A., Cappelluti, N., Urry, C. M., LaMassa, S., Marchesi, S., Ananna, T. T., Baloković, M., Sanders, D., Auge, C., Treister, E., et al. (2023). On the cosmic evolution of agn obscuration and the x-ray luminosity function: Xmm-newton and chandra spectral analysis of the 31.3 deg2 stripe 82x. *The Astrophysical Journal*, 943(2):162.

Perna, M., Arribas, S., Marshall, M., D'Eugenio, F., Übler, H., Bunker, A., Charlot, S., Carniani, S., Jakobsen, P., Maiolino, R., et al. (2023). The ultradense, interacting environment of a dual agn at z ∼ 3.3 revealed by jwst/nirspec ifs. *arXiv preprint arXiv:2304.06756.*

Peterson, B. M., Ferrarese, L., Gilbert, K., Kaspi, S., Malkan, M., Maoz, D., Merritt, D., Netzer, H., Onken, C., Pogge, R., et al. (2004). Central masses and broad-line region sizes of active galactic nuclei. ii. a homogeneous analysis of a large reverberation-mapping database. *The Astrophysical Journal*, 613(2):682.

Pezzulli, E., Valiante, R., and Schneider, R. (2016). Super-eddington growth of the first black holes. *Monthly Notices of the Royal Astronomical Society*, 458(3):3047–3059.

Piconcelli, E., Jimenez-Bailón, E., Guainazzi, M., Schartel, N., Rodríguez-Pascual, P., and Santos-Lleó, M. (2005). The xmm-newton view of pg quasars-i. x-ray continuum and absorption. *Astronomy & Astrophysics*, 432(1):15–30.

Pier, E. A. and Krolik, J. H. (1992). Infrared spectra of obscuring dust tori around active galactic nuclei. i-calculational method and basic trends. *Astrophysical Journal, Part 1 (ISSN 0004-637X), vol. 401, no. 1, p. 99-109.*, 401:99–109.

Pilyugin, L., Mattsson, L., Vílchez, J., and Cedrés, B. (2009). On the electron temperatures in high-metallicity h ii regions. *Monthly Notices of the Royal Astronomical Society*, 398(1):485–496.

Podigachoski, P., Rocca-Volmerange, B., Barthel, P., Drouart, G., and Fioc, M. (2016). Starbursts and dusty tori in distant 3cr radio galaxies. *Monthly Notices of the Royal Astronomical Society*, 462(4):4183–4196.

Prevot, M., Lequeux, J., Maurice, E., Prevot, L., and Rocca-Volmerange, B. (1984). The typical interstellar extinction in the small magellanic cloud. *Astronomy and Astrophysics (ISSN 0004-6361), vol. 132, no. 2, March 1984, p. 389-392.*, 132:389–392.

Prochaska, J. X., Worseck, G., and O'Meara, J. M. (2009). A direct measurement of the intergalactic medium opacity to h i ionizing photons. *The Astrophysical Journal*, 705(2):L113.

Proga, D. (2003). Numerical simulations of mass outflows driven from accretion disks by radiation and magnetic forces. *The Astrophysical Journal*, 585(1):406.

Proga, D. (2005). How much x-ray and uv radiation processes are coupled in accretion disks? the active galactic nucleus case. *The Astrophysical Journal*, 630(1):L9.

Pu, X., Luo, B., Brandt, W., Timlin, J. D., Liu, H., Ni, Q., and Wu, J. (2020). On the fraction of x-ray-weak quasars from the sloan digital sky survey. *The Astrophysical Journal*, 900(2):141.

Rakshit, S., Stalin, C., and Kotilainen, J. (2020). Spectral properties of quasars from sloan digital sky survey data release 14: the catalog. *The Astrophysical Journal Supplement Series*, 249(1):17.

Rałowski, M., Hryniewicz, K., Pollo, A., and Stawarz, Ł. (2023). Covering factor in agns: evolution versus selection. *arXiv preprint arXiv:2311.00072.*

Reddy, N. A., Sanders, R. L., Shapley, A. E., Topping, M. W., Kriek, M., Coil, A. L., Mobasher, B., Siana, B., and Rezaee, S. (2023). The impact of star-formation-rate surface density on the electron density and ionization parameter of high-redshift galaxies. *The Astrophysical Journal*, 951(1):56.

Reichard, T. A., Richards, G. T., Hall, P. B., Schneider, D. P., Berk, D. E. V., Fan, X., York, D. G., Knapp, G., and Brinkmann, J. (2003). Continuum and emission-line properties of broad absorption line quasars. *The Astronomical Journal*, 126(6):2594.

Ricci, C., Ichikawa, K., Stalevski, M., Kawamuro, T., Yamada, S., Ueda, Y., Mushotzky, R., Privon, G., Koss, M., Trakhtenbrot, B., et al. (2023). Bass. xlii. the relation between the covering factor of dusty gas and the eddington ratio in nearby active galactic nuclei. *The Astrophysical Journal*, 959(1):27.

Ricci, C., Kara, E., Loewenstein, M., Trakhtenbrot, B., Arcavi, I., Remillard, R., Fabian, A., Gendreau, K., Arzoumanian, Z., Li, R., et al. (2020). The destruction and recreation of the x-ray corona in a changing-look active galactic nucleus. *The Astrophysical Journal Letters*, 898(1):L1.

Ricci, C. and Paltani, S. (2023). Ray-tracing simulations and spectral models of x-ray radiation in dusty media. *The Astrophysical Journal*, 945(1):55.

Ricci, C., Trakhtenbrot, B., Koss, M. J., Ueda, Y., Del Vecchio, I., Treister, E., Schawinski, K., Paltani, S., Oh, K., Lamperti, I., et al. (2017). Bat agn spectroscopic survey. v. x-ray properties of the swift/bat 70-month agn catalog. *The Astrophysical Journal Supplement Series*, 233(2):17.

Ricci, C., Ueda, Y., Paltani, S., Ichikawa, K., Gandhi, P., and Awaki, H. (2014). Iron kα emission in type-i and type-ii active galactic nuclei. *Monthly Notices of the Royal Astronomical Society*, 441(4):3622–3633.

Ricci, F., Treister, E., Bauer, F. E., Mejía-Restrepo, J. E., Koss, M. J., Den Brok, J. S., Baloković, M., Bär, R., Bessiere, P., Caglar, T., et al. (2022). Bass. xxix. the near-infrared view of the broad-line region (blr): the effects of obscuration in blr characterization. *The Astrophysical Journal Supplement Series*, 261(1):8.

Richards, G. T., Berk, D. E. V., Reichard, T. A., Hall, P. B., Schneider, D. P., SubbaRao, M., Thakar, A. R., and York, D. G. (2002a). Broad emission-line shifts in quasars: an orientation measure for radio-quiet quasars? *The Astronomical Journal*, 124(1):1.

Richards, G. T., Fan, X., Newberg, H. J., Strauss, M. A., Berk, D. E. V., Schneider, D. P., Yanny, B., Boucher, A., Burles, S., Frieman, J. A., et al. (2002b). Spectroscopic target selection in the sloan digital sky survey: The quasar sample. *arXiv preprint astro-ph/0202251.*

Richards, G. T., Fan, X., Schneider, D. P., Berk, D. E. V., Strauss, M. A., York, D. G., Anderson Jr, J. E., Anderson, S. F., Annis, J., Bahcall, N. A., et al. (2001). Colors of 2625 quasars at 0< z< 5 measured in the sloan digital sky survey photometric system. *The Astronomical Journal*, 121(5):2308.

Richards, G. T., Kruczek, N. E., Gallagher, S., Hall, P. B., Hewett, P. C., Leighly, K. M., Deo, R. P., Kratzer, R. M., and Shen, Y. (2011). Unification of luminous type 1 quasars through c iv emission. *The Astronomical Journal*, 141(5):167.

Richards, G. T., Lacy, M., Storrie-Lombardi, L. J., Hall, P. B., Gallagher, S., Hines, D. C., Fan, X., Papovich, C., Berk, D. E. V., Trammell, G. B., et al. (2006). Spectral energy distributions and multiwavelength selection of type 1 quasars. *The Astrophysical Journal Supplement Series*, 166(2):470.

Riess, A. G., Macri, L. M., Hoffmann, S. L., Scolnic, D., Casertano, S., Filippenko, A. V., Tucker, B. E., Reid, M. J., Jones, D. O., Silverman, J. M., et al. (2016). A 2.4% determination of the local value of the hubble constant. *The Astrophysical Journal*, 826(1):56.

Riffel, R. A., Dors, O. L., Krabbe, A. C., and Esteban, C. (2021). Electron temperature fluctuations in seyfert galaxies. *Monthly Notices of the Royal Astronomical Society: Letters*, 506(1):L11–L15.

Risaliti, G., Elvis, M., and Nicastro, F. (2002). Ubiquitous variability of x-ray-absorbing column densities in seyfert 2 galaxies. *The Astrophysical Journal*, 571(1):234.

Risaliti, G. and Lusso, E. (2015). A hubble diagram for quasars. *The Astrophysical Journal*, 815(1):33.

Risaliti, G. and Lusso, E. (2019). Cosmological constraints from the hubble diagram of quasars at high redshifts. *Nature Astronomy*, 3(3):272–277.

Risaliti, G., Salvati, M., and Marconi, A. (2011). [o iii] equivalent width and orientation effects in quasars. *Monthly Notices of the Royal Astronomical Society*, 411(4):2223–2229.

Risaliti, G., Young, M., and Elvis, M. (2009). The sloan digital sky survey/xmm-newton quasar survey: Correlation between x-ray spectral slope and eddington ratio. *The Astrophysical Journal*, 700(1):L6.

Rivera, A. B., Richards, G. T., Gallagher, S. C., McCaffrey, T. V., Rankine, A. L., Hewett, P. C., and Shemmer, O. (2022). Exploring changes in quasar spectral energy distributions across c iv parameter space. *The Astrophysical Journal*, 931(2):154.

Robitaille, T. P., Tollerud, E. J., Greenfield, P., Droettboom, M., Bray, E., Aldcroft, T., Davis, M., Ginsburg, A., Price-Whelan, A. M., Kerzendorf, W. E., et al. (2013). Astropy: A community python package for astronomy. *Astronomy & Astrophysics*, 558:A33.

Saccheo, I., Bongiorno, A., Piconcelli, E., Testa, V., Bischetti, M., Bisogni, S., Bruni, G., Cresci, G., Feruglio, C., Fiore, F., et al. (2023). The wissh quasars project: Xi. the mean spectral energy distribution and bolometric corrections of the most luminous quasars. *Astronomy and Astrophysics*, 671:A34.

Sacchi, A., Risaliti, G., Signorini, M., Lusso, E., Nardini, E., Bargiacchi, G., Bisogni, S., Civano, F., Elvis, M., Fabbiano, G., et al. (2022). Quasars as high-redshift standard candles. *Astronomy & Astrophysics*, 663:L7.

Sądowski, A., Narayan, R., McKinney, J. C., and Tchekhovskoy, A. (2014). Numerical simulations of super-critical black hole accretion flows in general relativity. *Monthly Notices of the Royal Astronomical Society*, 439(1):503–520.

Salvestrini, F., Risaliti, G., Bisogni, S., Lusso, E., and Vignali, C. (2019). Quasars as standard candles ii-the non-linear relation between uv and x-ray emission at high redshifts. *Astronomy & Astrophysics*, 631:A120.

Sameshima, H., Kawara, K., Matsuoka, Y., Oyabu, S., Asami, N., and Ienaka, N. (2011). Implications from the optical to ultraviolet flux ratio of fe ii emission in quasars. *Monthly Notices of the Royal Astronomical Society*, 410(2):1018–1026.

Sameshima, H., Maza, J., Matsuoka, Y., Oyabu, S., Kawara, K., Yoshii, Y., Asami, N., Ienaka, N., and Tsuzuki, Y. (2009). Ultraviolet fe ii emission in z 2 quasars. *Monthly Notices of the Royal Astronomical Society*, 395(2):1087–1091.

Sameshima, H., Yoshii, Y., and Kawara, K. (2017). Chemical evolution of the universe at 0.7< z< 1.6 derived from abundance diagnostics of the broad-line region of quasars. *The Astrophysical Journal*, 834(2):203.

Sameshima, H., Yoshii, Y., Matsunaga, N., Kobayashi, N., Ikeda, Y., Kondo, S., Hamano, S., Mizumoto, M., Arai, A., Yasui, C., et al. (2020). Mg ii and fe ii fluxes of luminous quasars at z 2.7 and the evaluation of the baldwin effect in the flux-to-abundance conversion method for quasars. *The Astrophysical Journal*, 904(2):162.

Sanders, D. B., Salvato, M., Aussel, H., Ilbert, O., Scoville, N., Surace, J. A., Frayer, D. T., Sheth, K., Helou, G., Brooke, T., et al. (2007). S-cosmos: The spitzer legacy survey of the hubble space telescope acs 2 deg2 cosmos field i: survey strategy and first analysis. *The Astrophysical Journal Supplement Series*, 172(1):86.

Sarkar, A., Ferland, G., Chatzikos, M., Guzmán, F., Van Hoof, P., Smyth, R., Ramsbottom, C., Keenan, F., and Ballance, C. (2021). Improved fe ii emission-line models for agns using new atomic data sets. *The Astrophysical Journal*, 907(1):12.

Sazonov, S., Churazov, E., and Krivonos, R. (2015). Does the obscured agn fraction really depend on luminosity? *Monthly Notices of the Royal Astronomical Society*, 454(2):1202–1220.

Scannapieco, E., Silk, J., and Bouwens, R. (2005). Agn feedback causes downsizing. *The Astrophysical Journal*, 635(1):L13.

Schaye, J., Crain, R. A., Bower, R. G., Furlong, M., Schaller, M., Theuns, T., Dalla Vecchia, C., Frenk, C. S., McCarthy, I., Helly, J. C., et al. (2015). The eagle project: simulating the evolution and assembly of galaxies and their environments. *Monthly Notices of the Royal Astronomical Society*, 446(1):521–554.

Schlafly, E. F. and Finkbeiner, D. P. (2011). Measuring reddening with sloan digital sky survey stellar spectra and recalibrating sfd. *The Astrophysical Journal*, 737(2):103.

Schlegel, D. J., Finkbeiner, D. P., and Davis, M. (1998). Maps of dust infrared emission for use in estimation of reddening and cosmic microwave background radiation foregrounds. *The Astrophysical Journal*, 500(2):525.

Schneider, R., Valiante, R., Trinca, A., Graziani, L., Volonteri, M., and Maiolino, R. (2023). Are we surprised to find smbhs with jwst at z≥ 9? *Monthly Notices of the Royal Astronomical Society*, 526(3):3250–3261.

Scholtz, J., Maiolino, R., D'Eugenio, F., Curtis-Lake, E., Carniani, S., Charlot, S., Curti, M., Silcock, M. S., Arribas, S., Baker, W., et al. (2023). Jades: A large population of obscured, narrow line agn at high redshift. *arXiv preprint arXiv:2311.18731*.

Scodeggio, M., Franzetti, P., Garilli, B., Zanichelli, A., Paltani, S., Maccagni, D., Bottini, D., Le Brun, V., Contini, T., Scaramella, R., et al. (2005). The vvds data-reduction pipeline: Introducing vipgi, the vimos interactive pipeline and graphical interface. *Publications of the Astronomical Society of the Pacific*, 117(837):1284.

Scolnic, D. M., Jones, D., Rest, A., Pan, Y., Chornock, R., Foley, R., Huber, M., Kessler, R., Narayan, G., Riess, A., et al. (2018). The complete light-curve sample of spectroscopically confirmed sne ia from pan-starrs1 and cosmological constraints from the combined pantheon sample. *The Astrophysical Journal*, 859(2):101.

Scoville, N., Lee, N., Bout, P. V., Diaz-Santos, T., Sanders, D., Darvish, B., Bongiorno, A., Casey, C., Murchikova, L., Koda, J., et al. (2017). Evolution of interstellar medium, star formation, and accretion at high redshift. *The Astrophysical Journal*, 837(2):150.

Selsing, J., Fynbo, J. P., Christensen, L., and Krogager, J.-K. (2016). An x-shooter composite of bright 1< z< 2 quasars from uv to infrared. *Astronomy & Astrophysics*, 585:A87.

Shakura, N. I. and Sunyaev, R. A. (1973). Black holes in binary systems. observational appearance. *Astronomy and Astrophysics*, 24:337–355.

Shankar, F., Weinberg, D. H., and Miralda-Escudé, J. (2008). Self-consistent models of the agn and black hole populations: duty cycles, accretion rates, and the mean radiative efficiency. *The Astrophysical Journal*, 690(1):20.

Shastri, P., Wilkes, B. J., Elvis, M., and McDowell, J. (1993). Quasar x-ray spectra revisited. *Astrophysical Journal, Part 1 (ISSN 0004-637X), vol. 410, no. 1, p. 29-38.*, 410:29–38.

Shemmer, O., Brandt, W., Netzer, H., Maiolino, R., and Kaspi, S. (2008). The hard x-ray spectrum as a probe for black hole growth in radio-quiet active galactic nuclei. *The Astrophysical Journal*, 682(1):81.

Shen, Y. (2013). The mass of quasars. *arXiv preprint arXiv:1302.2643*.

Shen, Y. (2016). Rest-frame optical properties of luminous 1.5< z< 3.5 quasars: the hβ-[o iii] region. *The Astrophysical Journal*, 817(1):55.

Shen, Y. and Ho, L. C. (2014). The diversity of quasars unified by accretion and orientation. *Nature*, 513(7517):210–213.

Shen, Y. and Liu, X. (2012). Comparing single-epoch virial black hole mass estimators for luminous quasars. *The Astrophysical Journal*, 753(2):125.

Shen, Y., Richards, G. T., Strauss, M. A., Hall, P. B., Schneider, D. P., Snedden, S., Bizyaev, D., Brewington, H., Malanushenko, V., Malanushenko, E., et al. (2011). A catalog of quasar properties from sloan digital sky survey data release 7. *The Astrophysical Journal Supplement Series*, 194(2):45.

Shen, Y., Wu, J., Jiang, L., Bañados, E., Fan, X., Ho, L. C., Riechers, D. A., Strauss, M. A., Venemans, B., Vestergaard, M., et al. (2019). Gemini gnirs near-infrared spectroscopy of 50 quasars at z$\gtrsim$ 5.7. *The Astrophysical Journal*, 873(1):35.

Shi, Y., Rieke, G., Ogle, P., Su, K., and Balog, Z. (2014). Infrared spectra and photometry of complete samples of palomar–green and two micron all sky survey quasars. *The Astrophysical Journal Supplement Series*, 214(2):23.

Shields, G. A., Ludwig, R. R., and Salviander, S. (2010). Fe ii emission in active galactic nuclei: the role of total and gas-phase iron abundance. *The Astrophysical Journal*, 721(2):1835.

Shin, J., Nagao, T., Woo, J.-H., and Le, H. A. N. (2019). The fe ii/mg ii flux ratio of low-luminosity quasars at z 3. *The Astrophysical Journal*, 874(1):22.

Shin, J., Woo, J.-H., Nagao, T., Kim, M., and Bahk, H. (2021). Strong correlation between fe ii/mg ii ratio and eddington ratio of type 1 active galactic nuclei. *The Astrophysical Journal*, 917(2):107.

Shull, J. M., Stevans, M., and Danforth, C. W. (2012). Hst-cos observations of agns. i. ultraviolet composite spectra of the ionizing continuum and emission lines. *The Astrophysical Journal*, 752(2):162.

Signorini, M., Marchesi, S., Gilli, R., Brusa, M., Comastri, A., D'Amato, Q., Iwasawa, K., Lanzuisi, G., Mazzolari, G., Mignoli, M., et al. (2023a). X-ray properties and obscured fraction of agn in the j1030 chandra field. *Astronomy & Astrophysics*, 676:A49.

Signorini, M., Risaliti, G., Lusso, E., Nardini, E., Bargiacchi, G., Sacchi, A., and Trefoloni, B. (2023b). Quasars as standard candles-iv. analysis of the x-ray and uv indicators of the disc-corona relation. *Astronomy & Astrophysics*, 676:A143.

Signorini, M., Risaliti, G., Lusso, E., Nardini, E., Bargiacchi, G., Sacchi, A., and Trefoloni, B. (2024). Quasars as standard candles-v. accounting for the dispersion in the lx–luv relation down to ≤ 0.06 dex. *Astronomy & Astrophysics*, 687:A32.

Sigut, T. and Pradhan, A. K. (2003). Predicted fe ii emission-line strengths from active galactic nuclei. *The Astrophysical Journal Supplement Series*, 145(1):15.

Silk, J. and Rees, M. J. (1998). Quasars and galaxy formation. *arXiv preprint astro-ph/9801013*.

Simpson, C. (2005). The luminosity dependence of the type 1 active galactic nucleus fraction. *Monthly Notices of the Royal Astronomical Society*, 360(2):565–572.

Skidmore, W. et al. (2015). Thirty meter telescope detailed science case: 2015. *Research in Astronomy and Astrophysics*, 15(12):1945.

Skrutskie, M., Cutri, R., Stiening, R., Weinberg, M., Schneider, S., Carpenter, J., Beichman, C., Capps, R., Chester, T., Elias, J., et al. (2006). The two micron all sky survey (2mass). *The Astronomical Journal*, 131(2):1163.

Smith, H. E. (1975). Spectrophotometric observations of ionized hydrogen regions in nearby spiral and irregular galaxies. *Astrophysical Journal, vol. 199, Aug. 1, 1975, pt. 1, p. 591-610. Research supported by the University of California and NSF.*, 199:591–610.

Smyth, R., Ramsbottom, C., Keenan, F., Ferland, G., and Ballance, C. (2019). Towards converged electron-impact excitation calculations of low-lying transitions in fe ii. *Monthly Notices of the Royal Astronomical Society*, 483(1):654–663.

Sołtan, A. (1982). Masses of quasars. *Monthly Notices of the Royal Astronomical Society*, 200(1):115–122.

Springel, V., Di Matteo, T., and Hernquist, L. (2005). Modelling feedback from stars and black holes in galaxy mergers. *Monthly Notices of the Royal Astronomical Society*, 361(3):776–794.

Stalevski, M., Ricci, C., Ueda, Y., Lira, P., Fritz, J., and Baes, M. (2016). The dust covering factor in active galactic nuclei. *Monthly Notices of the Royal Astronomical Society*, 458(3):2288–2302.

Stepney, M., Banerji, M., Hewett, P. C., Temple, M. J., Rankine, A. L., Matthews, J. H., and Richards, G. T. (2023). No redshift evolution in the rest-frame ultraviolet emission line properties of quasars from z= 1.5 to z= 4.0. *Monthly Notices of the Royal Astronomical Society*, 524(4):5497–5513.

Stevans, M. L., Shull, J. M., Danforth, C. W., and Tilton, E. M. (2014). Hst-cos observations of agns. ii. extended survey of ultraviolet composite spectra from 159 active galactic nuclei. *The Astrophysical Journal*, 794(1):75.

Storchi-Bergmann, T., Schmitt, H. R., Calzetti, D., and Kinney, A. L. (1998). Chemical abundance calibrations for the narrow-line region of active galaxies. *The Astronomical Journal*, 115(3):909.

Sturm, E., González-Alfonso, E., Veilleux, S., Fischer, J., Graciá-Carpio, J., Hailey-Dunsheath, S., Contursi, A., Poglitsch, A., Sternberg, A., Davies, R., et al. (2011). Massive molecular outflows and negative feedback in ulirgs observed by herschel-pacs. *The Astrophysical Journal Letters*, 733(1):L16.

Sulentic, J., Marziani, P., and Dultzin-Hacyan, D. (2000a). Phenomenology of broad emission lines in active galactic nuclei. *Annual Review of Astronomy and Astrophysics*, 38(1):521–571.

Sulentic, J., Zwitter, T., Marziani, P., and Dultzin-Hacyan, D. (2000b). Eigenvector 1: an optimal correlation space for active galactic nuclei. *The Astrophysical Journal*, 536(1):L5.

Sun, J. and Shen, Y. (2015). Dissecting the quasar main sequence: insight from host galaxy properties. *The Astrophysical Journal Letters*, 804(1):L15.

Tanaka, T. and Haiman, Z. (2009). The assembly of supermassive black holes at high redshifts. *The Astrophysical Journal*, 696(2):1798.

Tananbaum, H., Avni, Y., Branduardi, G., Elvis, M., Fabbiano, G., Feigelson, E., Giacconi, R., Henry, J., Pye, J., Soltan, A., et al. (1979). X-ray studies of quasars with the einstein observatory. *Astrophysical Journal, Part 2-Letters to the Editor, vol. 234, Nov. 15, 1979, p. L9-L13. Research supported by the Science Research Council and US-Israel Binational Science Foundation.*, 234:L9–L13.

Tayal, S. and Zatsarinny, O. (2018). Electron-impact excitation of forbidden and allowed transitions in fe ii. *Physical Review A*, 98(1):012706.

Taylor, A. J., Finkelstein, S. L., Kocevski, D. D., Jeon, J., Bromm, V., Amorin, R. O., Haro, P. A., Backhaus, B. E., Bagley, M. B., Bañados, E., et al. (2024). Broad-line agn at $3.5 < z < 6$: The black hole mass function and a connection with little red dots. *arXiv preprint arXiv:2409.06772*.

Telfer, R. C., Zheng, W., Kriss, G. A., and Davidsen, A. F. (2002). The rest-frame extreme-ultraviolet spectral properties of quasi-stellar objects. *The Astrophysical Journal*, 565(2):773.

Temple, M. J., Ferland, G. J., Rankine, A. L., Chatzikos, M., and Hewett, P. C. (2021). High-ionization emission-line ratios from quasar broad-line regions: metallicity or density? *Monthly Notices of the Royal Astronomical Society*, 505(3):3247–3259.

Temple, M. J., Ferland, G. J., Rankine, A. L., Hewett, P. C., Badnell, N., Ballance, C. P., Del Zanna, G., and Dufresne, R. P. (2020). Fe iii emission in quasars: evidence for a dense turbulent medium. *Monthly Notices of the Royal Astronomical Society*, 496(3):2565–2576.

Temple, M. J., Matthews, J. H., Hewett, P. C., Rankine, A. L., Richards, G. T., Banerji, M., Ferland, G. J., Knigge, C., and Stepney, M. (2023). Testing AGN outflow and accretion models with CIV and HeII emission line demographics in z=2 quasars. *arXiv e-prints*, page arXiv:2301.02675.

Thomas, A. D., Kewley, L. J., Dopita, M. A., Groves, B. A., Hopkins, A. M., and Sutherland, R. S. (2019). The mass–metallicity relation of local active galaxies. *The Astrophysical Journal*, 874(1):100.

Thompson, K. L., Hill, G. J., and Elston, R. (1999). Lack of iron abundance evolution in high-redshift qsos. *The Astrophysical Journal*, 515(2):487.

Thuan, T. X., Bauer, F. E., Papaderos, P., and Izotov, Y. I. (2004). Chandra observations of the three most metal deficient blue compact dwarf galaxies known in the local universe, sbs 0335–052, sbs 0335–052w, and i zw 18. *The Astrophysical Journal*, 606(1):213.

Tibshirani, R. J. and Efron, B. (1993). An introduction to the bootstrap. *Monographs on statistics and applied probability*, 57(1):1–436.

Timlin III, J. D., Brandt, W., Ni, Q., Luo, B., Pu, X., Schneider, D., Vivek, M., and Yi, W. (2020). The correlations between optical/uv broad lines and x-ray emission for a large sample of quasars. *Monthly Notices of the Royal Astronomical Society*, 492(1):719–741.

Toba, Y., Oyabu, S., Matsuhara, H., Malkan, M., Gandhi, P., Nakagawa, T., Isobe, N., Shirahata, M., Oi, N., Ohyama, Y., et al. (2014). Luminosity and redshift dependence of the covering factor of active galactic nuclei viewed with wise and sloan digital sky survey. *The Astrophysical Journal*, 788(1):45.

Toba, Y., Ueda, Y., Gandhi, P., Ricci, C., Burgarella, D., Buat, V., Nagao, T., Oyabu, S., Matsuhara, H., and Hsieh, B.-C. (2021). How does the polar dust affect the correlation between dust covering factor and eddington ratio in type 1 quasars selected from the sloan digital sky survey data release 16? *The Astrophysical Journal*, 912(2):91.

Tombesi, F., Meléndez, M., Veilleux, S., Reeves, J., González-Alfonso, E., and Reynolds, C. (2015). Wind from the black-hole accretion disk driving a molecular outflow in an active galaxy. *Nature*, 519(7544):436–438.

Trakhtenbrot, B., Ricci, C., Koss, M. J., Schawinski, K., Mushotzky, R., Ueda, Y., Veilleux, S., Lamperti, I., Oh, K., Treister, E., et al. (2017). Bat agn spectroscopic survey (bass)–vi. the γx–l/l edd relation. *Monthly Notices of the Royal Astronomical Society*, 470(1):800–814.

Trefoloni, B. (2023). Searching for outflows in x-ray weak quasars. *arXiv preprint arXiv:2308.01345.*

Trefoloni, B., Gilli, R., Lusso, E., Marconi, A., Mazzolari, G., Nardini, E., Risaliti, G., and Signorini, M. (2024a). The near-infrared sed of blue quasars: what drives the evolution of the dusty torus? *arXiv preprint arXiv:2410.10941.*

Trefoloni, B., Ji, X., Maiolino, R., D'Eugenio, F., Übler, H., Scholtz, J., Marconi, A., Marconcini, C., and Mazzolari, G. (2024b). The missing feii bump in faint jwst agn: possible evidence for metal-poor broad-line regions at early cosmic times. *arXiv preprint arXiv:2410.21867.*

Trefoloni, B., Lusso, E., Nardini, E., Risaliti, G., Bargiacchi, G., Bisogni, S., Civano, F. M., Elvis, M., Fabbiano, G., Gilli, R., et al. (2023). The most luminous blue quasars at 3.0< z< 3.3-iii. lbt spectra and accretion parameters. *Astronomy & Astrophysics*, 677:A111.

Trefoloni, B., Lusso, E., Nardini, E., Risaliti, G., Marconi, A., Bargiacchi, G., Sacchi, A., and Signorini, M. (2024c). Quasars as standard candles vi: spectroscopic validation of the cosmological sample. *arXiv preprint arXiv:2404.07205.*

Treister, E., Krolik, J. H., and Dullemond, C. (2008). Measuring the fraction of obscured quasars by the infrared luminosity of unobscured quasars. *The Astrophysical Journal*, 679(1):140.

Treister, E. and Urry, C. M. (2006). The evolution of obscuration in active galactic nuclei. *The Astrophysical Journal*, 652(2):L79.

Trinca, A., Schneider, R., Valiante, R., Graziani, L., Zappacosta, L., and Shankar, F. (2022). The low-end of the black hole mass function at cosmic dawn. *Monthly Notices of the Royal Astronomical Society*, 511(1):616–640.

Tsuzuki, Y., Kawara, K., Yoshii, Y., Oyabu, S., Tanabé, T., and Matsuoka, Y. (2006). Fe ii emission in 14 low-redshift quasars. i. observations. *The Astrophysical Journal*, 650(1):57.

Übler, H., Maiolino, R., Curtis-Lake, E., Pérez-González, P. G., Curti, M., Perna, M., Arribas, S., Charlot, S., Marshall, M. A., D'eugenio, F., et al. (2023). Ga-nifs: A massive black hole in a low-metallicity agn at z 5.55 revealed by jwst/nirspec ifs. *Astronomy & Astrophysics*, 677:A145.

Übler, H., Maiolino, R., Pérez-González, P. G., D'Eugenio, F., Perna, M., Curti, M., Arribas, S., Bunker, A., Carniani, S., Charlot, S., et al. (2024). Ga-nifs: Jwst discovers an offset agn 740 million years after the big bang. *Monthly Notices of the Royal Astronomical Society*, 531(1):355–365.

Ueda, Y., Akiyama, M., Hasinger, G., Miyaji, T., and Watson, M. G. (2014). Toward the standard population synthesis model of the x-ray background: Evolution of x-ray luminosity and absorption functions of active galactic nuclei including compton-thick populations. *The Astrophysical Journal*, 786(2):104.

Ueda, Y., Akiyama, M., Ohta, K., and Miyaji, T. (2003). Cosmological evolution of the hard x-ray active galactic nucleus luminosity function and the origin of the hard x-ray background. *The Astrophysical Journal*, 598(2):886.

Ueda, Y., Hashimoto, Y., Ichikawa, K., Ishino, Y., Kniazev, A. Y., Väisänen, P., Ricci, C., Berney, S., Gandhi, P., Koss, M., et al. (2015). [o iii] λ5007 and x-ray properties of a complete sample of hard x-ray selected agns in the local universe. *The Astrophysical Journal*, 815(1):1.

Uomoto, A., Wills, B., and Wills, D. (1976). Image-tube photography of a complete sample of 4c radio sources. *The Astronomical Journal*, 81:905–912.

Urry, C. M. and Padovani, P. (1995). Unified schemes for radio-loud active galactic nuclei. *Publications of the Astronomical Society of the Pacific*, 107(715):803.

Valiante, R., Schneider, R., Volonteri, M., and Omukai, K. (2016). From the first stars to the first black holes. *Monthly Notices of the Royal Astronomical Society*, 457(3):3356–3371.

Veilleux, S. and Osterbrock, D. E. (1987). Spectral classification of emission-line galaxies. *Astrophysical Journal Supplement Series (ISSN 0067-0049), vol. 63, Feb. 1987, p. 295-310. NSERC-supported research.*, 63:295–310.

Verner, E., Bruhweiler, F., Verner, D., Johansson, S., and Gull, T. (2003). Revisited abundance diagnostics in quasars: Fe ii/mg ii ratios. *The Astrophysical Journal*, 592(2):L59.

Verner, E., Verner, D., Korista, K., Ferguson, J. W., Hamann, F., and Ferland, G. J. (1999). Numerical simulations of fe ii emission spectra. *The Astrophysical Journal Supplement Series*, 120(1):101.

Vestergaard, M. and Peterson, B. M. (2006). Determining central black hole masses in distant active galaxies and quasars. ii. improved optical and uv scaling relationships. *The Astrophysical Journal*, 641(2):689.

Vestergaard, M. and Wilkes, B. J. (2001). An empirical ultraviolet template for iron emission in quasars as derived from i zwicky 1. *The Astrophysical Journal Supplement Series*, 134(1):1.

Vietri, G., Piconcelli, E., Bischetti, M., Duras, F., Martocchia, S., Bongiorno, A., Marconi, A., Zappacosta, L., Bisogni, S., Bruni, G., et al. (2018). The wissh quasars project-iv. broad line region versus kiloparsec-scale winds. *Astronomy & Astrophysics*, 617:A81.

Vignali, C., Brandt, W., and Schneider, D. (2003). X-ray emission from radio-quiet quasars in the sloan digital sky survey early data release: the αox dependence upon ultraviolet luminosity. *The Astronomical Journal*, 125(2):433.

Vito, F., Brandt, W. N., Bauer, F. E., Calura, F., Gilli, R., Luo, B., Shemmer, O., Vignali, C., Zamorani, G., Brusa, M., et al. (2019). The x-ray properties of z> 6 quasars: no evident evolution of accretion physics in the first gyr of the universe. *Astronomy & Astrophysics*, 630:A118.

Vogelsberger, M., Genel, S., Springel, V., Torrey, P., Sijacki, D., Xu, D., Snyder, G., Nelson, D., and Hernquist, L. (2014). Introducing the illustris project: simulating the coevolution of dark and visible matter in the universe. *Monthly Notices of the Royal Astronomical Society*, 444(2):1518–1547.

Volonteri, M. (2010). Formation of supermassive black holes. *The Astronomy and Astrophysics Review*, 18:279–315.

Volonteri, M., Haardt, F., and Madau, P. (2003). The assembly and merging history of supermassive black holes in hierarchical models of galaxy formation. *The Astrophysical Journal*, 582(2):559.

Volonteri, M., Silk, J., and Dubus, G. (2015). The case for supercritical accretion onto massive black holes at high redshift. *The Astrophysical Journal*, 804(2):148.

Wada, K. (2012). Radiation-driven fountain and origin of torus around active galactic nuclei. *The Astrophysical Journal*, 758(1):66.

Wang, B., Leja, J., de Graaff, A., Brammer, G. B., Weibel, A., van Dokkum, P., Baggen, J. F., Suess, K. A., Greene, J. E., Bezanson, R., et al. (2024). Rubies: Evolved stellar populations with extended formation histories at z~7-8 in candidate massive galaxies identified with jwst/nirspec. *arXiv preprint arXiv:2405.01473*.

Wang, C., Luo, B., Brandt, W., Alexander, D., Bauer, F., Gallagher, S. C., Huang, J., Liu, H., and Stern, D. (2022a). Nustar observations of intrinsically x-ray weak quasar candidates: An obscuration-only scenario. *The Astrophysical Journal*, 936(2):95.

Wang, F., Yang, J., Fan, X., Hennawi, J. F., Barth, A. J., Banados, E., Bian, F., Boutsia, K., Connor, T., Davies, F. B., et al. (2021). A luminous quasar at redshift 7.642. *The Astrophysical Journal Letters*, 907(1):L1.

Wang, F., Yang, J., Hennawi, J. F., Fan, X., Sun, F., Champagne, J. B., Costa, T., Habouzit, M., Endsley, R., Li, Z., et al. (2023). A spectroscopic survey of biased halos in the reionization era (aspire): Jwst reveals a filamentary structure around az= 6.61 quasar. *The Astrophysical Journal Letters*, 951(1):L4.

Wang, J.-M., Du, P., Hu, C., Netzer, H., Bai, J.-M., Lu, K.-X., Kaspi, S., Qiu, J., Li, Y.-R., Wang, F., et al. (2014). Supermassive black holes with high accretion rates in active galactic nuclei. ii. the most luminous standard candles in the universe. *The Astrophysical Journal*, 793(2):108.

Wang, J.-M., Songsheng, Y.-Y., Li, Y.-R., Du, P., and Zhang, Z.-X. (2020). A parallax distance to 3c 273 through spectroastrometry and reverberation mapping. *Nature Astronomy*, 4(5):517–525.

Wang, S., Jiang, L., Shen, Y., Ho, L. C., Vestergaard, M., Bañados, E., Willott, C. J., Wu, J., Zou, S., Yang, J., et al. (2022b). Metallicity in quasar broad-line regions at redshift 6. *The Astrophysical Journal*, 925(2):121.

Wang, T., Brinkmann, W., and Bergeron, J. (1996). X-ray properties of active galactic nuclei with optical feii emission. *Astronomy and Astrophysics, v. 309, p. 81-96*, 309:81–96.

Wang, T., Zhou, H., Grupe, D., Yuan, W., Dong, X., and Lu, H. (2009). X-ray absorption and optical extinction in the partially obscured seyfert nucleus in mrk 1393. *The Astronomical Journal*, 137(4):4002.

Webb, N. A., Coriat, M., Traulsen, I., Ballet, J., Motch, C., Carrera, F. J., Koliopanos, F., Authier, J., de la Calle, I., Ceballos, M. T., Colomo, E., Chuard, D., Freyberg, M., Garcia, T., Kolehmainen, M., Lamer, G., Lin, D., Maggi, P., Michel, L., Page, C. G., Page, M. J., Perea-Calderon, J. V., Pineau, F. X., Rodriguez, P., Rosen, S. R., Santos Lleo, M., Saxton, R. D., Schwope, A., Tomás, L., Watson, M. G., and Zakardjian, A. (2020). The XMM-Newton serendipitous survey IX. The fourth XMM-Newton serendipitous source catalogue. *arXiv e-prints*, page arXiv:2007.02899.

Welch, B. L. (1947). The generalization of ‘student’s’problem when several different population varlances are involved. *Biometrika*, 34(1-2):28–35.

Wild, V., Groves, B., Heckman, T., Sonnentrucker, P., Armus, L., Schiminovich, D., Johnson, B., Martins, L., and LaMassa, S. (2011). Optical versus infrared studies of dusty galaxies and active galactic nuclei–i. nebular emission lines. *Monthly Notices of the Royal Astronomical Society*, 410(3):1593–1610.

Wilhite, B. C., Brunner, R. J., Grier, C. J., Schneider, D. P., and Vanden Berk, D. E. (2008). On the variability of quasars: a link between the eddington ratio and optical variability? *Monthly Notices of the Royal Astronomical Society*, 383(3):1232–1240.

Wilkes, B. J., Elvis, M., and McHardy, I. (1987). Is optical fe ii emission related to the soft x-ray properties of quasars? *Astrophysical Journal, Part 2-Letters to the Editor (ISSN 0004-637X), vol. 321, Oct. 1, 1987, p. L23-L27.*, 321:L23–L27.

Wilkes, B. J., Kuraszkiewicz, J., Green, P. J., Mathur, S., and McDowell, J. C. (1999). Investigation of the relation between the spectral energy distributions and emission lines in low-redshift quasars. *The Astrophysical Journal*, 513(1):76.

Worrall, D., Giommi, P., Tananbaum, H., and Zamorani, G. (1987). X-ray studies of quasars with the einstein observatory. iv-x-ray dependence on radio emission. *Astrophysical Journal, Part 1 (ISSN 0004-637X), vol. 313, Feb. 15, 1987, p. 596-606. Research supported by the Smithsonian Institution and CNR.*, 313:596–606.

Wright, E. L., Eisenhardt, P. R., Mainzer, A. K., Ressler, M. E., Cutri, R. M., Jarrett, T., Kirkpatrick, J. D., Padgett, D., McMillan, R. S., Skrutskie, M., et al. (2010). The wide-field infrared survey explorer (wise): mission description and initial on-orbit performance. *The Astronomical Journal*, 140(6):1868.

Wu, L., Wang, J.-X., Wang, H.-C., Kang, W.-Y., Hu, W.-D., Wang, T.-G., and Wang, H.-Y. (2023). Ensemble mapping the inner structure of luminous quasars. *Monthly Notices of the Royal Astronomical Society*, 522(1):1108–1117.

Wu, Q. and Shen, Y. (2022). A catalog of quasar properties from sloan digital sky survey data release 16. *The Astrophysical Journal Supplement Series*, 263(2):42.

Xie, X., Shen, S., Shao, Z., and Yin, J. (2015). An apparent redshift dependence of quasar continuum: implication for cosmic dust extinction? *The Astrophysical Journal Letters*, 802(2):L16.

Yang, J., Fan, X., Gupta, A., Myers, A. D., Palanque-Delabrouille, N., Wang, F., Yèche, C., Aguilar, J. N., Ahlen, S., Alexander, D. M., et al. (2023a). Desi $z \gtrsim 5$ quasar survey. i. a first sample of 400 new quasars at $z \sim 4.7$–6.6. *The Astrophysical Journal Supplement Series*, 269(1):27.

Yang, J., Wang, F., Fan, X., Barth, A. J., Hennawi, J. F., Nanni, R., Bian, F., Davies, F. B., Farina, E. P., Schindler, J.-T., et al. (2021). Probing early supermassive black hole growth and quasar evolution with near-infrared spectroscopy of 37 reionization-era quasars at $6.3 < z \leq 7.64$. *The Astrophysical Journal*, 923(2):262.

Yang, J., Wang, F., Fan, X., Hennawi, J. F., Barth, A. J., Bañados, E., Sun, F., Liu, W., Cai, Z., Jiang, L., et al. (2023b). A spectroscopic survey of biased halos in the reionization era (aspire): a first look at the rest-frame optical spectra of $z>$ 6.5 quasars using jwst. *The Astrophysical Journal Letters*, 951(1):L5.

Yang, J., Wang, F., Fan, X., Hennawi, J. F., Davies, F. B., Yue, M., Banados, E., Wu, X.-B., Venemans, B., Barth, A. J., et al. (2020). Pōniuā ‘ena: A luminous $z=$

7.5 quasar hosting a 1.5 billion solar mass black hole. *The Astrophysical Journal Letters*, 897(1):L14.

Yip, C., Connolly, A., Berk, D. V., Ma, Z., Frieman, J., SubbaRao, M., Szalay, A., Richards, G., Hall, P., Schneider, D., et al. (2004). Spectral classification of quasars in the sloan digital sky survey: Eigenspectra, redshift, and luminosity effects. *The Astronomical Journal*, 128(6):2603.

Yoshii, Y., Kobayashi, Y., Minezaki, T., Koshida, S., and Peterson, B. A. (2014). A new method for measuring extragalactic distances. *The Astrophysical Journal Letters*, 784(1):L11.

Young, M., Elvis, M., Risaliti, G., and Marscher, A. (2009). Disk-corona Connection In Quasars: The α_{ox}-l_{uv} Correlation. In *Bulletin of the American Astronomical Society*, volume 41 of *Bulletin of the American Astronomical Society*, page 454.

Yue, M., Eilers, A.-C., Annana, T. T., Panagiotou, C., Kara, E., and Miyaji, T. (2024). Stacking x-ray observations of" little red dots": Implications for their agn properties. *arXiv preprint arXiv:2404.13290.*

Zafar, T., Møller, P., Watson, D., Fynbo, J. P., Krogager, J.-K., Zafar, N., Saturni, F. G., Geier, S., and Venemans, B. P. (2015). Extinction curve template for intrinsically reddened quasars. *Astronomy & Astrophysics*, 584:A100.

Zajaček, M., Czerny, B., Khadka, N., Prince, R., Panda, S., Martínez-Aldama, M. L., and Ratra, B. (2023). Extinction biases quasar luminosity distances determined from quasar uv and x-ray flux measurements. *arXiv preprint arXiv:2305.08179.*

Zamfir, S., Sulentic, J., Marziani, P., and Dultzin, D. (2010). Detailed characterization of hβ emission line profile in low-z sdss quasars. *Monthly Notices of the Royal Astronomical Society*, 403(4):1759–1786.

Zamorani, G., Henry, J., Maccacaro, T., Tananbaum, H., Soltan, A., Avni, Y., Liebert, J., Stocke, J., Strittmatter, P., Weymann, R., et al. (1981). X-ray studies of quasars with the einstein observatory. ii. *Astrophysical Journal, Part 1, vol. 245, Apr. 15, 1981, p. 357-374. Research supported by the US-Israel Binational Science Foundation;*, 245:357–374.

Zappacosta, L., Piconcelli, E., Fiore, F., Saccheo, I., Valiante, R., Vignali, C., Vito, F., Volonteri, M., Bischetti, M., Comastri, A., et al. (2023). Hyperluminous quasars at the epoch of reionization (hyperion). a new regime for the x-ray nuclear properties of the first quasars. *arXiv preprint arXiv:2305.02347.*

Zappacosta, L., Piconcelli, E., Giustini, M., Vietri, G., Duras, F., Miniutti, G., Bischetti, M., Bongiorno, A., Brusa, M., Chiaberge, M., et al. (2020). The wissh quasars project-vii. the impact of extreme radiative field in the accretion disc and x-ray corona interplay. *Astronomy & Astrophysics*, 635:L5.

Zhang, P. (2008). Dimming of supernovae and gamma-ray busts by compton scattering and its cosmological implications. *The Astrophysical Journal*, 682(2):721.

Zheng, W., Kriss, G. A., Telfer, R. C., Grimes, J. P., and Davidsen, A. F. (1997a). A composite hst spectrum of quasars. *The Astrophysical Journal*, 475(2):469.

Zheng, W., Kriss, G. A., Telfer, R. C., Grimes, J. P., and Davidsen, A. F. (1997b). A composite hst spectrum of quasars. *The Astrophysical Journal*, 475(2):469.

Zhou, H., Wang, T., Yuan, W., Lu, H., Dong, X., Wang, J., and Lu, Y. (2006). A comprehensive study of 2000 narrow line seyfert 1 galaxies from the sloan digital sky survey. i. the sample. *The Astrophysical Journal Supplement Series*, 166(1):128.

Zhuang, M.-Y., Ho, L. C., and Shangguan, J. (2018). The infrared emission and opening angle of the torus in quasars. *The Astrophysical Journal*, 862(2):118.

Zinn, P.-C., Middelberg, E., Norris, R. P., and Dettmar, R.-J. (2013). Active galactic nucleus feedback works both ways. *The Astrophysical Journal*, 774(1):66.

Zubovas, K. and King, A. (2013). Bal qsos and extreme ufos: the eddington connection. *The Astrophysical Journal*, 769(1):51.

Ringraziamenti

Non possum esimermi da questa doverosa sezione. Non posso, neppure questa volta. Anzi, forse meno che mai questa volta. Al tempo stesso, diventa sempre più difficile compilare questo lungo elenco che si snoda e si accavalla in una lunga teoria di "grazie" e "sentiti ringraziamenti", senza diventare scontato e ripetitivo, banale, prolisso. Ma cominciamo dunque.

Il primo ringraziamento deve andare alla famiglia tutta, cioè Babbo, Mamma, Nonna, l'ordine è solo alfabetico. Anche se siamo rimasti soltanto questi, devo ringraziare tutti gli altri che sono passati e hanno seminato qualcosa che non sono riusciti a raccogliere. Un grazie tenero a Claudia, che mi ha accompagnato in questo percorso, anzi ad essere preciso, da un po' prima. Ha visto la genesi della mia volontà di intraprenderlo, l'insicurezza nell'attraversarlo, e la soddisfazione -a tratti faticosa- nel concluderlo. Grazie per avermi prestato la tua determinazione, quando mi sembrava di girare a vuoto e che niente di quello che stavo facendo avesse un senso (il chè è accaduto spesso). E con Claudia viene anche tutta la famiglia acquisita, Lucia, Davide, Chiara e Gabriele, ora anche Bernardo, zie, zii e cugini.

Un ringraziamento sincero a Beta, Emanuele e Guido, anche qui l'ordine è solo alfabetico, perchè è difficile mettere su una scala chi mi abbia aiutato di più. Sicuramente devo ringraziarvi per avere riposto in me la fiducia che sarei potuto essere un dottorando in grado di fare davvero qualcosa. Avete investito tempo ed energie su di me, e se ho imparato qualcosa, lo devo in gran parte a voi. Sempre sullo stesso piano, devo ringraziare anche Roberto Maiolino, e Roberto Gilli, l'uno per l'accoglienza sia umana che scientifica al KAVLI, l'altro per la collaborazione, due esperienze che davvero ricordo con piacere.

Non possono mancare i ringraziamenti ai "colleghi", anche se mi sento ancora non poco a disagio a pensare a quello che sto facendo come a un lavoro. Grazie quindi a Matilde per tutti i dubbi ovvi e le stupide domande, ovviamente i miei intendo. Prima o poi imparerò (?). Grazie anche al biondo Cosimo, che poi biondo non è, ma ce lo chiamo lo stesso. Spero che continui a guardare le cose e gli AGN con quell'aria distaccata e irriverente. Grazie anche alle altre e agli altri incontrati lungo la strada, Giovanni e Giulia, che sono volati in Germania, Martina e Lorenzo che non so dove andranno, ma sicuramente faranno bene. In bocca al lupo.

Un saluto affettuoso anche alle inquiline agli inquilini del 153 Victoria Road, Cambridge CB4 3BU, UK, ormai l'ho imparato a mente per mandare i pacchi. Forse un giorno tornerò, ma chissà chi ci sarà rimasto.

Passiamo poi agli amici, qui tutti insieme in un potpourri, senza distinzioni nè ordini. Gli amici di scuola, della Contrada, del rugby, gente con cui ho passato qualche momento bello. Perchè alla fine forse sì, sono quella manciata di momenti belli strappati dal flusso delle cose che danno la voglia di continuare a sbattere la testa su quello che non capisco. Anche se non penso di sapere perchè.

Ciao e grazie, davvero. *Ad maiora.*